

The Pennsylvania State University
The Graduate School
Eberly College of Science

**LONGITUDINAL DOUBLE-SPIN
ASYMMETRY OF FORWARD NEUTRAL
PIONS FROM $\sqrt{s} = 510$ GEV POLARIZED
PROTON-PROTON COLLISIONS AT STAR**

A Dissertation in
Physics
by
Christopher J. Dilks

© 2018 Christopher J. Dilks

Submitted in Partial Fulfillment
of the Requirements
for the Degree of
Doctor of Philosophy

December 2018

The dissertation of Christopher J. Dilks was reviewed and approved* by the following:

Steven Heppelmann
Professor of Physics
Dissertation Adviser
Chair of Committee

Mark Strikman
Distinguished Professor of Physics

Anna Stasto
Associate Professor of Physics

Stéphane Coutu
Professor of Physics and of Astronomy & Astrophysics

Donghui Jeong
Assistant Professor of Astronomy & Astrophysics

Nitin Samarth
Professor of Physics
Department Head

* Signatures are on file in the Graduate School.

Abstract

Longitudinally polarized proton-proton scattering experiments provide access to the gluon polarization contribution to the overall proton spin via a measurement of the longitudinal double-spin asymmetry, A_{LL} . During RHIC data-taking periods in 2012 and 2013, a significant sample of π^0 s scattered in the forward direction was acquired from proton-proton collisions with a center-of-mass energy of 510 GeV and beam polarizations of $\sim 55\%$. The π^0 kinematics were measured by the STAR Forward Meson Spectrometer, an electromagnetic calorimeter spanning a forward pseudorapidity range of $2.5 < \eta < 4$ and a transverse momentum range of $2 < p_T < 10$ GeV/ c . This forward region is primarily sensitive to π^0 s originating from a hard quark, carrying a significant fraction x of the proton momentum, scattering with a soft, low- x gluon. The polarized gluon distribution function, $\Delta g(x)$, which represents the gluon spin contribution to the proton spin, is positive at high x but is rather unconstrained at low x . There are many more gluons than quarks at lower x , and their contribution to the proton spin remains unknown. This new measurement of A_{LL} presented in this dissertation will help place constraints on $\Delta g(x)$ in this important region, down to $x \sim 10^{-3}$.

Contents

List of Figures	x
List of Tables	xv
List of Acronyms	xvi
List of Symbols	xviii
Acknowledgements	xx
1 Introduction	1
1.1 Overview	1
1.2 Quantum Chromodynamics in the Proton	3
1.2.1 Protons and Neutrons	3
1.2.2 Quarks and Gluons	4
1.2.3 Color	6
1.2.3.1 Hadrons and Confinement	6
1.2.3.2 A Note on Feynman Diagrams	7
1.2.3.3 Gluon Color	9
1.2.3.4 Color Antiscreening	10
1.2.3.5 Hadronization	12
1.2.4 Proton Spin Composition	12
1.3 Proton-Proton Scattering	15
1.3.1 Parton Kinematics	15
1.3.2 Parton Distribution Functions	17
1.3.3 Polarized Parton Distribution Functions	20
1.3.4 Spin Sum Rules	23
1.3.5 Parton Scattering: the QCD Subprocess	25
1.3.6 Fragmentation Functions	30

1.3.7	Factorization in pp Scattering	31
1.4	Spin Asymmetries	32
1.4.1	How to Measure a Spin Asymmetry: A_{LL}	32
1.4.2	Single-Spin Asymmetries	34
1.4.3	Transverse Spin Asymmetries	35
1.4.3.1	Transverse Single-Spin Asymmetries	35
1.4.3.2	Transverse Double-Spin Asymmetries	36
1.5	Recent Measurements of $A_{LL}^{\pi^0}$	36
2	Experimental Apparatus	40
2.1	The Relativistic Heavy Ion Collider	40
2.2	The STAR Experiment	44
2.3	The Forward Meson Spectrometer	47
2.3.1	Electromagnetic Showers in the FMS	48
2.3.2	Pion Event Reconstruction Summary	50
2.3.3	FMS Trigger	51
2.3.3.1	General Trigger Logic and Data Flow	52
2.3.3.2	FMS DSM Tree	53
2.3.3.3	FMS Trigger Set	56
2.3.4	Radiation Damage	60
2.4	The Scaler Systems	61
2.5	Polarimetry	62
3	Event Selection	64
3.1	Data Set and Quality Assurance	64
3.2	π^0 Kinematics and FMS Acceptance	70
3.3	Inner and Outer Pseudorapidity Regions	71
3.4	Event Reconstruction	73
3.4.1	Trigger Matching	73
3.4.2	Shower Shapes	75
3.4.3	Distinguishing Between 1-photon and 2-photon Clusters	76
3.4.4	Clustering Algorithm	78
3.4.5	Energy Dependence of the Mass	79
3.5	Gain Corrections	80
3.5.1	Time-Dependent Corrections – The LED Flasher System	81
3.5.2	Nonlinear Energy-Dependent Response Correction	82
3.5.2.1	Nonlinear Gain Correction Model	82

3.5.2.2	Including Radiation Damage	85
3.5.2.3	Application of the Correction	87
3.6	Hot Tower Masking	91
3.7	Pion Event Selection	97
3.7.1	General Kinematic Cuts	97
3.7.2	p_T Threshold Cut	98
3.7.3	Mass Cut	100
3.7.4	Kinematics Distributions	106
4	Relative Luminosity	111
4.1	Basic Computation Algorithm	111
4.2	Accidentals and Multiples Corrections	115
4.2.1	CDF Accidentals Correction	116
4.2.2	CDF Multiple Interactions Correction	118
4.2.3	Rate-Safe Accidentals and Multiples Corrections	120
4.3	R_3 Results	121
4.4	R_3 Cross-Checks	125
4.5	Miscellaneous	131
4.5.1	Anomalous Bunch Crossings	131
4.5.2	N_{bx} vs. Bunch Crossing	131
5	Systematic Uncertainties	133
5.1	Relative Luminosity Systematic	133
5.1.1	Direct VPD and ZDC Comparison: Δ_{R_3} Method	134
5.1.2	Comparison of $A_{LL}^{\pi^0}$ via VPD and ZDC: δ_{ALL} Method	136
5.1.3	Intrinsic Scaler Double-Spin Asymmetries: Δ_{SLL} Method	136
5.1.3.1	Bunch Fitting Algorithm	137
5.1.3.2	Scaler Asymmetry Measurement	137
5.1.4	Scaler Self-Consistency via A_N Cross Ratio: Δ_{DN} Method	141
5.1.5	Correlations of Run 13 Δ_{R_3} and S_{LL} with Spin Patterns	144
5.1.6	Summary of Relative Luminosity Systematics	152
5.2	Polarization Transverse Component Systematic	152
5.3	p_T Uncertainty	156
5.3.1	Energy Uncertainty	157
5.3.1.1	Energy Resolution	157
5.3.1.2	Calibration Anchor Point	160
5.3.1.3	Nonlinear Response	160

5.3.2	Position Uncertainty	162
5.3.3	Vertex Uncertainty	164
5.3.4	Correlation Terms in p_T Uncertainty	164
5.3.5	p_T Uncertainty Result	165
5.4	Summary of Systematic Uncertainties	167
6	$A_{LL}^{\pi^0}$ Analysis Procedure	168
6.1	Kinematic Binning and Means	168
6.2	Polarization	169
6.2.1	Scale Systematic on $A_{LL}^{\pi^0}$	170
6.3	Maximum Likelihood Method A_{LL} Computation	173
6.4	Background Corrections	174
6.4.1	Implementation	174
6.4.2	Signal and Background Fitting	175
6.4.3	Purity Results	179
7	$A_{LL}^{\pi^0}$ Measurement Result	185
7.1	Preliminary $A_{LL}^{\pi^0}$ Measurement	185
7.2	Final $A_{LL}^{\pi^0}$ Measurement	188
7.3	Discussion and Outlook	190
	Appendices	193
A	Decay Kinematics of $\pi^0 \rightarrow \gamma + \gamma$	194
A.1	Invariant Mass	194
A.2	Note on Small Angles from π^0 Decay Cones	200
B	Spin Asymmetries and their Relative Luminosities	201
B.1	Notation	201
B.2	Nine Asymmetries and Relative Luminosities	202
C	Local Polarimetry and Residual Transverse Component Systematic	204
C.1	Local Polarimetry	204
C.2	Relating Local Polarimetry to A_{LL} Systematic	206
D	Decomposing Cross Sections in terms of Spin Asymmetries	208
D.1	Longitudinal Components	208
D.2	Transverse Components	211

D.3	Application: Systematic Uncertainty on A_{LL} due to Nonzero Transverse Polarization	212
E	Shower Shape Derivation and Incident Angle Corrections	213
E.1	Derivation of the Symmetric Shower Shape	213
E.1.1	1-Dimensional Shower Shape	214
E.1.1.1	The Cauchy Distribution	214
E.1.1.2	Segmenting the Line into Cells	215
E.1.1.3	Multiple Photon Sources	216
E.1.2	2-Dimensional Shower Shape	216
E.1.2.1	The FMS Shower Shape Parameterization	218
E.2	Incident Angle Corrections	219
E.2.1	Longitudinal Slices of Symmetric Shower Shapes	219
E.2.2	Simpler Alternative: Cherenkov Parameterization	220
F	Additional Relative Luminosity Figures	225
G	Rate-Safe Counting Derivation	234
G.1	Rate-Safe-Corrected Scaler Counts	234
G.2	A Note on Accidental Coincidences	237
G.3	Corrected Statistical Uncertainty	238
H	Bunch Fitting and Scaler Asymmetries	240
H.1	General Bunch Fitting Algorithm	240
H.2	Uncertainty Propagation	241
H.3	Scaler Asymmetries	242
I	Polarization Uncertainties	244
I.1	Single Beam Polarization	244
I.2	Beam Polarization Product	246
I.3	Combining Uncertainties over Two RHIC Runs	248
I.4	Results	248
J	Including Photon Uncertainties in p_T Uncertainty	252
K	Maximum Likelihood Method for A_{LL} Measurement	254
K.1	Maximum Likelihood Method	254
K.2	Maximum Likely A_{LL}	256

K.3 Statistical Uncertainty	257
L Curing Radiation Damage in the FMS by Photobleaching	259
L.1 Solar Photobleaching	259
L.2 Photobleaching with UV-LEDs	262
 Bibliography	 268

List of Figures

1.1	QED fundamental vertex	9
1.2	QCD vertices and color	10
1.3	Hadronization process	13
1.4	Proton spin structure illustration	14
1.5	Diagram of DIS	16
1.6	Diagram of pp scattering	17
1.7	Parton distribution functions	19
1.8	Polarized parton distribution functions (u, d, \bar{u}, \bar{d})	21
1.9	Polarized parton distribution functions (s, g)	22
1.10	Polarized gluon distribution functions (DSSV14)	22
1.11	ΔG constraints for low- x vs. high- x	24
1.12	Tree-level QCD $2 \rightarrow 2$ Diagrams	26
1.13	Parton-level asymmetry \hat{a}_{LL} vs. COM scattering angle	28
1.14	Fractional contributions of QCD subprocesses to forward π^0 production	29
1.15	Simulation of partonic x accessible within FMS acceptance	30
1.16	π^0 fragmentation functions	31
1.17	A_{LL} for forward π^0 s	37
1.18	A_{LL} for intermediate rapidity π^0 s	38
1.19	A_{LL} for central rapidity π^0 s	39
2.1	Siberian snakes' effect	42
2.2	RHIC schematic	44
2.3	STAR 3D diagram	45
2.4	STAR top view diagram	45
2.5	FMS geometry schematic	48
2.6	EM shower diagram in an FMS Cell	50
2.7	FMS channel to QT board map	54
2.8	FMS DSM tree	55

2.9	FMS jet patch regions	57
2.10	Trigger overlap matrix	59
3.1	Run 12 f_T vs. run index	66
3.2	Run 13 f_T vs. run index	67
3.3	Run 12 Ratio of f_T to fit value vs. run index	68
3.4	Run 13 Ratio of f_T to fit value vs. run index	69
3.5	Scattering coordinates notation	71
3.6	M vs. η and η boundaries	72
3.7	FMS schematic and pseudorapidity boundaries	73
3.8	Sample shower shape	77
3.9	35 mrad cone size with respect to FMS	80
3.10	Photon pair α vs. E with M contours	81
3.11	Photon pair M vs. E with α contours	81
3.12	M vs. E and M vs. α for π^0 s and η -mesons; before $g(E)$ correction	83
3.13	M vs. E and M vs. α for π^0 s and η -mesons; after $g(E)$ correction	84
3.14	$g(E_t)$ model	85
3.15	Pseudorapidity factor $\lambda(\eta)/\lambda_0$ vs. η	88
3.16	Slope factor $R(t)$ vs. days of radiation damage	88
3.17	E_t vs. E_o via $g(E)$ correction	88
3.18	Day-0 Δp_T vs. p_{T_o}	90
3.19	Day-D Δp_T vs. p_{T_o}	90
3.20	Hot spot search algorithm	92
3.21	Hot spot identification result for Run 12 outer region	94
3.22	Hot spot identification result for Run 12 inner region	95
3.23	Hot spot identification result for Run 13 outer region	96
3.24	Hot spot π^0 -masking algorithm	97
3.25	p_T vs. run index for Run 12 outer region	99
3.26	p_T vs. run index for Run 12 inner region	99
3.27	p_T vs. run index for Run 13 outer region	100
3.28	Photon pair M distributions in E bins for outer region	102
3.29	Photon pair M distributions in E bins for inner region	103
3.30	π^0 mass windows vs. runset index for Run 12 outer region	104
3.31	π^0 mass windows vs. runset index for Run 13 outer region	104
3.32	π^0 mass windows vs. runset index for Run 12 inner region	105
3.33	π^0 p_T vs. E	107

3.34	π^0 y -position vs. x -position	108
3.35	π^0 Z distribution	109
3.36	π^0 p_T distribution and bin boundaries for outer region	110
3.37	π^0 p_T distribution and bin boundaries for inner region	110
4.1	Example spin patterns	113
4.2	Scaler bit counts	115
4.3	CDF accidentals and multiples corrections schematic	116
4.4	Scale and physical process probabilities schematic	117
4.5	Fractional change in CDF corrected counts	119
4.6	Fractional change in rate-safe corrected counts	122
4.7	R_3 from VPD for Run 12	123
4.8	R_3 from VPD for Run 13	124
4.9	Comparison of R_3 via CDF and rate-safe correction methods for Run 12	127
4.10	Comparison of R_3 via CDF and rate-safe correction methods for Run 13	128
4.11	Comparison of R_3 from ZDC and VPD for Run 12	129
4.12	Comparison of R_3 from ZDC and VPD for Run 13	130
4.13	N_{bx} vs. bunch crossing number	132
5.1	$R_3^{\text{ZDC}} - R_3^{\text{VPD}}$ distribution for Run 12	134
5.2	$R_3^{\text{ZDC}} - R_3^{\text{VPD}}$ distribution for Run 13	134
5.3	Spin patterns for Run 12	139
5.4	Spin patterns for Run 13	139
5.5	S_{LL} via VPD/ZDC for Run 12	140
5.6	S_{LL} via VPD/ZDC for Run 13	140
5.7	D_N distributions	143
5.8	Bunch crossing distributions showing afterpulsing	145
5.9	Deconvolved afterpulse signal	147
5.10	Deconvolved afterpulse signal noise	147
5.11	Afterpulse effect correlation to post-abort gap bunch crossing removals	149
5.12	Afterpulse effect correlation to pre-abort gap bunch crossing removals	149
5.13	S_{LL} distributions for post-abort gap bunch crossing removals for Run 12	150
5.14	S_{LL} distributions for post-abort gap bunch crossing removals for Run 13	151
5.15	Run 12 ε_T in ZDC-SMD local polarimeter	154
5.16	Run 12 ε_L in ZDC-SMD local polarimeter	154
5.17	Run 13 ε_L in ZDC-SMD local polarimeter	155
5.18	A_Σ vs. p_T from Run 11	155

5.19	p_T uncertainty schematic	157
5.20	FNAL PMT-to-Pb-glass optical coupling test results	159
5.21	p_T distribution comparison for day-0 and day- D	161
5.22	Vertex distribution	164
5.23	p_T uncertainty σ_{p_T} vs. p_T	166
6.1	Polarization vs. run index for Run 12	171
6.2	Polarization vs. run index for Run 13	172
6.3	Sample M distribution signal+background fits for outer region	178
6.4	Sample M distribution signal+background fits for inner region	179
6.5	π^0 purities for p_T bin 1	181
6.6	π^0 purities for p_T bin 2	181
6.7	π^0 purities for p_T bin 3	182
6.8	π^0 purities for p_T bin 4	182
6.9	Overall π^0 purities for each p_T bin	183
6.10	$A_{LL}^{\pi^0}$ background correction implementation for outer region	184
6.11	$A_{LL}^{\pi^0}$ background correction implementation for inner region	184
7.1	Preliminary measurement of $A_{LL}^{\pi^0}$ vs. E	187
7.2	Preliminary measurement of $A_{LL}^{\pi^0}$ vs. p_T	187
7.3	Final measurement of FMS $A_{LL}^{\pi^0}$ vs. p_T	189
7.4	Running integrals $\Delta G _{x_{\min}}^1$ and $\Delta \Sigma _{x_{\min}}^1$	191
A.1	α vs. E plane with M contours for fixed Z	196
A.2	M vs. E plane with α contours for fixed Z	197
A.3	M vs. Z plane with α contours for fixed E	198
A.4	E_2 vs. E_1 and E vs. Z planes with α contours for $M = M_{\pi^0}$	199
A.5	E_2 vs. E_1 and E vs. Z planes with α contours for $M = M_{\eta}$	199
E.1	1-dimensional Cauchy distribution physical picture	214
E.2	2-dimensional Cauchy distribution physical picture	217
E.3	New shower shape parameterization result	224
F.1	R_3 from ZDC for Run 12	226
F.2	R_3 from ZDC for Run 13	227
F.3	Comparison of R_3 from E and W for Run 12	228
F.4	Comparison of R_3 from E and W for Run 13	229
F.5	Comparison of R_3 from E and X for Run 12	230

F.6	Comparison of R_3 from E and X for Run 13	231
F.7	Comparison of R_3 from W and X for Run 12	232
F.8	Comparison of R_3 from W and X for Run 13	233
L.1	Light source spectrum used for Pb-glass transmission spectra	260
L.2	Pb-glass transmittance spectra with and without radiation damage	260
L.3	Pb-glass transmittance spectra ratios	261
L.4	UV-LED curing tests	262
L.5	Radiation damage vs. η	265
L.6	UV-LED array schematic	265
L.7	UV-LED FMS curing result	266
L.8	UV-LED array power distribution schematic	266
L.9	UV-LED and FMS HV controller screenshot	267

List of Tables

2.1	FMS trigger bit locations	58
3.1	Shower shape fit parameters	76
3.2	$g(E)$ model parameters	85
3.3	$g(E)$ model radiation damage parameters	87
3.4	Hot spot search parameters	93
4.1	Scaler bit recombinations	114
4.2	Consistent R_3 measurement requirements	126
5.1	Double-spin patterns	135
5.2	Double-spin state differences for post-abort bunch crossings	148
5.3	Summary of relative luminosity systematic uncertainties	152
5.4	p_T systematic uncertainty contribution G	162
5.5	W and X_0 values for FMS Pb-glass	163
5.6	Summary of $A_{LL}^{\pi^0}$ systematic uncertainties	167
6.1	Kinematic binning for $A_{LL}^{\pi^0}$	169
6.2	Kinematic bin means for $A_{LL}^{\pi^0}$	169
6.3	Overall polarizations and uncertainties	170
7.1	$A_{LL}^{\pi^0}$ measurement numerical values	190
B.1	Nine asymmetries and their relative luminosities	202

List of Acronyms

ADC Analog-to-Digital Converter
AND Boolean Logical AND
BBCE,BBCW,BBCX BBC scaler counts E,W,X
BBC Beam Beam Counter
BG Background
BNL Brookhaven National Laboratory
BS Board Sum trigger
CDF Collider Detector at Fermilab
DAQ Data Acquisition
DIS Deep Inelastic Scattering
DSA Double Spin Asymmetry
DSM Data Storage and Manipulation
E East-single scaler count
FMSOR OR of LgBS, SmBS, JP triggers
FMS Forward Meson Spectrometer
FNAL Fermi National Accelerator Laboratory
HPSS High Performance Storage System
HT High Tower trigger
HV High Voltage
JP Jet Patch trigger
L2sum Level 2 sum (trigger)
LED Light Emitting Diode
LgBS Large Board Sum trigger
MB Minimum Bias
MLM Maximum Likelihood Method
NDF Number of Degrees of Freedom
OR Boolean Logical OR
PDU Power Distribution Unit

PHENIX Pioneering High Energy Nuclear Interaction Experiment
PMT Photomultiplier Tube
QA Quality Assurance
QCD Quantum Chromodynamics
QED Quantum Electrodynamics
QT8 8-channel QT card
QT Charge (Q) Time integration
RADPHI Radiative Phi Decay Experiment
RHIC Relativistic Heavy Ion Collider
RMS Root Mean Square
SLAC Stanford Linear Accelerator Center
SmBS Small Board Sum trigger
SSA Single Spin Asymmetry
STAR Solenoidal Tracker at RHIC
TAC Time-to-Amplitude Converter
TCU Trigger Control Unit
TSSA Transverse Single Spin Asymmetry
UV-LED Ultraviolet Light Emitting Diode
VPDE,VPDW,VPDX VPD scaler counts E,W,X
VPD Vertex Position Detector
W West-single scaler count
X East-and-west coincidence scaler count
ZDCE,ZDCW,ZDCX ZDC scaler counts E,W,X
ZDC Zero Degree Calorimeter
ZDC-SMD Zero Degree Calorimeter Shower Maximum Detector

List of Symbols

- \oplus Quadrature summation: $A \oplus B = \sqrt{A^2 + B^2}$
- a_i Shower shape parameter
- A Position uncertainty from incident angle effect
- A_B Background A_{LL}
- A_{LL} Longitudinal double-spin asymmetry
- $A_{LL}^{\pi^0}$ Longitudinal double-spin asymmetry of π^0 s
- A_L Longitudinal single-spin asymmetry
- A_M Measured (signal+BG) A_{LL}
- A_{NN} Full transverse double-spin asymmetry
- A_N Transverse single-spin asymmetry
- A_{TT} Transverse double-spin asymmetry (amplitude of azimuthal modulation)
- A_S Signal (π^0 , *i.e.*, BG-subtracted) A_{LL}
- A_Σ Transverse double-spin asymmetry (overall offset)
- b_i Shower shape parameter
- C Energy uncertainty from calibration
- D_N Difference in A_N via relative luminosity and cross-ratio
- E Energy (usually of a photon pair)
- $E_{1(2)}$ Energy of photon 1(2)
- $E_{+(-)}$ Energy of photon with higher- E (lower- E)
- E_o Observed E (before application of $g(E)$)
- E_t True E (after application of $g(E)$)
- F π^0 purity
- $g(E)$ Nonlinear E -dependent gain correction
- G Energy uncertainty from additional nonlinearity from radiation damage
- h Distance between FMS hit and beam axis
- h_B Helicity of blue beam proton
- h_Y Helicity of yellow beam proton
- $L_{\pm\pm}$ Integrated luminosity for given double-spin state (\pm, \pm)

M Invariant mass (usually of a photon pair)
 $N_{\pm\pm}$ Yield for given double-spin state (\pm, \pm)
 P_B Polarization of blue beam for a fill
 P_Y Polarization of yellow beam for a fill
 \mathbb{P}_B Luminosity-weighted average polarization of blue beam
 \mathbb{P}_Y Luminosity-weighted average polarization of yellow beam
 pp Proton-Proton collisions
 p_T Transverse momentum
 p_{T_o} Observed p_T (before application of $g(E)$)
 p_{T_t} True p_T (after application of $g(E)$)
 Q Energy resolution
 Q^2 Momentum transfer squared in inelastic scattering
 R_i Relative luminosity i (*e.g.*, $i = 3$ for double-spin asymmetries)
 R_z Nominal distance between FMS and vertex
 s Square of center-of-mass energy (Mandelstam variable)
 S_{LL} Scaler system's A_{LL}
 W Position resolution component from energy resolution
 X_0 Radiation length
 x Horizontal direction (see y and z for orientation); also denotes Bjorken- x
 y Vertical (upward) direction
 z Beam direction (toward the FMS)
 Z Energy imbalance
 α Opening angle of 2-photon decay
 γ Photon
 $\Delta_{A_{LL}}$ Shift systematic uncertainty on A_{LL}
 ε_L Raw longitudinal single-spin asymmetry
 ε_T Raw transverse single-spin asymmetry
 η Pseudorapidity (also sometimes refers to η -meson)
 θ Scattering angle
 π^0 Neutral pion
 $\sigma_{\pm\pm}$ Cross section for given double-spin state (\pm, \pm)
 σ_{\max} Max eigenvalue of 2nd moment matrix of hit cluster
 σ_V Uncertainty of variable V (not to be confused with cross section)
 ϕ Azimuthal angle
 Ω Efficiency times acceptance

Acknowledgements

This material is based upon work supported by the National Science Foundation under Award No. 1613939. Any opinions, findings, and conclusions or recommendations expressed in this publication are those of the author(s) and do not necessarily reflect the views of the National Science Foundation. Work at the Relativistic Heavy Ion Collider at Brookhaven National Laboratory is supported in part by the Office of Nuclear Physics within the U.S. DOE Office of Science.

First and foremost, I would like to thank my advisor Steve Heppelmann for teaching me countless things about physics and the world in general, and inspiring a lifelong analytical way of thinking. I would also like to thank my undergraduate physics professor, Leonard Gamberg, for inspiring me to pursue a career in physics in the first place. Many thanks to Stephen Trentalange for guiding me on the hardware side of experimental particle physics, and teaching me many things about how to operate a detector as well as many other fascinating topics in physics in general. I must also thank my labmate and fellow graduate student at Penn State, Branden Summa, who was always happy to discuss anything from physics analysis to computer glitches.

I thank Mark Strikman for not only his particle physics classes, but also for the many interesting discussions we've had. I must also thank the other members of my committee, Anna Stasto, Stephane Coutu, and Donghui Jeong. Many thanks to Stephane Coutu for thoroughly reading this dissertation and catching grammar and style errors, many of which were easy to miss without a careful eye.

This analysis could not have been done without the guidance of several members of the STAR spin physics working group, including Carl Gagliardi, Oleg Eyser, Renee Fatemi, Elke-Caroline Aschenauer, Jim Drachenberg, Anselm Vossen, Adam Gibson, and several others. I also owe many thanks to David Kapukchyan for thoroughly reviewing the most critical algorithms in my analysis code. On the experimental operations side, I owe thanks to Akio

Ogawa, Bill Christie, Bob Soja, Oleg Tsai, and many others for all their help.

I owe many thanks to the many fellow graduate students and postdoctoral researchers, which are too numerous to list without forgetting someone. In particular I'd like to thank Len Eun, Yuxi Pan, Chong Kim, Aishwarya Kumar, Cody Messick, Tommy Foley, Dasha Pankova, Zilong Chang, Jinlong Zhang, Mriganka Mondal, and Chanaka De Silva. I would also like to thank Daner Ferhadi, Dan Pearson, Rosan Patel, Lance Boyer, and Tom Pengilly, close friends from my undergraduate days who still inspire me to think more deeply about physics and mathematics. I must also thank Andre Harner for all of the time we spent playing music together, providing a creative outlet during all of my time in graduate school.

And last but most certainly not least, I thank my parents and family for inspiring me to pursue a career in a field that I'm genuinely interested in. Finally I have to thank my grandmother, Norma Overholtzer, for always asking simple, but rather deep physics questions, as well as for the interesting discussions that always followed.

“It is imperative in science to doubt. It is absolutely necessary, for progress in science, to have uncertainty as a fundamental part of your inner nature. To make progress in understanding, we must remain modest and allow that we do not know. Nothing is certain or proved beyond all doubt. You investigate for curiosity, because it is unknown, not because you know the answer.”

— Richard P. Feynman

Chapter 1

Introduction

1.1 Overview

The spin of the proton and its relation to the spin and orbital angular momenta of its partons, quarks and gluons, are still not fully understood. Modern models decompose the proton spin as a sum of the quark and gluon spins and orbital angular momenta. Historical models, however, assumed that since the proton is stable it is in its lowest energy configuration, which is a spherically symmetric state with orbital angular momentum quantum number $l = 0$. This assumption implies that the net contribution of partonic orbital angular momentum to the proton spin is zero [1]. Since the proton is in a spherically symmetric state, its potential, mediated by the gluons, is also likely spherically symmetric and the gluon angular momentum was therefore assumed to not contribute to the proton spin. The quark spin was the only contribution to the proton spin that was thought to be nonzero [2].

Since the proton and the quarks are all spin-1/2 particles and the proton is composed of three constituent quarks, two up quarks and one down quark, it was assumed that the projection of the proton spin along any axis, say the z axis, is the sum of the quark spins projected along z : two of the quarks have spin aligned with the proton spin and the other anti-aligned. Typically the two up quarks' spins were thought to be aligned with the proton spin and the down quark's anti-aligned, however this configuration is not the only possibility. No matter which quark has which spin, the assumption was that if the proton spin projection is $+1/2$, then that is equal to the sum of two $+1/2$ quark spins and one $-1/2$ quark spin from the third.

The EMC experiment [3, 4] shattered this simple model in 1987, by performing a measurement that revealed the quark spins only contribute a fraction ($\sim 4 - 24\%$) to the overall proton spin. This measurement led to the so-called *proton spin crisis*, giving rise to the question of the true origin of the proton spin. Modern measurements have constrained the

quark spin contribution to ~ 0.24 , at a scale given by the momentum transfer squared $Q^2 = 10 \text{ GeV}^2/c^2$ [5, 6, 7, 8, 9]. To solve the crisis, the gluon angular momentum and partonic orbital angular momentum must also contribute substantially to the proton spin [10, 11, 12].

We now know the gluon angular momentum, *i.e.*, helicity, also contributes a non-negligible fraction to the proton spin. The contribution from gluons which carry a fraction x of the proton longitudinal momentum in the range $0.05 < x < 1.0$ is around 0.23 ± 0.06 [13] or $0.20_{-0.07}^{+0.06}$ [14]. On the other hand, the partonic orbital angular momentum has not yet been measured, however it likely accounts for the remainder of the proton spin.

The naive picture of a proton as being composed of three quarks with mediating gluons is a mere cartoon; one must instead attempt to consider *all* of the partons within the proton, including the sea quark and antiquark pairs, along with the soft gluons. The number density of partons within a proton is modelled as a probability density distribution dependent on x . For $x > 0.03$, the up and down quarks dominate the partonic densities, however as x decreases toward lower values, the gluons begin to *vastly* dominate. Furthermore, models which describe the contribution to the spin of the proton from gluon helicity are rather unconstrained for $x < 0.05$, which leaves one to question how much this myriad of soft, low- x gluons is contributing to the proton spin.

This dissertation presents a measurement of the longitudinal double-spin asymmetry, A_{LL} , for forward-scattered neutral pions [15], which is directly sensitive to the gluon helicity contribution down to $x \sim 10^{-3}$, a region abundant with soft gluons. This is the first time this important region of gluonic x has been sampled with this level of sensitivity. The measurement agrees with extrapolations of theoretical models that predict the low- x gluon helicity contribution is nearly zero; however, given the large uncertainties on these predictions at low x , this measurement ultimately places constraints on the models. Analyses of all available A_{LL} data, including measurements from inclusive jets and dijets at lower rapidities, *i.e.*, at more-central scattering angles, along with our new measurement for forward neutral pions, will bring the gluon helicity contribution into clearer focus, especially for this important low- x region.

This chapter begins with an introduction of quantum chromodynamics, which provides sufficient background to begin discussing the partonic model of proton-proton scattering. Building on this foundation, the definition of A_{LL} will be presented and its direct sensitivity to the gluon helicity will be emphasized. Finally, a survey of recent A_{LL} measurements that are pertinent to this analysis will be presented.

Chapter 2 then follows with details of the experiment itself, which took place at the Relativistic Heavy Ion Collider (RHIC) in the STAR experimental hall. Chapter 3 details the

event selection, which is used to select for neutral pions, chapter 4 details a measurement of the relative luminosity, which is needed in order to measure A_{LL} , and chapter 5 discusses various contributions to the systematic uncertainty on A_{LL} and on pion transverse momentum. Chapter 6 then brings everything together, illustrating how A_{LL} was measured from the pion sample and relative luminosity, along with proton beam polarizations. Lastly, the A_{LL} measurement result is presented in chapter 7, along with a discussion thereof. Derivations, along with other topics that are relevant but a bit digressive, are found in the appendices.

1.2 Quantum Chromodynamics in the Proton

Most of the matter we humans interact with is composed of atoms. The atom, the so-called building block of matter, derives its name from the Greek word *atomos*, meaning “indivisible.” This is a bit of a misnomer, however, as the atom is composed of a hard, dense nucleus, surrounded by electrons. The nucleus itself is composed of nucleons: positively charged protons and neutral neutrons. The divisibility of matter does not stop here, however. The nucleons are further composed of quarks and gluons, the fundamental particles which interact under the *strong interaction*. The associated strong force is what holds the nucleus together, and without it, the electrical repulsion between the protons would cause the nucleus to fall apart. The topic of this dissertation focuses on the proton as a probe into the world of quantum chromodynamics (QCD), the quantum mechanical understanding of the strong interaction. For introductory-level material on this topic and on particle physics in general, see textbooks such as [16, 17, 18].

1.2.1 Protons and Neutrons

The proton is the primary object of study in this thesis. Given the electron charge of $-e \approx -1.6 \times 10^{-19}$ Coulombs, the proton has a positive charge of $+e$. Furthermore, its spin quantum number is $s = 1/2$, the same as the electron; the spin angular momentum of a spin-1/2 particle measured along a particular axis will only be $s_z = +\hbar/2$, called spin-up, or $s_z = -\hbar/2$, called spin-down, where $\hbar = h/2\pi$ is the reduced Planck’s constant. This *quantization* of the electron spin was observed in the Stern-Gerlach experiment, where electrons were sent through a magnetic field, perpendicular to their momentum, and the spin-up electrons deflected one way while the spin-down electrons deflected the other [19, 20]. Since the proton has a half-integer spin, it is classified as a fermion, as opposed to bosons, which have an integer values of s . Finally, the mass of the proton is 1.67×10^{-27} kg, or in units more useful in high energy physics, $938.3 \text{ MeV}/c^2$ [21], which makes use of the

mass-energy equivalence in special relativity, $E = mc^2$.

As an aside, it is common in high energy physics literature to use a set of units where the speed of light in a vacuum, $c \approx 3.00 \times 10^8$ m/s, is set simply to 1, with no units, that is, *dimensionless* 1. The energy-momentum relation in special relativity, $E^2 = (mc^2)^2 + (pc)^2$, simplifies to $E^2 = m^2 + p^2$, which causes both mass m and momentum p to each have units of energy. Many other such conveniences also occur and this $c = 1$ convention, along with $\hbar = 1$, will be assumed throughout this dissertation.

The neutron is very similar to the proton, enough so that the neutron and proton are in general referred to as nucleons, since they are the constituents of the atomic nucleus. The neutron is electrically neutral, also has a spin quantum number of $s = 1/2$, and has a mass of 939.6 MeV/ c^2 (or MeV, with $c = 1$ units) [21]. As will be discussed later, the quantum chromodynamic properties of the constituents of the proton can be studied by accelerating protons in an accelerator, and colliding them with other protons or nuclei in a collider. The neutron cannot be directly accelerated, however, since it is not charged (although it can be studied via the deuteron, which is a nucleus with one neutron and one proton). Therefore, the proton is the most appropriate “lab” in which we can study QCD.

1.2.2 Quarks and Gluons

The internal structure of an atom was first explained by Ernest Rutherford in 1911 [22], during experiments performed in 1908–1913 by Hans Geiger and Ernest Marsden in collaboration with Rutherford, *viz.*, [23]. In the cited experiment, α particles, which are nuclei composed of two protons and two neutrons, were directed at a thin sheet of metal; if an α particle scattered back on the same side of the metal, it was observed as a scintillation in a zinc sulfide screen. Of the metals tested, gold produced the highest rate of observed scintillations; moreover, a small rate of scintillations was even observed when no metal sheet was in place, due to scattering off atoms in the air. These “back-scatterings” of α particles can only be explained by hard-scatterings of α particles on some dense concentration of electric field within the atoms: this dense object is the atomic nucleus.

If atoms were just diffuse distributions of charge, most of the α particles would deflect at small angles, but since large scattering angles are observed, the atom has some internal *hard* structure. The same sort of question can be asked about the nucleons, for example by directing electrons at protons in an experiment called Deep Inelastic Scattering (DIS). Such experiments were first performed at the Stanford Linear Accelerator Center (SLAC), where an electron beam was directed at a liquid hydrogen target, composed of mostly protons, from the perspective of the incoming electrons. The deflection of electrons to high scattering

angles was observed [24] [25], and similar to the Rutherford experiment, the observation of high scattering angles in DIS was indicative of internal, hard structure within the proton.

It is now known that protons are composed of quarks (q), antiquarks (\bar{q}), and gluons (g), particles which are collectively called partons. There are six types of quarks, called flavors: up (u), down (d), charm (c), strange (s), top (t), and bottom (b). The u , c , and t quarks have a charge of $+2e/3$ whereas the d , s , and b quarks have a charge of $-e/3$. All quarks have spin quantum number $1/2$ and are therefore fermions. The u and d quarks each have a mass of a few MeV, but defining bare quark mass is difficult to do, for reasons which will be revisited after some discussion of quantum chromodynamic phenomena.

The gluons, on the other hand, have some properties identical to the photon: no mass (and therefore also propagate at the speed of light), spin $s = 1$ (bosonic), and electrical neutrality. Whereas the photons are the *mediators* of the electromagnetic interaction, the gluons mediate the strong interaction. When one charged particle moves, the change in the electric field around that particle propagates at the speed of light; this “ripple of change” in the field can be thought of as a photon, and another charged particle nearby does not feel the effect of the change in the electromagnetic field until the ripple (photon) reaches it. This model is a cartoon picture of quantum electrodynamics (QED), simply stating that the photon mediates or “carries” the electromagnetic force. An analogous picture can be thought of for the strong force, where the gluons mediate the strong interaction between quarks in QCD.

The proton is composed of two u quarks and a d quark; that is not completely true, as will be discussed later, but for now the notion is sufficient. Let us assess how the quark properties combine to give the proton properties. Adding the quark charges together, one obtains $2(2e/3) - e/3 = e$, the correct proton charge. Regarding the spin, if one imagines that the u quarks’ spin projections are aligned with the proton spin projection, while the d quark spin is anti-aligned, then the full spin adds as $2(1/2) - 1/2 = +1/2$, which is indeed the spin of the proton. This composition of the proton spin is not what is observed experimentally however, and we will return to this important point after discussing more on parton properties in general. Finally, adding the quark masses together of a few MeV each does not nearly account for the full ~ 1 GeV mass of the proton, leading one to question where the rest of the proton mass comes from. It turns out that the binding energy of the quarks, provided by the mediating gluons, actually accounts for the vast majority of the mass. Consequently, the mass of most observed matter in the universe actually comes from the energy holding the nuclei together.

1.2.3 Color

The prefix *chromo-* in “chromodynamics” derives from the Greek word *khroma*, meaning “color.” The color in QCD is not the same color which corresponds to wavelengths of visible light; instead QCD color refers to a type of *charge* associated with the strong force: color charge. While objects with electric charge participate in the electromagnetic interaction, objects with color participate in the strong interaction, and quarks and gluons are the only known particles with color.

In the electromagnetic interaction, there is only one type of charge, the electric charge, which can either be positive or negative. On the other hand, in the strong interaction there are three color charges: red, green, and blue. There is a notion of positivity and negativity for each color: quarks can be red (r), green (g), or blue (b), whereas antiquarks can be antired (\bar{r}), antigreen (\bar{g}), or antiblue (\bar{b}). The quarks and antiquarks not only have electromagnetic charge, which allows them to participate in the much weaker electromagnetic interaction, but they also have color charge, which allows them to also participate in the dominant strong interaction.

1.2.3.1 Hadrons and Confinement

In the electromagnetic interaction, a charge-neutral system has an equal number of positive and negative charges (or the trivial case of *no* charges). Similarly in the strong interaction, a quark-antiquark pair with the same color charges but opposite in sign has a net color charge of zero; this gives us three possible color-neutral systems: $r\bar{r}$, $b\bar{b}$, and $g\bar{g}$. Furthermore, the combination of three quarks, each colored differently, forms the color-neutral system rgb , as does the antiquarks in $\bar{r}\bar{g}\bar{b}$; these combinations of three colors explain the inspiration for using the word “color,” since shining red, green, and blue spotlights toward the same area on a screen reveals the combination of the three colors is the colorless white.

One of the most striking properties of QCD is color confinement: the observation of a single color-charged object so far seems to be impossible, and all particles directly observable in nature are color-neutral. A quark prefers to be either paired with an antiquark or with two other quarks, such that the final system is color-neutral. These color-neutral systems which are composed of quarks and gluons are composite particles called *hadrons*, and those which are composed of a quark and an antiquark are called *mesons*, with the color part of the wave function

$$\psi_c^{q\bar{q}} = \frac{1}{\sqrt{3}} (r\bar{r} + g\bar{g} + b\bar{b}), \quad (1.1)$$

while hadrons with a color-neutral system of three quarks (or three antiquarks) are called

baryons, with the color wave function

$$\psi_c^{qqq} = \frac{1}{\sqrt{6}}(rgb + gbr + brg - bgr - rbg - grb). \quad (1.2)$$

The meson color wave function is symmetric, that is, if two colors are exchanged then the sign of $\psi_c^{q\bar{q}}$ does not change; on the other hand, exchanging two colors does change the sign of the baryon color wave function, which is antisymmetric. Thus mesons are bosons with integer spin, whereas baryons are fermions with half-integer spin.

We now mention some example hadrons, focusing on those pertinent to this thesis. An important example meson is the pion, composed of up and down quarks and antiquarks. Since the u and d quarks are the least massive flavors, the pions are the least massive of all the hadrons. The charged pions, the π^+ and π^- , are composed of $u\bar{d}$ and $d\bar{u}$, respectively, while the neutral pion, denoted π^0 , is composed of a quantum superposition of $u\bar{u}$ and $d\bar{d}$ and is the primary observable discussed in this thesis. Regarding baryons, the proton is one composed of uud quarks, as is the neutron, being composed of ddu quarks. Any other combination of the 6 quark flavors into $q\bar{q}$ mesons or qqq baryons (or $\bar{q}\bar{q}\bar{q}$ antibaryons) is possible, and names are given to each observed or predicted hadron; higher order color-neutral combinations are also theoretically possible, such as penta-quarks, which are composed of 5 quarks (typically rgb plus a color+anticolor pair), as well as *glue balls*, which are color-neutral bundles of gluons, since gluons also carry color (and anticolor) and can even self-interact.

1.2.3.2 A Note on Feynman Diagrams

Before discussing gluon color, we pause here to briefly introduce Feynman diagrams. The interactions in QCD, or in any quantum field theory in general, are described by scattering amplitudes, the square of which gives the associated scattering differential cross sections. Feynman diagrams are used to calculate these amplitudes, but this use of them is outside the scope of this dissertation (see instead standard textbooks such as [26, 27]); instead, diagrams will be used here only in order to help classify the types of possible interactions as needed.

In quantum field theory, one defines an interaction as the transformation from a set of initial states, *e.g.*, incoming particles with specific 4-momenta, to a set of final states, outgoing particles with 4-momenta, such that energy and momentum are conserved overall. The scattering amplitude for any interaction can be expressed as a sum of terms in a perturbative expansion, with each one of these terms represented by a Feynman diagram. Each diagram is a *graph*, as in a graph from the mathematical field of graph theory, built with lines and vertices. Lines on a Feynman diagram represent *propagators*, which describe the transit of

a particle with a certain 4-momentum from one moment in time to another. The endpoints of a propagator represent these moments, which can be either at a *vertex* or a *source*. A vertex represents a fundamental interaction in the quantum field theory, where 3 or more propagators can meet at a point such that sum of all incoming particles' 4-momenta balances the sum of all outgoing particles'. A source, on the other hand, represents a particle in either the initial or final state of the overall interaction, defined at times sufficiently far in the past or the future from the interaction time.

In order to interpret a single diagram, one mandates a time-ordering in order to distinguish the final states from the initial states. For internal propagators, which are those with each endpoint at a vertex, the time-ordering is often ambiguous; for those propagators, the perturbative summation basically sums over the two possibilities, thus their time-ordering does not really matter. These internal propagators are called *virtual particles* and while not observed in the interaction, they are still considered in the scattering amplitude calculation.

Regarding notation, a line with an arrow represents a fermion or antifermion propagator: it is a fermion (antifermion) if the arrow is pointing along (opposite) the time-ordering direction. Again, since time-ordering for virtual particles is ambiguous, an internal, arrowed propagator represents both a fermion and an antifermion. Wavy lines denote photon propagators and looped lines denote gluon propagators; neither of these have arrows because each is its own antiparticle.

Any quantum field theory, such as QCD or QED, has a set of fundamental vertices which describes all allowed fundamental interactions within that theory. All possible Feynman diagrams for any interaction, no matter how complicated, can be constructed as graphs using only the fundamental vertices and propagators. The only fundamental vertex in QED is a fermion-antifermion-photon vertex, as shown in figure 1.1. In order to interpret this vertex, let f represent a fermion, \bar{f} an antifermion, and γ a photon. The six possible time-orderings are:

- $f \rightarrow \gamma f$: a fermion emits a photon, continuing on with less momentum
(time direction \searrow)
- $f\gamma \rightarrow f$: a fermion absorbs a photon, continuing on with more momentum
(time direction \nearrow)
- $\bar{f} \rightarrow \gamma \bar{f}$: an antifermion emits a photon, continuing on with less momentum
(time direction \swarrow)
- $\bar{f}\gamma \rightarrow \bar{f}$: an antifermion absorbs a photon, continuing on with more momentum
(time direction \nwarrow)

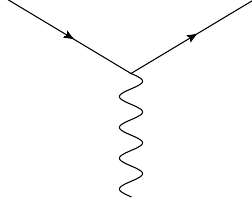


Figure 1.1: QED fundamental vertex.

- $f\bar{f} \rightarrow \gamma$: a fermion and an antifermion annihilate, becoming a photon (time direction \downarrow)
- $\gamma \rightarrow f\bar{f}$: a photon with sufficient energy pair-produces a fermion-antifermion pair (time direction \uparrow)

QCD is somewhat analogous to QED, with a similar fundamental vertex: quark-antiquark-gluon. The presence of color charge, however, allows for additional fundamental vertices pertaining to gluon self-interactions. This self-interaction ultimately introduces two additional fundamental vertices to QCD.

1.2.3.3 Gluon Color

While the photon mediates the electromagnetic force in QED, it does not carry electric charge. The gluon of QCD does, however, carry color charge; in fact, gluons carry both color and anticolor. For example, if a red quark and a green quark scatter by exchanging a gluon, then the red quark could become green and the green quark will become red; in this case the gluon carried red+antigreen or green+antired (technically, the sum of the two in terms of QCD scattering amplitudes via Feynman diagrams). Because the gluons carry color, they can also interact with one another. One gluon can become two, or two can become one, and both of these are enumerated in the 3-point gluon vertex. There is also a 4-point gluon vertex, which represents any of the processes $G \rightarrow GGG$, $GG \rightarrow GG$, or $GGG \rightarrow G$; we temporarily use a capital G to denote gluon, to distinguish it from the green color charge g .

When drawing Feynman diagrams in QCD, arrowed lines are used for quark and antiquark propagators, as they are used for fermions in QED and in general. Looped lines are drawn for gluon propagators. One can also draw the “flow” of color in these diagrams, as shown in figure 1.2, which illustrates the possible QCD vertices in the left column and example color flows in the right column. The first vertex is the $q\bar{q}G$ vertex, which represents gluon absorption or emission by a quark, gluon absorption or emission by an antiquark, quark-antiquark annihilation into a gluon, and pair-production of a quark-antiquark pair. The middle vertex and bottom vertex represent the gluon 3-point and 4-point vertices, respectively.

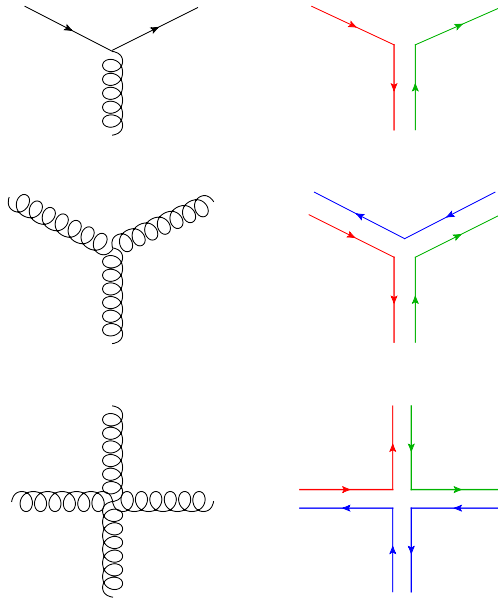


Figure 1.2: QCD vertices (left column) and associated sample color flow diagrams (right column). The top vertex represents a $q\bar{q}G$ interaction, the middle a gluon 3-point vertex, and the bottom a gluon 4-point vertex.

The right column of figure 1.2 illustrates an example of color charges that the interacting partons could have. In the $q\bar{q}G$ vertex, time-ordered left-to-right, a quark comes in with color r , emits or absorbs a gluon carrying a color of $(r\bar{g} + g\bar{r})/\sqrt{2}$, and then emerges from the interaction as a g quark. For the gluon 3-point and 4-point vertices, the color flow diagrams are examples involving all three colors, but other combinations of colors are possible. The main point of these color flow diagrams is to keep track of the conservation of color: analogous to the conservation of electrical charge in the electromagnetic interaction, the color charge is a conserved quantity in the strong interaction. Therefore, each QCD vertex must have the same amount of color charge going in as it does going out.

1.2.3.4 Color Antiscreening

Antiscreening, or *charge screening* in general, is a quantum mechanical effect which emerges from asking the following question: how close can one really get to a point charge? In QED, an example electrical point charge is an electron, since the electron has no observed internal substructure (it is thus called a fundamental particle). Just like in DIS, one can imagine an attempt to probe the structure of an electron by colliding other charged particles with it. In the particle-wave duality picture, a particle with momentum p has a de Broglie wavelength of $\lambda = 2\pi/p$ (with $h = 2\pi$ since $\hbar = 1$). In order to probe the very small, short-distance structure of the electron, one must use a particle probe with a comparably

short wavelength; in other words, exploring smaller substructure requires the use of higher energy probe particles.

Imagine the probe as another charged particle, say, another electron. As the energy of the probe electron increases, the mediating virtual photon will eventually have enough energy to sustain the production of a virtual electron+positron pair, where the positron has identical properties to the electron, but with a charge of $+e$. The number of electron-positron pairs increases as the energy of the probe increases, so the closer one gets to the target electron, the more electron-positron pairs appear “in the way.” The virtual positrons tend to be closer to the target electron than the virtual electrons are, which causes a net polarization (of the vacuum) and effectively *screens* the apparent charge of the target electron. The closer one gets to an electron, the higher its effective charge becomes, and this phenomenon is called charge screening (also called running coupling in QED).

A similar effect appears in the strong interaction, but in a different manner. The strength of the electromagnetic force decreases as a function of distance, in agreement with the decrease of the effective electrical charge as a function of distance from the charge. The strong force behaves differently: its strength does not decrease as a function of distance.¹ If one could pull two quarks apart, the energy of the mediating gluons between them increases as a function of distance, which means quark+antiquark pairs can appear, as well as gluon pairs, triplets, *etc.* due to the gluon self-interactions. Consequently, antiscreening of the apparent color charge of the quarks is observed.

The apparent color charge of a quark increases as a function of distance from that charge. When one is extremely close to a quark, the strong interaction is very weak and the quark becomes apparently free as one asymptotically approaches the infinitesimal distance scale of the quark; this is called *asymptotic freedom*. On the other hand, at larger distances the confinement barrier is reached, where the strong interaction is very strong and therefore keeps the proton held together when probed with a low energy particle. Some models indicate that color antiscreening fully accounts for confinement, effectively making any color source appear color-neutral to an outsider from a sufficient distance away [29], however the true mechanism of confinement is still an open question (see, for example, [30]). Exploring the QCD dynamics of the proton requires probes with high enough energy to break the confinement barrier.

¹ There is a subtlety here: it is assumed that attempting to separate a quark and antiquark causes the mediating gluons (and additional quark-antiquark pairs between) to be concentrated in a *color flux tube* between them (see figure 1.3). This color flux tube model implies the strong potential is linear, hence the strong force between them is constant no matter the distance [28]; however, as the distance between the quark and antiquark increases, the color flux tube will contain more and more quark-antiquark pairs, leading to hadronization, discussed below.

1.2.3.5 Hadronization

Given that one needs high-energy probes to see the internal structure of the proton, an interesting question to consider is what happens if one pulls a single quark out of a proton, or any hadron in general. To achieve this, one would need to scatter a high energy particle off of that quark, which can be done with a high-energy particle collider, such as the Relativistic Heavy Ion Collider (RHIC).

It is simpler to explain what happens to that struck quark in the following thought experiment: imagine simply pulling a quark away from another quark, as illustrated in figure 1.3, where the two quarks are represented by black dots. In step (1), the quarks are bound to each other by a single gluon. As the distance between that quark and the other quarks in the hadron increases in step (2), the strong interaction resists. There is more binding energy between the quarks, allowing for the formation of quark+antiquark pairs as well as more gluons. The resistance of quark separation can be thought of as a color flux tube, which contains gluons, quarks, and antiquarks that are trying to hold the original quarks together, and step (3) shows an even more extreme case with several quark+antiquark loops and gluon self-interactions.

The color flux tube behaves analogously to a rubber band, in that the more the rubber band is stretched, the harder the rubber band tries to relax. At some point, however, the rubber band snaps, and a similar behavior occurs in the color flux tube. At some point, the available energy between the quark and the rest of the hadron is so high that the formation of additional hadrons from the colored partons in the color flux tube can occur: the color flux tube “snaps” and all of the available color charges reassemble themselves into color-neutral hadrons, such that color charge is completely conserved. This process, called *hadronization*, is illustrated in step (4), where the dashed lines indicate momentum vectors. These color-neutral hadrons that have similar momenta toward the left or toward the right form two *jets* of hadrons. These outgoing hadrons (and/or their decay products) are subsequently observable in particle detectors and provide insight into the behavior of partons within the proton.

1.2.4 Proton Spin Composition

In the early days of understanding the constituent structure of the proton, the total proton spin of $S_p = 1/2$ was assumed to be entirely from the quark spins: the two up quarks have spins S_u aligned with the proton spin while the down quark has spin S_d aligned opposite the proton spin. In this model, if $S_p = 1/2$, then $S_u = 1/2$ and $S_d = -1/2$, which add sensibly as $S_p = 2S_u + S_d$. In 1987, an experiment by the European Muon Collaboration (EMC)

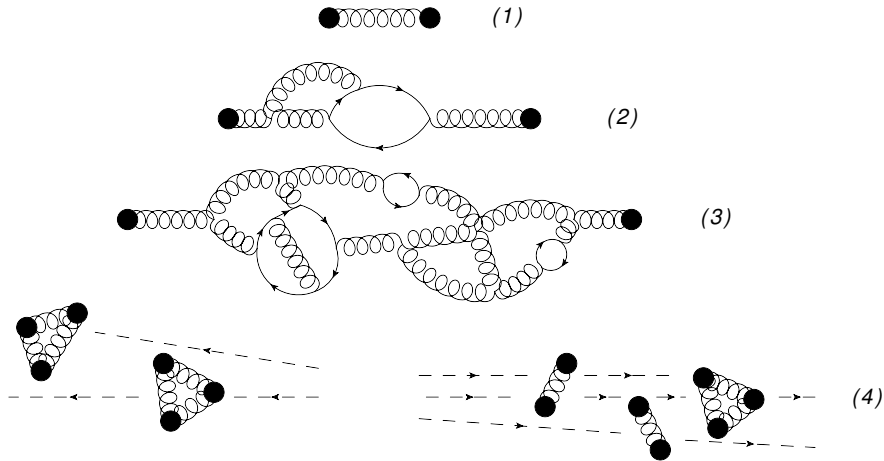


Figure 1.3: Illustration of hadronization. See text for an explanation of the steps.

disproved this idea [3, 4] and characterized the quark spin contribution to be a rather small fraction ($\sim 4 - 24\%$) of the overall proton spin. This result was rather unexpected at the time and given the title “proton spin crisis,” or the less foreboding “proton spin puzzle.” For a summary of the history of the proton spin puzzle, see [31].

In this EMC experiment, longitudinally polarized muons were scattered off of a polarized proton target, and the difference in cross sections between the case where the muon and proton spins are parallel and the case where they are antiparallel was measured. The ratio of this difference in cross sections to the total cross section is called a spin asymmetry, and the asymmetry measured in this experiment was directly sensitive to the difference between quark spins aligned and anti-aligned with the parent proton spin. Since they measured a spin asymmetry consistent with a quark spin contributing only a small fraction to the proton spin, they speculated the remainder of the proton spin comes from the gluon spin as well as the orbital angular momenta of the partons.

The model of a proton as just consisting of three quarks and the binding gluons is not quite complete. If one boosts the proton such that it is moving very fast, then quark+antiquark pairs as well as additional gluons can appear inside the proton, such that color-neutrality is maintained. These additional quarks+antiquarks are called *sea quarks*, while the three *uud* quarks are called *valence quarks*. It turns out that the proton spin also involves contributions from the spins of the sea quarks and antiquarks, as well as the spins of the gluons. Furthermore, the orbital angular momenta are also thought to contribute to the proton spin, since the partons can be pictured as swirling around each other. Figure 1.4 shows an illustration of these spin contributions (right-hand diagram) compared to the naive quark spin picture (left). How these contributions add up to the proton spin will be expounded on below, however the current understanding can be stated now: the total quark spin accounts

Proton Spin Composition

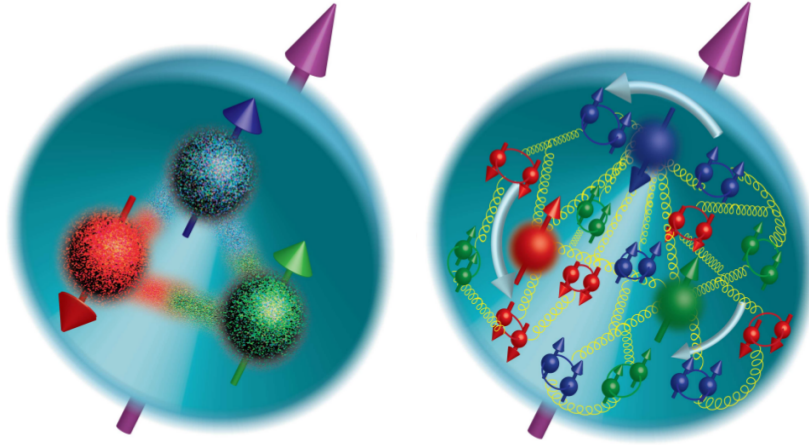


Figure 1.4: Illustration of proton spin structure. The arrows indicate the spins and orbital angular momenta. The left diagram is the naive model, which assumed the proton spin only comes from the quark spins: two of the quarks have spins aligned with the proton and the third has spin anti-aligned. The right diagram shows the more appropriate model, which also includes sea quark spins, gluon helicities, and orbital angular momenta. Adapted from [32].

for $\sim 20 - 30\%$ of the proton spin [5, 6, 7, 8, 9], while the gluon helicity contribution, although still somewhat unconstrained, may account for another $\sim 20 - 30\%$ [13, 14]. The orbital angular momentum contribution has not yet been measured, and ideas for how the experimentalist would attempt to do so are still being discussed.

This dissertation focuses on a measurement that will help constrain the gluon spin contribution to the proton spin. This measurement is of another type of spin asymmetry, the longitudinal double-spin asymmetry for forward-going neutral pions, and like the spin asymmetry measured in the EMC experiment, is a difference of cross sections for given initial spin states divided by the total cross section. As will be detailed in the following sections, every part of the theoretical calculation of this asymmetry is well-constrained, except for the gluon polarization component. Thus by measuring this asymmetry, constraints on the gluon spin contribution can be improved.

1.3 Proton-Proton Scattering

The introduction of QCD discussed above sets the foundation for the experiment: the collision of partons from within two colliding protons. At RHIC, the proton spins can be controlled, that is, ensembles of protons circulating around the accelerator synchrotrons can be polarized. This section begins with a discussion of the kinematics of proton-proton scattering, building up to a full description of the asymmetry measurement presented in this thesis. It then explains why this particular measurement is sensitive to the gluon spin contribution. For details on proton-proton scattering, see standard textbooks such as [16], and for details on the double-spin asymmetry regarding its sensitivity to gluon helicity, see for example [33] and references therein.

1.3.1 Parton Kinematics

In order to introduce the variables that are used to describe parton dynamics and proton structure, consider DIS, as illustrated in figure 1.5. This figure shows the process $e^-p \rightarrow e^-X$, where e^- denotes an electron, p denotes the proton, and X denotes the remnants of the struck proton. The target proton is represented by three quark propagators and has a total momentum P , while the incoming electron has momentum k . Before the interaction with the electron, one of the quarks is selected from the proton, as represented by the blob labelled f which denotes a parton distribution function and is discussed in the next section. This quark carries a fraction ξ of the proton momentum. The electron interacts with this quark via the exchange of a virtual photon with momentum q . The scattered electron leaves with momentum k' and the scattered quark leaves with momentum p' . The subsequent blob, labelled H , represents hadronization of the scattered quark (and any surrounding partons which *dress* this quark) into hadrons, which are collectively labelled as X ; note that the remnant partons from the incoming proton also hadronize, and are part of X .

In inelastic scattering, it is conventional to define the variable $Q^2 = -q^2 = -(k' - k)^2$ as the negative square of the 4-momentum transfer (for the sake of keeping signs of momenta consistent, we assume without loss of generality that the photon is emitted by the electron and absorbed by the quark). Assuming the respective energies E and E' of the incoming and outgoing electrons are much higher than the electron mass, then

$$Q^2 \approx 4EE' \sin^2 \frac{\theta}{2}, \quad (1.3)$$

where θ is the scattering angle of the outgoing electron. This equation justifies the sign convention, since $Q^2 > 0$.

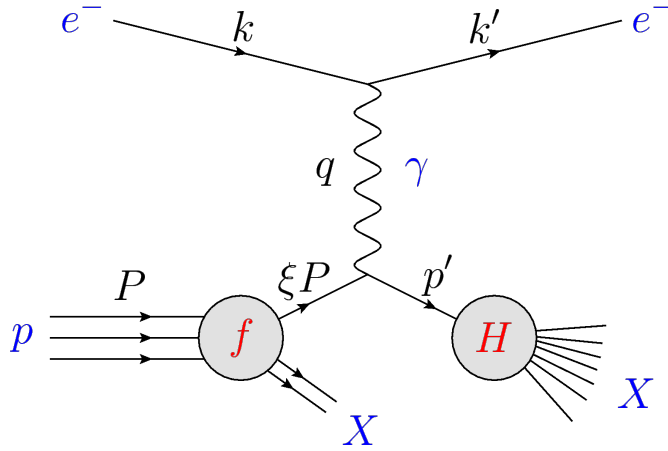


Figure 1.5: Diagram of Deep Inelastic Scattering (DIS), the process $e^-p \rightarrow e^-X$; see text for details.

Another variable typically used in inelastic scattering is called Bjorken- x , typically denoted simply as x , and is named after QCD pioneer James Bjorken. It is defined as

$$x := \frac{Q^2}{2Pq} \quad (1.4)$$

and it is dimensionless and Lorentz-invariant. To gain intuition of what this variable represents, let us boost the proton to a frame in which it is moving extremely fast (*i.e.*, with energy $E_p \gg m_p$), where we may neglect any transverse motion of the partons; this is called the infinite momentum frame (IMF). Consequently, the invariant mass m_q of the quark is negligible when compared to the momenta: we may assume $m_q^2 = \xi^2 P^2 \approx 0$ in the IMF. The invariant mass of the struck quark is $m_q^2 = (\xi P + q)^2 \approx -Q^2 + 2\xi Pq$, which is also approximately zero in this frame. Solving for ξ reveals that $\xi = x$, therefore Bjorken- x for a given parton can be interpreted as the fraction of the proton momentum carried by that parton, in the IMF.

One can, of course, choose not to neglect the transverse momenta of the partons within the proton. This is the study of the *transverse structure* of the proton and is another focus of polarized proton scattering at RHIC. For the analysis presented in this thesis, we can safely ignore the transverse structure, since this analysis is based on the collision of longitudinally polarized protons. In the following sections, the additional complexity that arises from considering transverse parton motion will be mentioned, but not emphasized, as it is outside the scope of this dissertation.

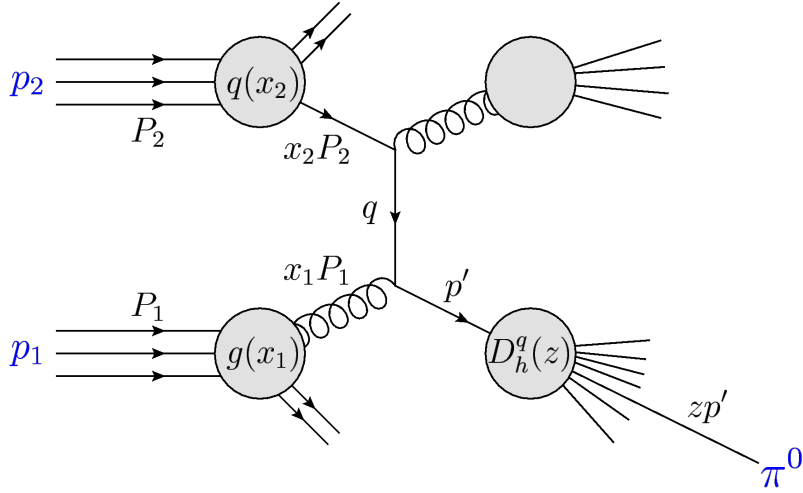


Figure 1.6: Diagram of proton-proton scattering, emphasizing the process $pp \rightarrow \pi^0 X$; see text for details.

1.3.2 Parton Distribution Functions

The kinematic variables Q^2 and x are also defined in pp scattering in the same way. Figure 1.6 illustrates the collision of two protons p_1 and p_2 and the production of a π^0 from the hadronization is emphasized. The protons have momenta P_1 and P_2 , and a gluon from p_1 with $x = x_1$ scatters with a quark from p_2 with $x = x_2$. The momentum transfer, carried by a quark with momentum q , is $Q^2 = -q^2$. A π^0 is produced in the hadronization initialized by the scattered quark; that quark momentum is p' , while the π^0 , which is said to have *fragmented* from the quark, carries a momentum fraction z of p' .

Figure 1.6 represents only one interaction that could occur in a pp collision: it exemplifies a $qg \rightarrow qg$ QCD subprocess. In DIS the interaction is typically via photon exchange, and of the partons, only the quarks can interact with the photon; the DIS experiment is therefore sensitive to the quarks more than the gluons. Note that it is also possible for the virtual photon to have enough energy to fluctuate into a quark+antiquark pair and then interact with the proton; a weak interaction can also occur, in particular the exchange of a Z boson. In pp scattering, however, the subprocess is dominantly a QCD interaction, which probes quarks and gluons, and there are many more types of QCD subprocesses which will be discussed in a following section.

The selection of the gluon in p_1 is modelled by a probability density distribution, $g(x_1, Q^2)$, and the selection of the quark in p_2 is given by $q(x_2, Q^2)$. These probability density distributions are called Parton Distribution Functions (PDFs) and are defined as a function of x for each type of parton, for fixed values of Q^2 . PDFs represent probability density distributions

for partons with a given x for an interaction scale (momentum transfer) of Q^2 ; a PDF can be interpreted as a number density, where the integral of a PDF over the range $a \leq x \leq b$ at a fixed Q^2 gives the number of partons in that x range at that Q^2 . Note that it is common to denote PDFs by the notation used for the parton, for example, the up quark PDF is written $u(x, Q^2)$ and the down antiquark PDF is $\bar{d}(x, Q^2)$.

With the definition of PDFs in hand, we may now define how the proton consists of 2 u quarks and 1 d quark via the following sum rules:

$$\int_0^1 dx [u(x, Q^2) - \bar{u}(x, Q^2)] = 2, \quad (1.5)$$

$$\int_0^1 dx [d(x, Q^2) - \bar{d}(x, Q^2)] = 1, \quad (1.6)$$

$$\int_0^1 dx [s(x, Q^2) - \bar{s}(x, Q^2)] = 0. \quad (1.7)$$

Clearly if the proton consisted of *only* valence quarks, there would be no \bar{u} or \bar{d} quarks and equations 1.6 and 1.7 count how many valence quarks there are. Now suppose a quark+antiquark pair is produced within the proton: the quark and antiquark will have the same flavor, so that their contributions to the integrands in the above sum rules would cancel. Thus these integrands, which are called *valence distributions*, are basically the PDFs of the valence quarks. Regarding the strange quarks, they are entirely sea quarks, therefore the number of s quarks exactly equals the number of \bar{s} antiquarks.

The PDFs are drawn as blobs in figure 1.6 and illustrate the choice of a particular parton with a momentum xP (in the IMF). Conserving momentum in this blob means that the sum of all of the parton momenta must equal the proton momentum. Since $f(x)dx$ represents the probability of finding a parton f with momentum between xP and $(x+dx)P$, the momentum conservation is expressed as

$$\sum_{f \in \{q, \bar{q}, g\}} \int_0^1 dx xP f(x) = P, \quad (1.8)$$

which gives us the momentum sum rule:

$$\sum_{f \in \{q, \bar{q}, g\}} \int_0^1 dx x f(x) = 1. \quad (1.9)$$

Summing over the quarks and antiquarks gives ~ 0.5 , which means the other half of the proton momentum is carried by the gluons.

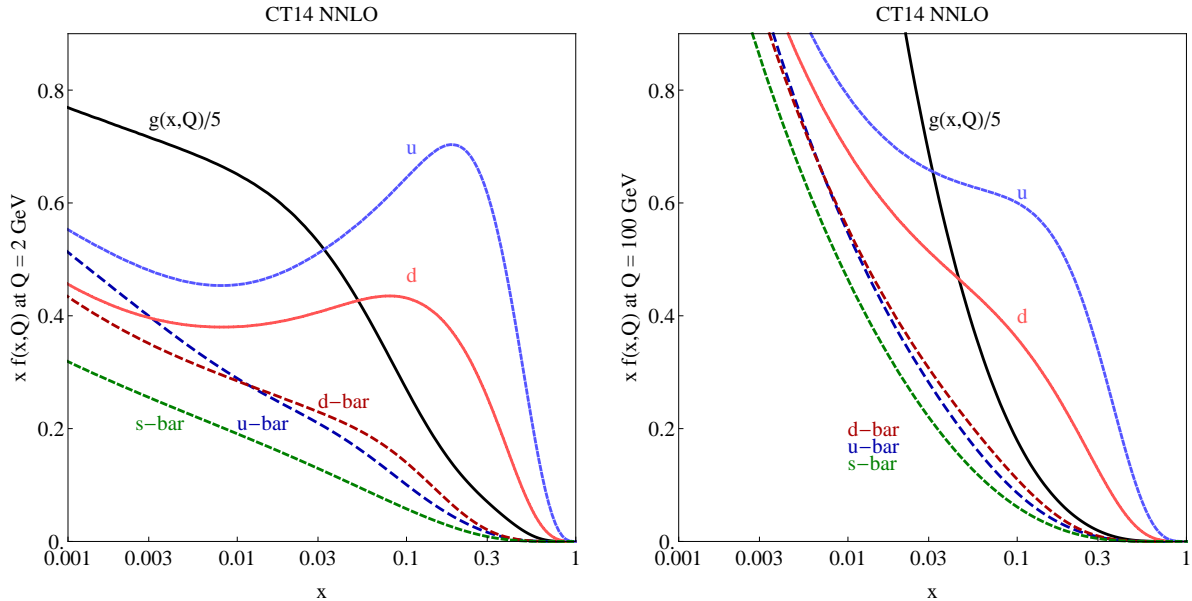


Figure 1.7: Parton distribution functions from the CTEQ-TEA global analysis [34]. The left panel shows $xf(x)$ vs. x at $Q = 2$ GeV and the right panel shows that at $Q = 100$ GeV. Note that the gluon distribution $xg(x)$ is scaled down by a factor of $1/5$.

The shape of the PDFs as a function of x and Q^2 can be determined from an analysis of data provided from various scattering experiments, including DIS and pp scattering, by combining them together in a *global analysis*. Figure 1.7 shows the PDFs determined from the CTEQ-TEA global analysis [34]; the plots are of $xf(x)$ vs. x for a fixed $Q = 2$ GeV (left) and $Q = 100$ GeV (right). Note that, given the momentum sum rule, $xf(x)dx$ represents the fraction of P carried by partons f , each having momenta between xP and $(x + dx)P$.

The high- x region is dominated by the valence u and d quarks. The valence quark distributions, $u(x) - \bar{u}(x)$ and $d(x) - \bar{d}(x)$, are large relative to the sea quark distributions at low Q^2 . At high Q^2 however, the valence quark distributions are reduced relative to the sea quark distributions, which are enhanced; this is because as Q^2 increases, the appearances of sea quark+antiquark pairs also increase.

At low x , the sea quarks and antiquarks and especially the gluons dominate (note that $xg(x)$ is scaled by a factor of $1/5$ in figure 1.7). It is not known how these distributions behave as $x \rightarrow 0$; surely at some point there ought to be so many gluons in the proton that the gluon self-interactions would cause $g(x)$ to stop increasing so fast. This predicted levelling-off of the gluon distribution at low x is called saturation, and has not been observed in experiment. The fact that there are so many gluons at low x begs one to question how much these low- x gluons contribute to the proton spin. This is exactly the question that the

measurement presented in this dissertation is aiming to help answer.

1.3.3 Polarized Parton Distribution Functions

We may now introduce how the spin of the proton is modelled, beginning with a discussion of the polarized parton distribution functions. For recent, introductory reviews of this topic and on proton spin in general, see [35] and [36].

The PDFs we have been discussing so far are *unpolarized*, in the sense that they do not take into account the spin of the parton or the proton. The *polarized* PDF for a parton f is defined as

$$\Delta f(x, Q^2) := [f_{\leftarrow\leftarrow}^{\leftarrow}(x, Q^2) + f_{\Rightarrow\Rightarrow}^{\rightarrow}(x, Q^2)] - [f_{\Rightarrow\leftarrow}^{\leftarrow}(x, Q^2) + f_{\leftarrow\Rightarrow}^{\rightarrow}(x, Q^2)], \quad (1.10)$$

where the unpolarized PDFs, $f(x, Q^2)$, are decomposed into the four terms dependent on proton spin, given by the double arrow ($\leftarrow\leftarrow, \Rightarrow\Rightarrow$), and on parton f spin, given by the single arrow (\leftarrow, \rightarrow). In words, the polarized PDF is the PDF with the parton and proton spins aligned, minus the PDF with the parton and proton spins anti-aligned. If the value of Δf is positive (negative), the parton f spin tends to be aligned (anti-aligned) with the proton spin. In order to measure polarized PDFs, one needs to perform an experiment where polarized protons are involved, such as the scattering of polarized electrons on a polarized hydrogen target, in a process called polarized DIS, or in the scattering of two polarized protons, as is done at RHIC.

The up and down quark and antiquark polarized PDFs are shown in figure 1.8, where two global analyses are compared: DSSV08 [5] and NNPDFpol1.1 [13]. The up quarks are aligned with the proton spin at high x , while the down quarks are anti-aligned. The low- x up and down quarks contribute very little to the proton spin. Figure 1.9 shows the strange quark and gluon polarized PDFs. For the strange quark, the global analyses disagree, especially on the sign of Δs at high x . Finally, regarding the gluons, both analyses agree on positive Δg at high x , but as x decreases, Δg becomes rather unconstrained, especially in the NNPDFpol1.1 analysis.

The polarized gluon distribution is better constrained by the DSSV08 analysis, however there exists an updated version of this global analysis, called DSSV14 [14] and presented in figure 1.10. In this figure, the solid red line is the new DSSV14 fit, and the black dashed line is the DSSV08 fit (the blue dashed line is the DSSV* fit, another fit prior to DSSV14). Note that the uncertainties shown in the DSSV14 fit differ from those shown in DSSV08 in figure 1.9; in DSSV14 the dashed lines surrounding the best fit are alternative fit results that are within the 90% confidence level limit. At high x , these alternative fits agree that the gluon

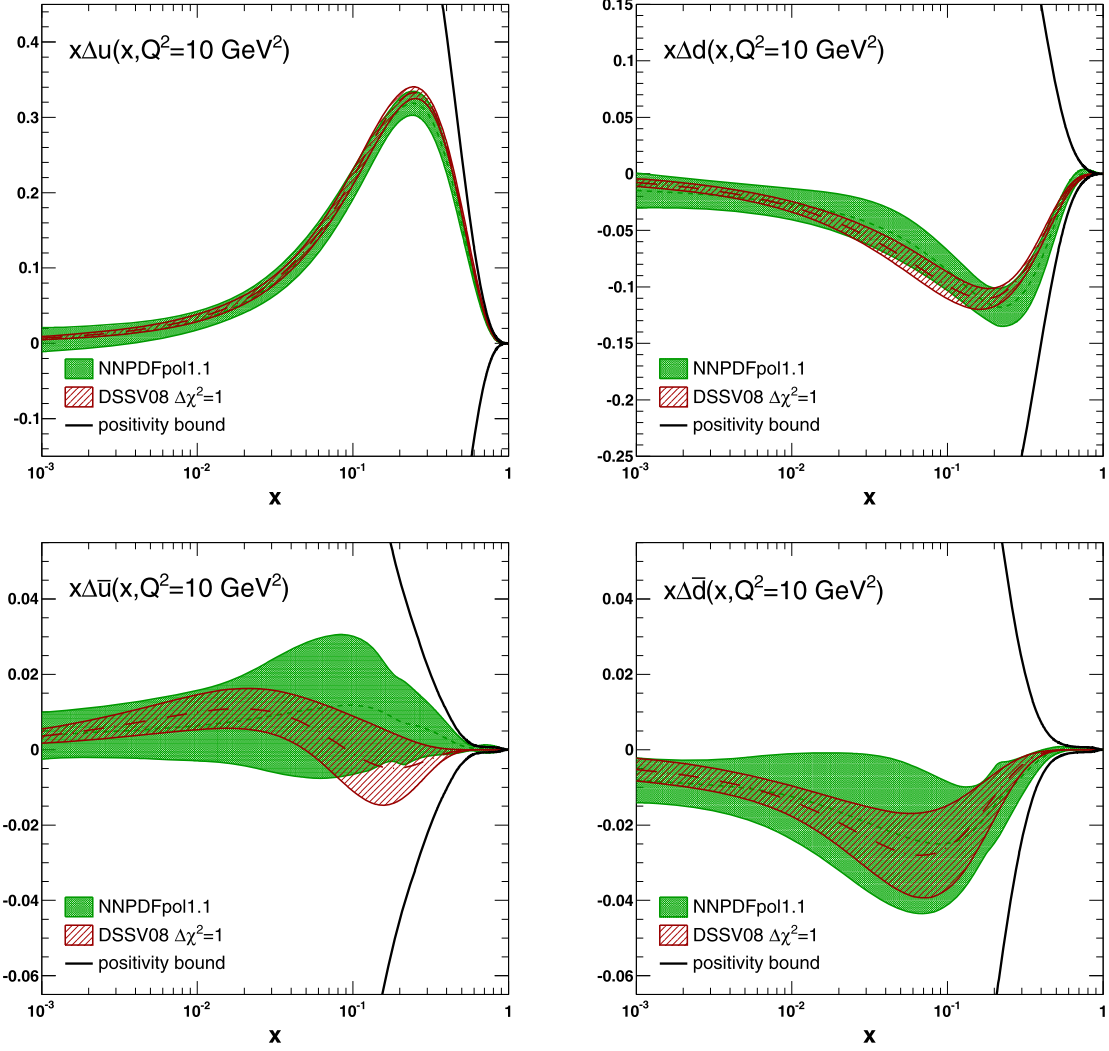


Figure 1.8: Polarized parton distribution functions from DSSV08 [5] and NNPDFpol1.1 [13] (the latter being from where this image was cropped). Values of $x\Delta f(x)$ vs. x are plotted for up and down quarks and antiquarks.

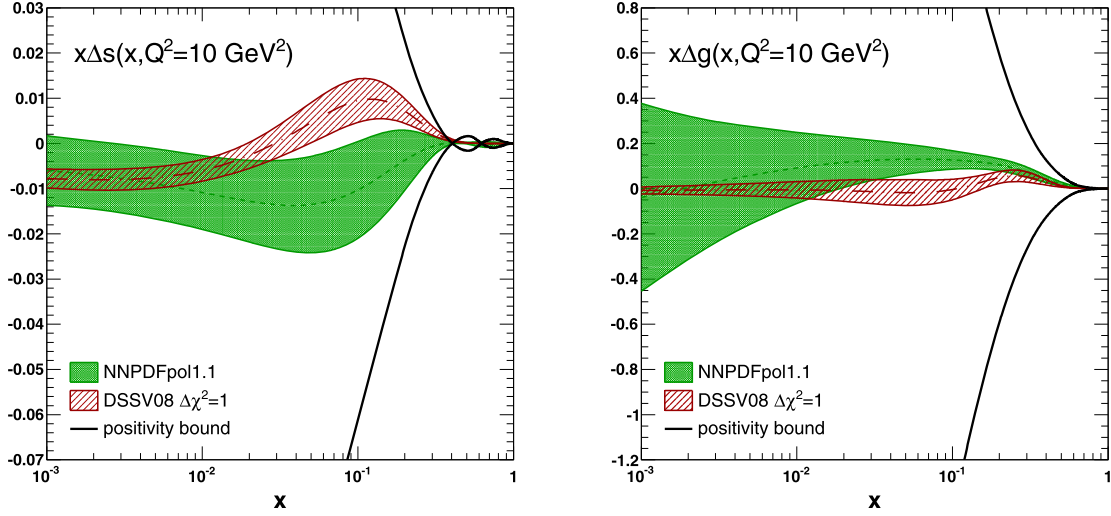


Figure 1.9: Polarized parton distribution functions from DSSV08 [5] and NNPDFpol1.1 [13] (the latter being from where this image was cropped). Values of $x\Delta f(x)$ vs. x are plotted for strange quarks and for gluons.

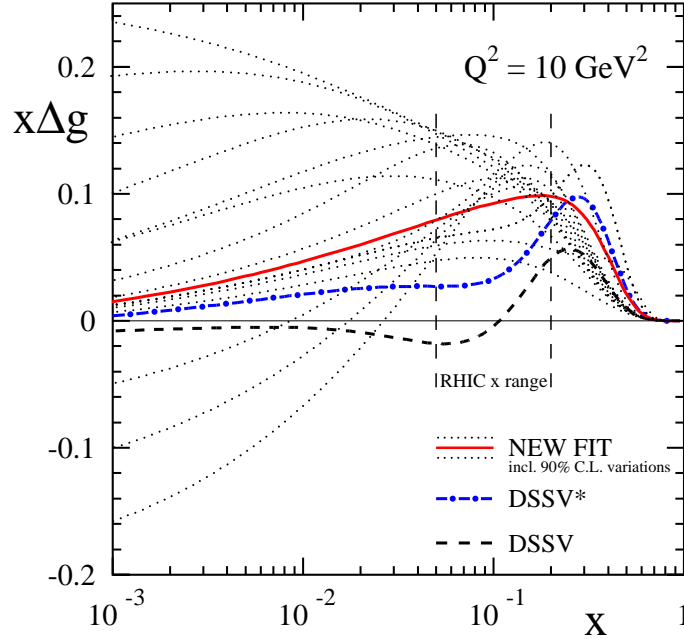


Figure 1.10: Polarized gluon distribution function, $x\Delta g(x)$ at $Q^2 = 10 \text{ GeV}^2$ from the DSSV14 global analysis [14]. The solid red line is the DSSV14 updated fit, with dotted lines indicating a sense of the uncertainty. The black dashed line is the DSSV08 fit (shown in figure 1.9) and the blue dashed line is an update of that fit, prior to DSSV14. Vertical dashed lines indicate the x sensitivity probed by RHIC data which was included in this global fit.

tends to have its spin aligned along with the proton. For $x \lesssim 0.05$, the fit becomes rather unconstrained. The measurement presented in this thesis aims to push sensitivity to $\Delta g(x)$ down to values of $x \sim 0.001$, helping constrain the contribution of the numerous soft gluons to the overall proton spin.

The integral over x of a parton's polarized PDF (with Q^2 fixed) measures the contribution of that parton's spin to the proton spin. The quark contribution is

$$\Delta\Sigma(Q^2) = \sum_{f \in \{q, \bar{q}\}} \int_0^1 dx \Delta f(x, Q^2). \quad (1.11)$$

According to NNPDF, the quark contribution is $\Delta\Sigma(10 \text{ GeV}^2) = 0.23 \pm 0.15$, determined by integrating over $x \in [10^{-3}, 1]$ [13].

The gluon spin contribution to the proton spin is

$$\Delta G(Q^2) = \int_0^1 dx \Delta g(x, Q^2). \quad (1.12)$$

Figure 1.11 shows the current understanding of ΔG . The horizontal axis is the integral of $\Delta g(x)$ over the range $x \in [0.05, 1]$, while the vertical axis is the integral over $[0.001, 0.05]$. The points represent ΔG values, where the red circle is for the DSSV14 fit. The corresponding 90% confidence level fit result is given by the blue hatched region. The DSSV08 fit is given by the black triangle, with its 90% confidence level region given by the green solid region. The DSSV14 is a clear improvement over DSSV08, since for the first time at high x , the gluon spin contribution is definitively positive: $\Delta G \sim 0.2$. The low- x region, however, is still unconstrained, and even the sign of ΔG is not yet known.

1.3.4 Spin Sum Rules

Before continuing with the description of the pp scattering model, it is useful to pause here and consider the meaning of these polarized PDFs in the context of the proton spin. Polarized PDFs are used in the spin sum rules, which aim to explain how the contributions from the quark and gluon orbital and spin angular momenta sum together to form the total spin $1/2$ of the proton. $\Delta\Sigma$ and ΔG represent the quark and gluon spins' contribution to the proton spin, while their orbital angular momenta are denoted by l_q and l_g .

Summing all contributions together gives the proton spin $S_p = 1/2$ as

$$S_p = \Delta\Sigma/2 + \Delta G + l_q + l_g, \quad (1.13)$$

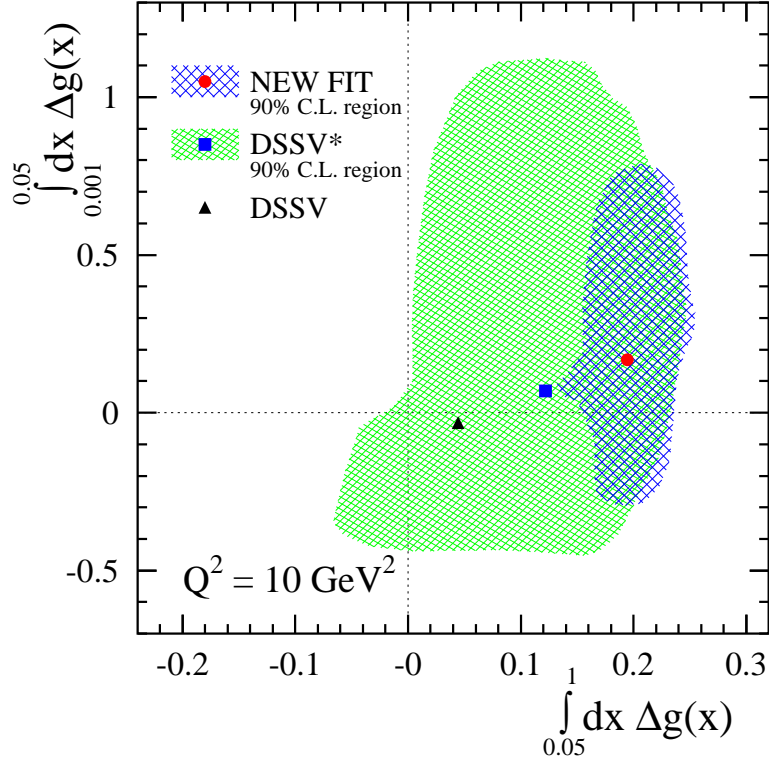


Figure 1.11: ΔG constraints for low- x vs. high- x ranges. See text for details. From the DSSV14 global analysis [14].

which is the Jaffe-Manohar spin sum rule [11]. The quark contribution, measured over a wide range of x , is constrained near $\Delta\Sigma \sim 0.24$, at $Q^2 = 10 \text{ GeV}^2$ [5, 6, 7, 8, 9]. On the other hand, ΔG is coming into focus, as was discussed in the previous section. The orbital angular momenta terms have yet to be measured, and there is ongoing discussion on how to do so; see, for example, [37].

The Jaffe-Manohar spin sum rule is valid only in the IMF, with a particular gauge [38]. The decomposition of the gluon angular momentum into spin and orbital components cannot be done in a gauge invariant manner, despite claims of this decomposition being possible for photons in laser optics experiments [39]. An alternative formulation is the Ji spin sum rule [40],

$$S_p = \Delta\Sigma/2 + L_q + J_g, \quad (1.14)$$

where $J_g = \Delta G + l_g + J_{\text{pot}}$ combines the gluon spin and orbital angular momentum, along with a *potential* angular momentum term J_{pot} , and $L_q = l_q - J_{\text{pot}}$. Although these two spin sum rules basically say the same thing, Ji's rule has the advantage that each of the three terms is frame-independent and gauge invariant. For a review of proton spin and decompositions

of angular momentum in general, see [1].

To understand the frame-independence issue regarding the gluons, consider the two primary types of gluons: Coulomb gluons and radiation gluons. A quark at rest is surrounded by a color field, a gluon *Coulomb field*, analogous to the electric field around a stationary charge. A moving quark will radiate gluons, but in the IMF of the proton, the QCD analogues of electric and magnetic fields are contracted onto the plane transverse to the quark momentum. The longitudinal components of the quark's color field, the so-called *longitudinal gluons*, are suppressed in the IMF, and only the radiative gluons are present; this assumption is called the Weizsacker-Williams approximation.

In this approximation, ΔG is a physical observable representing the contribution of the gluon helicity to the proton helicity; however, to make a frame-independent (and gauge invariant) spin sum rule, one must also consider the Coulomb gluons, which contribute to the orbital angular momentum. This idea motivated Ji to combine ΔG and l_g into one frame-independent term, J_g , which in the IMF decomposes as $\Delta G + l_g + J_{\text{pot}}$. It may be possible to probe J_g and L_q , or the parton orbital angular momenta in general, via a process called Deeply Virtual Compton Scattering (DVCS), which could be realized at the Electron Ion Collider (EIC), a proposed polarized synchrotron collider [32].

1.3.5 Parton Scattering: the QCD Subprocess

In pp scattering, a strong interaction *subprocess* occurs when one parton within one proton scatters off another parton within the other. There are many ways this can proceed, as illustrated in figure 1.12, which shows some of the tree-level Feynman diagrams for various QCD $2 \rightarrow 2$ processes. They are organized into groups of processes, with each row representing one group. Note that when the quark lines are colored, flavor is to be taken into account: if two quark lines have the same (different) colors, then they must have the same (different) flavors. Interaction $qq \rightarrow qq$ in row B can be $uu \rightarrow uu$ or $dd \rightarrow dd$, for example, but not $ud \rightarrow ud$ (which would be categorized in row C, since $q \neq q'$).

For studying the parton spin dependence of the scattering cross section, it is useful to define the parton level spin asymmetry. For a particular parton scattering process, labelled r , the differential cross section is written $d\hat{\sigma}^r/dK$, where K denotes a set of kinematic variables. This cross section for two partons with helicities h_1 and h_2 is the sum over the four possible initial parton helicity states $(h_1, h_2) \in \{(+, +), (+, -), (-, +), (-, -)\}$, where the \pm signs denote positive and negative helicity. Letting $d\hat{\sigma}_{h_1 h_2}^r/dK$ denote the differential cross section

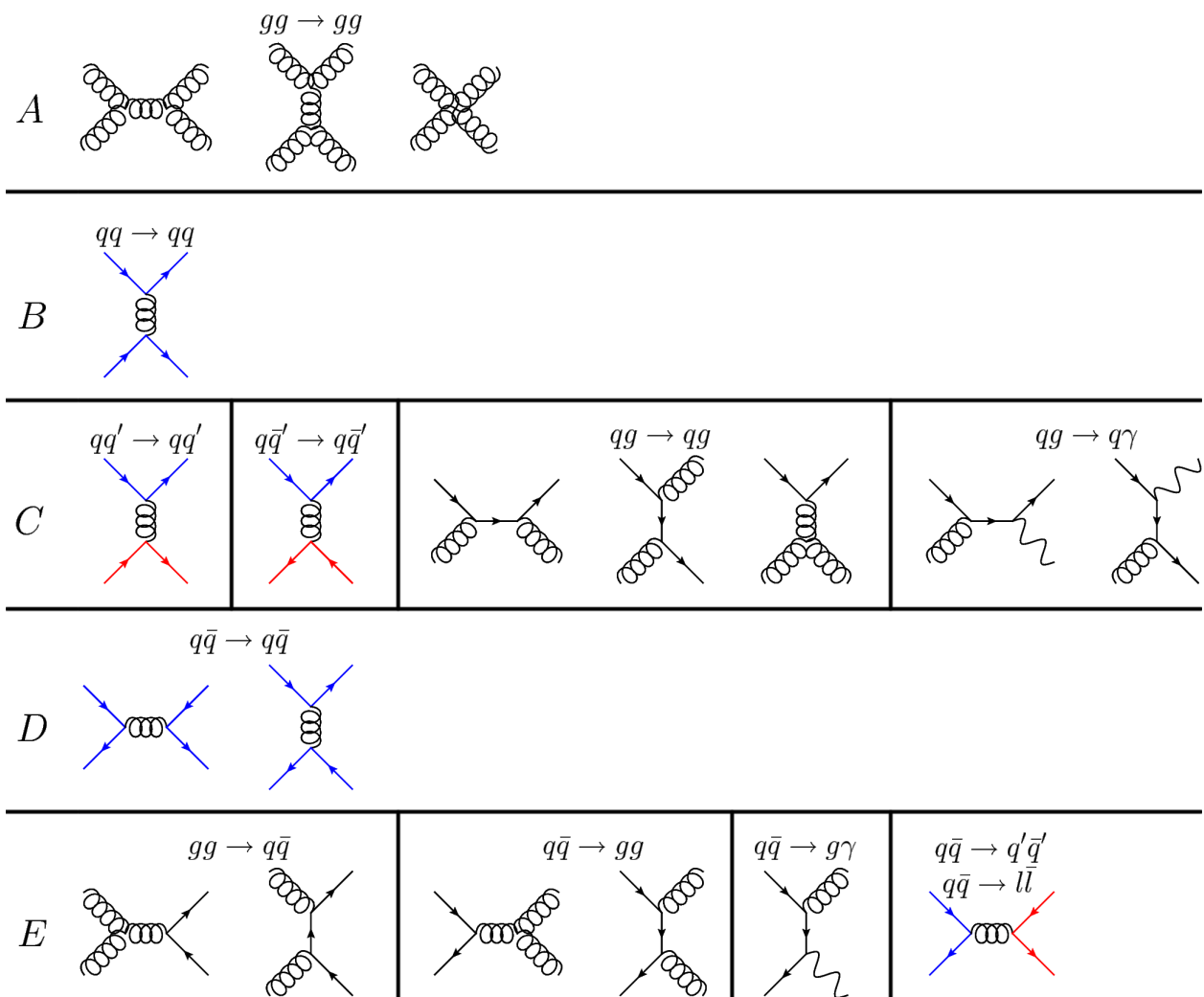


Figure 1.12: Tree-level QCD $2 \rightarrow 2$ Diagrams. Note that most u -channel diagrams are not drawn. If a quark line is colored, then the flavor of the quark matters, in the sense that different (same) colors means different (same) flavors. The letters A through E correspond to the processes indicated by the legend in figure 1.13.

for the process r with the specified helicities, the *polarized* cross section is

$$\frac{d\Delta\hat{\sigma}^r}{dK} = \frac{1}{4} \left[\left(\frac{d\hat{\sigma}_{++}^r}{dK} + \frac{d\hat{\sigma}_{--}^r}{dK} \right) - \left(\frac{d\hat{\sigma}_{+-}^r}{dK} + \frac{d\hat{\sigma}_{-+}^r}{dK} \right) \right]. \quad (1.15)$$

The parton spin asymmetry for r is the ratio of the polarized cross section to the total cross section:

$$\hat{a}_{LL}^r = \frac{d\Delta\hat{\sigma}^r}{d\hat{\sigma}^r} = \frac{(d\hat{\sigma}_{++}^r + d\hat{\sigma}_{--}^r) - (d\hat{\sigma}_{+-}^r + d\hat{\sigma}_{-+}^r)}{(d\hat{\sigma}_{++}^r + d\hat{\sigma}_{--}^r) + (d\hat{\sigma}_{+-}^r + d\hat{\sigma}_{-+}^r)}. \quad (1.16)$$

To interpret this quantity, consider the following three cases: (1) when $\hat{a}_{LL}^r = 0$ the process r does not at all depend on the helicities of the incoming partons, (2) when $\hat{a}_{LL}^r = 1$ the process only occurs if the incoming parton helicities are the same, and (3) when $\hat{a}_{LL}^r = -1$ the incoming parton helicities must be opposite. As a technical note, since the quarks have mass one could always boost to a frame moving faster than the quark, causing the helicity to change sign; technically we are referring to quark *chiralities* in \hat{a}_{LL} , however in the approximation of quark mass being much smaller than the energies involved, this detail does not matter much.

Plots of \hat{a}_{LL} as a function of the cosine of the center-of-mass frame scattering angle are shown in figure 1.13. This is a lowest-order perturbative QCD calculation [41, 42]. The QCD subprocesses in this figure are labelled by letters A through E and correspond to the Feynman diagram groups drawn in figure 1.12. Regarding the scattering angle, $\cos\theta = -1$ corresponds to a center-of-mass scattering angle of π , that is, the momenta of the outgoing partons are opposite the momenta of the incoming partons in this frame. At $\cos\theta = 0$, the outgoing partons scatter at 90° and at $\cos\theta = 1$ the partons “pass through” each other and do not deflect.

All of these parton-level asymmetries are positive, except for the processes in group E , where $\hat{a}_{LL} = -1$. For all of the E processes, the incoming parton helicities must be opposite. To understand why this is so, consider the quark-quark-gluon vertex. If a left-handed quark emits or absorbs a gluon, the quark will remain left-handed; by changing the time-ordering of this vertex such that we now have quark-antiquark annihilation into a gluon, the left-handed outgoing quark becomes a right-handed incoming antiquark, and annihilates with the left-handed quark. As a consequence, all of the $q\bar{q} \rightarrow X$ processes in E can only occur if the helicities (chiralities) of the q and \bar{q} are opposite; furthermore, since $gg \rightarrow q\bar{q}$ is the time-reversal of $q\bar{q} \rightarrow gg$, it also has the same \bar{a}_{LL} of -1 for all scattering angles.

The process $gg \rightarrow gg$ (group A) has maximal \hat{a}_{LL} at $\theta = \pi/2$, as does $qq \rightarrow qq$ (B), which has a lower asymmetry than $gg \rightarrow gg$; both of these processes have their asymmetries go to zero as θ approaches 0 or π . Group C has a maximum \hat{a}_{LL} of 1 at $\theta = \pi$ and decreases

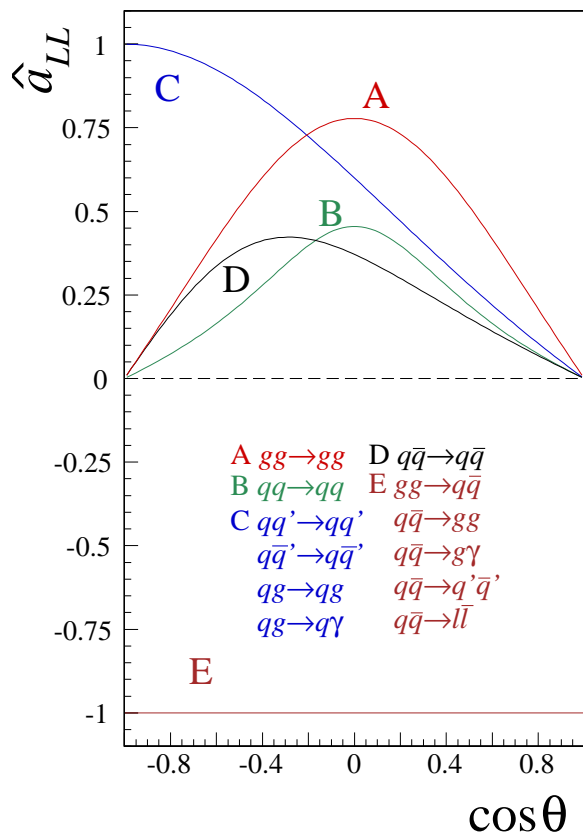


Figure 1.13: Parton-level double spin asymmetry \hat{a}_{LL} vs. cosine of the center-of-mass scattering angle, for various subprocesses. From [43].

toward 0 as θ decreases toward 0. The analysis presented in this dissertation is primarily sensitive to high- x quarks scattering off low- x gluons, as will be described below, thus group C is the most relevant for this analysis. Regarding process D , the s -channel diagram clearly has $\hat{a}_{LL} = -1$, following the discussion of group E processes; however, the t and u -channels also contribute, which have asymmetries similar to group C . The result is therefore similar to group C , but is relatively diminished by the s -channel contribution.

The analysis presented in this dissertation uses data from the Forward Meson Spectrometer (FMS), which is positioned to detect forward² π^0 s, which scattered from pp collisions at relatively small angles. For the FMS, π^0 s with lab frame scattering angles between approximately 1.5° and 9.5° will be observed; more precisely, the π^0 s' decay products, which are most-likely pairs of photons, will deposit energy in the FMS.

² Other regions of interest include the central (midrapidity) region, for scattering angles around 90° , and the intermediate (rapidity) region, which lies between the central and forward regions. At smaller scattering angles than the forward region is the region where diffractive effects may appear, such as the observation of one or both of the protons after they have collided; this is the region of ultra-peripheral collisions.

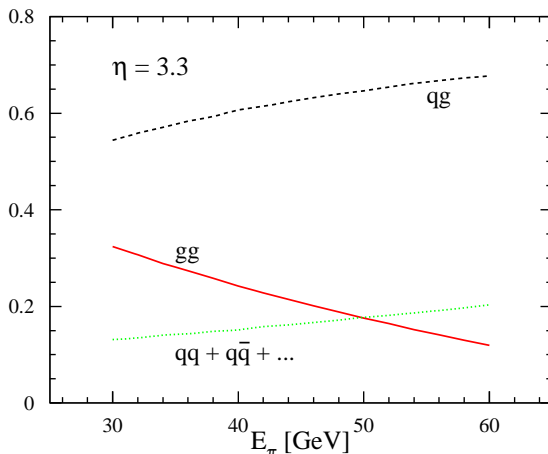


Figure 1.14: Fractional contributions of QCD subprocesses to forward π^0 production, as a function of π^0 energy. Quark-gluon scattering is dominant, followed by gluon-gluon scattering, *et al.* From [44]; see also [45].

In the forward region, the longitudinal component of the π^0 momentum will be a significant fraction x_F of the proton momentum; this fraction is called Feynman- x , and x_F is typically greater than 0.1 in the forward region. A π^0 with such an x_F likely originated from the scattering of a mid-to-high- x quark in the proton that was heading toward the FMS. For this quark to scatter at such forward angles, it likely struck a soft, low- x parton within the other proton. Since at low x the gluons vastly dominate the parton density, the most likely observed parton scattering subprocess for the π^0 s seen in the FMS is the asymmetric hard q + soft g collision.

Figure 1.14 shows the fractional contributions to the π^0 production cross section for center-of-mass energy $\sqrt{s} = 200$ GeV; this is for the same aforementioned forward region (pseudorapidity $\eta = 3.3$, see section 2.2 for definition of η). The fractions are plotted as a function of pion energy, which is within the FMS acceptance. Although the analysis presented in this thesis is of pp scattering at a higher center-of-mass energy of $\sqrt{s} = 510$ GeV, the same general idea holds: the dominant subprocess we are sensitive to is quark-gluon scattering.

Figure 1.15 shows results of a PYTHIA simulation of the values of x_1 and x_2 reached for π^0 s produced within the FMS kinematic acceptance. Parton 1 is the forward-going (*i.e.*, toward the FMS) parton, thus x_2 is likely that of the soft gluon. Details of the simulation may be found in [15].

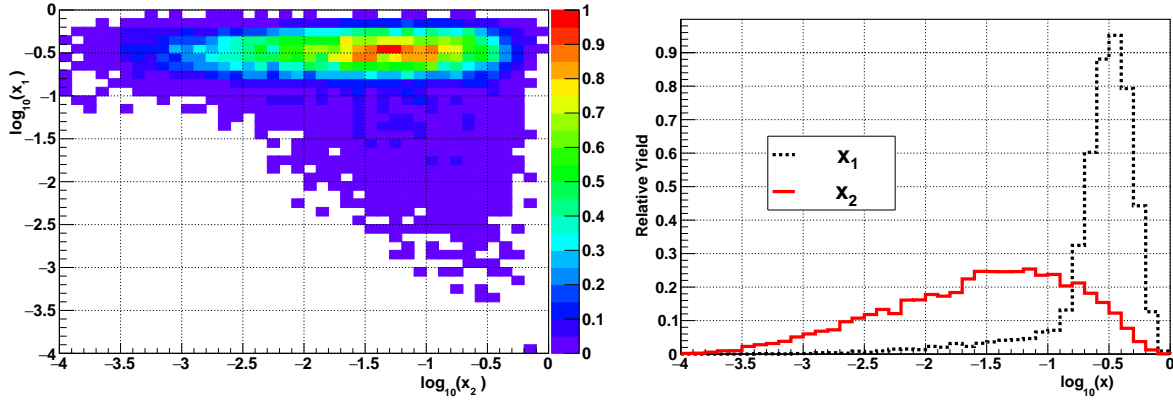


Figure 1.15: Monte Carlo (PYTHIA) simulations of x_1 and x_2 from $\sqrt{s} = 510$ GeV proton-proton collisions, constrained to π^0 s produced within the acceptance applicable to this $A_{LL}^{\pi^0}$ analysis. The forward direction (*i.e.*, toward the FMS) is given by parton 1.

1.3.6 Fragmentation Functions

The final piece to discuss in the pp scattering model, drawn back in figure 1.6, is the fragmentation function. It is generally denoted $D_q^h(z)dz$, which represents the probability that a scattered quark q with momentum p' will hadronize to a hadron h with momentum between zp' and $(z + dz)p'$. The fragmentation functions are symmetric with respect to charge conjugation and isospin symmetry (which is the replacement $u \leftrightarrow d$); for example, the charged pions' fragmentation functions have the following equivalences:

$$D_u^{\pi^+}(z) = D_{\bar{u}}^{\pi^-}(z) = D_d^{\pi^-}(z) = D_{\bar{d}}^{\pi^+}(z). \quad (1.17)$$

The neutral pion fragmentation function is the same for up and down quarks and antiquarks,

$$D_u^{\pi^0}(z) = D_{\bar{u}}^{\pi^0}(z) = D_d^{\pi^0}(z) = D_{\bar{d}}^{\pi^0}(z), \quad (1.18)$$

but is different for strange quarks, with $D_s^{\pi^0}(z) = D_{\bar{s}}^{\pi^0}(z)$.

The fragmentation function for π^0 s, as a function of z , are plotted in figure 1.16; various models are shown and their descriptions can be found in [46] and references therein. In all cases, the pion will typically carry $\sim 10\%$ of the fragmenting quark's momentum, where the rest of the quark momentum is likely distributed among other hadrons into which it fragmented. A spray of hadrons within a cone, which likely originated from a single fragmenting parton, is called a jet and is itself a valid object worthy of study, but is beyond the scope of this dissertation.

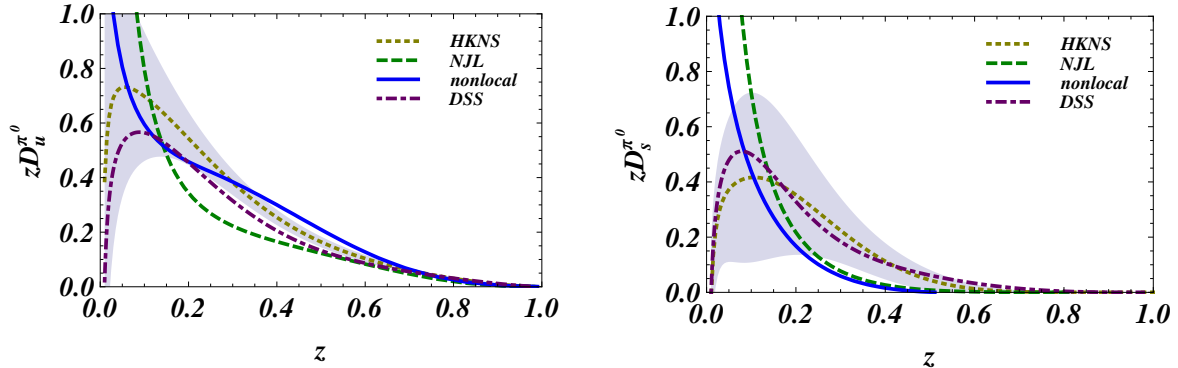


Figure 1.16: π^0 fragmentation functions as a function of fraction of fragmenting quark momentum. Left panel is for up and down (anti)quarks and right panel is for strange (anti)quarks. From [46].

1.3.7 Factorization in pp Scattering

We have now discussed all the components of pp scattering in figure 1.6. The two (polarized) parton distribution functions represent the initial partons which will scatter, followed by the hard QCD scattering subprocess; finally one of the outgoing partons will hadronize and a resulting π^0 will be observed. These four components of pp scattering are all assumed to occur separately enough in spacetime such that none of them interferes with any of the others. Furthermore, none of them depends on transverse parton dynamics, which is the collinear approximation and assumes that all parton momenta are parallel to the proton momentum (by not assuming the collinear approximation, one studies the *transverse* structure of the proton, which an interesting topic on its own).

Since the PDFs, QCD subprocess, and fragmentation occur separately enough in space-time, the overall amplitude for the $pp \rightarrow \pi^0 X$ scattering process is *factorized* into the convolution of two PDFs, a QCD subprocess amplitude, and a fragmentation function (see, for example, [47]). The hard scattering is separable from the PDFs, since the partons within a proton are assumed to be spacelike-separated from each other, up until the point of collision [48]. For an appropriate set K of kinematic variables, the factorized differential pp scattering cross section for π^0 production is (following [43]):

$$\begin{aligned} \frac{d\sigma^{pp \rightarrow \pi^0 X}}{dK} &= \sum_{f_1, f_2, f_3} \int_0^1 dx_1 dx_2 dz f_1(x_1) f_2(x_2) \times \\ &\times \frac{d\hat{\sigma}^{f_1 f_2 \rightarrow f_3 X'}}{dK} (x_1 p_1, x_2 p_2, p_{\pi^0}/z) D_{f_3}^{\pi^0}(z). \end{aligned} \quad (1.19)$$

This, of course, is defined at a particular scale Q^2 . The analogous polarized cross section is

$$\begin{aligned} \frac{d\Delta\sigma^{pp\rightarrow\pi^0 X}}{dK} &= \sum_{f_1, f_2, f_3} \int_0^1 dx_1 dx_2 dz \Delta f_1(x_1) \Delta f_2(x_2) \times \\ &\times \frac{d\Delta\hat{\sigma}^{f_1 f_2 \rightarrow f_3 X'}}{dK}(x_1 p_1, x_2 p_2, p_{\pi^0}/z) D_{f_3}^{\pi^0}(z), \end{aligned} \quad (1.20)$$

which convolves the polarized PDFs with the polarized QCD subprocess cross section, along with the usual fragmentation function.

This dissertation presents a measurement of the longitudinal double-spin asymmetry for π^0 production, denoted $A_{LL}^{\pi^0}$, which may now be defined in terms of the factorized cross sections:

$$A_{LL}^{\pi^0} = \frac{d\Delta\sigma^{pp\rightarrow\pi^0 X}/dK}{d\sigma^{pp\rightarrow\pi^0 X}/dK} = \frac{\sum_{f_1, f_2, f_3} \Delta f_1 \otimes \Delta f_2 \otimes \left[d\hat{\sigma}^{f_1 f_2 \rightarrow f_3 X'} \hat{a}_{LL}^{f_1 f_2 \rightarrow f_3 X'} \right] \otimes D_{f_3}^{\pi^0}}{\sum_{f_1, f_2, f_3} f_1 \otimes f_2 \otimes d\hat{\sigma}^{f_1 f_2 \rightarrow f_3 X'} \otimes D_{f_3}^{\pi^0}}, \quad (1.21)$$

where the \otimes symbol denotes convolution. As discussed, the shapes of all of the probability density distributions and hard scattering cross sections (and asymmetries) are fairly well-known, except for the polarized gluon PDF, especially at low x . Therefore, a measurement of A_{LL} is sensitive to $\Delta g(x)$, and ΔG , given the current knowledge of everything else.

Of course, the π^0 is not the only observable we could use to measure A_{LL} ; one can measure it with any particle or jet, or combination thereof. One important property of the PDFs, hard scattering, and fragmentation functions, is that they are thought to be *universal*, meaning that they are valid for all scattering processes. This is not completely true, however, and still remains to be fully tested; there is some evidence of universality violation in a class of spin asymmetries called transverse single spin asymmetries [49], however for a global analysis aimed at extracting $\Delta g(x)$, universality is accepted as true.

1.4 Spin Asymmetries

Having illustrated the spin asymmetry A_{LL} from the perspective of pp scattering and factorization, we will now discuss its measurement, along with some other asymmetries. Some references for proton spin and asymmetries in general are [35, 36, 50, 51, 52].

1.4.1 How to Measure a Spin Asymmetry: A_{LL}

In order to measure a spin asymmetry, in particular $A_{LL}^{\pi^0}$, it is easier to measure the π^0 yields for each of the initial proton spin states, that is, the number of detected π^0 s. Define the

luminosity L as the detected event rate dN/dt divided by the interaction cross section σ :

$$L(t) = \frac{dN/dt}{\sigma}. \quad (1.22)$$

Luminosity is dependent on the parameters of the colliding beams, and measures the observed event rate with respect to the probability of interaction (cross section); the higher the luminosity, the more events one will see, for a particular cross section.

After a period of data-taking between times t_1 and t_2 , the total integrated luminosity is

$$L_{\text{int}} = \int_{t_1}^{t_2} L(t) dt \quad (1.23)$$

and it is measured in units of inverse cross section, typically inverse picobarns (denoted pb^{-1} , where $1 \text{ b} = 10^{-28} \text{ m}^2$). Integrated luminosity gives one an idea of how much data was taken, given a particular cross section for the type of events observed: the number of events is $N = \sigma L_{\text{int}}$. Detectors are not perfect however, and have their own efficiencies, due to many causes, such as calibration and acceptance subtleties. Letting Ω denote the overall detector efficiency, the number of events is actually $N = \Omega \sigma L_{\text{int}}$.

The $A_{LL}^{\pi^0}$ measurement takes place in a collider, which sends *bunches* of $\sim 10^{10}$ protons head-on at each other. Not all of the protons within each bunch will have the desired spin, motivating one to define the polarization P for each beam:

$$P = \frac{n_+ - n_-}{n_+ + n_-}. \quad (1.24)$$

n_+ is the number of protons in the beam which have spins aligned to the desired polarization, and n_- is the number which are anti-aligned (see, for example, chapter 12 of [53]). The value of P ranges from -1 to $+1$, but we typically only use the positive values, quoting the number as a percentage. For example, a beam polarization of 50% means that $n_+ = 3n_-$.

Without accounting for polarization, one measures the *raw* asymmetry, written

$$\varepsilon_{LL} = \frac{(\sigma_{++} + \sigma_{--}) - (\sigma_{+-} + \sigma_{-+})}{(\sigma_{++} + \sigma_{--}) + (\sigma_{+-} + \sigma_{-+})}, \quad (1.25)$$

where the differential cross sections have been integrated over appropriate kinematic ranges corresponding to the acceptance of the detector. The measured asymmetry is then $A_{LL} = \varepsilon_{LL}/P_B P_Y$, where P_B and P_Y are the two beams' polarizations.

We can write the cross sections in terms of particle yields, keeping in mind that those,

along with the integrated luminosities, are dependent on the proton helicities h_1 and h_2 :

$$\sigma_{h_1 h_2} = \frac{N_{h_1 h_2}}{\Omega L_{h_1 h_2}}. \quad (1.26)$$

The double-spin asymmetry becomes

$$A_{LL} = \frac{1}{P_B P_Y} \frac{(N_{++} + N_{--}) / (L_{++} + L_{--}) - (N_{+-} + N_{-+}) / (L_{+-} + L_{-+})}{(N_{++} + N_{--}) / (L_{++} + L_{--}) + (N_{+-} + N_{-+}) / (L_{+-} + L_{-+})}, \quad (1.27)$$

where the efficiency factors have cancelled. To simplify this expression, we define the relative luminosity R_3 as

$$R_3 = \frac{L_{++} + L_{--}}{L_{+-} + L_{-+}}. \quad (1.28)$$

The suffix “3” on the relative luminosity is a STAR notation convention, where 8 other standard relative luminosities can be defined for other spin asymmetries (see appendix B).

Finally, in terms of the measurable particle yields, relative luminosity, and beam polarizations, the asymmetry is written

$$A_{LL} = \frac{1}{P_B P_Y} \frac{(N_{++} + N_{--}) - R_3 (N_{+-} + N_{-+})}{(N_{++} + N_{--}) + R_3 (N_{+-} + N_{-+})}. \quad (1.29)$$

A measurement of A_{LL} therefore requires three coincident measurements: yields (*e.g.*, of π^0 s) for each incoming proton spin combination, relative luminosities, and beam polarizations. All three of these quantities are time-dependent, and we determine the *maximum likelihood* value of A_{LL} over the entire data set, as will be described later in section 6.3.

1.4.2 Single-Spin Asymmetries

Up until this point we have been focusing on double-spin asymmetries. A single-spin asymmetry, written A_L , is an asymmetry which concerns the spin of only one beam. Letting σ_h denote the cross section given proton 1 had the initial spin h , the raw single spin asymmetry is

$$\varepsilon_L = \frac{\sigma_+ - \sigma_-}{\sigma_+ + \sigma_-} \quad (1.30)$$

and $A_L = \varepsilon_L / P$, with P the polarization of the corresponding beam.

Unlike the double-spin asymmetry, A_L changes sign under a parity transformation, since helicity also changes sign. A nonzero measurement of A_L is therefore indicative of a preference of one scenario over its parity-transformed scenario: this is parity violation. Since the strong and electromagnetic interactions do not violate parity, a nonzero A_L could only occur in an

observable involving a weak interaction subprocess, which *can* violate parity. Since the W^+ and W^- bosons couple to the u and d quarks and antiquarks in different ways, observing the leptonic decay channels $W^\pm \rightarrow e^\pm + \nu$ gives two A_L values (positive and negative leptons), which are sensitive to sea quark polarized PDFs [54, 55].

In the $A_{LL}^{\pi^0}$ measurement presented in this thesis, we expect $A_L = 0$ because π^0 production is dominantly from a strong interaction subprocess; nonetheless, confirming $A_L = 0$ in this observable is a useful diagnostic. There are several other asymmetries one could measure as diagnostics; see appendix B for a comprehensive list. All of them are confirmed to be consistent with zero in this analysis.

1.4.3 Transverse Spin Asymmetries

Polarizing the protons along the direction of their momenta is of course not the only possibility; one can collide protons with their spins aligned on an axis perpendicular to their momenta, typically the vertical axis. The single and double-spin asymmetries are defined the same, with the replacement of positive and negative helicities with spin up (\uparrow) and spin down (\downarrow).

The projection of a produced particle's momentum vector onto the plane transverse to the beam is called its transverse momentum vector \vec{p}_T , and on this transverse plane, \vec{p}_T makes an angle with respect to the horizontal axis, called the azimuth and denoted ϕ . Because the transverse spin asymmetry is defined with respect to a particular transverse axis, the asymmetry is dependent on the azimuth of the observable.

1.4.3.1 Transverse Single-Spin Asymmetries

The transverse single-spin asymmetry, denoted A_N and sometimes also called *analyzing power*, is defined via

$$\frac{1}{P} \frac{N_\uparrow(\phi) - RN_\downarrow(\phi)}{N_\uparrow(\phi) + RN_\downarrow(\phi)} = B + A_N \cos \phi, \quad (1.31)$$

where R is the appropriate relative luminosity (R_1 or R_2 in STAR notation) and B accounts for an overall offset caused by the relative luminosity (if $R = 1$ then $B = 0$).

One can exploit a symmetry given by rotations around the beam axis: a spin-up proton scattering to the left is the same as a spin-down proton scattering to the right. Following [56], the relative luminosity factors cancel, and the asymmetry can be measured via the

cross-ratio formula:

$$\frac{1}{P} \frac{\sqrt{N_{\uparrow}^L N_{\downarrow}^R} - \sqrt{N_{\downarrow}^L N_{\uparrow}^R}}{\sqrt{N_{\uparrow}^L N_{\downarrow}^R} + \sqrt{N_{\downarrow}^L N_{\uparrow}^R}} = \frac{1}{P} \frac{\sqrt{N_{\uparrow}(\phi) N_{\downarrow}(\phi + \pi)} - \sqrt{N_{\downarrow}(\phi) N_{\uparrow}(\phi + \pi)}}{\sqrt{N_{\uparrow}(\phi) N_{\downarrow}(\phi + \pi)} + \sqrt{N_{\downarrow}(\phi) N_{\uparrow}(\phi + \pi)}} = A_N \cos \phi, \quad (1.32)$$

where one only needs the particle yields and their azimuths.

Measurements of A_N have revealed unexpectedly large asymmetries since the late 1970s [57] (see also [35]); such large asymmetries have also been seen in the FMS, where the asymmetry is higher for more-isolated π^0 s [58]. The exact physical origin of such large asymmetries still remains a debated mystery, however.

1.4.3.2 Transverse Double-Spin Asymmetries

The transverse double-spin asymmetry can also be defined, however it is modulated by $\cos(2\phi)$:

$$\frac{1}{P_B P_Y} \frac{[N_{\uparrow\uparrow}(\phi) + N_{\downarrow\downarrow}(\phi)] - R_3 [N_{\uparrow\downarrow}(\phi) + N_{\downarrow\uparrow}(\phi)]}{[N_{\uparrow\uparrow}(\phi) + N_{\downarrow\downarrow}(\phi)] + R_3 [N_{\uparrow\downarrow}(\phi) + N_{\downarrow\uparrow}(\phi)]} = A_{\Sigma} + A_{TT} \cos(2\phi). \quad (1.33)$$

Both A_{Σ} and A_{TT} can be measured, but one cannot exploit rotational symmetry, which necessitates a simultaneous measurement of the relative luminosity. These asymmetries are not discussed nearly as much in the literature, however they could be sensitive to the analogue of polarized PDFs in the transverse polarized case, the *transversity PDFs* [50, 59]. In this $A_{LL}^{\pi^0}$ analysis, A_{Σ} and A_{TT} will make an appearance again during the discussion of systematic uncertainties due to a possible nonzero transverse component of beam polarizations.

1.5 Recent Measurements of $A_{LL}^{\pi^0}$

This measurement of $A_{LL}^{\pi^0}$ in the forward direction is not the first time it has been measured with these π^0 kinematics; it is therefore useful to survey recent measurements of this asymmetry in order to give our measurement appropriate context. A measurement of $A_{LL}^{\pi^0}$ corresponding to the same forward region as our new measurement is shown in figure 1.17 [60]. The asymmetry is plotted versus Feynman- x , and since $\sqrt{s} = 200$ GeV, the π^0 energy is given by $x_F \times 100$ GeV. These data were taken from predecessors of the FMS: the Forward Pion Detector (FPD) and the FPD++, which can be thought of as smaller versions of the FMS. The data agree with the theoretical prediction, the curve labelled by GRSV Std, and are consistent with zero. The analysis presented in this dissertation extends this analysis

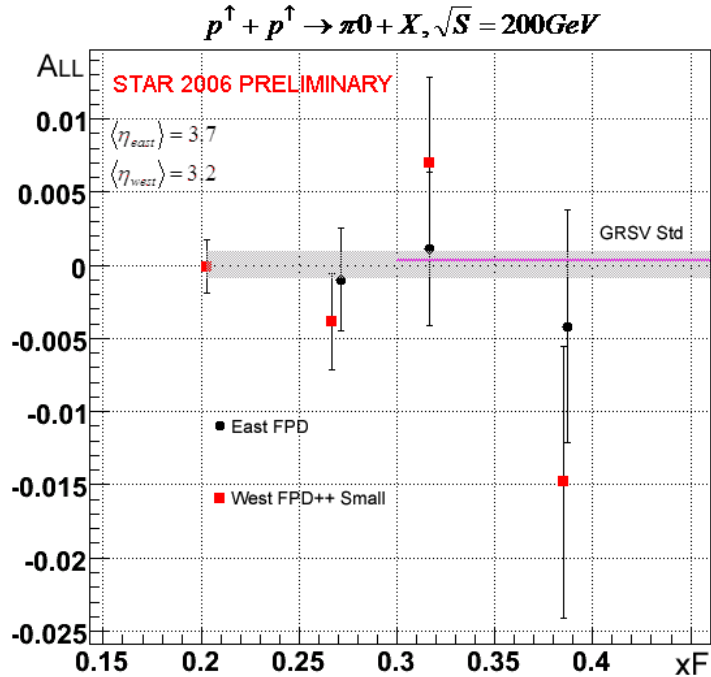


Figure 1.17: A_{LL} for forward π^0 s versus Feynman- x ; the vertical error bars are statistical, and the GRSV Std model $A_{LL}(x_F)$ curve is also plotted. From [60].

to a higher \sqrt{s} of 510 GeV, with much greater π^0 statistics using a detector with a larger kinematic acceptance.

Proceeding toward larger scattering angles into the *intermediate rapidity* region, figure 1.18 shows A_{LL} for π^0 s produced between roughly 15° and 45° (pseudorapidity $0.8 < \eta < 2$) [61]. It is plotted versus π^0 transverse momentum and is also from $\sqrt{s} = 200$ GeV collisions. The data (and theory models) are consistent with zero in this region as well. Note that while the qg subprocess still dominates for this kinematic region, followed by the gg subprocess (see [44]), the more-central regions do not probe as low of x as the forward region does, since hard, mid-to-high- x parton scattering becomes the dominant subprocess. A_{LL} measured for production at larger scattering angles, or lower pseudorapidities, is therefore sensitive to gluon polarization at higher x . For example, for dijets produced at $0.8 < \eta < 1.8$, the sensitivity of A_{LL} to $\Delta g(x)$ extends down to $x \sim 0.01$ for $\sqrt{s} = 200$ GeV collisions [62]; for the typical higher collision energy of 510 GeV at RHIC, the x range can be multiplied by 200/510, since in $2 \rightarrow 2$ dijet kinematics, x of either parton is inversely proportional to \sqrt{s} .

In the central (midrapidity) region, where scattering angles are around 90° , non-zero $A_{LL}^{\pi^0}$ is observed, as shown in figure 1.19 [63]. Scattering angles for these π^0 s are within $90^\circ \pm 20^\circ$ ($|\eta| < 0.35$). Data from $\sqrt{s} = 200$ and 510 GeV are shown and agree with the theory models

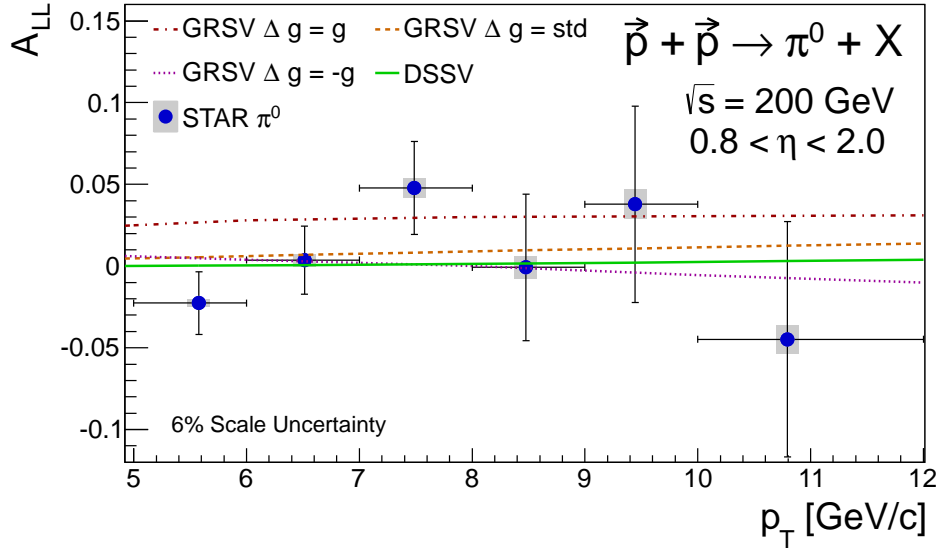


Figure 1.18: A_{LL} for intermediate rapidity π^0 s versus transverse momentum; from [61].

(and approximately with each other); this measurement is sensitive to gluon polarization down to $x \sim 0.01$. The asymmetry is plotted versus x_T , corresponding to p_T via $x_T\sqrt{s}/2$. The measurement of a positive A_{LL} for pions in the central region is therefore an indication of a positive $\Delta g(x)$ at high x . Large, positive A_{LL} values have also been observed in central region inclusive jets and dijets at STAR, for example, at $\sqrt{s} = 200 \text{ GeV}$, which is sensitive to $\Delta g(x)$ for $x > 0.05$ [64, 65]; analyses of $\sqrt{s} = 510 \text{ GeV}$ data are ongoing [66].

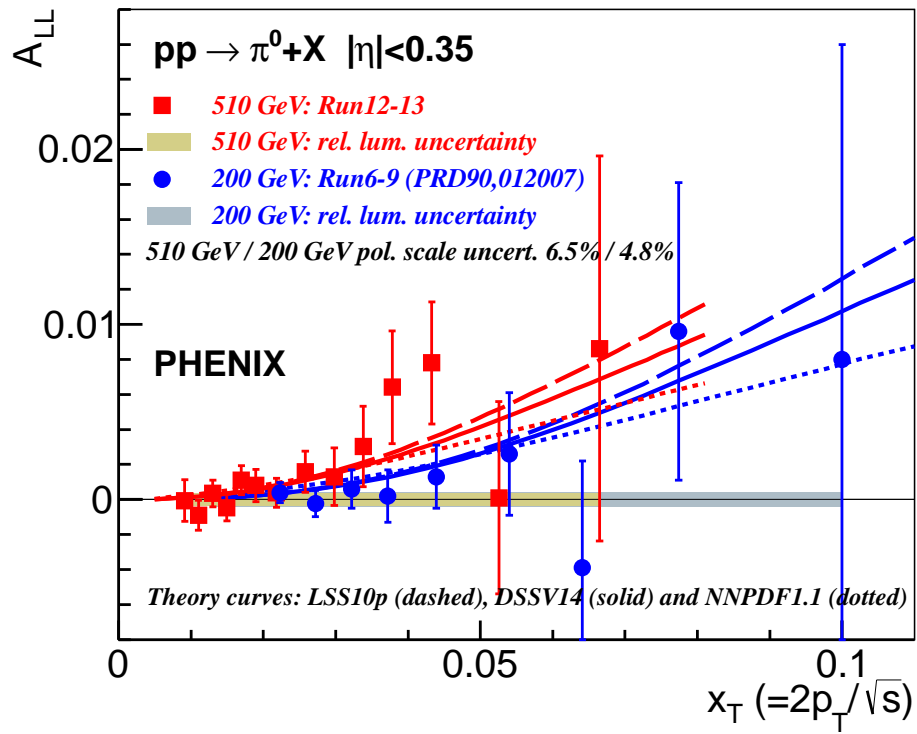


Figure 1.19: A_{LL} for central rapidity π^0 s versus x_T ; from [63].

Chapter 2

Experimental Apparatus

2.1 The Relativistic Heavy Ion Collider

The measurement of A_{LL} presented in this dissertation is from proton-proton collisions provided by the Relativistic Heavy Ion Collider (RHIC), located at Brookhaven National Laboratory, on Long Island about 60 miles east of New York City. It is currently the world's only (and first) polarized synchrotron collider, where the polarized proton beams collide head-on; all spin particle physics experiments prior to RHIC were fixed target experiments, where the target and/or the incoming particle beam was/were polarized. RHIC is capable of reaching center-of-mass energies up to ~ 510 GeV for pp scattering (*i.e.*, up to 255 GeV per nucleon), but as its name suggests, RHIC is also capable of colliding heavier nuclei, such as gold or aluminum. Since the focus of this dissertation is on the proton spin, we will not discuss heavy ion collisions, which are a probe of some of the collective properties of QCD, such as the quark gluon plasma. For further information on the design of RHIC, see [67].

RHIC accelerates *bunches* of polarized protons, where each bunch contains about 10^{10} protons. Typically there are 102 bunches circulating in each synchrotron ring, where in one ring they circulate clockwise and in the other counterclockwise. At certain parts of RHIC, the bunches are allowed to collide, and this collision of proton bunches is called a bunch crossing. RHIC has a bunch crossing rate of approximately 9.38 MHz, and typically one proton-proton collision occurs per bunch crossing.

Only the protons can be polarized at RHIC, and since a synchrotron accelerates charged particles using a vertical magnetic field, the proton polarization prefers to be aligned or anti-aligned vertically, *i.e.*, the proton bunches are polarized *transversely*. Thomas precession, which is a relativistic effect related to boosts and rotations [68], causes the proton spins to precess about the vertical axis; this effect, along with imperfections in the guiding magnetic fields, present challenges in maintaining optimal polarization during proton beam

acceleration and storage.

Let \vec{B}_\perp and \vec{B}_\parallel denote the transverse and longitudinal components of the synchrotron guiding magnetic field, \vec{S} denote the proton spin, with charge e and mass m_p , moving with velocity \vec{v} , and define the Lorentz factor $\gamma = (1 - v^2)^{-1/2}$. Given the anomalous magnetic moment G of the proton as $G \approx 1.793$, the time-dependence of the proton spin vector is given by the Thomas-BMT equation [69]:

$$\frac{d\vec{S}}{dt} = \frac{e}{\gamma m_p} \vec{S} \times \left[(1 + G\gamma) \vec{B}_\perp + (1 + G) \vec{B}_\parallel \right]. \quad (2.1)$$

On the other hand, using the proton momentum $\vec{P} = \gamma m_p \vec{v}$ and the Lorentz force law, we have

$$\frac{d\vec{v}}{dt} = \frac{e}{\gamma m_p} \vec{v} \times \vec{B}_\perp. \quad (2.2)$$

Comparing equation 2.1 to equation 2.2, assuming $B_\parallel = 0$, reveals that the spin of the proton precesses $G\gamma$ times per full revolution within the synchrotron. This quantity $G\gamma$ is called the spin tune, where if $G\gamma = 1$ for example, then the spin precesses twice as fast as the orbit around the ring.

Any accelerator will have imperfections or defects in the guiding magnetic fields. Suppose there is a defect that perturbs a passing proton's spin so that it slightly rotates in a clockwise direction about the beam axis. Each time a particular bunch of polarized protons passes through this perturbation, a larger fraction of these protons becomes depolarized: such a perturbation is called a depolarizing resonance. These resonances are more likely to occur when the spin tune is an integer value, where the spin precession traces out the exact same path during each revolution (assuming no guiding field defects). At RHIC these resonances occur roughly every 0.5 GeV energy step during the acceleration, and pose a challenge to maintaining proton beam polarization up to high energies of 255 GeV.

In order to mitigate the effect of depolarization resonances, RHIC employs devices called Siberian snakes [70], which have the net effect of rotating the spin axis about the vertical precession axis by 180° for each revolution; note that this net effect is for integer spin tunes, however for non-integer spin tunes, the effect generalizes. Figure 2.1 shows a diagram of a RHIC ring in grey, with two Siberian snakes S_1 and S_2 at the bottom and top. A single Siberian snake is composed of four helical dipole magnets, which effectively rotate the spin 180° about a specific axis.

In the figure, snake S_1 causes the spin to rotate about an axis in the horizontal plane, pointing 45° to the outside of the RHIC ring, as indicated by the green arrow. Snake S_2 causes the spin to rotate about an axis pointing 45° to the inside of the ring. The figure

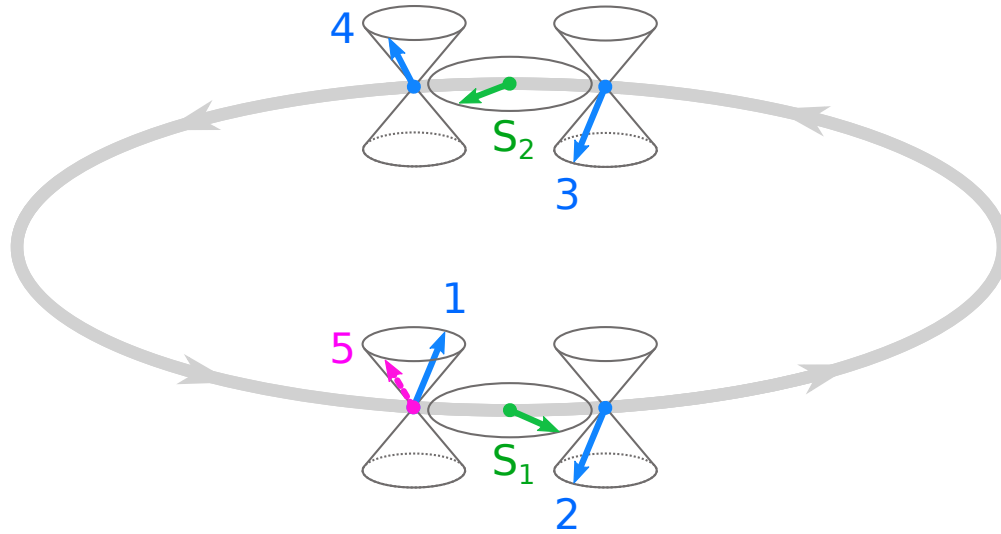


Figure 2.1: Siberian snakes' effect example. See text for details.

shows an example of how a particular proton's spin precesses and flips through the ring and snakes, as the proton travels in the counter-clockwise direction. We begin with a spin-up proton, where its spin vector is represented by the blue vector at position 1; the precession cones are drawn, and at position 1, the proton's spin is pointing forward and toward the inside of the ring. We now step through this example, which assumes a spin tune of 1:

- Position 1: initial state, proton is spin-up, with spin vector pointing forward and toward the inside of the ring; this is the state *just before* entering snake S_1 (the diagram is not to scale, for clarity's sake)
- Position 2: just after passing through S_1 , the proton emerges as spin-down, and now points backward and toward the outside of the ring
- Position 3: the proton has now gone through half of a revolution, which means it precesses 180° about the vertical axis (in its frame); thus the proton is now pointing forward and toward the inside
- Position 4: after passing through S_2 , the proton is now spin-up, with spin vector pointing forward and toward the inside
- Position 5: after another half revolution, the proton is spin-up, with spin vector pointing backward and toward the outside, as indicated by the magenta dashed arrow. Notice that this spin vector is equivalent to the original spin vector, rotated by 180° about the vertical axis.

Therefore the second time the proton passes through any position, it has the spin vector pointing the opposite direction, but is still in the same spin-up or spin-down state. Consequently, oscillations of the spin direction are induced by depolarization-causing perturbations, rather than total depolarization. Siberian snakes are a key ingredient in being able to maintain polarized proton beams in a synchrotron collider.

In order to achieve longitudinal polarization of the protons, which is needed to measure A_{LL} or A_L , the proton bunch polarizations must be rotated to the longitudinal axis just prior to collision, and rotated back again thereafter. In all RHIC experimental halls, that is *where* the observed collisions occur, there are spin rotators positioned such that the beams will pass through them just before entering and after exiting the collision area. The spin rotators are built similarly to the Siberian snakes, in that they are also composed of four helical dipole magnets, but configured such that a spin up (down) proton will have its spin rotated to be aligned (anti-aligned) with its momentum. Polarimetry detectors within each experimental hall measure the transverse components of the polarizations of the colliding proton beams; verifying these transverse components of the beam polarizations are close to zero for supposed longitudinally polarized collisions is an important systematics check for longitudinal spin asymmetry measurements.

Figure 2.2 shows a schematic of RHIC. Protons are initially accelerated by a linear accelerator (LINAC) in the bottom left corner, and proceed into a booster, where they are further accelerated and subsequently injected into the Alternating Gradient Synchrotron (AGS). The AGS was the former primary synchrotron collider at BNL, and now serves as another booster for RHIC. After accelerating in the AGS, the protons enter the AGS-to-RHIC transfer line and are injected into RHIC such that they circulate in a clockwise (blue curves) or a counterclockwise (yellow curves) direction; scientists at RHIC refer to these two beams as the “blue beam” and the “yellow beam.”

It is useful to identify components of the RHIC ring by using the numbers on an analog clock as a sort of coordinate system. Letting 12 o’clock be at the top of the RHIC diagram, Siberian snakes are located at 3 o’clock and 9 o’clock; the snakes at 3 o’clock (9 o’clock) rotate the spin about an axis that points 45° to the outside (inside) of the RHIC rings, and together they cancel out depolarizing resonances up to a maximum operating energy of 255 GeV. Throughout the rings there are 6 possible places where the beams can collide, located at the even-numbered clock-face hours. The STAR experiment is the experimental hall situated at the 6 o’clock position and is where this $A_{LL}^{\pi^0}$ measurement was conducted. The PHENIX experiment is located at 8 o’clock and provides complementary data to STAR. Four spin rotators, two for each beam, are shown in the diagram, just outside of STAR and of PHENIX. Other experiments have been conducted at the other possible intersections,

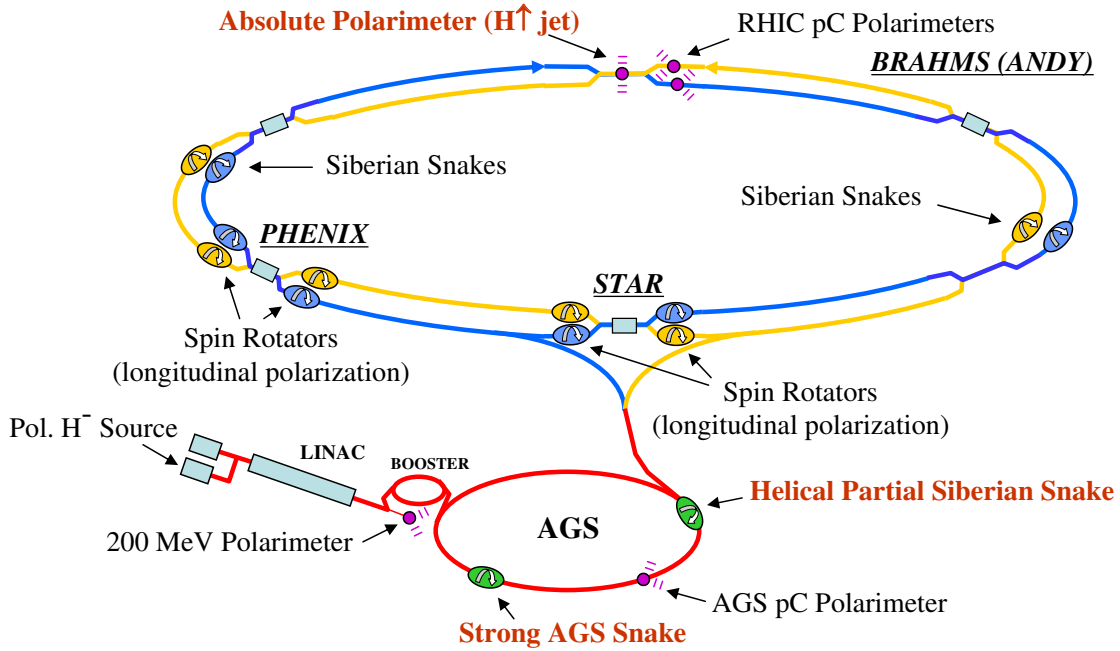


Figure 2.2: RHIC schematic. See text for details. From [71].

such as BRAHMS at 2 o'clock. Finally, polarimeters situated at 12 o'clock are used to track the proton beam polarizations, independently of any experimental hall's local polarimetry measurement.

2.2 The STAR Experiment

The name STAR refers to not only the entire experimental hall at the 6 o'clock collision region, but also to what the acronym stands for, the Solenoidal Tracker at RHIC, which is drawn in figure 2.3, along with the FMS. In the figure, proton p_1 is contained in the blue beam and proton p_2 is in the yellow beam; these protons (bunches) collide at the center of STAR and produce a π^0 which quickly decays into two photons that are observed in the FMS.

Several other particles are produced in typical pp collisions, which are observable in the many other detector systems in the STAR experimental hall. Figure 2.4 shows a top view of the STAR experimental hall, along with some of the detectors and a 1 meter distance scale. For an overview of the main detectors in STAR, along with those in PHENIX, see [72]. This section will briefly describe the detectors labelled in the figure.

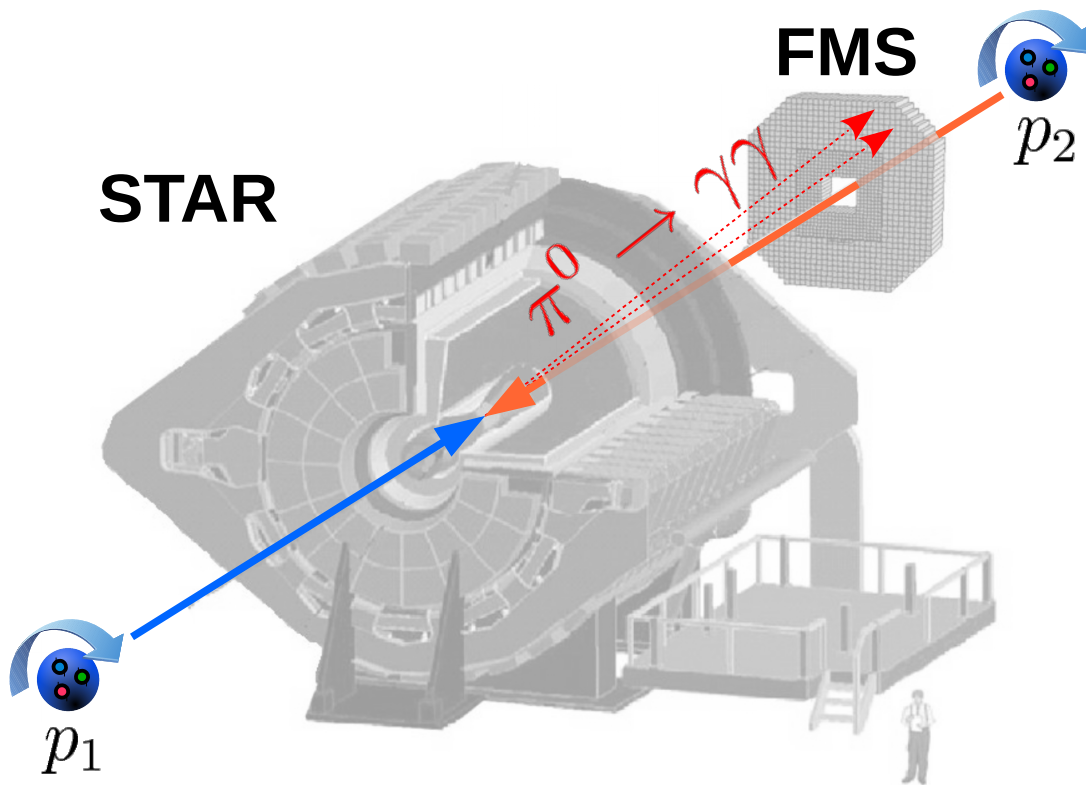


Figure 2.3: Diagram of STAR along with the FMS. Longitudinally polarized proton p_1 collides with polarized proton p_2 in the center of STAR and produces a π^0 , which quickly decays to a photon pair (red dotted lines) which is observed in the FMS.

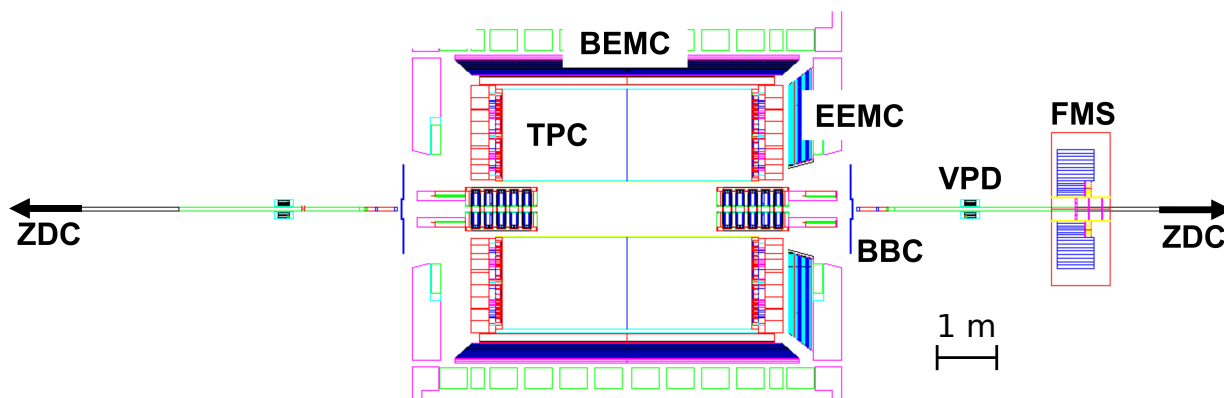


Figure 2.4: Top view of STAR experimental hall; see text for description of the labelled detectors.

In order to describe the detectors' acceptances, we typically use two parameters: azimuth and pseudorapidity. Defining cylindrical coordinates where the cylinder axis is along the proton beam, the polar angle about the beam axis is the azimuthal angle, ϕ . Most detectors in STAR cover the full azimuthal range of $0 \leq \phi < 2\pi$. The other parameter, pseudorapidity η is related to the scattering angle θ , defined as:

$$\eta := -\ln\left(\tan\frac{\theta}{2}\right). \quad (2.3)$$

A scattering angle of 90° corresponds to $\eta = 0$, $\theta = 45^\circ$ corresponds to $\eta = 0.88$, and $\eta \rightarrow \infty$ as $\theta \rightarrow 0^\circ$. Negative η corresponds to backward scattering angles.

The detectors shown in figure 2.4, along with their η ranges, are:

- TPC – Time Projection Chamber: this is the main tracking detector. It is a cylindrical chamber filled with a gaseous mix of 90% argon with 10% methane. At the center where the particles collide is a negatively charged plane, called the cathode. At the outer endcaps of the chamber are two positively charged anode planes. A charged particle which is produced from a collision will ionize the gas, leaving behind a path of free electrons which then drift toward one of the anode planes; the anodes are segmented such that the electron positions and timings will be measured as they hit the anode. Each original charged particle track can thus be reconstructed, forming a 3-dimensional picture of all charged tracks which came out of the collision. Furthermore, the TPC is surrounded by the STAR magnet, which is a solenoid that generates a relatively uniform magnetic field along the proton beam direction. The STAR magnet causes particle tracks to curve, and the radius of curvature is directly related to the particle's momentum.
- BEMC – Barrel Electromagnetic Calorimeter: this detector surrounds the cylindrical TPC and is sensitive to photons, electrons, positrons, and other particles which decay electromagnetically, such as pions. After a particle passes through the TPC, it passes through the BEMC; for charged particles observed in both detectors, the TPC provides tracking and momentum measurement while the BEMC provides complementary energy measurement (calorimetry). The BEMC covers the central (midrapidity, $|\eta| < 1$) region.
- EEMC – Endcap Electromagnetic Calorimeter: another calorimeter is positioned on one of the STAR magnet pole tips, where the pole tips are “caps” positioned on the ends of the STAR solenoidal barrel that help keep the solenoidal magnetic fringe fields

from straying too far outside the STAR magnet. The EEMC is also sensitive to electromagnetic decays, covers the intermediate ($1 < \eta < 2$) region, and is on the same side of STAR as the FMS.

- BBC – Beam Beam Counter: there are two BBCs placed on either side of STAR, and they are composed of hexagonal scintillator tiles. They are connected to the scaler system, which is used for tracking collision rates and luminosities; the scaler system is used for measuring the relative luminosity and will be described later. The BBCs occupy the forward and backward regions ($2.2 < |\eta| < 5$) [73].
- VPD – Vertex Position Detector: this is another scintillator based detector, used for measuring the vertex position; the interaction point of the collision can vary up to ± 100 cm, and the VPD helps track this for every event. Like the BBC, there are two VPDs on either side of STAR, and both are also connected to the scaler system. The VPD detects particles at even more forward scattering angles than the FMS ($4.24 < |\eta| < 5.1$). Using time differences between the two VPDs, the vertex position can be determined; for $\sqrt{s} = 510$ GeV pp collisions, the resolution on the vertex position is ~ 2.4 cm [74].
- ZDC – Zero Degree Calorimeter: as its name suggests, this detector is situated in the very forward region, primarily sensitive to neutrons scattering at angles of $\theta < 4$ mrad [75]. This detector is not only also connected to the scaler system, but also serves as a local polarimeter for STAR, providing a measurement of the local beam polarizations which complement those from the RHIC polarimeters at 12 o'clock.
- FMS – Forward Meson Spectrometer: Finally we mention the FMS, which is the primary detector used in the $A_{LL}^{\pi^0}$ measurement. It covers the forward ($2.5 < \eta < 4$) region and the detector is described in detail in the following section.

2.3 The Forward Meson Spectrometer

The FMS is an electromagnetic calorimeter, composed of 1,264 lead-glass cells, each with a photomultiplier tube (PMT) optically coupled to the back end. It is situated at a pseudorapidity range of approximately $2.5 < \eta < 4$ and the cells are stacked in a square array spanning an octagonal region of size 2 m, approximately 7.2 m from the nominal collision point. Figure 2.5 shows the transverse geometry of the FMS, along with rings of constant η . The black lines indicate divisions between sections of the FMS which are considered for the trigger, and the grey lines divide the individual square-shaped cells. Grey-colored cells, which are along the outer edges of the FMS, are not considered in the trigger system logic,

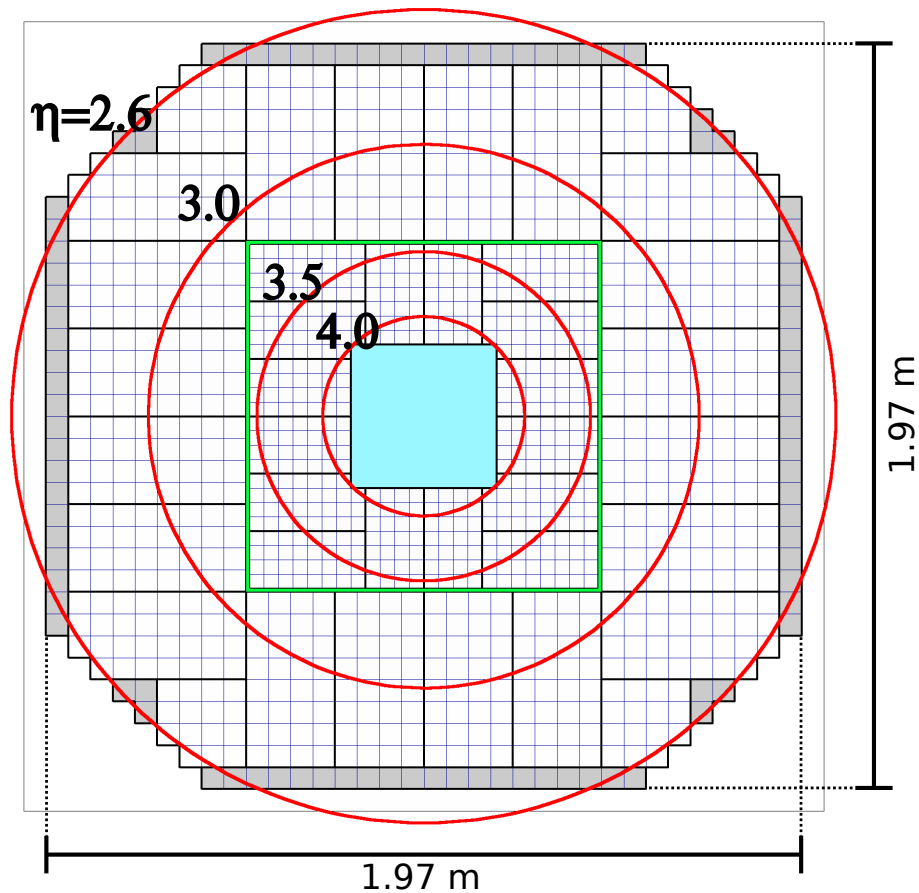


Figure 2.5: FMS geometry schematic; see text for legend.

but their data are still read-out. The green square indicates the boundary between the outer large cells, measuring $5.8 \text{ cm} \times 5.8 \text{ cm} \times 60 \text{ cm}$ each [76], and the inner small cells, measuring $3.8 \text{ cm} \times 3.8 \text{ cm} \times 45 \text{ cm}$ each [77]. Finally, the cyan square represents a hole in the center through which the RHIC beam passes.

2.3.1 Electromagnetic Showers in the FMS

The primary observable in the FMS is the decay of the neutral pion into two photons: $\pi^0 \rightarrow \gamma\gamma$. Cross sections of the neutral pion within the FPD, a smaller, predecessor version of the FMS, can be found in [78]. The π^0 is a pseudoscalar meson with quark composition $|\pi^0\rangle = (|u\bar{u}\rangle - |d\bar{d}\rangle)/\sqrt{2}$. Its fundamental properties [21] are:

- Primary decay modes: $\gamma\gamma$ (98.82%), $e^+e^-\gamma$ (1.17%), and others with branching ratios less than 6×10^{-4}

- Mass: 135 MeV
- Spin: $S = 0$
- Charge: $Q = 0$
- Parity: $P = -1$
- Lifetime: $\tau = 8.5 \times 10^{-17}$ s

Since the primary observables in the FMS are photon pairs from π^0 decays, consider a single photon incident on a Pb-glass cell; at STAR the photon energies are typically 15–30 GeV. As the incident photon passes near a heavy Pb nucleus (or another heavy nucleus in the glass), it will pair-produce an electron-positron pair. The nucleus will absorb the necessary momentum in order to properly conserve momentum, since while in the rest frame of the electron-positron pair the net momentum is zero, there is no rest frame of the photon where its momentum is zero; instead the photon scatters off the electromagnetic field of a nucleus, which provides the necessary momentum absorption. This pair production probability increases as a function of approximately Z^2 , where Z is the atomic number of the nucleus (82 for Pb).

Electrons and positrons which have been pair-produced then pass by more heavy nuclei in the glass and re-radiate photons via the bremsstrahlung process: the electrons and positrons interact with the electromagnetic field surrounding the heavy nuclei and are deflected, radiating the energy lost as photons. These bremsstrahlung photons can, in turn, pair-produce as well, thereby repeating the cycle. This cascade of electrons, positrons, and photons is called an electromagnetic shower, and is shown schematically for a single FMS cell in figure 2.6. See [79] for more details on electromagnetic showers, which is also a good reference for detectors in general.

When the electron or positron energy is low enough, the dominant energy loss mechanism switches from bremsstrahlung to ionization, which for a Pb recoil nucleus, happens around 10 MeV. In order for photons to pair produce, the energy must be at least twice the electron or positron mass, $M_{e^{+(-)}} \approx 0.51$ MeV; however, photon energy loss becomes dominated by Compton scattering by about 10 MeV. Therefore, when the electromagnetic shower particles have energies near the critical 10 MeV, the shower terminates. In the longitudinal profile of the shower, this region of shower termination has the largest number of particles, and is referred to as *shower max*.

Both the large and small FMS cells are 18–19 radiation lengths long, where a radiation length is defined as roughly 7/9 of the mean free path of a photon before pair-production, or the distance an electron or positron travels before losing a fraction $1/e$ of its energy due

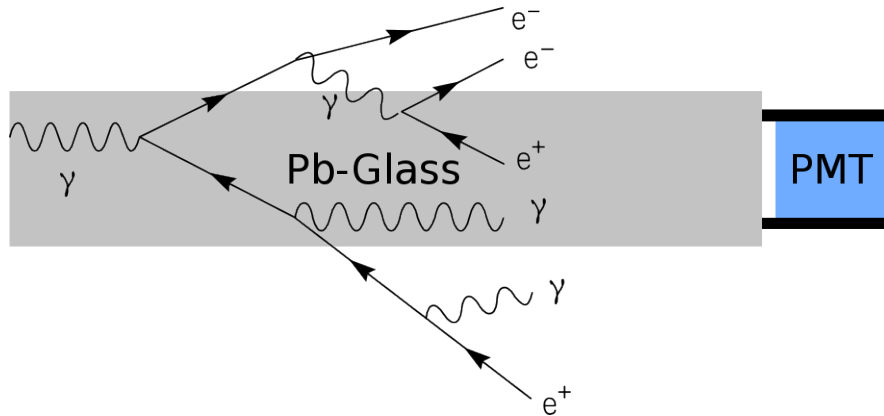


Figure 2.6: Diagram of an electromagnetic shower in a single FMS cell; note that in reality there are significantly many more photons, electrons, and positrons, and that the shower itself spreads into adjacent cells as well.

to bremsstrahlung. The longitudinal length of the Pb-glass cells is sufficient for most of the electromagnetic shower to develop; some of the energy does, however, leak into neighboring cells.

While the electromagnetic shower is developing, the electrons and positrons are moving faster than the speed of light can in the Pb-glass, which has index of refraction $n \approx 1.65$. They therefore radiate Cherenkov radiation in the blue-to-ultraviolet region of the electromagnetic spectrum. This Cherenkov radiation (and other photons of similar energy) is within the spectral sensitivity range of the PMTs.

When a photon of sufficient energy is incident on the front face photo-cathode of a PMT, the photo-electric effect will cause electrons to be emitted from its surface. These photo-electrons are attracted to an electrode in the PMT (under vacuum), and upon interacting with it, cause secondary emission of more electrons, which in turn are attracted to another electrode. These electrodes, called dynodes, are arranged such that each subsequent dynode is at a higher electric potential. After ~ 12 dynodes, the original photo-electric signal is amplified enough to be measured as an electric current; the time integral of the overall current signal generated from the part of the electromagnetic shower which is sampled by the PMT can then be directly related to the incident photon energy.

2.3.2 Pion Event Reconstruction Summary

Neutral pions are identified as two nearby electromagnetic showers, initiated by two decay photons from the π^0 . The invariant mass of the two photons is a function of the energies of the photons and their decay opening angle; these parameters are measurable by analyzing

the electromagnetic shower relative positions and energy depositions, therefore the original π^0 mass can be reconstructed from energy deposition measurements in clusters of FMS cells. The invariant mass $M_{\gamma\gamma}$ of a two photon decay seen in the FMS is determined by

$$M_{\gamma\gamma} \approx \frac{E_{\gamma\gamma} D_{xy}}{2R_z} \sqrt{1 - Z_{\gamma\gamma}^2}, \quad (2.4)$$

where, given E_1 and E_2 as the photon energies, $E_{\gamma\gamma} = E_1 + E_2$ is the total energy, D_{xy} is the transverse distance between the detected photon pair, R_z is the distance between the FMS and the interaction point, and $Z_{\gamma\gamma} = |E_1 - E_2|/E_{\gamma\gamma}$ is the energy imbalance. For further details on π^0 decay kinematics and the derivation of equation 2.4, see section 3.2 or appendix A.

The identification of photon events in the FMS begins with the observation of a distribution of energy, where typically $\sim 80\%$ of the photon energy is deposited into a single cell and the remaining $\sim 20\%$ is deposited within the adjacent cells. Note that the cells are optically isolated from one another by 25 μm of aluminized Mylar. The distribution of energy in the cells which are considered (along with factoring in a low-energy noise cutoff) is compared to a shower shape, which models the fraction of energy deposited as a function of transverse distance from the location where the incident photon initiated the shower. If the energy distribution is similar to the expectation from the shower shape model, the photon is then considered valid; its point of entry in the FMS is accurate to within 1/10th of a cell width. See section 3.4.2 for more details.

Looking more carefully at equation 2.4, one sees that the energy dependence of the opening angle α of the photons is approximately

$$\alpha \approx \frac{M_{\gamma\gamma}}{\sqrt{E_1 E_2}}. \quad (2.5)$$

Thus higher energy π^0 s have smaller opening angles. Within the large cells, two-photon clusters begin to merge for energies above approximately 50 GeV, whereas within small cells, they merge above approximately 80 GeV. This cluster merging turns out to be one of the major obstacles of π^0 reconstruction, as it is non-trivial to distinguish between a single photon cluster and a two-photon cluster. More on this will be discussed in sections 3.4.3 and 3.4.5.

2.3.3 FMS Trigger

The RHIC bunch crossing rate is approximately 9.38 MHz, that is, there is a possible collision at STAR every 107 ns. Since detector data-taking times are typically on the time scale of

reconstruction in the central calorimeter, vertex finding, *etc.* Like level 2, if level 3 decides to reject the event, it is simply deleted from the DAQ system. By the time level 3 decides to accept the event, the event will be built and ready to be packaged with all other events in the data-taking period in order to be sent to the High Performance Storage System (HPSS) for long-term storage.

The RHIC data-taking period for the presented $A_{LL}^{\pi^0}$ measurement is RHIC Runs 12 and 13, which occurred in 2012 and 2013, respectively. During these Runs, STAR was able to acquire data at a rate of about 1 kHz, with 300–400 Hz of the bandwidth dedicated to the FMS. Improvements to the trigger and DAQ systems are always underway between RHIC Runs; DAQ rates in the 2017 run were as high as 6 kHz overall.

2.3.3.2 FMS DSM Tree

The FMS triggering information is first handled by four QT crates, where the acronym QT stands for charge (Q) from time (T) integration of current. The current which is integrated comes from the PMTs; the resultant charge is *digitized* to a 12-bit integer ranging from 0 to 4,095, denoted as number of ADC (Analog-to-Digital Conversion) counts. The time interval over which the integrals of the PMT signals are taken is phase-locked to the RHIC bunch crossing rate and long enough to contain the typical PMT pulse widths. Each of the four QT crates is associated with a single quadrant of the FMS; the trigger logic explained below is replicated for each crate.

Each QT crate contains 11 QT boards, 10 of which are used in the FMS trigger; all FMS channels are mapped into the QT boards. Each QT board contains 4 cards, called QT8 cards, with 8 inputs each. PMT signals are directly connected to the QT8 card inputs through a patch panel, which provides a mapping “dictionary” between the FMS channels and the trigger system.

Figure 2.7 shows a diagram of the FMS mapping into the QT system. The bold black lines separate channels which are mapped into QT boards, which are labelled with a letter from A to J. Within each QT board, the stripes separated by dashed lines denote QT8 cards and are labeled with a number from 0 to 3 for each QT board. Note that the outermost rows and columns as well as 3 cells in each corner are not in the trigger and are colored grey in the diagram; their PMT signals are still sent to the 11th QT board for digitization, however.

The output of the QT boards is sent into the DSM tree, as shown in figure 2.8; each QT board outputs to the DSM tree 32 bits, composed of 5 bits representing a truncated ADC sum from each QT8 card, plus 12 bits encoding the ADC and channel number of the cell with the highest ADC, called the High Tower (HT).

These 32-bits from all 40 QT boards are then sent into layer 0 of the DSM tree, which,

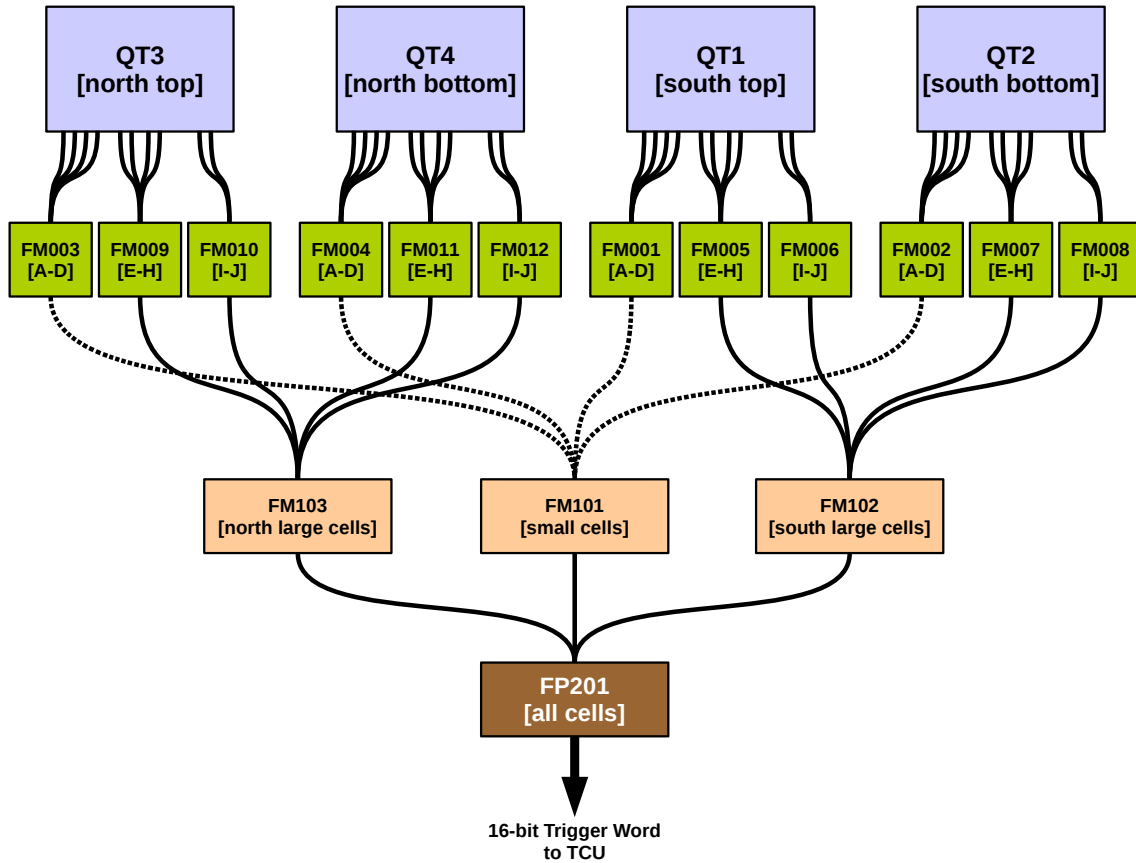


Figure 2.8: FMS DSM tree. Analog data enter the QT boards at the top of the diagram, where 11 boards are housed per QT crate (QT1-QT4). 10 QT boards in each quadrant output logic data to DSM layer 0 (FM001-FM012), which output to layer 1 (FM101-FM103), then finally to layer 2 (FP201), whose output is a 16-bit word sent to the TCU. All connectors between boards transmit a 32-bit logic signal.

$$- \text{sumGH} = G2 + G3 + H0 + H1$$

$$- \text{sumIJ} = I2 + I3 + J0 + J1$$

This *board sum* technique is essentially a very fast but very crude, low-level cluster finding algorithm. Layer 0 also compares the HT ADC to two thresholds and ORs the results together. In total, the 12 layer 0 DSM boards each output 32 bits encoding the QT8 sums and the HT threshold comparisons.

The 12×32 -bit trigger data stream from layer 0 is then sent to 3 layer 1 DSM boards: one for the south large cells, one for the north large cells, and one for all the small cells. The HT threshold bits are ORed together from all four quadrants and compared to thresholds,

forming the HT trigger. Sums of QT8 sums within FMS sectors are also taken and compared to cluster thresholds, forming the large and small board sum triggers and the basis of the jet patch trigger. The sector sums are then latched for output as well as their comparisons to cluster thresholds. In total, 32 bits are output from the small cells and 64 bits from the large cells (32 bits for both north and south).

The layer 2 DSM board is responsible for combining all the data into a final 16-bit output trigger word. In this layer, quadrant sums are combined in various ways to form 6 overlapping Jet Patch (JP) sums, shown in figure 2.9. Other high-level triggers can also be defined here, such as the dijet trigger (not used in this analysis). The final 16-bit trigger word is composed of comparisons of ADC sums to various thresholds: 2 HT bits, 2 small cell board sum bits, 3 large cell board sum bits, 3 jet patch bits, and the dijet bit. Since layer 2 is the last DSM in the tree, these bits are forwarded to the TCU. These comparisons make up 11 bits, where the other 5 bits of the 16-bit word were not used in this analysis or were reserved for coincidences with other detectors.

The FMS data are not manipulated by any higher level triggers. If the event is ultimately determined to be valid, the digitized data are written out to the *trigger files*, as well as the trigger word which was sent to the TCU and the prescaled (and dead-time corrected) trigger word from trigger level 2, called the *L2 sum*. These trigger words are then used in data analysis to filter events of interest.

An additional trigger that comes from the FMS but is not particularly used in overall trigger decisions is the FMS LED trigger. In front of every channel of the FMS is the output of a fiber optic cable, which is connected to an LED flasher system, configured to flash at 1 Hz. Looking at FMS LED events helps track time-dependence of the gain of the PMTs as well as radiation damage in the Pb-glass. The LED trigger is configured on an independent DSM board, which is used for other miscellaneous triggers in STAR.

2.3.3.3 FMS Trigger Set

In total, 9 FMS triggers were defined in RHIC Runs 12 and 13:

- Jet Patch (JP) Triggers
 - JP1
 - JP2 (take-all)
- Large Board Sum (LgBS) Triggers
 - LgBS0

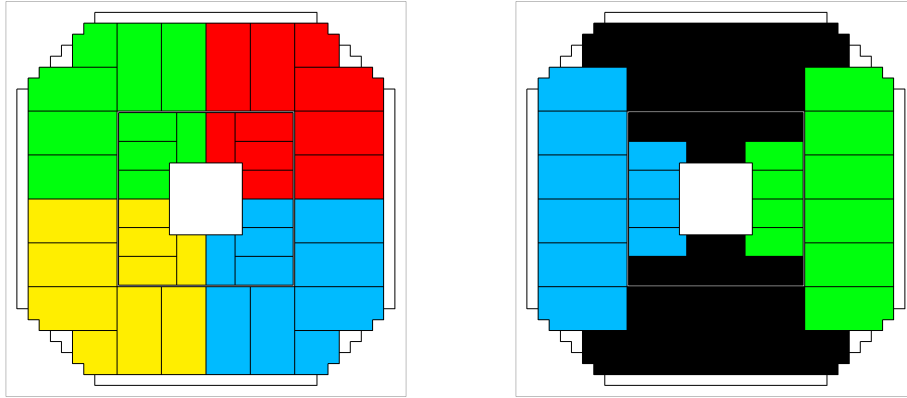


Figure 2.9: The 6 regions (colored) of the FMS which are summed together as jet patch sums; the top and bottom sectors in the right-hand figure are not included as jet patches.

- LgBS1 (take-all)
- Small Board Sum (SmBS) Triggers
 - SmBS0
 - SmBS1 (take-all)
- High Tower (HT) Trigger (take-all)
- Dijet (DJ) Trigger (take-all)
- LED Trigger (take-all)

The *take-all* triggers are those which are not prescaled, *i.e.*, $\rho = 1$. The fact that there are two JP, SmBS, and LgBS triggers is because two thresholds are used: the take-all triggers have higher ADC sum thresholds than their associated prescaled triggers.

In the data files, for every event the ADC counts and timing for every channel are available, as well as the trigger word which was sent into the TCU, denoted `lastDSM`, and the trigger word after prescaling, denoted `L2sum`, since it is determined at trigger level 2. In order to filter events with specific triggers, naturally the `L2sum` variable is preferable; this variable is composed of two 32-bit integers forming a 64-bit trigger mask. There was a software bug present in 2012 and 2013, however, in which the lower 32 bits of `L2sum` was simply copied into the upper 32 bits; only the lower 32 bits are correct. Fortunately, the only triggers which were defined in the upper 32-bit half were take-all triggers, and hence one can instead use the `lastDSM` trigger words for those triggers, since their prescale factors are

unity. Table 2.1 shows a summary of the triggers and which trigger bits define them. `L2sum` is given as a hexadecimal trigger mask, representing a single bit out of the 64 bits (divided into upper and lower 32 bits), whereas `lastDSM` is given as which DSM output channel the trigger bit occupies. The right-most column states which trigger bit mask is ultimately used in order to filter events in analysis.

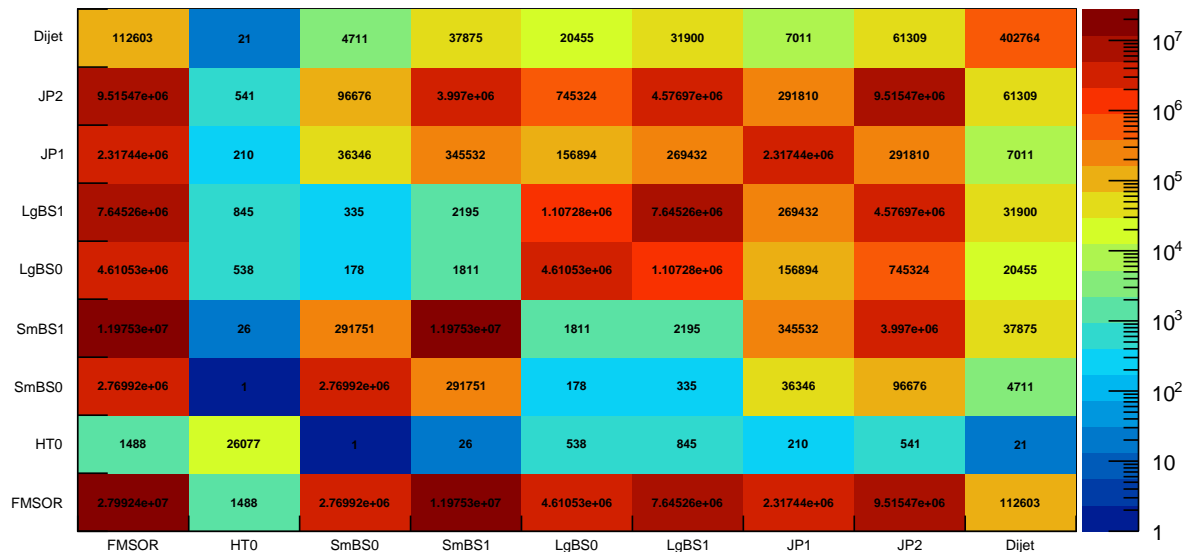
Trigger	L2sum high bitmask	L2sum low bitmask	lastDSM bit	Take-all?	Which trigger bit mask to use
HT	0x0	0x1000000	0	no	L2sum
SmBS0	0x0	0x400000	2	no	L2sum
SmBS1	0x2000	0x0	3	yes	lastDSM
LgBS0	0x0	0x800000	5	no	L2sum
LgBS1	0x1000	0x0	6	yes	lastDSM
JP1	0x0	0x2000000	9	no	L2sum
JP2	0x800	0x0	10	yes	lastDSM
Dijet	0x8000	0x0	11	yes	lastDSM

Table 2.1: Trigger bit locations in the last DSM (FP201) 16-bit output word and the 32+32-bit trigger bitmask from trigger level 2. The state of whether or not each trigger is take-all is also shown, along with which trigger bit mask is ultimately used in analysis.

For this $A_{LL}^{\pi^0}$ analysis, we have chosen the following combination of trigger bits: the overall OR of SmBS0, SmBS1, LgBS0, LgBS1, JP1, and JP2. This was chosen to avoid the Dijet and HT triggers, which are not as well-understood as the others, while at the same time maximizing the statistics analyzed. In terms of bit masks, this trigger combination corresponds to an L2sum bit mask of 0x2c00000 on the lower 32 bits for the prescaled triggers, Ored with the OR of bits 3, 6, and 10 on the lastDSM output word for the take-all triggers. In this analysis, this combination of triggers is denoted as “FMSOR.”

Figure 2.10 shows the overlap of the triggers, including FMSOR, for candidate π^0 events (more on π^0 event selection later). The overlap is given as a matrix, where each entry is the number of events satisfying both the trigger on the horizontal axis and that on the vertical axis. The diagonal then represents the overall distribution of triggers. The overlap between SmBS and LgBS is quite small, as expected, while the overlap between the BS and JP triggers is significant. The HT trigger (written in the figure as HT0) has very low statistics, as does the dijet trigger, and neither of these are used in the $A_{LL}^{\pi^0}$ analysis.

π^0 FMS trigger overlap matrix



π^0 FMS trigger overlap matrix

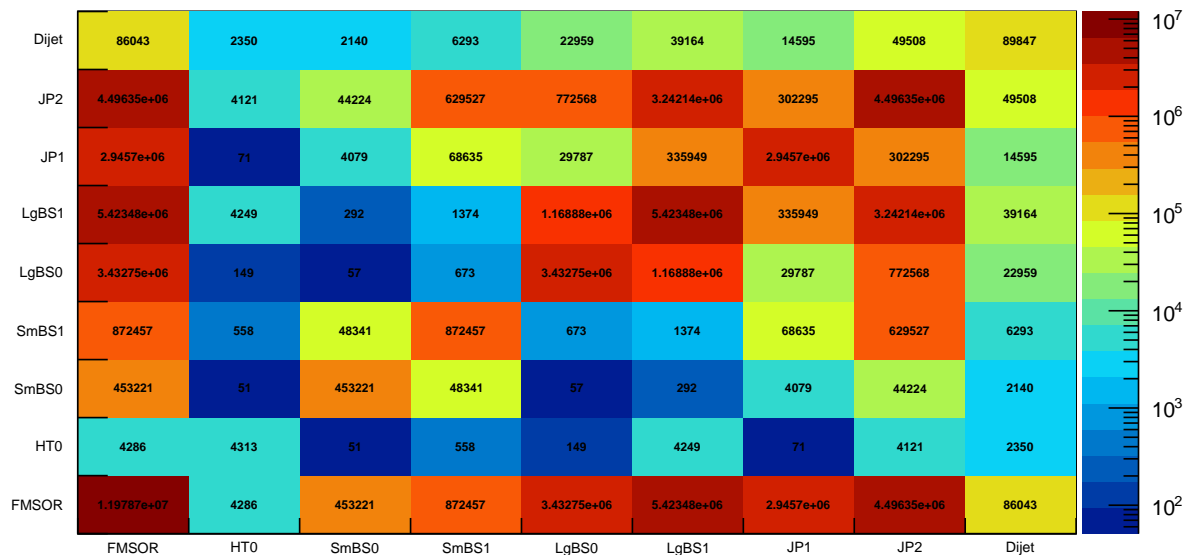


Figure 2.10: Trigger overlap matrix for Run 12 (top) and Run 13 (bottom); color scale is logarithmic and corresponds to the number of times the trigger on one axis is coincident with the trigger on the other axis.

2.3.4 Radiation Damage

Having discussed the FMS trigger in detail, we now turn to a pathology in the FMS detector that is responsible for causing a reduction of the overall trigger rate as a function of time: radiation damage in Pb-glass. The electromagnetic radiation which passes through the Pb-glass is ionizing radiation, which can strip electrons from atoms within the glass, ionizing them. While the stripped electrons may be able to ionize additional atoms, these electrons will likely find their way back to the valence shell of some other ion within the lattice; the net result is that some ions become more positively charged, while others become more negatively charged, which does not affect calorimetry overall. This effect is not all that happens, however.

Some electrons (as well as holes) will end up elsewhere such as in an anionic vacancy, or in/associated with some other type of crystallographic defect. These “misplaced” electrons are called color centers or F-centers (where F stands for *farbe*, German for color), and for Pb-glass, they absorb photons mostly in the visible part of the spectrum. The accumulation of F-centers causes the glass to begin darkening, which reduces detector efficiency [82]. The overall optical absorption spectrum is rather broad, because it represents a superposition of all of the F-centers’ absorption bands, which could be at multiple different wavelengths. This formation of F-centers is typical of irradiated glass in general; for a discussion of this for lead glass fibers, see [83].

In all RHIC Runs up to Run 13, the FMS accumulated radiation damage, causing an overall monotonic decrease in the trigger rates within each Run. After Run 13, the Pb-glass cells were unstacked, and since the F-center accumulation is proportional to the electromagnetic shower density, a relative darkening or “browning” of the glass, proportional to the longitudinal shower profile, was observed. More damage was seen in cells closer to the beam line than in those farther away, because of the higher amount of irradiation there.

The purpose of unstacking the FMS was to *photobleach* the cells: exposing the glass to radiation within the ultraviolet (UV) region was found to reverse the radiation damage. UV radiation likely excites trapped electrons, which subsequently could find their way back to the valence shell of some ions. Consequently, the number of F-centers decreases and the glass becomes clear again. The exact mechanism of bleaching depends on the material being bleached and the types of F-centers which form; see for example [84, 85, 86]. Thermal bleaching could have also been done, which involves slowly heating the glass to a high temperature then slowly cooling it, which basically anneals it; however, given the fragility of Pb-glass in general, we chose photobleaching instead. Both thermal bleaching and UV photobleaching have proven effective at curing radiation damage in Pb-glass [87]. During the summer of 2013, all cells of the FMS were exposed to 48 hours of direct sunlight. After

photobleaching, the cells were much more transparent and cured. The FMS was subsequently re-stacked in 2014, and refurbished for use in Run 15 in 2015 and beyond.

During Run 15, the higher luminosity was found to cause the Pb-glass to accumulate radiation damage more rapidly than before. Since unstacking the FMS, exposing all cells to sunlight, and re-stacking the glass is a very labor-intensive task, we sought an alternative solution: photobleaching by a UV-emitting light that we could install in front of the FMS. Several sample radiation-damaged cells were exposed to various sources of UV radiation, ranging from tanning bed lights, bug lights, UV lasers, to UV-LEDs. It turned out that the most effective and practical bleaching method came from UV-LEDs, which were shown to fully cure the glass within approximately 48 hours.

The optimal wavelength was determined to be 375 nm, given our choices of UV-LEDs, and an array of roughly 1,000 such UV-LEDs was built. Because of design limitations, the array had to be built in small modules and then be connected together after installation; furthermore, the UV-LEDs needed to be cooled. All LEDs were mounted on aluminum plates that were embedded with copper pipes carrying cooling water. The entire array was installed facing the front face of the Pb-glass, with higher LED densities closer to the higher-radiation region near the beam pipe. This UV-LED array was built in 2016, installed prior to Run 17, and ultimately turned out to be a very successful method to keep the radiation damage minimal during the entire Run. More details on the UV-LED system, as well as on the 2013 sunlight photobleaching, can be found in appendix L.

2.4 The Scaler Systems

A scaler system is basically a counting system: if, for example, the ZDC sees enough hits above a given threshold, the associated scaler counter will increment by one count, called a scale count. The BBC, VPD, and ZDC are all connected to the *scaler boards*, which are able to increment their counters at the same rate as the bunch crossing rate of 9.38 MHz. The data from these scaler boards are essential in determining the relative luminosity, in coincidence with particle yields, in order to measure a spin asymmetry.

For each bunch crossing, there is a 24-bit¹ readout of the scaler detectors, where each bit corresponds to a particular counter or number. For some of the bits, if a particular signal, such as the sum of ADC counts from the cells in the VPD, is above a certain threshold, the corresponding scaler bit will be set to 1, otherwise it will be set to 0. Other scaler bits correspond to coincidence signals, which occur when two signals are above their thresholds and occur within a certain time window. For example, if both of the VPDs on either side of

¹In Run 12 it was 24-bit, but for Run 13 and beyond it has been 32 bits

STAR each see a large enough signal with a small time difference between the two, the VPD coincidence bit will be set to 1; in fact, the time difference between the two signals can be used to measure the vertex position of the collision.

The lower 17 bits of the 24-bit readout correspond to such above-threshold and coincidence signals. The upper 7 bits correspond to the bunch crossing number, a number between 0 and 119 that corresponds to one of the 120 bunches in one beam crossing with another in the other beam. Since the requested spin of each bunch is known, the incoming spins of the protons are known for every bunch crossing (but with a polarization, of course), and recording the bunch crossing number provides a way of associating the scale counts with particular proton collision spin combinations.

The 24-bit readout is the input to the scaler boards, which are composed of 2^{24} addressable 5 byte memory cells [88]. Every possible combination of the 24 readout bits corresponds to a particular memory cell on a scaler board: the 24-bit readout is simply an input address on the scaler board. When this address is called, the 5 byte number stored in the corresponding memory cell is incremented by one. This memory is sometimes referred to as histogramming memory, and in theory, the scaler boards are capable of histogramming the data at the bunch crossing rate for up to 24 hours.

Most often these scaler boards are used during the data-taking period for monitoring collision rates and background. The RHIC beams are held in the synchrotron rings for 8 hour periods called *fills*, after which the beams are dumped and new ones are injected. During each fill, collisions are occurring which remove protons from the beam, causing the actual collision rate to decrease with respect to the constant bunch crossing rate. Such time-dependent rates can be monitored by, for example, coincidence rates of the ZDC, since a coincidence bit will likely only be true if there was a collision.

In the $A_{LL}^{\pi^0}$ analysis, the scaler board data are used for measuring the relative luminosity and will be discussed in chapter 4. Since the bunch crossing number is recorded along each event's scaler detector readouts, the number of scale counts for each of the spin combinations can be recorded. Since these counts are directly proportional to the luminosities for each of the spin combinations, ratios of these counts directly measure the relative luminosities. The BBC, ZDC, and VPD can each be used to independently measure the relative luminosity, and comparisons between them provide an estimate of its uncertainty.

2.5 Polarimetry

To measure any spin asymmetry, the polarization P of the colliding particle(s) must be known, since a spin asymmetry A is related to the raw, measured asymmetry ε via $A = \varepsilon/P$.

The 12 o'clock interaction region houses the RHIC polarimeters: the hydrogen gas jet (H-jet) and the proton-carbon (pC) polarimeters. See [89] for a summary of polarimetry at RHIC, and the references therein.

The H-jet polarimeter consists of a vertical jet of longitudinally polarized hydrogen gas. Since the proton beams are transversely polarized while they pass through the polarimetry region, the spins of the beam protons are aligned or anti-aligned with the spins of the target jet protons. The H-jet polarization, p_{target} , is monitored by its own polarimeter. Elastic collisions between the beam protons and H-jet protons are observed: arrays of silicon strip detectors observe the scattered H-jet protons. The measurement of the transverse single spin asymmetry for this process, $A_N^{pp \rightarrow pp}$, is known well enough such that measurements of the raw asymmetries $\varepsilon_{\text{target}}$ and $\varepsilon_{\text{beam}}$ (between left-scattered and right-scattered protons) can be used to extract the beam polarization P_{beam} via

$$A_N^{pp \rightarrow pp} = \frac{\varepsilon_{\text{beam}}}{P_{\text{beam}}} = -\frac{\varepsilon_{\text{target}}}{P_{\text{target}}}. \quad (2.6)$$

The H-jet polarimeter is a bit slow, taking a couple of days to obtain a statistical uncertainty of $\sim 5\%$, but it is useful for providing an absolute polarization measurement which is used to normalize the pC polarimeter measurement.

The pC polarimeter is a fast polarimeter, taking only 30 seconds to provide a statistically significant measurement. It is therefore used multiple times a fill to track the time-dependence of the overall depolarization. The polarimeter target is a thin carbon ribbon, and recoil carbon nuclei are detected by six silicon strip detectors, arranged hexagonally around the target. These detectors provide a measurement of the raw asymmetry ε , and combined with the known $A_N^{pp \rightarrow pC}$ gives $P_{\text{beam}} = -\varepsilon/A_N^{pp \rightarrow pC}$. For the $A_{LL}^{\pi^0}$ measurement, the pC polarimeter normalized measurements are used. These measurements, along with their errors, are provided for every fill by the RHIC polarimetry group.

In addition to the RHIC polarimeters, the STAR and PHENIX experimental halls each have their own local polarimetry. For STAR, polarimetry is typically measured by the ZDC (see section 5.2); having a polarimeter near the collision region is useful for confirmation of, for example, proper configuration of the spin rotators for longitudinally polarized collisions. During RHIC runs with transversely polarized collisions, local polarimetry measurements can be compared to those from the H-jet and pC polarimeters.

Chapter 3

Event Selection

This chapter outlines the data selection procedure, which aims for a clean and well-understood sample of π^0 s while maximizing the overall statistics. The data are from the RHIC Runs 12 and 13, taken in 2012 and 2013, from longitudinally polarized pp collisions with a center-of-mass energy of $\sqrt{s} = 510$ GeV.

3.1 Data Set and Quality Assurance

We begin with a general description of the data set. The data are typically acquired in 30 minute intervals, called *runs* (or sometimes *DAQ runs*). These runs allow for the ability to look at the overall data set for an entire RHIC Run (a RHIC Run will henceforth be capitalized, to differentiate it from a 30-minute run) as a time series and cull out any runs which had anomalies, such as abnormally high trigger rates or dead time.

A basic run Quality Assurance (QA) test was first used to filter runs which are reasonably consistent with each other. For each trigger T in each run, the following quantity is computed:

$$f_T = \frac{N_T \cdot \rho_T}{N_{MB} \cdot \rho_{MB}}, \quad (3.1)$$

where N is the number of triggers, ρ is the prescale factor of that trigger, and the subscript MB is for a minimum bias trigger, given by the BBC, VPD, or ZDC; in this analysis, the BBC is used as a minimum bias trigger. The numerator of f_T is proportional to the T trigger rate, which decreases steadily within each fill simply due to the decrease in collision rates during the fill. Dividing the trigger rate by a minimum-bias trigger's rate takes this fill-structure out of f_T , and under ideal conditions, f_T should be relatively constant throughout a RHIC Run. Issues such as radiation damage, however, can cause f_T to decrease over time; moreover, changes in trigger thresholds can introduce steps up or down in f_T . Ultimately

f_T is useful as a means to filter out “outlier” runs, which are those that could have had abnormally high or low trigger rates, or other related pathologies.

The ratio f_T is plotted in figures 3.1 and 3.2 as a function of a run index, in chronological order. Any time there was a major change in the system, such as a threshold change, beam condition change, *etc.*, a vertical line was drawn; these vertical lines separate the trigger data into *epochs*, defined as contiguous time periods over which the trigger conditions were the same. Any epoch with red-colored points was marked as bad overall, such as all runs before run index ~ 240 in Run 13, and all of the runs in a bad epoch are omitted from the analysis.

Within each epoch, f_T tends to decrease exponentially as a function of time. Since f_T is proportional to trigger rate, the FMS trigger rate as a whole is decaying. The culprit of this decay is radiation damage within the Pb-glass cells. As the Pb-glass cells darken, the amount of light which reaches the PMTs decreases, which in turn causes a reduction in the trigger rates. Within each epoch, an exponential fit was performed, as shown by the red curves in figures 3.1 and 3.2. In some epochs, the exponential fit was not as good as it could have been, usually because there were too many outliers; however, all fits are good enough overall for a reasonable outlier filter.

Figures 3.3 and 3.4 shows the value of f_T normalized to the value given by the fit function for each run. The run QA was then performed by visually selecting boundaries around the normalized f_T values in order to remove any outliers; runs within these boundaries pass the QA test and are defined as “good.” These boundaries are drawn in the figures as horizontal lines, and although this is more of a qualitative QA method, it is sufficient to cull a more reasonable and consistent data set from the whole, serving as a decent starting point for analysis.

Run 12 f_T vs Run Index

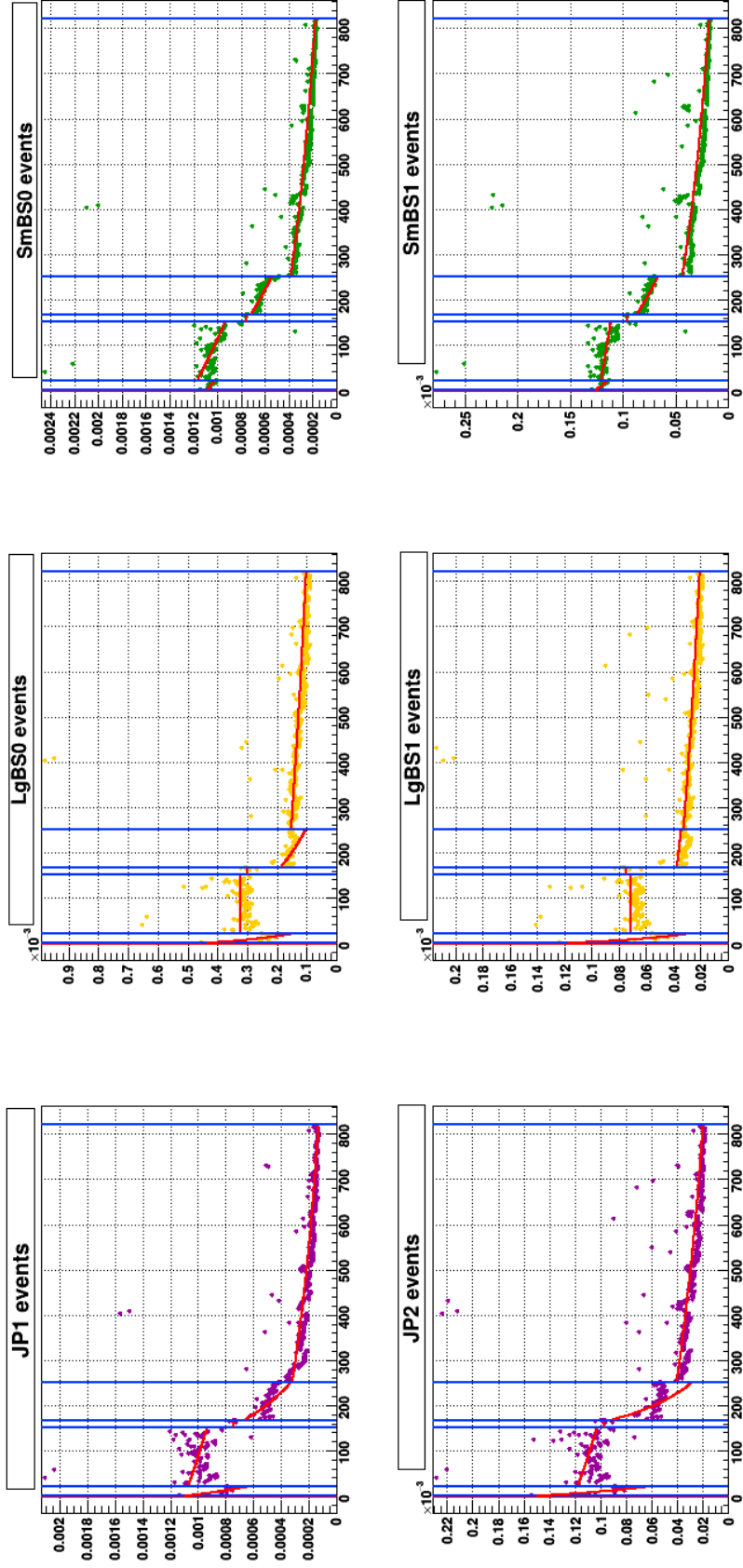


Figure 3.1: f_T vs. data-taking run index (chronological order) for each trigger used in $A_{LL}^{\pi^0}$ analysis for Run 12. Vertical lines divide epochs.

Run 13 f_T vs Run Index

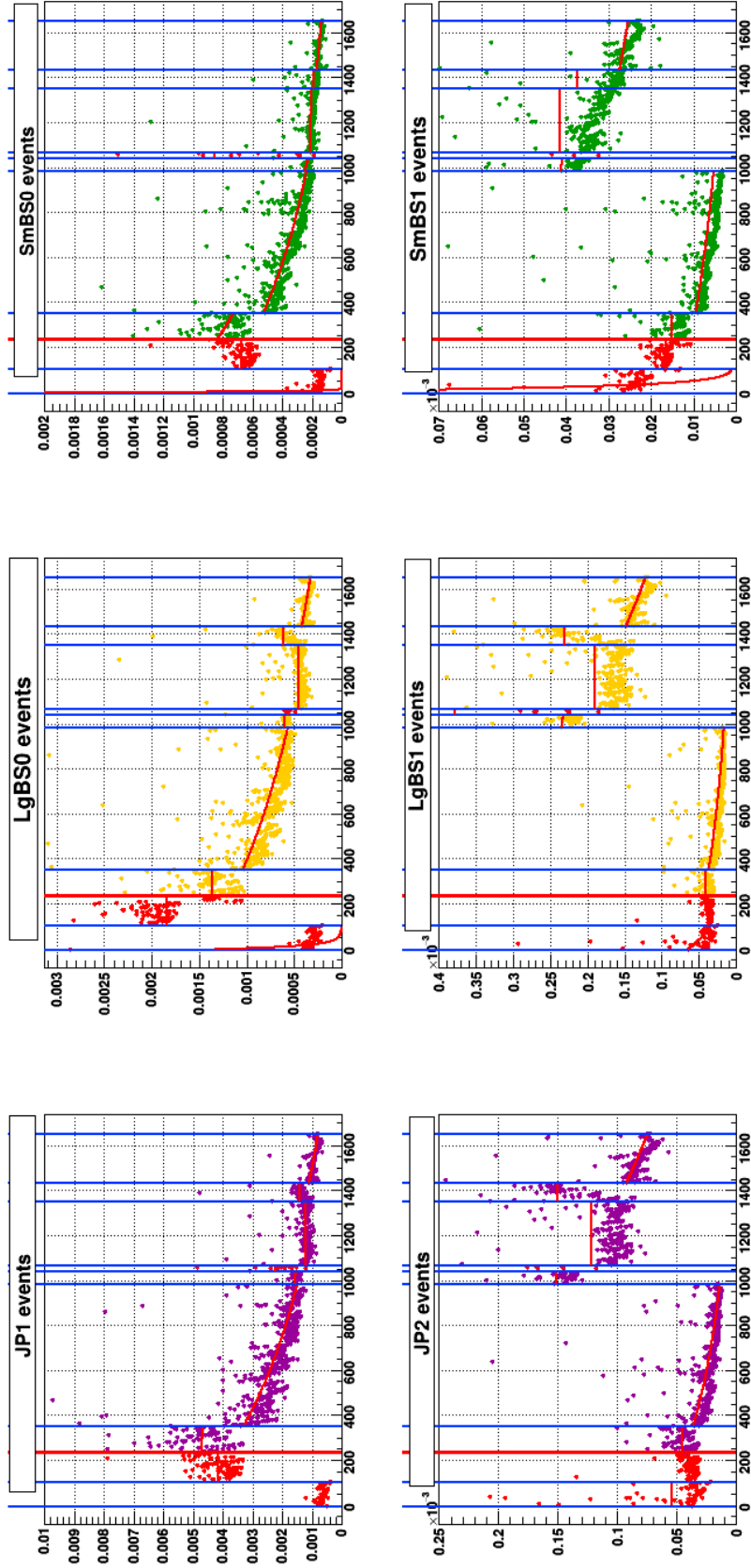


Figure 3.2: f_T vs. data-taking run index (chronological order) for each trigger used in $A_{LL}^{\pi^0}$ analysis for Run 13. Vertical lines divide epochs.

Run 12 Epoch-normalized f_T vs Run Index:

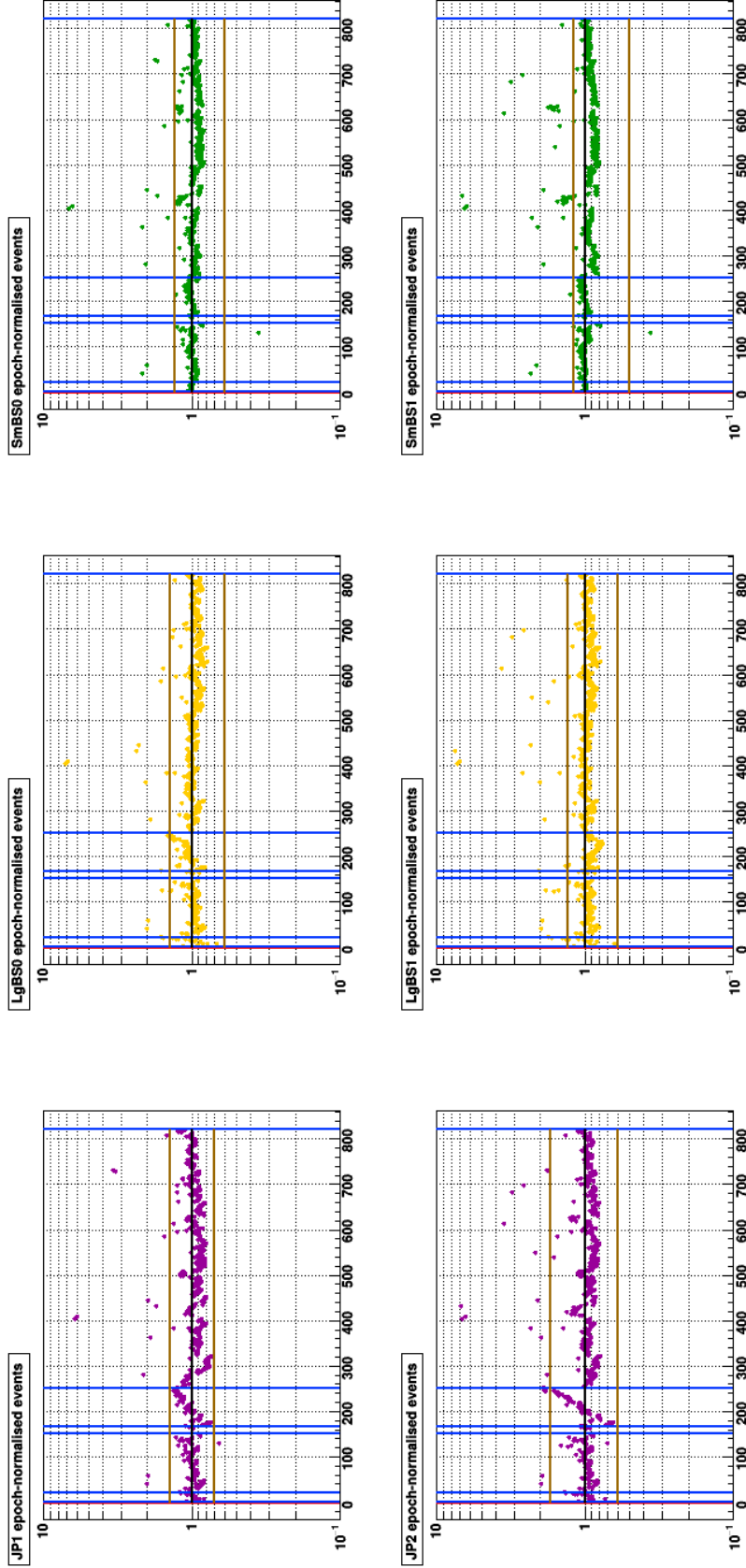


Figure 3.3: Run 12 f_T divided by epoch exponential fit vs. data-taking run index. Vertical axis is log scale, a bold black horizontal line is drawn at unity, and the brown horizontal lines represent the QA cuts. A run is “good” if it is within the brown horizontal lines.

Run 13 Epoch-normalized f_T vs Run Index:

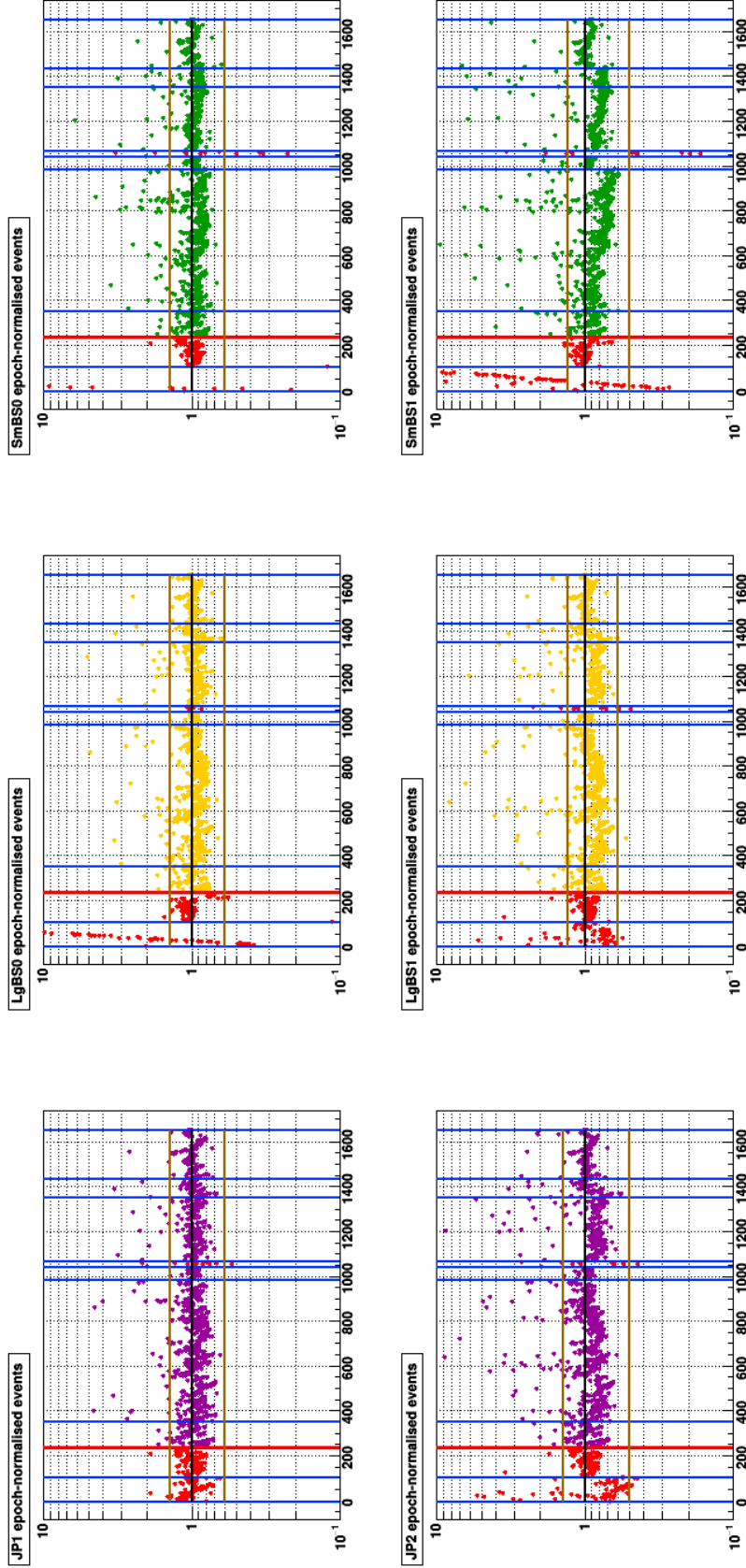


Figure 3.4: Run 13 f_T divided by epoch exponential fit vs. data-taking run index. Vertical axis is log scale, a bold black horizontal line is drawn at unity, and the brown horizontal lines represent the QA cuts. A run is “good” if it is within the brown horizontal lines.

3.2 π^0 Kinematics and FMS Acceptance

In order to specify the constraints on the π^0 sample used in this analysis, let us begin with a discussion of π^0 kinematics. Consider a π^0 with energy E which decays into two photons of energies E_+ and E_- , and with a decay opening angle of α . These energy variables (E_+, E_-) of the 2-photon system can be transformed into two variables (E, Z) , associated with the π^0 : the total energy $E = E_+ + E_-$ and the energy imbalance

$$Z := \frac{E_+ - E_-}{E}. \quad (3.2)$$

The subscripts “+” and “-” were chosen so that $E_{\pm} = E(1 \pm Z)/2$, with $E_+ \geq E_-$. The invariant mass, M , depends on the photon energies and opening angle as

$$M = 2 \cdot \sqrt{E_+ E_-} \cdot \sin \frac{\alpha}{2} = E \cdot \sqrt{1 - Z^2} \cdot \sin \frac{\alpha}{2}. \quad (3.3)$$

For further details on π^0 decay kinematics, see appendix A.

In addition to the π^0 E , Z , and α , two angles are also needed to fully describe the π^0 momentum p : the azimuthal angle ϕ and the scattering angle θ . Referring to figure 3.5, let the positive z axis be along the proton beam, pointing toward the FMS, and the y axis point upward, with the origin centered at the nominal proton-proton interaction point. The azimuth ϕ is defined as the angle between the positive x axis and transverse momentum vector p_T , which is the projection of the momentum vector p on the xy plane. The scattering angle θ , defined as the angle between p and the positive z axis, is more commonly given in terms of the pseudorapidity η , defined in equation 2.3. In practical data analysis, the variables used to classify π^0 kinematics are $\{E, Z, M, p_T, \eta, \phi\}$.

The FMS is situated about 7.2 m from the nominal interaction point, and occupies about a 2 m \times 2 m transverse size; it spans a pseudorapidity range of $2.5 < \eta < 4.2$ over full azimuth. Note that the outer boundary of the FMS is octagonal and that the inner boundary is square; thus the η boundary rings listed here are only approximate bounds of the FMS geometry boundaries. Given typical values of \sqrt{s} of 200 and 510 GeV as well as trigger thresholds and reconstruction limitations, typical energy and momentum ranges of π^0 s are $10 < E < 100$ GeV and $2 < p_T < 10$ GeV. An upper limit on Z is also typically employed, in order to omit high-energy photons which could have been mis-identified as a π^0 ; a typical constraint is $Z < 0.8$. All of these kinematic limits provide an estimate of the overall FMS acceptance for π^0 s.

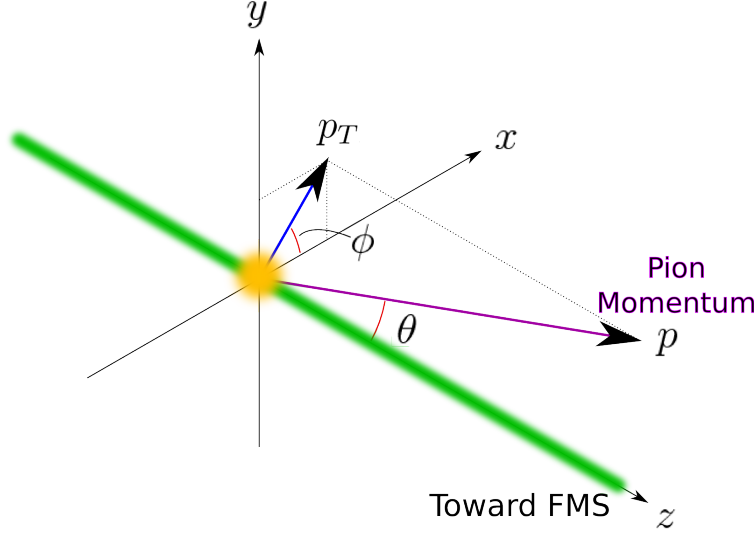


Figure 3.5: Scattering coordinates notation.

3.3 Inner and Outer Pseudorapidity Regions

Before discussing specific kinematic cuts that define the π^0 sample, it is worth mentioning that the $A_{LL}^{\pi^0}$ analysis is separated into two η regions which approximately separate the large cells and the small cells. Figure 3.6 shows the distribution of 2-photon invariant mass plotted versus their pseudorapidity (of their parent π^0 , η -meson, *etc.*). The outer black vertical lines represent overall η cuts of 2.65 and 3.9. The events selected here have all of the nominal π^0 kinematic cuts (omitting the mass cut), which will be discussed later in this chapter.

Although the FMS is composed of large cells and small cells taken together, one must keep in mind that the large cells and small cells behave differently, due to their PMT differences, glass cell size and composition differences, and different relative amounts of radiation damage. They are therefore calibrated a bit differently, and the two corresponding pseudorapidity regions can be discerned from figure 3.6. Looking at Run 12, $\eta = 3.15$ was chosen as an appropriate boundary, and was also applied to Run 13, since the two Runs need to have the same η constraints in order to merge them into one $A_{LL}^{\pi^0}$ analysis. Furthermore, for Run 13, the small cells were too heavily damaged from radiation and were consequently omitted from the analysis. Therefore, the event selection is broken down in the following manner:

- Outer region: $2.65 < \eta < 3.15$ – mostly large cells – analyzed Runs 12 and 13
- Inner region: $3.15 < \eta < 3.9$ – mostly small cells – analyzed Run 12 only

Figure 3.7 shows a schematic of the FMS with the above pseudorapidity cuts.

Note that the most dominant part of the mass distribution shown in figure 3.6 is higher than the expected π^0 peak at 0.135 GeV; this is because there is an energy-dependent effect

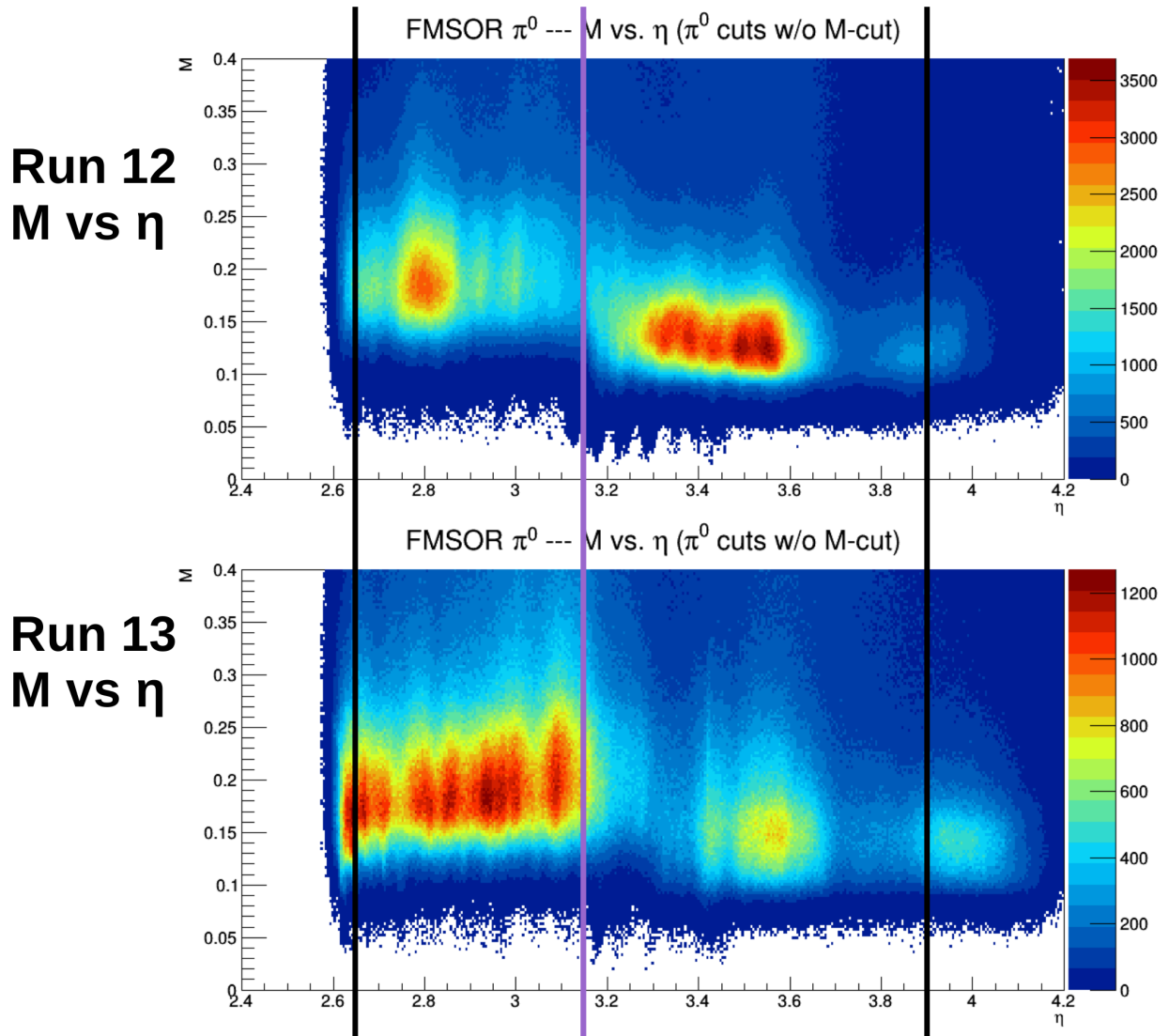


Figure 3.6: 2-photon invariant mass vs. pseudorapidity for Run 12 (top) and Run 13 (bottom), given reasonable π^0 kinematic cuts, without a mass cut. Outer black vertical lines represent overall η cuts, and the inner magenta vertical line represents the inner/outer regions' boundary.

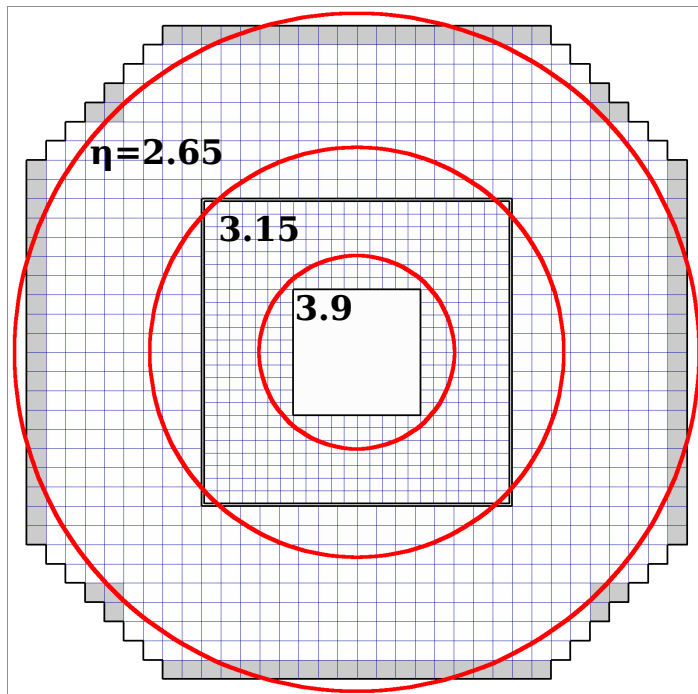


Figure 3.7: FMS schematic and pseudorapidity boundaries.

in the π^0 reconstruction, which causes the reconstructed mass to rise as a function of energy. This effect will be discussed in detail later.

3.4 Event Reconstruction

We now turn to how π^0 events are reconstructed from photon hits. This section describes the photon-finding and clustering algorithms, and how π^0 candidates are selected from the results.

3.4.1 Trigger Matching

Events which satisfy an FMS trigger are those which have *clusters* of cells with nonzero ADC counts; for example, a single photon that hits the center of one FMS cell will deposit $\sim 80\%$ of its energy in that cell and the remaining $\sim 20\%$ in the surrounding cells. Essentially, the trigger will fire if one of these clusters will cause a subsequent ADC sum (in a higher DSM

layer) to be above threshold, so it does not matter which cluster or set of clusters actually fired the trigger: the clusters are basically “ORed” together.

A given trigger, either Board Sum (BS) or Jet Patch (JP), is defined in a geometric segmentation of the FMS, as in figures 2.7 (BS) and 2.9 (JP). The segmentation divides the FMS into “patches” where, for example, in figure 2.7 each letter corresponds to a single BS patch; note that patches in general can overlap with each other, so that any cluster is very likely fully contained in some patch.

Each patch contains some number of cells, and for a given event, each cell will report an ADC count. The sums of the cells’ ADC counts in a given patch is called the “patch sum”. Depending on the trigger algorithm, these patches could then be further combined into “patches of patches”, which then have their sums (of sums). This combination of sums forms the tree structure of the DSM tree (see figure 2.8). The last layer of the DSM tree contains the final set of ADC sums which are then compared to thresholds (defined during data-taking), each of which returns a boolean 1 for sum above threshold or a 0 otherwise. The key point here is that the OR of all of these booleans is taken: so as long as at least one of the patches had something trigger-worthy in it, the overall trigger is satisfied. This OR result then defines the output trigger Level 0 bit (one for each trigger), defined as 1 if the trigger fired and 0 if not.

These output trigger bits, which are the output of trigger Level 0, go through the TCU and prescaling *etc.*, resulting with the Level 2 output trigger bits. It is these level 2 output bits which we use to filter for FMS-triggered events.

Event reconstruction is done on all trigger events, and one can of course impose a restriction on FMS triggers only. Kinematic cutoffs (minimum E and p_T) are applied, which approximately match what was defined in the original trigger thresholds, but since the trigger threshold applies in ADC space and then ADC counts for each cells are converted to E (and p_T), the actual trigger threshold gets smeared in E (or p_T) space. The E or p_T threshold is smeared by the fact that there is a variation on the cell gains throughout the whole detector, where a gain is defined as the proportionality between ADC counts and E . In particular, the FMS is calibrated such that the target gains are a function of η . In the reconstruction algorithm, we apply a soft energy cutoff as well as a $p_T > 1.5$ GeV cut so that only clusters which very likely satisfied the trigger DSM algorithm are considered. In the $A_{LL}^{\pi^0}$ analysis, tighter constraints on p_T and E are made, ensuring that all of the photon pairs considered for π^0 s candidates are above trigger thresholds and satisfied the trigger.

3.4.2 Shower Shapes

In order to reconstruct the transverse (x, y) position of a photon which hit the FMS, we fit the corresponding cluster of cell energies to a model of the transverse distribution of the electromagnetic shower: the shower shape. Consider a point source of light at a distance b from a plane. Let (x, y) represent the coordinates of a point on the plane, where $(0, 0)$ is the point that is a distance b from the source. If the point source emits photons uniformly, the probability density distribution $f(x, y; b)$ of photons hitting the plane follows a Cauchy distribution:

$$f(x, y; b) = \frac{1}{2\pi} \frac{b}{(b^2 + x^2 + y^2)^{3/2}}. \quad (3.4)$$

If the plane were to be segmented into squares, each with side length d , one can determine the fraction of light seen in each square. Consider a square which is centered about a point (x_c, y_c) with boundaries that range from $(x_c - d/2, y_c - d/2)$ at one corner to $(x_c + d/2, y_c + d/2)$ at the opposite. To evaluate the total fraction of photons hitting this square, one uses the cumulative distribution function of $f(x, y; b)$:

$$\begin{aligned} F(x, y; b) &= \int_{-\infty}^x \int_{-\infty}^y d\hat{x}d\hat{y} f(\hat{x}, \hat{y}; b) = \\ &= \frac{1}{4} + \frac{1}{2\pi} \left[\arctan\left(\frac{x}{b}\right) + \arctan\left(\frac{y}{b}\right) + \arctan\left(\frac{xy}{b\sqrt{b^2 + x^2 + y^2}}\right) \right]. \end{aligned} \quad (3.5)$$

The total fraction of light (which would hit the plane) that is detected in this square is then

$$\begin{aligned} G(x_c, y_c) &= F\left(x_c + \frac{d}{2}, y_c + \frac{d}{2}; b\right) - F\left(x_c - \frac{d}{2}, y_c + \frac{d}{2}; b\right) - \\ &\quad - F\left(x_c + \frac{d}{2}, y_c - \frac{d}{2}; b\right) + F\left(x_c - \frac{d}{2}, y_c - \frac{d}{2}; b\right), \end{aligned} \quad (3.6)$$

where the four terms correspond to the four corners of the square.

The shower shape model which is employed in FMS photon reconstruction is a linear combination of Cauchy distributions,

$$f_{\Sigma}(x, y) = \sum_{i=1}^N a_i f(x, y; b_i), \quad (3.7)$$

and the aforementioned detector squares correspond to individual FMS cells. To maintain normalization, $\sum_i a_i = 1$ is enforced. A fit was performed by [90] with $N = 3$ terms; this used the equivalent of FMS small cells with $d = 4$ cm and the resulting fit parameters are

given in table 3.1. The third term is a bit strange, given $a_3 < 0$, but the fit algorithm did not impose positivity of the a_i parameters; nonetheless the fit was found to be sufficient for position reconstruction.

i	a_i	b_i
1	0.8	0.8 cm
2	0.3	0.2 cm
3	-0.1	7.6 cm

Table 3.1: Fit parameters of the shower shape model described in [90]

The geometrical interpretation of b_i as a longitudinal source distance was also never enforced in the fit. It is suspected that this variable could help correct for asymmetric shower shapes which occur with high incident angle photons; however, such attempts only resolve photons which, given the FMS geometry, are up to a conservative maximum of 0.5 cm away from the symmetric shower shape photon reconstructed positions, which use the parameterization in table 3.1. Furthermore, the reconstructed position is much more sensitive to the z plane upon which the photon trajectory is projected: for an angle of incidence of 5° (large cells region), projecting to the front of the FMS at 720 cm would give a position that is almost 4 cm different from a position determined by projecting to the maximum of the longitudinal shower, which is typically at 735 cm.

The effect of incident angle corrections is very small in the context of other uncertainties which contribute to the $A_{LL}^{\pi^0}$ measurement and they are therefore not implemented in this analysis. Instead, the parameterization in table 3.1 is used. For further details on shower shapes as well as incident angle correction attempts, see appendix E.

Figure 3.8 shows a sample shower shape for small cells, in 1-dimension. At $x_c = 0$, the photon was deposited in the exact center of the cell: this cell will get roughly 80% of the energy deposition, according to the vertical axis of the figure. As x_c approaches the size of the small cells, ± 3.8 cm, the amount of energy deposited in the cell which the photon hit decreases. At $x_c = 5$ cm, for example, the photon actually hit the next adjacent cell, and only a few percent of the photon’s energy was deposited in the cell centered at (x_c, y_c) .

3.4.3 Distinguishing Between 1-photon and 2-photon Clusters

At high energies, it becomes difficult to distinguish 2-photon clusters from 1-photon clusters, because the opening angle of 2 photons from a $1 \rightarrow 2$ body decay decreases as a function of energy. In order to distinguish 1-photon clusters from 2-photon clusters, a principal components analysis is performed. The goal is to establish a sense of the “width” of the

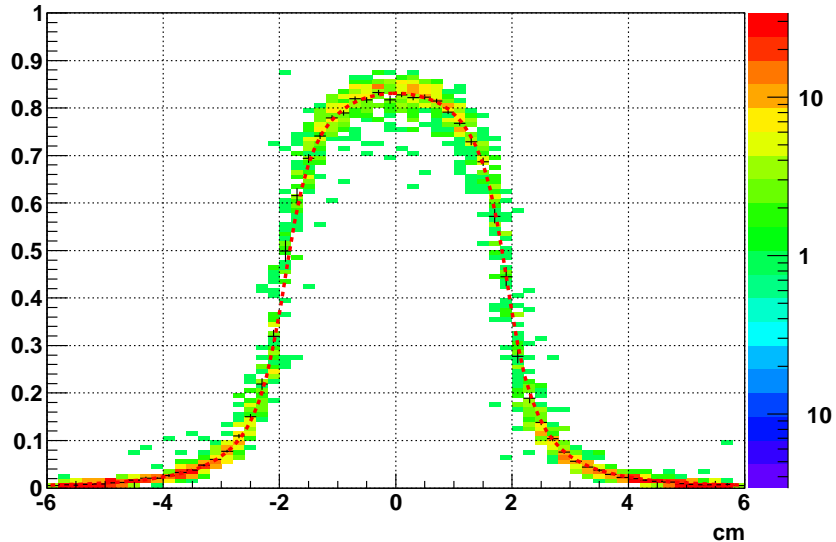


Figure 3.8: Sample shower shape in 1 dimension. The vertical axis is $G(x_c)$, the fraction of light a cell C would see, had the photon struck the FMS at a transverse distance of x_c from the center of cell C ; the horizontal axis is x_c in units of centimeters. The histogrammed data are from simulation and the dashed line is the shower shape $G(x_c)$ for FMS small cells. From [91].

cluster, along the direction of maximum width, *i.e.*, along the direction of the first principal component. For more details, see [92, 56, 91]; the implementation of this method is sketched here. Also note that the cluster merging complicates the shower shape model a bit, but is not too difficult to resolve; see the aforementioned references.

Let i represent the i th cell in a given cluster, with energy E_i , centered at transverse position (x_i, y_i) . Consider the following weighted centroid of the distribution, given $a \in \{x, y\}$ as indexing x -position or y -position:

$$\langle x^a \rangle = \frac{\sum_i w_i x_i^a}{\sum_i w_i}. \quad (3.8)$$

The sums run over all cells in the cluster, and the weights w_i are defined as $w_i = \log(E_i + E_0)$, where $E_0 = 0.5$ GeV. According to [92], this choice of E_0 is arbitrary and is designed to mitigate 1–2 ADC count fluctuations, assuming a typical resolution of 0.2 GeV/count. With this centroid in hand, we calculate the covariance matrix elements σ^{ab} :

$$\sigma^{ab} = \langle x_i^a x_i^b \rangle - \langle x^a \rangle \langle x^b \rangle. \quad (3.9)$$

The eigenvalues of the covariance matrix correspond to eigenvectors which point along the

two principal axes of the cluster. The higher eigenvalue corresponds to the eigenvector which points along the direction of maximum width (log- E -weighted variance) of the cluster; this eigenvalue measures this width. The two eigenvalues are

$$\lambda_{\pm} = \frac{1}{2} \left[\sigma^{xx} + \sigma^{yy} \pm \sqrt{(\sigma^{xx} - \sigma^{yy})^2 + 4(\sigma^{xy})^2} \right] \quad (3.10)$$

and we define the principal variances $\sigma_{\max}^2 = \lambda_+$ and $\sigma_{\min}^2 = \lambda_-$. The eigenvectors are

$$V_{\pm} = \left(\frac{\sigma^{xx} - \sigma^{yy} \pm \sqrt{(\sigma^{xx} - \sigma^{yy})^2 + 4(\sigma^{xy})^2}}{2\sigma^{xy}}, 1 \right) \quad (3.11)$$

and the variance along V_+ is equivalent to σ_{\max}^2 .

The variable σ_{\max} , plotted as a function of cluster energy, reveals two bands: one which is mostly 1-photon clusters and another which is mostly 2-photon clusters. See [92] for more details on how cuts on σ_{\max} are used to separate the 1-photon clusters from the 2-photon clusters. Basically, if σ_{\max} is large enough, it is likely a 2-photon cluster.

3.4.4 Clustering Algorithm

Given a list of photons for an event, the next step is to start to look for photon pairs in order to begin identifying π^0 candidates; the most trivial way to do this for an event with n photons is to consider all of the $\binom{n}{2}$ possible pairs, however in practice it is more efficient to bias pair-finding toward proximal photons. The pair-finding is performed by a type of clustering algorithm, which organizes all photons into groups of photons, called *cone-clusters*, limited in size by *isolation cones*. The isolation cone technique uses a cone of a fixed radius, defining the maximum size of a cone-cluster. If the isolation cone radius is very high, only highly isolated π^0 s will be identified; on the other hand, if the isolation cone radius is too low, splitting of photon pairs between adjacent cone-clusters becomes an issue. Ideally, for an inclusive analysis one wants a cone radius which is low enough such that π^0 s of any level of isolation are found, but high enough such that π^0 s are unlikely to have their photons split between adjacent cone-clusters. An example of a 35 mrad cone with respect to the FMS size is shown in figure 3.9; this particular cone size turned out to be the most optimal choice in providing an inclusive-like sample of π^0 s, when compared to several other isolation cone radii.

The cone-clustering algorithm begins by sorting all photons in the event in descending order of energy. An isolation cone is drawn around the first, highest- E photon, centered

on its trajectory; this photon begins the first cone-cluster. Each subsequent photon on the sorted list is then compared to the current list of cone-clusters, and if the photon is within an isolation cone radius of any cone-cluster on that list, then it is added to that cone-cluster; that cone-cluster’s isolation cone is then re-centered on the cone-cluster energy centroid. On the other hand, if the photon is not within any defined cone-cluster, a new cone-cluster is started for that photon. The algorithm proceeds until all of the photons (with energy greater than a soft energy cutoff) of the event are organized into cone-clusters. Finally, the cone-clusters themselves are sorted by energy and stored in a data tree for that event, along with their kinematics.

Given the sorted list of cone-clusters, one can then begin to search for π^0 s. Only cone-clusters with at least two photons are candidates for containing a π^0 ; of these cone-clusters, the highest energy pair in the highest energy cone-cluster of each event was found to give the cleanest sample of π^0 candidates. For an inclusive measurement, one wants the maximum π^0 mass signal with the minimum background; furthermore, given the clustering algorithm, one must be mindful of cases where the photon pairs are split between adjacent cone-clusters, which cause combinatorial losses of π^0 s. Various samples of photon pairs were compared using a variety of isolation cone sizes, minimum photon energy cutoffs, and minimum pair transverse momentum cutoffs. Looking at the highest energy photon pair in the highest energy cone-cluster of each event, an isolation cone of 35 mrad (figure 3.9), a minimum photon energy of 3 GeV, and a minimum photon pair p_T of 1.5 GeV provided the best inclusive-surrogate sample, when compared to all other tested samples. Combinatorial losses due to pair-splitting between adjacent cone-clusters are limited to 2%. This sample of photon pairs is the closest we are able to get to a “true” inclusive sample of π^0 s and is the sample used for the $A_{LL}^{\pi^0}$ analysis.

3.4.5 Energy Dependence of the Mass

Once pairs of photons have been selected, one may begin to look at their invariant masses; the determination of invariant mass depends on the photon energies as well as their opening angle, as was shown in section 3.2. The fit algorithm for fitting clusters of energy deposits in the FMS to a shower shape has a tendency to overestimate the decay photon opening angle, α , at higher pair energies. Figure 3.10 shows an example of this effect, where the monochrome histogram is of α vs. E . The red lines in this figure indicate constant M contours (π^0 mass contour is solid) for fixed values $Z = 0$ (left), $Z = 0.44$ (middle), and $Z = 0.8$; while the α vs. E data in these three figures are the same, the position of the $M(\alpha, E)$ contours still has a dependence on Z , thus M contours for three values of Z are shown. The data histograms

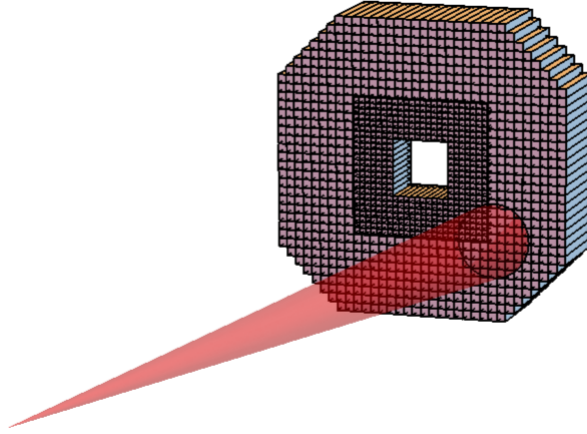


Figure 3.9: Sample 35 mrad isolation cone projected onto the FMS; the vertex of the cone is situated at the nominal interaction point.

contain data in the range $0 \leq Z \leq 0.8$ in all three plots and show that α decreases as a function of E , however the decrease is not as rapid as the contours indicate it should be. These data show a clear overestimation of the value of α , which worsens as the E increases.

Figure 3.11 shows the pair invariant mass, M , as a function of E ; contours of constant α are plotted, again for three values of Z . These contours show that for a specific value of α and Z , the mass increases monotonically with respect to the energy. Since the value of α is not falling rapidly enough with respect to E , the data tend toward following these α contours, rather than remaining flat on a line of constant M . In other words, we see a monotonic increase in the reconstructed M as a function of E , directly associated with the overestimation of α as E increases.

To compensate for this overestimate of α , one could implement an α -dependent dependent correction; this correction could be done in such a way that the E -dependence on the mass would become flat. Instead, however, we decided to simply implement an E -dependent mass cut scheme, as will be discussed in section 3.7.3.

3.5 Gain Corrections

This section outlines the corrections to the gains of each FMS cell, where gain is defined as the proportionality between ADC counts and energy. While the voltages of each FMS cell were adjusted during data-taking so that specific gains are achieved which set the reconstructed π^0 mass peaks to be around the proper π^0 mass, additional corrections to the gains can be made after the data acquisition period. These corrections arise from radiation damage effects, as well as from a nonlinearity in the response of the FMS PMTs.

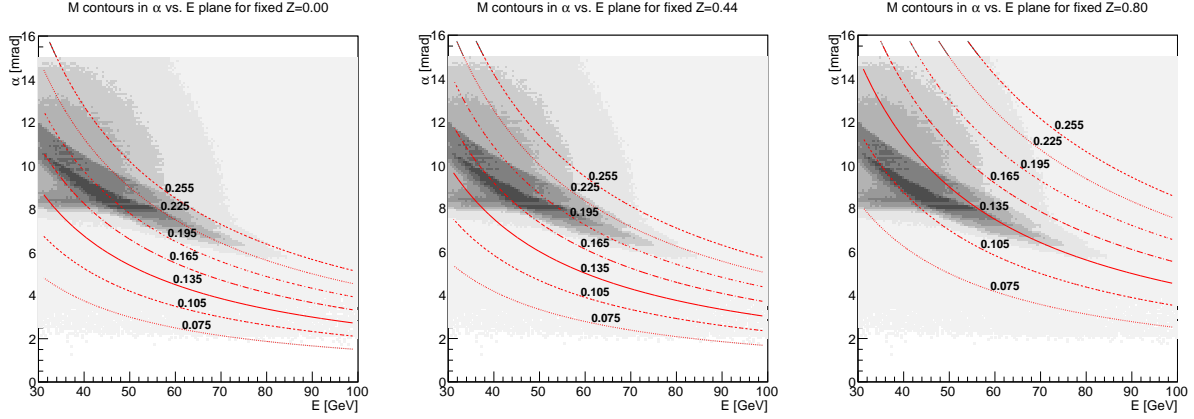


Figure 3.10: Pair opening angle α vs. pair energy E , where Run 12 data are shown in monochrome. The red lines are contours of constant mass M , given a value of $Z = 0$ (left), $Z = 0.44$ (middle), and $Z = 0.8$ (right); the ideal π^0 mass contour is drawn solidly.

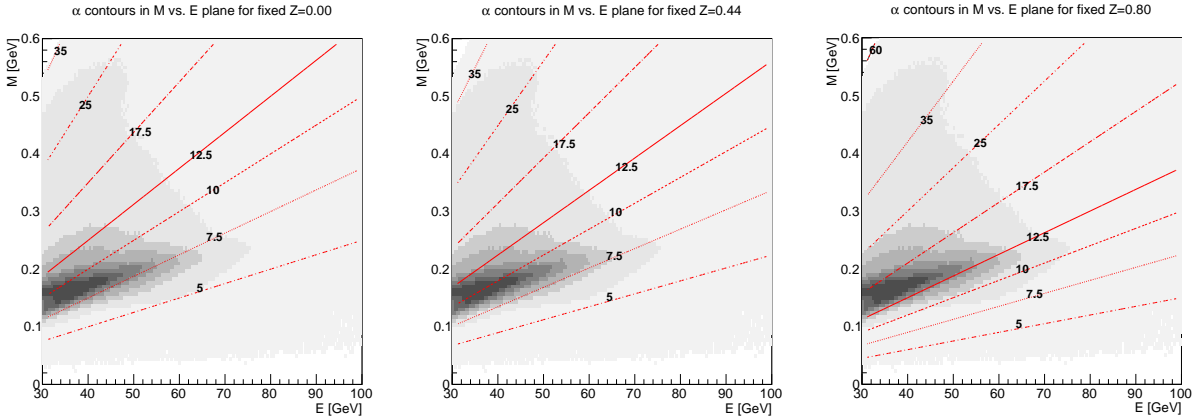


Figure 3.11: Pair mass M vs. pair energy E , where Run 12 data are shown in monochrome. The red lines are contours of constant opening angle α , given a value of $Z = 0$ (left), $Z = 0.44$ (middle), and $Z = 0.8$ (right).

3.5.1 Time-Dependent Corrections – The LED Flasher System

The radiation damage caused a time-dependent degradation in the overall PMT response. Furthermore, the PMT responses had a tendency to vary in time during all Runs before Run 15, due to malfunctioning Zener diodes in the PMT bases. These time-dependent variations in PMT responses are corrected for by making use of data collected from the FMS LED flasher system.

The LED flasher system used in Runs 12 and 13 was composed of a set of LEDs pulsing at 1 Hz, where the LED light outputs were directed into a tree of fiber optic cables such that each cell had a fiber optic LED light output directed at its transverse center. Although

there was an independent STAR trigger used for the LED system, it was more practical to pick the LED events from the overall trigger data by looking for events which had very high ADC sums (over all cells). Since the LED flasher system pulses light into all channels simultaneously, the resultant ADC sum from any LED pulse is much higher than the typical ADC sums seen during usual data taking, and the LED events are therefore very easy to identify.

The time-dependent variations in gain of all of the PMTs can be tracked by looking at the time-dependence of the ADC distributions seen from LED events. This tracking gives one the ability to correct for these effects, by simply introducing a time-dependent gain correction, which tracks the variations and mostly corrects for them.

3.5.2 Nonlinear Energy-Dependent Response Correction

Another piece of the gain correction comes from a nonlinear dependence on energy of the PMT response. This effect is mostly due to the dependence of the electromagnetic shower shape on the depth, z , in the Pb-glass cells; for example, the effective z -position of the shower maximum depends on incident energy and on incident angle. This dependence is the source of different effective attenuation lengths, which in turn causes a nonlinearity in the relationship between the energy measured by the PMT, the “observed energy,” and the energy of the incident photon, the “true energy.” In order to correct for this behavior, an additional nonlinear energy-dependent gain correction is applied.

3.5.2.1 Nonlinear Gain Correction Model

To model the nonlinearity, we first take a closer look at the monotonically increasing dependence of the reconstructed pion mass on the energy. The left panel of figure 3.12 shows reconstructed π^0 masses as a function of one of the photon energies in green, in comparison to η -mesons in black. These data are from Run 15, however, the dependence is similar in Runs 12 and 13; data from Run 15 is shown here since the η -meson signal was much cleaner than in Runs 12 and 13. One observes a slow rise in M at low E , relatively flat M at mid-range E , and a slow rise of M at higher E .

The right panel of figure 3.12 shows a ratio of the reconstructed M to the ideal meson M , as a function of the two-photon opening angle, α . The low- E η -mesons, with $\alpha \sim 40$ mrad, barely fit into the FMS acceptance, causing a cutoff at high α due to geometry. The low- E π^0 s have a lot of background under the mass peak, however, they are produced with values of α similar to those in high- E $\eta \rightarrow \gamma\gamma$ decays; this region of event overlap is approximately $\alpha \in [20, 30]$ mrad and shows a mis-match of reconstructed mass to meson masses. Modelling

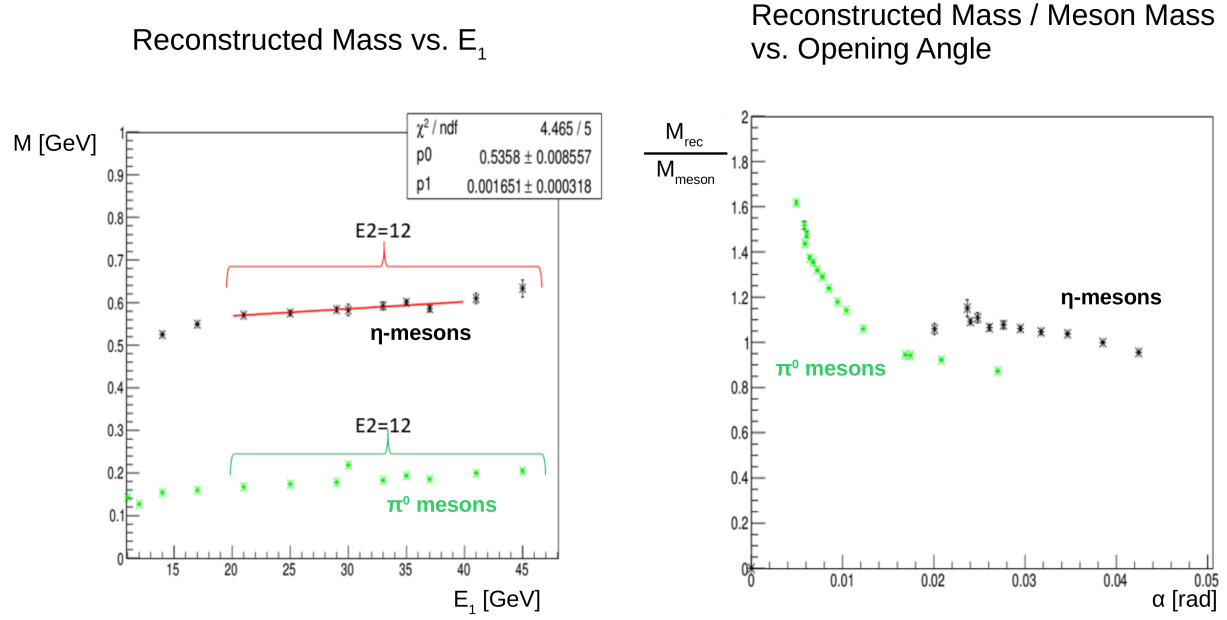


Figure 3.12: Left: reconstructed mass versus energy of one photon (E_1) for π^0 s in green and η -mesons in black; in the bracketed region, the energy of the other photon is ~ 12 GeV. Right: ratio of reconstructed mass to true meson mass versus two-photon opening angle.

the nonlinearities observed in the E -dependence of M could help improve this α -dependence matching.

The high- E π^0 s show a steep rise in the mass ratio as α decreases; this effect is from the aforementioned opening angle overestimation as the photon clusters merge closer and closer. This effect is correctable by dividing the mass by an α -dependent factor, but such a correction is not implemented in this analysis. Instead, an energy-dependent (and time-dependent) mass cut compensates for this by tracking the π^0 mass peak location and width in bins of energy.

The E -dependence of the M in figure 3.12 motivates the following nonlinear E -dependent gain correction. Define this correction as $g(E_t) = E_o/E_t$, where E_o is the observed energy and E_t is the “true” energy, defined as the corrected energy. The gain correction $g(E_t)$ is modelled as a piecewise linear function over three energy regions $\{A, B, C\}$:

$$g(E_t) = \begin{cases} g_A(E_t) = 1 - (N - K_t^A) \varepsilon_B - (K_t^A - E_t) \varepsilon_A & \forall E_t \leq K_t^A \\ g_B(E_t) = 1 - (N - E_t) \varepsilon_B & \forall K_t^A \leq E_t \leq K_t^C \\ g_C(E_t) = 1 - (N - K_t^C) \varepsilon_B - (K_t^C - E_t) \varepsilon_C & \forall E_t \geq K_t^C \end{cases} \quad (3.12)$$

The parameter N is the normalization energy point, since $g(N) = 1$ and is a fixed value in

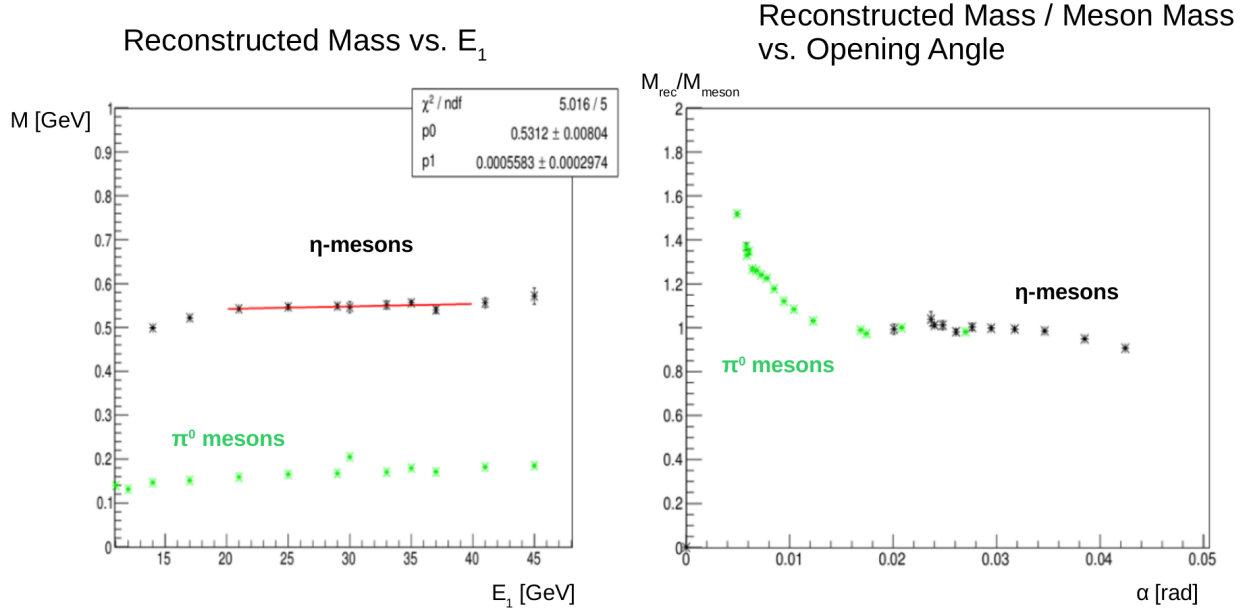


Figure 3.13: Left: reconstructed mass versus energy of one photon (E_1) for π^0 s in green and η -mesons in black; in the bracketed region, the energy of the other photon is ~ 12 GeV. Right: ratio of reconstructed mass to true meson mass versus two-photon opening angle. This figure is a repeat of figure 3.12, but with the nonlinear E -dependent gain correction implemented.

region B. It can be thought of as $1/2$ the π^0 mass calibration anchor energy, that is, the energy at which the calibration is performed, which is needed so that the E -dependence of the mass does not impact calibration. The factor $1/2$ originates from assuming that most π^0 s decay to 2 equal- E photons; this assumption is not exactly true since the energy imbalance, Z , is not always 0 and does not average out to 0 either, but this assumption is a sufficient starting anchor point for this $g(E_t)$ model. The energies $\{K_t^A, K_t^C\}$ are boundaries between the energy regions; they are subscripted by t to indicate that these “crossover” energy points represent region boundaries in E_t -space, as opposed to boundaries in E_o -space. Finally, the parameters $\{\varepsilon_A, \varepsilon_B, \varepsilon_C\}$ are slopes of $g(E_t)$ in each of the three energy regions.

The effect of an example correction of the form of equation 3.12 is plotted in figure 3.13, which shows the same plots as figure 3.12, but now with the new gain correction implemented. The E -dependence of the mass has flattened out a bit; furthermore, the matching of low- E π^0 s with high- E η -mesons has significantly improved. Figure 3.13 is, again, from Run 15 data, but the effect is the same in Runs 12 and 13.

The parameters of equation 3.12 were refined using a Geant4 simulation of the FMS. By analyzing the photon yield at the photo-cathodes as a function of thrown incident photon energy, the fit parameters given in table 3.2 were obtained. This parameterization is plotted

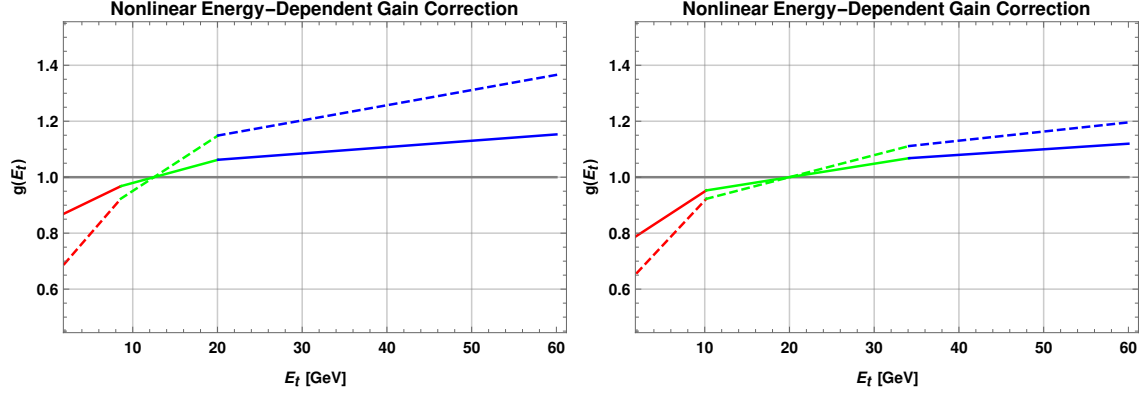


Figure 3.14: Nonlinear energy-dependent gain correction model for large cells (left) and small cells (right). Colors red, green, and blue indicate energy regions A , B , and C , respectively. The solid line is the day-0 model, with baseline radiation damage, and the dashed line is the day-300 model, the modified form of $g(E_t)$ after 300 days worth of radiation damage.

as the solid line in figure 3.14. Region A , the low energy region, has a high slope which corresponds to the rising mass at low energy as seen in figure 3.12; this is the aforementioned overlap region, where high- α π^0 s overlap with low- α η -mesons. On the other hand, regions B and C have flatter E -dependences.

Cells Type	N	K_t^A	K_t^B	ε_A	ε_B	ε_C
Large Cells	12.5 GeV	8.6 GeV	20.1 GeV	0.015	0.0082	0.0023
Small Cells	20 GeV	10.2 GeV	34.1 GeV	0.020	0.0048	0.0020

Table 3.2: Values of parameters in $g(E_t)$ model, equation 3.12.

3.5.2.2 Including Radiation Damage

We now turn to considering the effect of radiation damage on this gain correction. The longitudinal dependence of the radiation damage when considered along with the shower shape is the origin of additional nonlinearity in the gain correction, which cannot be factored out directly. As a starting point, we attempt to model the radiation damage accumulation as a function of time. The amount of accumulated radiation damage is proportional to the number of F-centers which have formed, where F-centers are electrons which occupy anionic vacancies in the glass. Assuming the rate of F-center formation is proportional to the number of unfilled anionic vacancies, the rate of radiation damage accumulation decreases linearly with respect to the amount of accumulated radiation damage. Therefore the time-dependence of a general variable R , which characterizes the amount of radiation damage,

evolves with respect to time t as

$$\frac{dR}{dt} = \lambda [R_\infty - R(t)] \implies R(t) = R_\infty - (R_\infty - R_0) e^{-\lambda t}, \quad (3.13)$$

where $R_0 = R(0)$, $R_\infty = \lim_{t \rightarrow \infty} R(t)$, and $\lambda = 1/\tau$ with τ the time constant.

To evaluate effects of radiation damage, another simulation was performed. The radiation damage longitudinal profile was assumed to match the typical energy deposition longitudinal profiles, which was obtained from minimum-bias PYTHIA events thrown at a model FMS with undamaged, clear Pb-glass. Under this assumption, for any specified amount of radiation damage, the radiation damage in the glass can be simulated by a modification of the attenuation coefficients. The photon yield as a function of thrown photon energy was assessed for a range of days' worth of radiation damage accumulation and it showed that the relative strength of the nonlinear gain correction increases as a function of accumulated radiation damage.

The simulation was performed for photons thrown at the large cells in an η range of 3.1 ± 0.05 and at the small cells in an η range of 3.9 ± 0.05 ; these values of η are approximate maximum values of η for the large cells and small cells and they represent the regions of highest radiation damage for each cell type. For each simulated day, the photon yield as a function of energy was fit with the $g(E)$ model in equation 3.12, with fixed crossover energies and constrained to unity at the anchor point energies. For all three energy regions, the slopes of the fits were observed to evolve similarly in time; consequently, a time-dependent model of the effect of radiation damage on the nonlinear gain correction can be captured simply by a ‘‘slope factor’’, which multiplies all slopes in $g(E)$. This slope factor was ultimately chosen as the variable $R(t)$, with time-dependence given in equation 3.13.

The slope factor, $R(t)$, was evaluated for one (small range around a) value of η for large cells and another for small cells, but it can be extrapolated to apply to all pseudorapidities. Cells closer to the beam line will receive more radiation damage than those farther away. This η -dependence can be folded in to the time constant as follows: first assume that at pseudorapidity η_0 the amount of radiation damage was Δt days' worth. The cells with pseudorapidity $\eta < \eta_0$ therefore experienced less than Δt days' worth of damage. Now let the time constant be τ_0 at the value of $\eta = \eta_0$, and let η_0 be where the $g(E)$ fits were performed. For $\eta < \eta_0$, the radiation damage is expected to be less, and consequently the time constant should be longer. Therefore, we assume

$$\lambda \rightarrow \lambda(\eta) = \lambda_0 e^{-h_0 + h_1 \eta}, \quad (3.14)$$

where λ_0 , h_0 , and h_1 are fit parameters and are constrained by $\lambda(\eta_0) = \lambda_0$. Their explicit

values were determined by looking at ratios in flasher LED amplitudes as a function of η .

Finally, the full radiation damage parameterization is given table 3.3. Figure 3.15 shows the plot of the η -dependence of the factor $\lambda(\eta)/\lambda_0$, which is unity at the chosen fit points η_0 , and decreases with decreasing η . Figure 3.16 shows the behavior of $R(t)$ as a function of days worth of radiation damage (using Run 15 luminosities); it is plotted for various values of η . The value of $R(t)$ increases with respect to t and also with respect to η .

Cells Type	R_∞	R_0	λ_0 [day ⁻¹]	h_0	h_1
Large Cells	4.46	1.0	0.0028	7.37	2.38
Small Cells	3.44	1.0	0.0022	7.44	1.91

Table 3.3: Values of parameters used in radiation damage extension of $g(E)$ model.

The radiation damage accumulation rate was assumed to be a 0.5% degradation per day for the large cells and a 1.5% degradation per day for small cells; these values are specific to Run 15, but it is straightforward to translate a Run 15 day’s worth of radiation damage to a Run 12 or 13 day’s worth. Runs 12 and 13 had approximate delivered luminosities of 4.0 pb⁻¹ per day (during the analyzed data period) and Run 15 had about 2.4 pb⁻¹ per day. Furthermore, the beam energy for Run 15 was 100 GeV, whereas that for Runs 12 and 13 was 255 GeV; the ratio of these beam energies accounts for different amounts of radiation damage delivered per unit luminosity between Runs 12+13 and Run 15. Therefore, one Run 12 or 13 day corresponds to an estimate of (1 Run 12+13 Day) \times (4.0/2.4) \times (255 GeV/100 GeV) = 4.2 Run 15 days’ worth of radiation damage.

Ultimately, the effects of two forms of the nonlinear gain correction are evaluated. Let $g^0(E_t)$ represent the “day-0” model, that is, the state of the $g(E_t)$ before additional radiation damage accumulated. This $g^0(E_t)$ was plotted as the solid line in figure 3.14 (and since $t = 0$, it does not depend on η). A model after D days’ worth of radiation damage was also considered, called the “day- D ” model and denoted $g^D(E_t)$. For each run in the $A_{LL}^{\pi^0}$ data set, D was set to the number of days of running after the beginning of Run 12, times the aforementioned 4.2 Run 15 days per Run 12+13 day factor; the maximum value of D analyzed was 281. In figure 3.14, the $g^{300}(E_t)$ model is plotted as the dashed line, given the pseudorapidities of 2.9 and 3.5 for the large and small cells, respectively.

3.5.2.3 Application of the Correction

In order to make use of $g(E_t)$, one must obtain $E_t(E_o)$ by solving the quadratic equation $E_o = E_t \cdot g(E_t)$. Letting $I \in \{A, B, C\}$ denote a region, the physically relevant solution is

$$E_t(E_o) = \frac{1}{2\varepsilon_I} \left[-g_I(0) + \sqrt{4\varepsilon_I E_o + g_I(0)^2} \right] \quad (3.15)$$

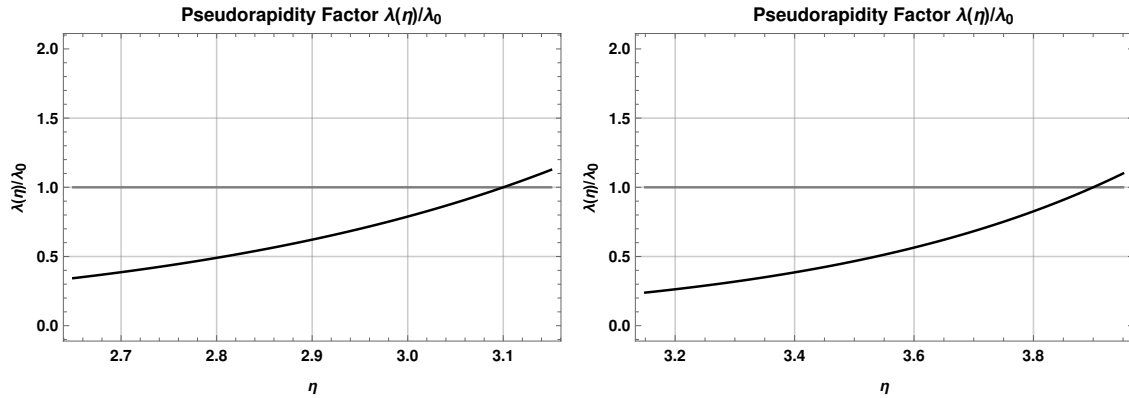


Figure 3.15: Pseudorapidity factor $\lambda(\eta)/\lambda_0$ in equation 3.14 for large cells (left) and small cells (right).

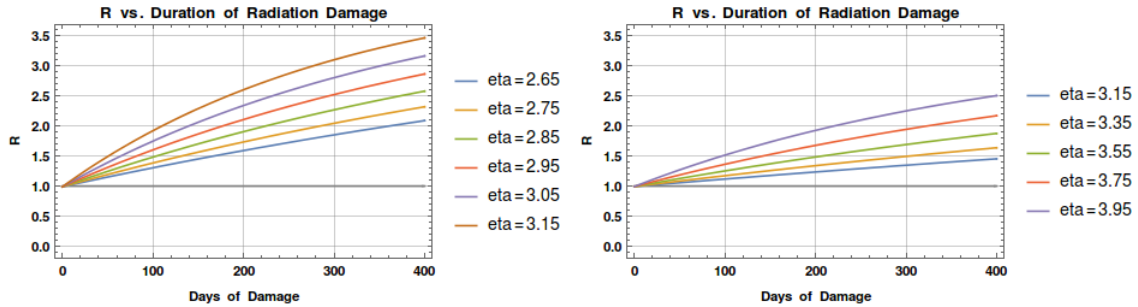


Figure 3.16: Slope factor $R(t)$ in equation 3.13 for large cells (left) and small cells (right), for various values of η .

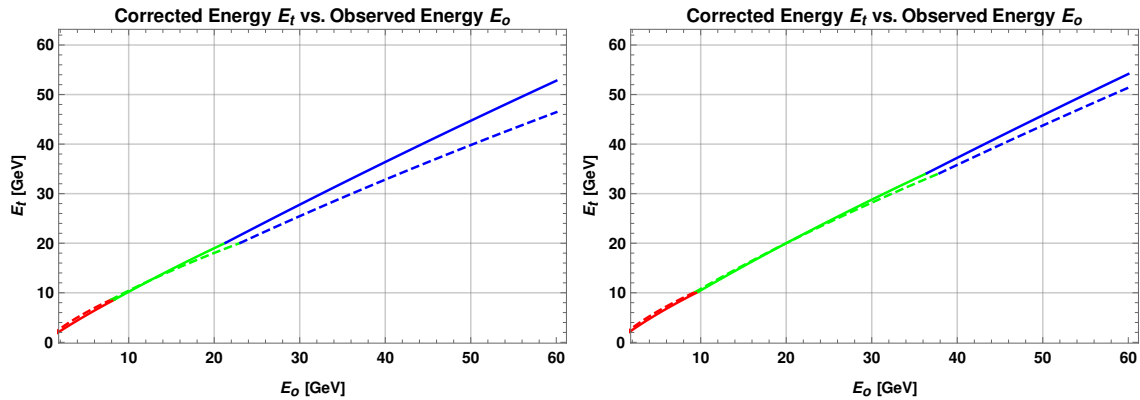


Figure 3.17: Corrected energy E_t , that is, the supposed thrown energy, plotted as a function of observed energy E_o for large cells (left) and small cells (right). Colors red, green, and blue indicate energy regions A , B , and C , respectively. Solid line is day-0 model and dashed line is day-300.

and the crossover energy points in E_o -space are $K_o^I = K_t^I \cdot g(K_t^I)$. Figure 3.17 shows the true (thrown) energy as a function of the observed energy, as given by equation 3.15. The fractional difference between the day-0 and day-300 corrected energies can be up to 5%.

In order to assess the impact this gain correction has on π^0 s for the $A_{LL}^{\pi^0}$ analysis, the shift in p_T must be measured, since we ultimately measure $A_{LL}^{\pi^0}$ as a function of p_T . The shifted p_T , defined as p_{T_t} , is

$$p_{T_t} = \frac{\sqrt{E_t^2 - M_t^2}}{\cosh \eta}, \quad (3.16)$$

where $E_t = E_{1_t}(E_{1_o}) + E_{2_t}(E_{2_o})$ is the corrected total energy and $M_t = M_o / \sqrt{g(E_{1_t})g(E_{2_t})}$ is the corrected mass. The corrected Z is also straightforward to compute. Both the corrected η and ϕ are obtained via the sum of the corrected 4-momenta of the photons, but the fractional changes in these values are small.

Given the day-0 and day- D models' corrected p_T values, figures 3.18 and 3.19 respectively show the fractional change in p_T , defined as $\Delta p_T = (p_{T_t} - p_{T_o}) / p_{T_o}$ versus the original p_{T_o} . The day-0 model on average reduces p_T by about 3–8% whereas the day- D model reduces it by about 5–10%.

Outer Region Day-0 Δp_T vs. p_{T_0}

Inner Region Day-0 Δp_T vs. p_{T_0}

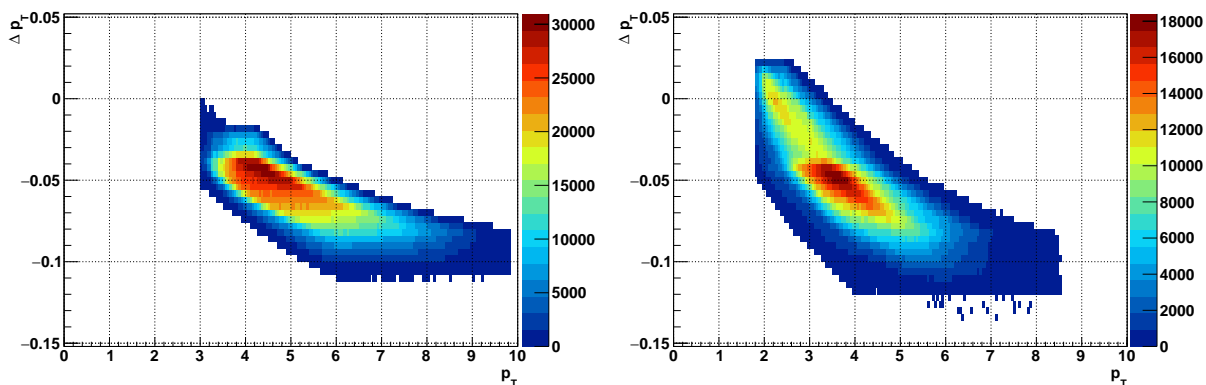


Figure 3.18: Fractional change in p_T , denoted Δp_T , vs p_{T_0} for outer region (left) and inner region (right); this is for the day-0 model.

Outer Region Day- D Δp_T vs. p_{T_0}

Inner Region Day- D Δp_T vs. p_{T_0}

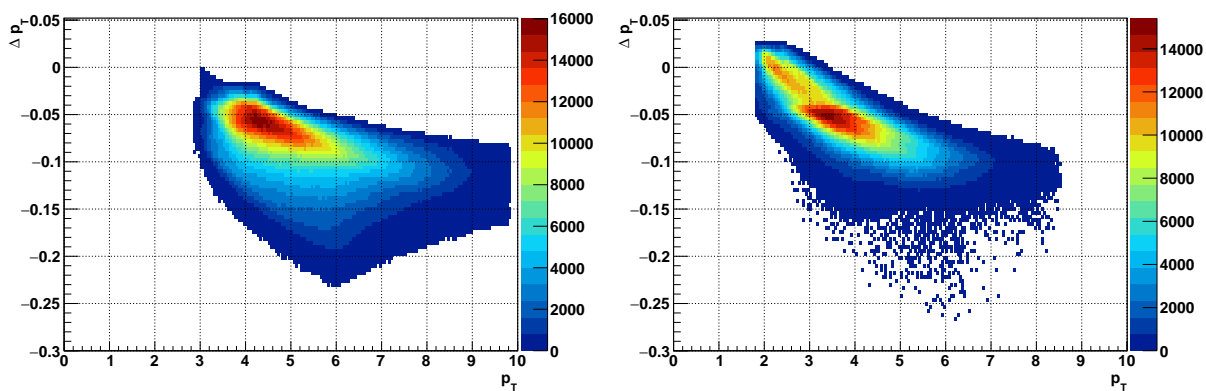


Figure 3.19: Same as figure 3.18, but for day- D .

3.6 Hot Tower Masking

After full pion reconstruction was executed, there were some specific, small areas of the FMS geometry (or of kinematics distributions) that had several more events than other regions. Occasionally during the data-taking period, a single PMT gain would change such that it would be dominantly firing the trigger. Such a pathology is called a *hot tower* and during data-taking, monitoring tools enabled detector operators to find and suppress hot towers, but not all could be suppressed in a timely manner.

Hot towers primarily appear as sharp peaks in the photon (or pion) position distributions. They can also sometimes appear as single isolated spikes in E , p_T , or even in M distributions. Runs which have a spike in any of these three distributions were excluded from the $A_{LL}^{\pi^0}$ analysis. The majority of all the data, however, have a few such spikes in the photon position distributions, which needs a more careful treatment.

The omission of cells or regions around cells which were hot is called hot tower masking, and must be done before photon reconstruction. The decision to implement hot tower masking occurred long after the data were reconstructed, however, and given that reconstruction is a rather long, CPU-intensive process, we decided to simply mask out *hot spots* in the photon position distributions instead. Pions that have photons too close to any hot spot are removed from the analysis.

Figure 3.20 illustrates the hot spot search algorithm, which takes a photon position distribution and iteratively searches for hot spots; this is done for each runset, which is a set of 5–10 subsequent runs, all of which are in the same fill. Some of the hot spot peaks are much higher than others, so the algorithm begins at the highest peak and scans downward. Starting from the highest peak, it is first checked for certain criteria which define a hot spot; if the criteria are satisfied, then this peak is added to the list of hot spots. Whether or not this peak is added to the list of hot spots, it and its small local neighborhood are deleted from the position distribution so that the next highest distribution bin the algorithm finds is not some “foothill” of any peak which was already analyzed. Furthermore, subsequent candidate hot spots must be sufficiently far from any other hot spots already on the list of hot spots.

For each candidate hot spot, defined as the position distribution’s current highest bin, the following metrics are computed:

- i is the number of hot spots added to the list
- H is the number of entries in the hot spot’s tallest bin
- P is the number of entries in a 3 bins \times 3 bins neighborhood centered around the

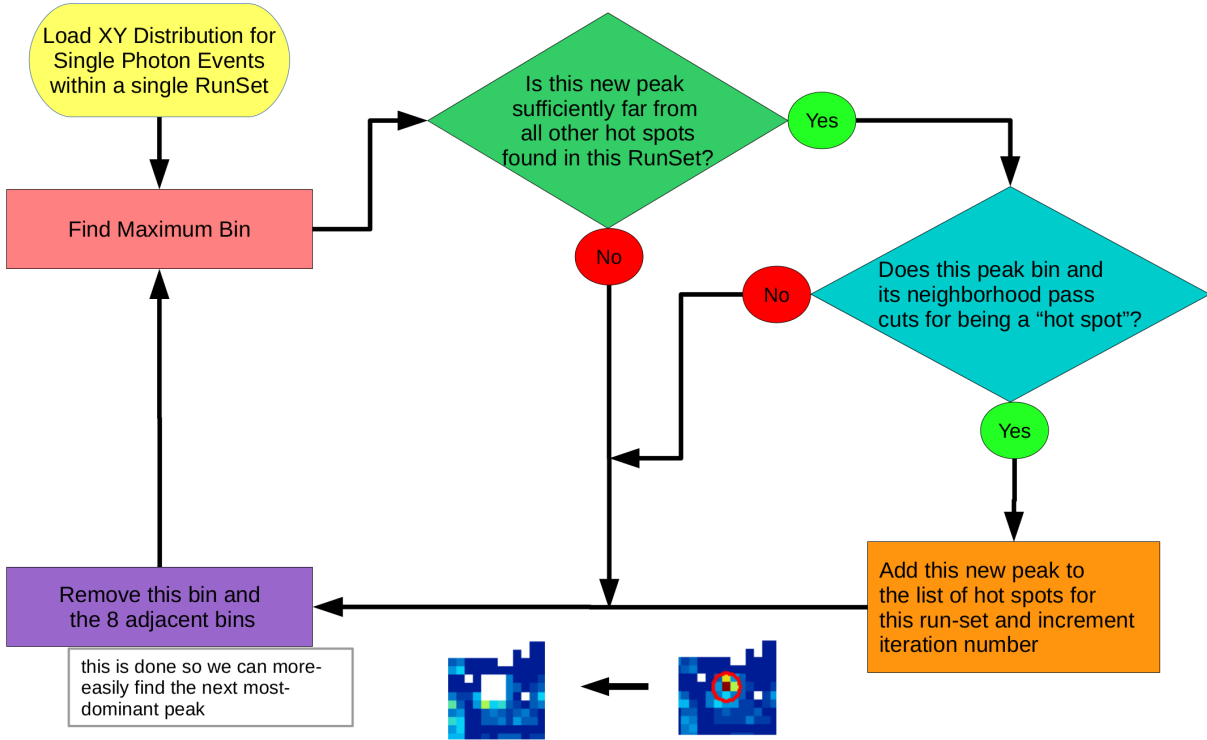


Figure 3.20: Hot spot search algorithm; a sample removal of a hot spot candidate’s peak bin and its 8 adjacent bins (*i.e.*, the patch) is shown at the bottom of the figure.

tallest bin; this neighborhood is called the *patch*

- A is the average number of events over all the nonzero bins in the entire position distribution
- σ_{\max} is the maximum eigenvalue of the moment matrix of the patch and is defined analogously to the σ_{\max} used in single and 2-photon cluster separation.

Using these metrics, several criteria are defined. First, i should be limited and be no higher than some value i_{\max} , so that only a few hot spots are considered; removing too many causes the algorithm to start identifying local maxima of the usual noise in the position distributions. The sharpness of the peak is roughly given by the ratio of H to P ; if it is too low, then the hot spot candidate peak is rather wide and likely not from a single isolated hot tower. Another characterization of the peak width is given by σ_{\max}^2 and if this value is too high, then the candidate hot spot is too wide; H/P and σ_{\max}^2 are approximately anti-correlated with each other. Finally, the value of H above the overall distribution average A should be rather high, that is, the peak should be at least $[H/A]_{\min}$ times taller than the distribution average. This last criterion is one which, if satisfied, overrides all the aforementioned criteria; it is rarely satisfied for $i > 5$. The full criterion for a hot spot candidate to

be accepted as a hot spot is the boolean

$$\left(i < i_{\max} \text{ AND } H/P > [H/P]_{\min} \text{ AND } \sigma_{\max}^2 < [\sigma_{\max}^2]_{\max} \right) \text{ OR } H/A > [H/A]_{\max}. \quad (3.17)$$

The values have been tuned to the data and the effects of the algorithm on the hot spot candidate’s distributions of σ_{\max}^2 and H/P versus i are shown in figures 3.21-3.23. For all three data sets, Run 12 outer region, Run 12 inner region, and Run 13 outer region, the values used in equation 3.17 are given in table 3.4.

Data Sector	i_{\max}	$[H/P]_{\min}$	$[\sigma_{\max}^2]_{\max}$	$[H/A]_{\min}$
Run 12 Outer	6	0.3	0.8	20
Run 12 Inner	5	0.4	0.8	15
Run 13 Outer	7	0.4	0.7	20

Table 3.4: Values of parameters use to set limits on which hot spots are removed.

After a list of hot spots is generated for all runsets in the dataset, a masking algorithm is applied on all candidate π^0 s in the $A_{LL}^{\pi^0}$ analysis. Basically, if either photon which makes the π^0 is too close to a hot tower, its parent π^0 is omitted from the analysis; here “too close” is defined as within a square of side-length $3 \times [\text{cell width}]$ centered around any hot spot. This π^0 masking procedure is summarized in figure 3.24.

Run 12 Outer Region Hot Spot Removal

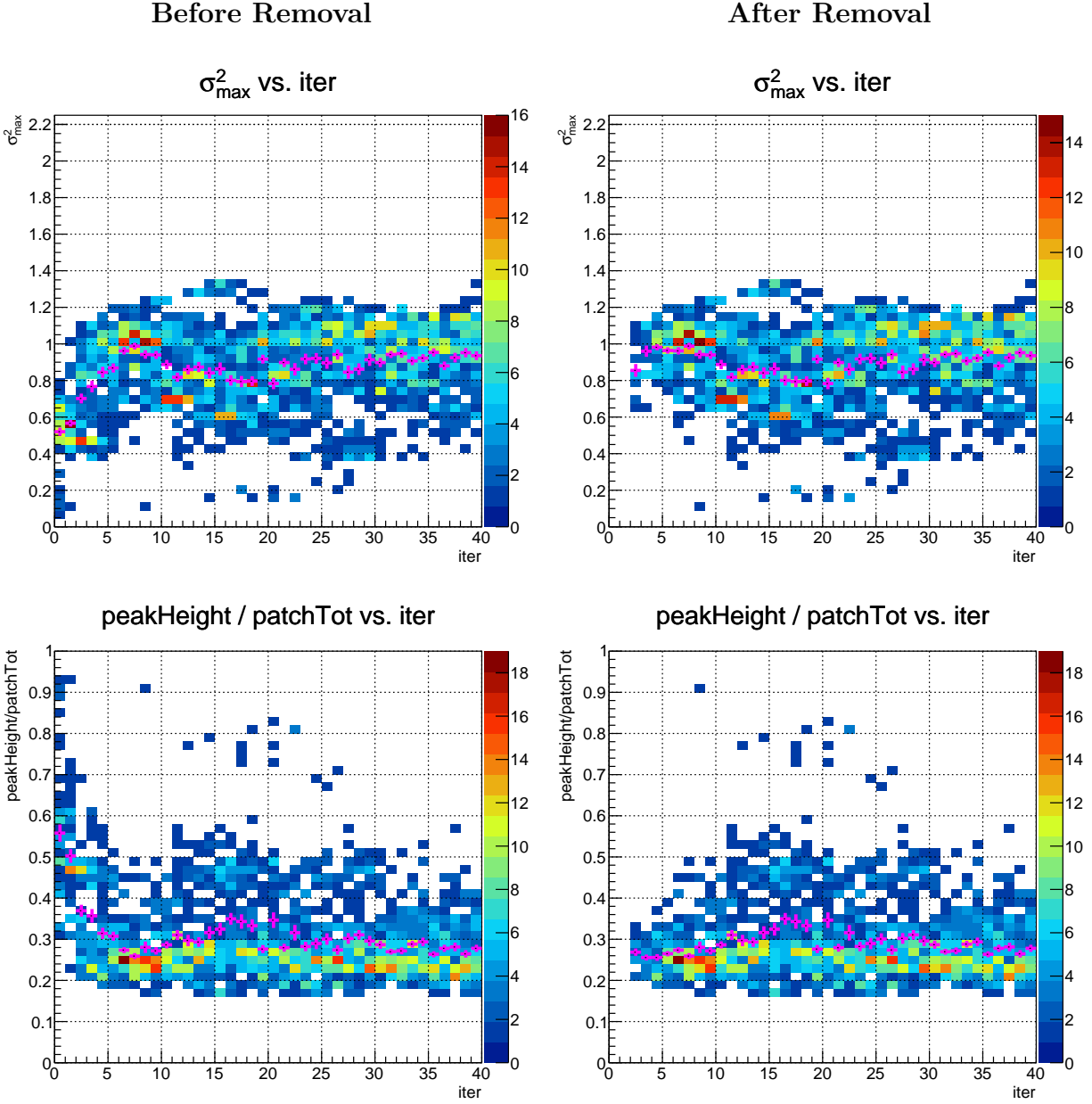


Figure 3.21: For Run 12 outer region, distributions of hot spot candidate σ_{\max}^2 versus i (top) and H/P versus i (bottom) before hot spots are removed (left figures) compared to after hot spot masking (right figures).

Run 12 Inner Region Hot Spot Removal

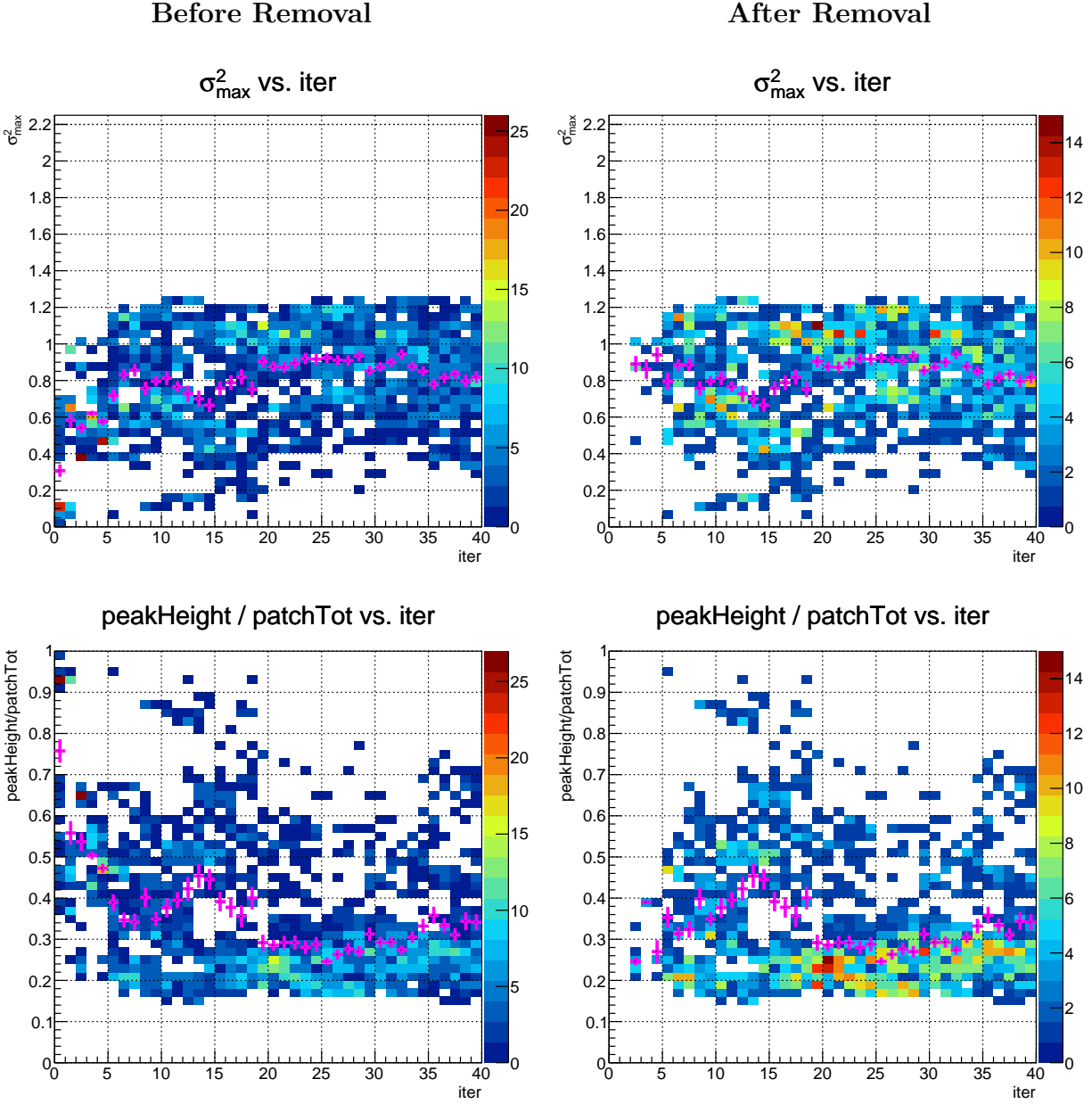


Figure 3.22: For Run 12 inner region, distributions of hot spot candidate σ_{\max}^2 versus i (top) and H/P versus i (bottom) before hot spots are removed (left figures) compared to after hot spot masking (right figures).

Run 13 Outer Region Hot Spot Removal

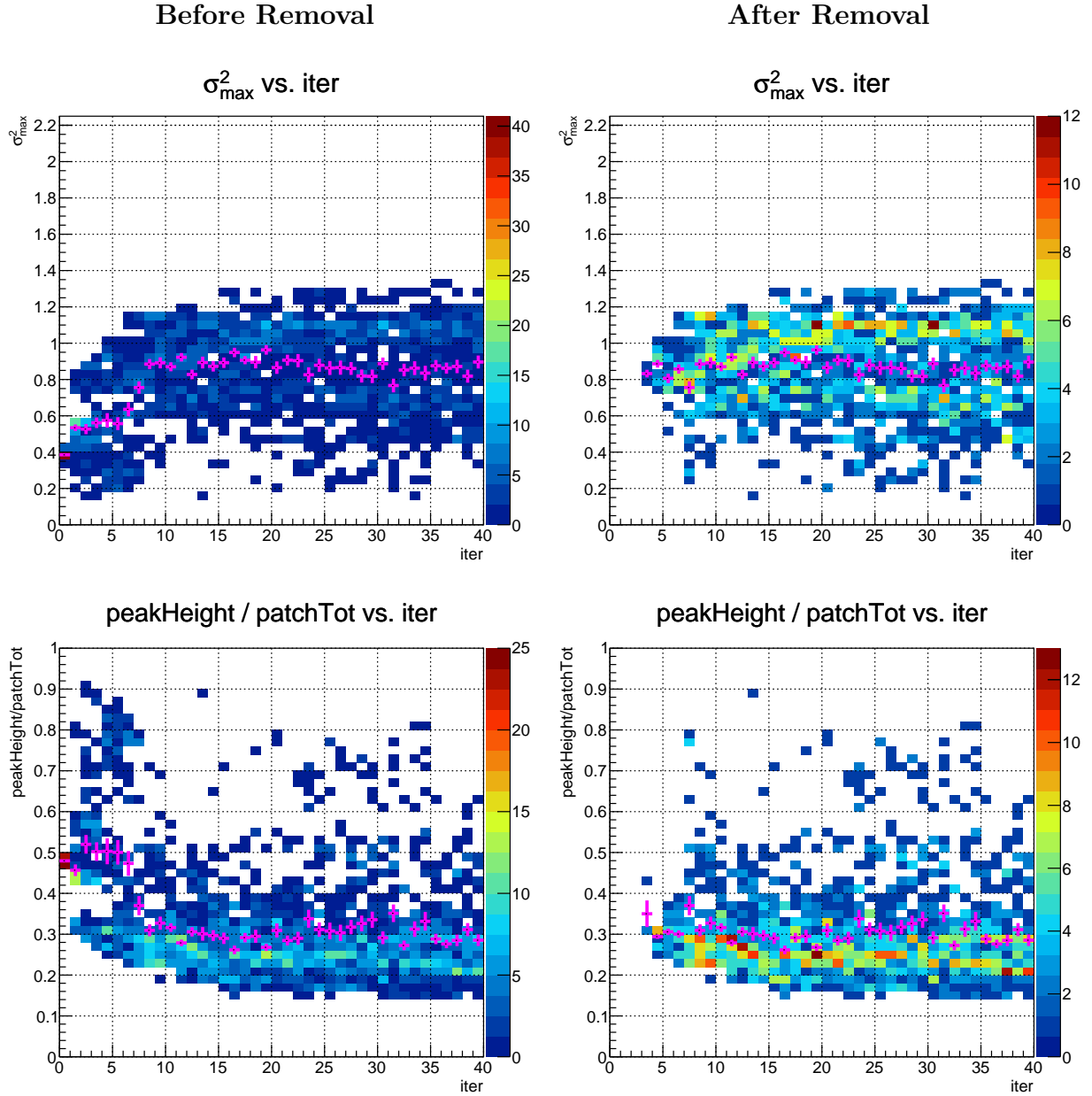


Figure 3.23: For Run 13 outer region, distributions of hot spot candidate σ_{\max}^2 versus i (top) and H/P versus i (bottom) before hot spots are removed (left figures) compared to after hot spot masking (right figures).

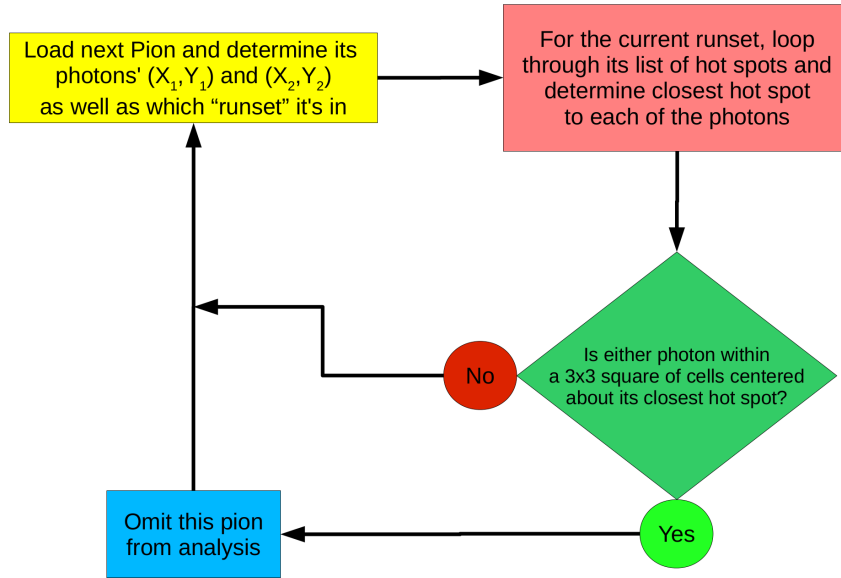


Figure 3.24: Hot spot π^0 -masking algorithm.

3.7 Pion Event Selection

Finally, we specify the set of kinematic cuts used to define the analyzed π^0 sample for the $A_{LL}^{\pi^0}$ measurement.

3.7.1 General Kinematic Cuts

The set of cuts used to identify π^0 s are:

- Highest energy pair in the highest energy cone-cluster in the event
- Pseudorapidity:
 - Outer Region: $\eta \in [2.65, 3.15]$
 - Inner Region: $\eta \in [3.15, 3.9]$
- Energy:
 - Outer Region: $E \in [30, 70]$ GeV
 - Inner Region: $E \in [30, 100]$ GeV
- Transverse Momentum: p_T greater than time-dependent threshold (details below); the upper limit of p_T is restricted by the lower limit on η and the upper limit on E
 - Outer Region: $p_T \in [p_T^{\text{thresh}}, 9.8]$ GeV

– Inner Region: $p_T \in [p_T^{\text{thresh}}, 8.6]$ GeV

- Energy Imbalance: $Z \in [0, 0.8)$
- Energy-and-time-dependent Mass Cut (details below)

3.7.2 p_T Threshold Cut

Because of the ever-increasing radiation damage during Runs 12 and 13, several side effects occurred. One of the most noticeable ones in the π^0 kinematics is a slow increase in the overall p_T distribution and threshold. In order to maintain an appropriate lower bound on the π^0 p_T , a time-dependent p_T threshold cut was implemented. Each DAQ run's π^0 p_T distribution was first fit to a Gaussian in order to approximate the rise and fall in p_T just above the nominal threshold. The p_T lower bound was then selected as the p_T value at which the distribution is 2/3 of the Gaussian fit height, on the low side of the p_T distribution. This algorithm provided a consistent p_T cut for all runs analyzed.

Figures 3.25-3.27 show p_T distributions on the vertical axis versus run on the horizontal axis, for all runs analyzed in $A_{LL}^{\pi^0}$; each run's distribution is normalized by its integral and the runs are plotted in chronological order. The black line indicates the p_T lower cutoff as determined by the fits and the magenta dots indicate the distribution means. Both the distribution means and the p_T lower cutoffs increase as a function of time. Sometimes a step up or down in the distributions is observed, for example in the Run 12 outer region around run index 100; these steps are indicative of trigger threshold adjustments during the data-taking period.

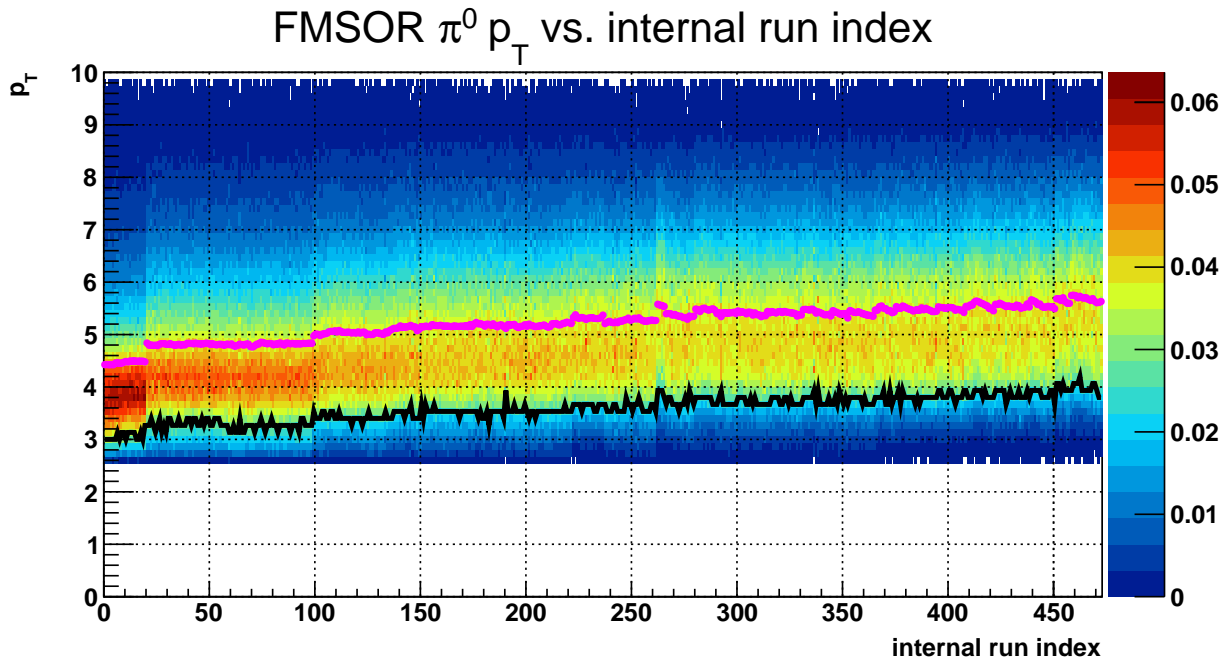


Figure 3.25: $\pi^0 p_T$ normalized distribution vs internal run index for Run 12 outer η region.

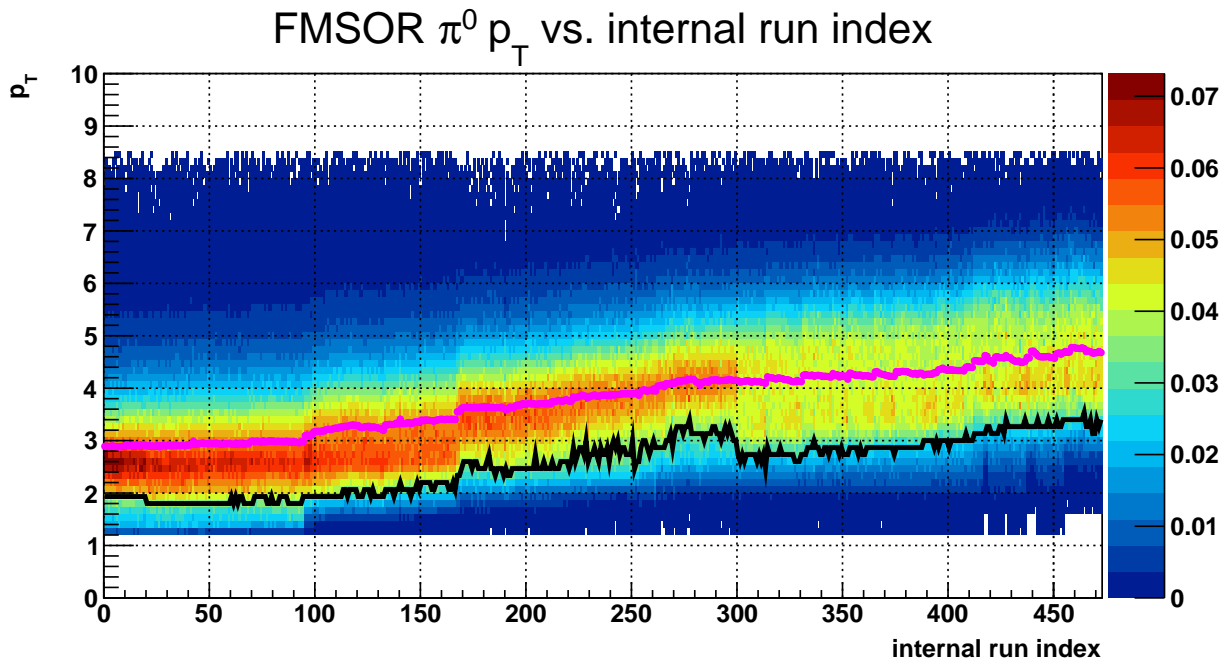


Figure 3.26: $\pi^0 p_T$ normalized distribution vs internal run index for Run 12 inner η region.

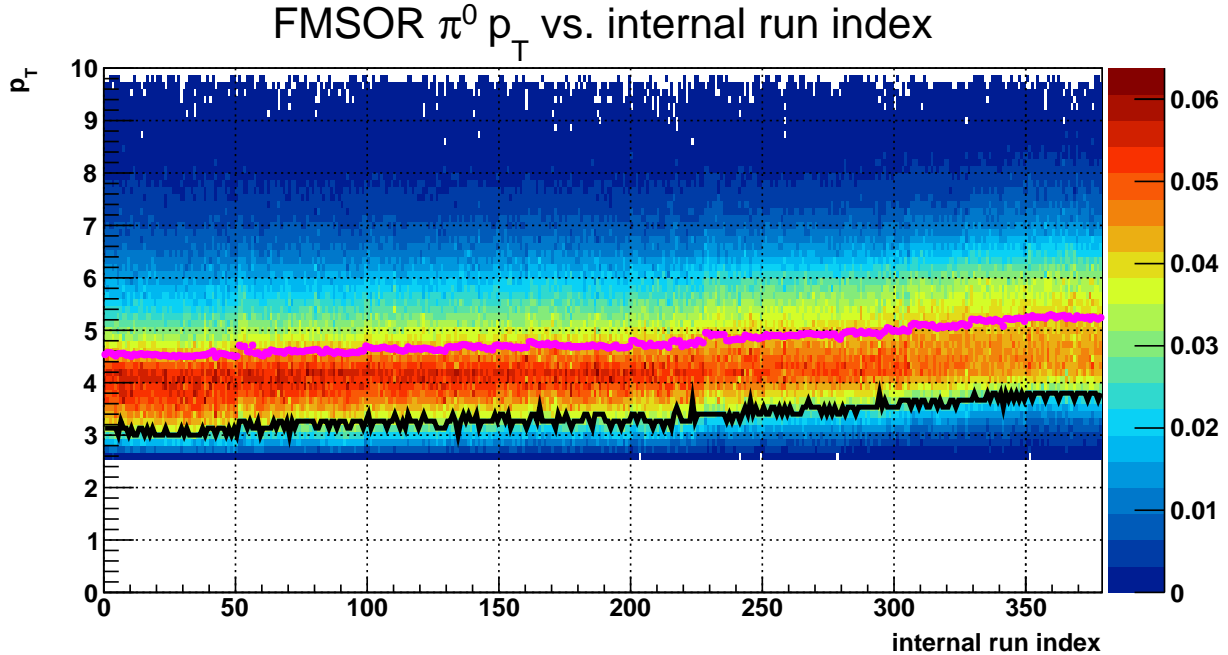


Figure 3.27: π^0 p_T normalized distribution vs internal run index for Run 13 outer η region.

3.7.3 Mass Cut

Recall from section 3.4.5 that the source of the energy dependence of the mass is that the fit algorithm for clusters has a tendency to overestimate the decay photon opening angle, α . Instead of implementing an α -dependent energy correction, the 2-photon sample, which satisfies all π^0 cuts except for the mass cuts, is divided into bins of energy. The invariant mass distribution of 2-photon events within each bin is fit with a skewed Gaussian; this is done on a runset-by-runset basis. The skewed Gaussian is used to determine a value which approximates the π^0 peak maximum, that is, the approximate mode of the mass distribution had it been smoothed; using the fit to determine the peak maximum provides more of a stable maximum than the distribution maximum itself would.

Starting from the maximum of the fit, the lower and upper bounds of the mass window are established by tracing down each side of the skewed Gaussian function until its value is such that the fit function is a fraction f of the value of the distribution maximum; the fraction $f = 0.2$ is used for the lower bound and $f = 0.3$ for the upper bound, for both inner and outer regions. Alternate mass cut determination algorithms were attempted, such as using the fit parameters to determine the skewed Gaussian mean and standard deviation, however, the implemented algorithm provides more of a stable result than other attempts did. The choices of how far one slides on either side were determined empirically and provide a reasonable set of cuts for all E bins, both η regions, for all runsets throughout Runs 12

and 13.

Figures 3.28 and 3.29 show a sample runset's mass distributions for each energy bin, for the outer region and inner region respectively. The energy bins, plotted in order from left-to-right, top-to-bottom, are: [30, 40), [40, 50), [50, 60), [60, 70), [70, 85), [85, 100) GeV, where the last two bins are only plotted for the inner region. The overall mass cuts used in the $A_{LL}^{\pi^0}$ analysis as a function of a chronological runset index are provided in figures 3.30-3.32. The fit maxima are plotted as the points and their error bars represent the full mass window of π^0 s considered for $A_{LL}^{\pi^0}$.

A sideband region is also obtained using these mass cuts and fits. This sideband region is a sample of background events between the π^0 and η -meson mass peaks, which is used to determine a background A_{LL} and later subtracted out of the full $A_{LL}^{\pi^0}$. The upper bound of the π^0 mass window is used as the lower bound of this sideband region. The sideband upper bound is set such that the width of the sideband region is equal to the width of the region between the fit maximum and the π^0 mass window upper bound; this definition is sufficient to keep the sideband region from crossing into the η -meson mass peak around 0.55 GeV. Like the π^0 mass windows, these sidebands are defined on a runset-by-runset basis for each E bin.

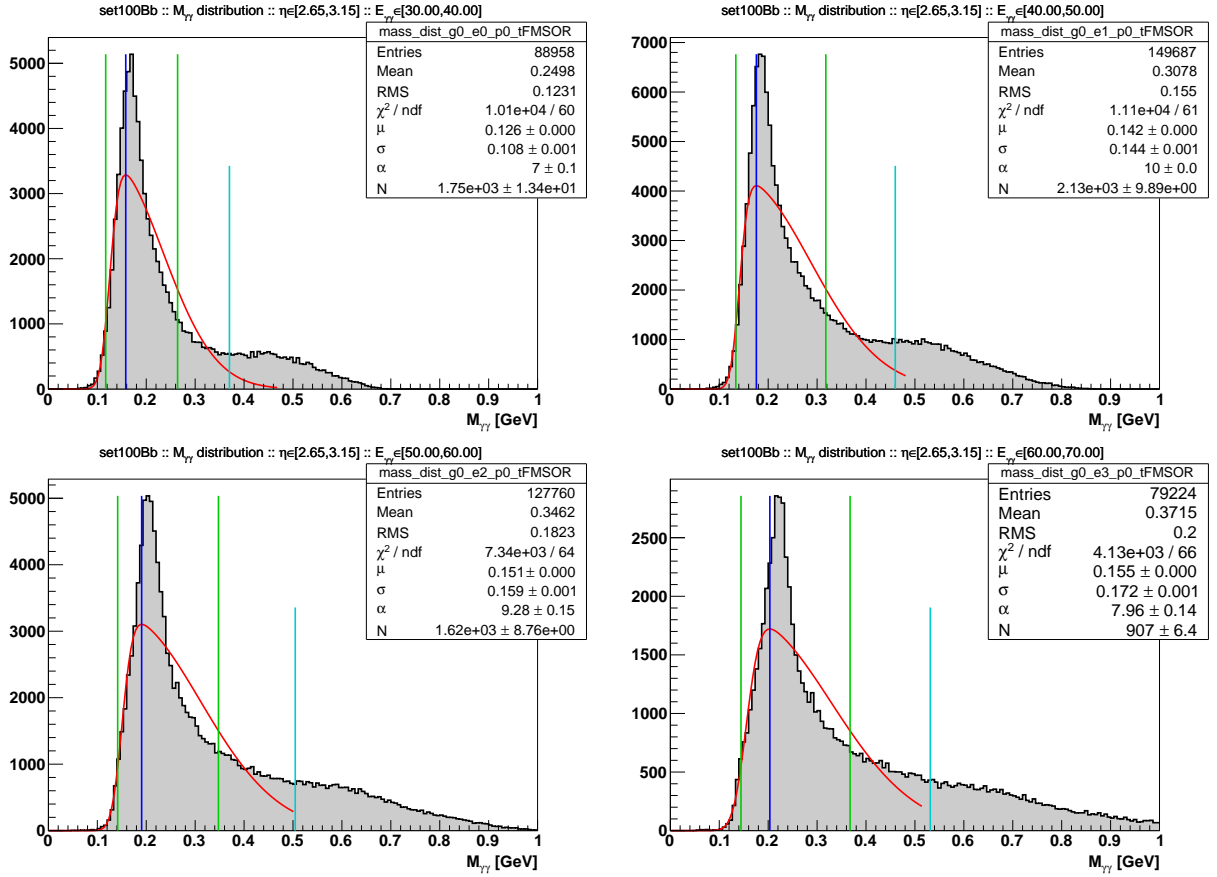


Figure 3.28: Sample 2-photon mass distributions for the outer region for various E bins (given in text); tall green lines indicate π^0 mass cuts, in between which is a blue line indicating the distribution maximum as approximated by the fit (red curve). The short cyan line is the upper bound of the sideband region.

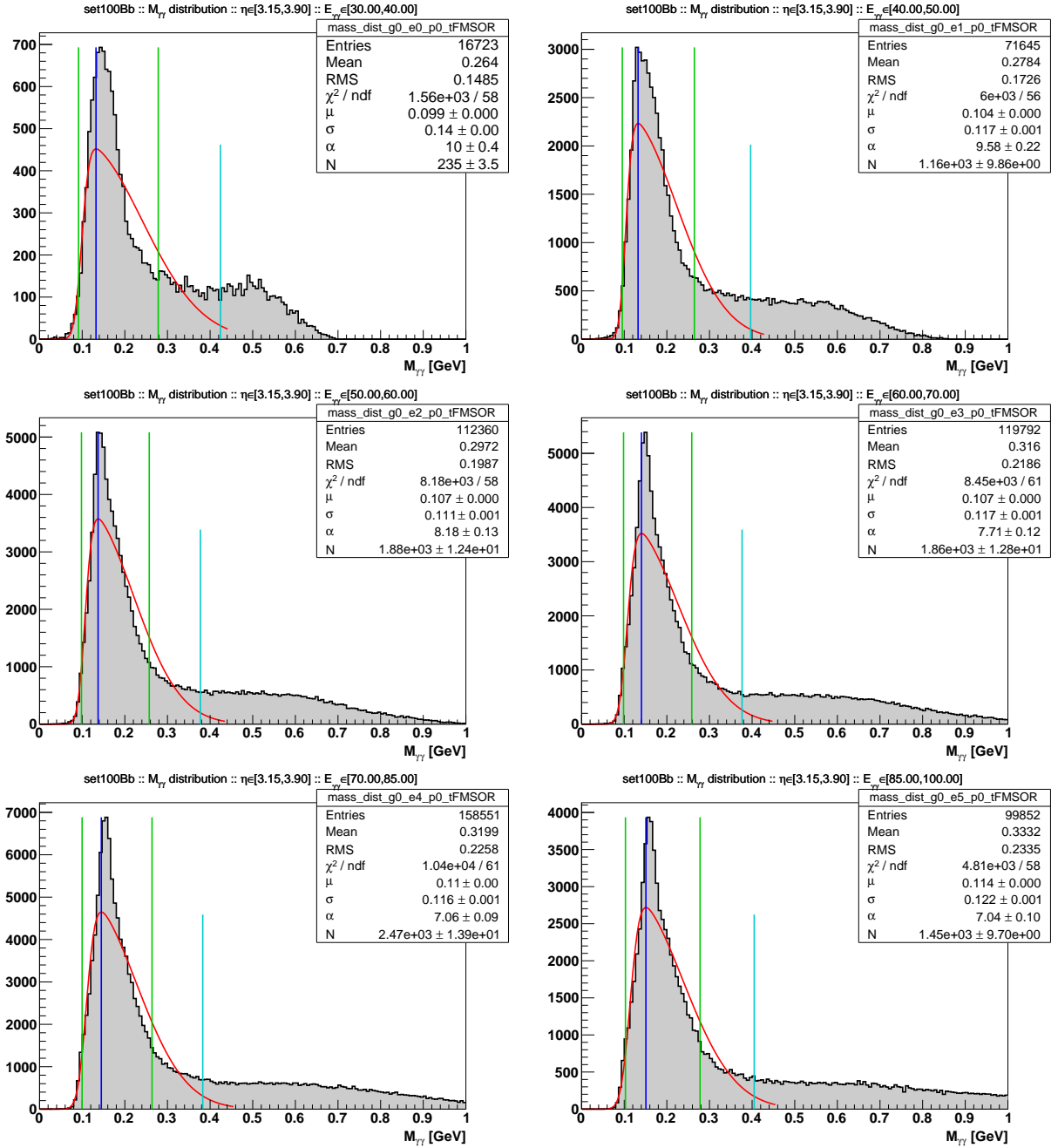


Figure 3.29: Sample 2-photon mass distributions for the inner region for various E bins (given in text).

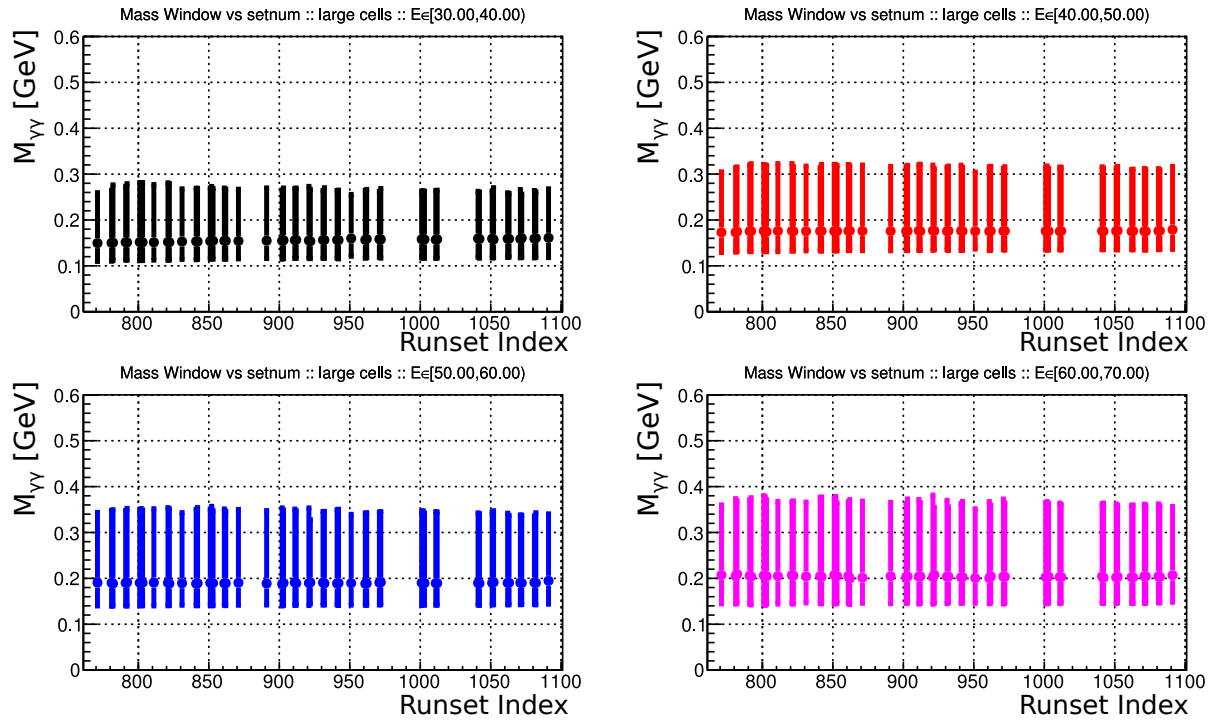


Figure 3.30: π^0 mass windows vs. runset index for Run 12 outer region.

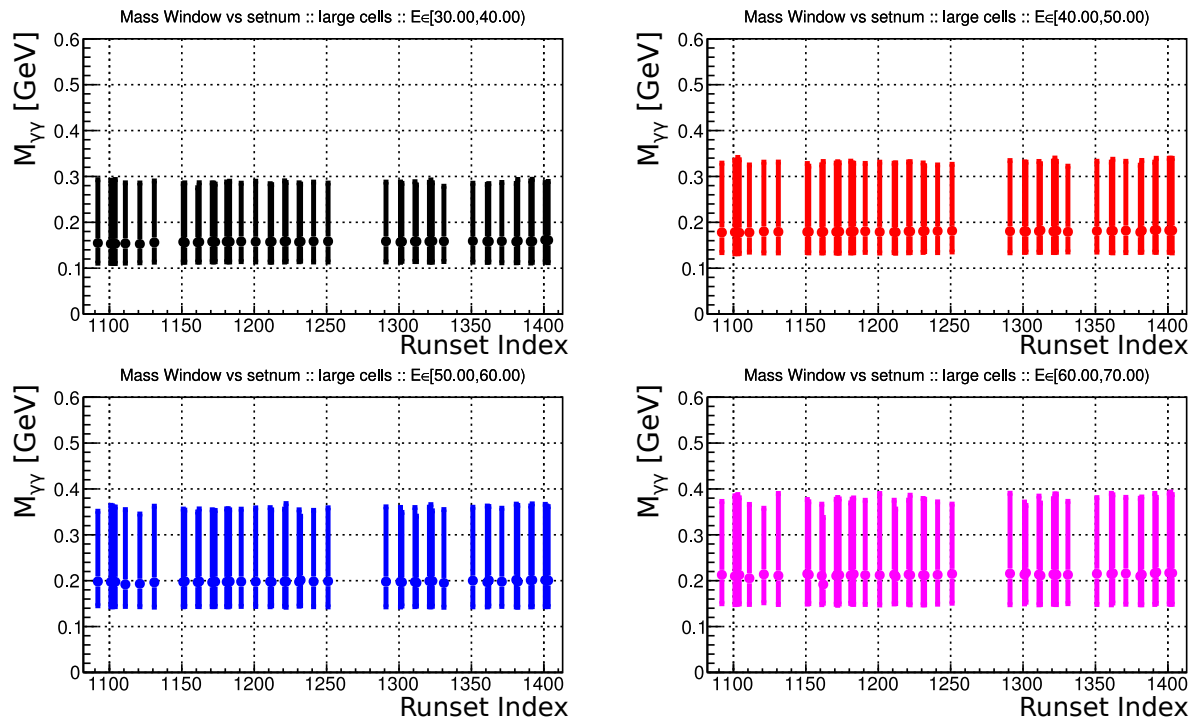


Figure 3.31: π^0 mass windows vs. runset index for Run 13 outer region.

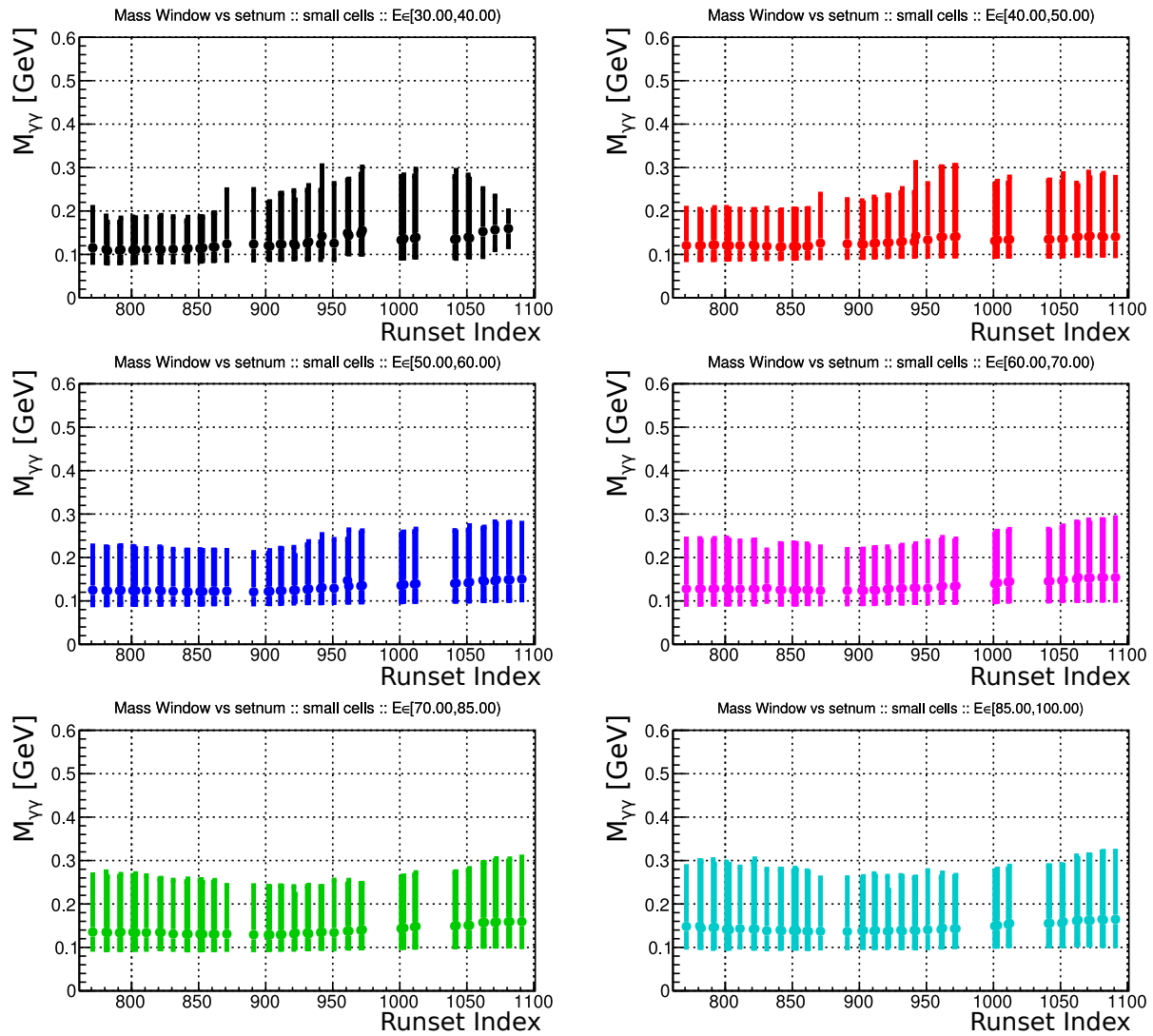


Figure 3.32: π^0 mass windows vs. runset index for Run 12 inner region.

3.7.4 Kinematics Distributions

Now that all of the π^0 cuts have been discussed, the resulting π^0 dataset's kinematic distributions are presented. Figure 3.33 shows the π^0 p_T vs. E plane. In this plane, bands are visible, which follow lines of constant pseudorapidity. The data in this plot are bounded by two diagonal lines given by the pseudorapidity bounds, a lowest time-dependent p_T threshold minimum, and lower and upper E bounds. The data peaks within a p_T range of 3.5–6 GeV for the outer region and 2.5–4.5 GeV for the inner region.

The position-space distributions of reconstructed π^0 trajectories are plotted in figure 3.34. There are some relatively “warm” areas of the detector, which are small regions which have more than average π^0 hits. These areas have survived the hot spot masking algorithm, which served to remove the worst-case hot spots; removing these additional warm areas does not meaningfully impact the $A_{LL}^{\pi^0}$ results. In some cases, hot spots persisted for most or all of the $A_{LL}^{\pi^0}$ dataset, and appear as holes in these distributions.

In Run 13, there was a problem with the upper-left quadrant of the detector; figure 3.34 shows that there is much less data there. This was because trigger crate QT3 malfunctioned shortly after the beginning of the data-taking period and was subsequently disabled for the remainder of the data-taking period. Fortunately, $A_{LL}^{\pi^0}$ is not dependent on azimuth and is thus not affected by this issue.

Figure 3.35 shows the Z -distributions, without the $Z < 0.8$ cut applied. The absolute upper limit on Z is determined by the energy cuts: $Z_{\max} = \left[\left(E_{\max}^{\pi^0} - E_{\min}^{\gamma} \right) - E_{\min}^{\gamma} \right] / E_{\max}^{\pi^0}$. In the photon reconstruction algorithm, there is a soft-energy cutoff demanding that the photon energy be at least $E_{\min}^{\gamma} = 6$ GeV. The values of $E_{\max}^{\pi^0}$ are 70 GeV and 100 GeV for the outer and inner regions, as discussed. Therefore, Z_{\max} is 0.83 for the outer region and 0.88 for the inner region. The $Z < 0.8$ cut impacts the inner region more than the outer region.

Figures 3.36 and 3.37 show the full $A_{LL}^{\pi^0}$ pion p_T distributions as well as the binning used for the $A_{LL}^{\pi^0}$ calculation, indicated by the tall vertical black lines. The $A_{LL}^{\pi^0}$ calculation occurs for four p_T bins over the two η regions, separately, integrating over the other kinematic variables (see section 6.1 for numerical bin boundary values). The p_T binning has been chosen to roughly equalize the pion yields within each bin, rounded to the nearest sensible number. Each bin has a red cross-shaped marker: its horizontal position indicates the p_T bin means and its horizontal extent indicates the bin RMS values. The overall lower bounds are given by the p_T threshold cuts and the overall upper bounds are constrained by kinematics: $p_T^{\max} \approx E_{\max}^{\pi^0} / \cosh \eta_{\min}$. For the outer region, $p_T^{\max} = 9.8$ GeV and for the inner region, 8.6 GeV. The minimum value of p_T allowed by kinematics, $p_T^{\min} \approx E_{\min}^{\pi^0} / \cosh \eta_{\max}$, is below the p_T thresholds over the entire dataset.

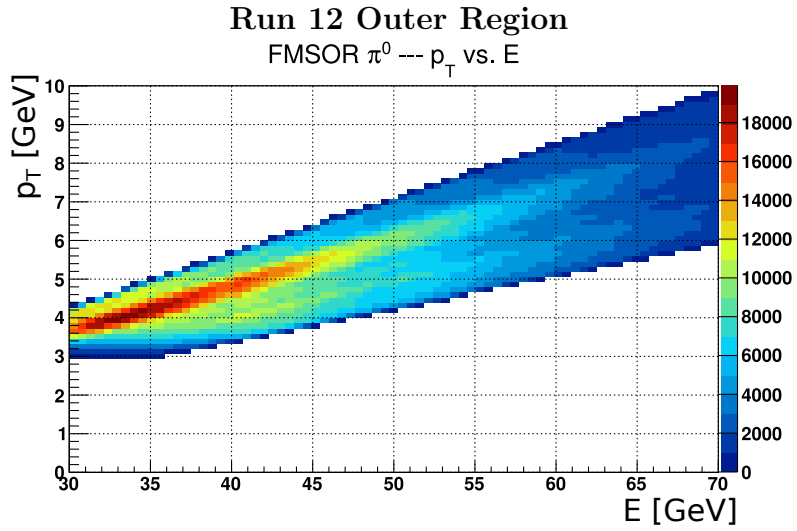


Figure 3.33: π^0 p_T vs E for Run 12 outer region (top), Run 12 inner region (middle) and Run 13 outer region (bottom).

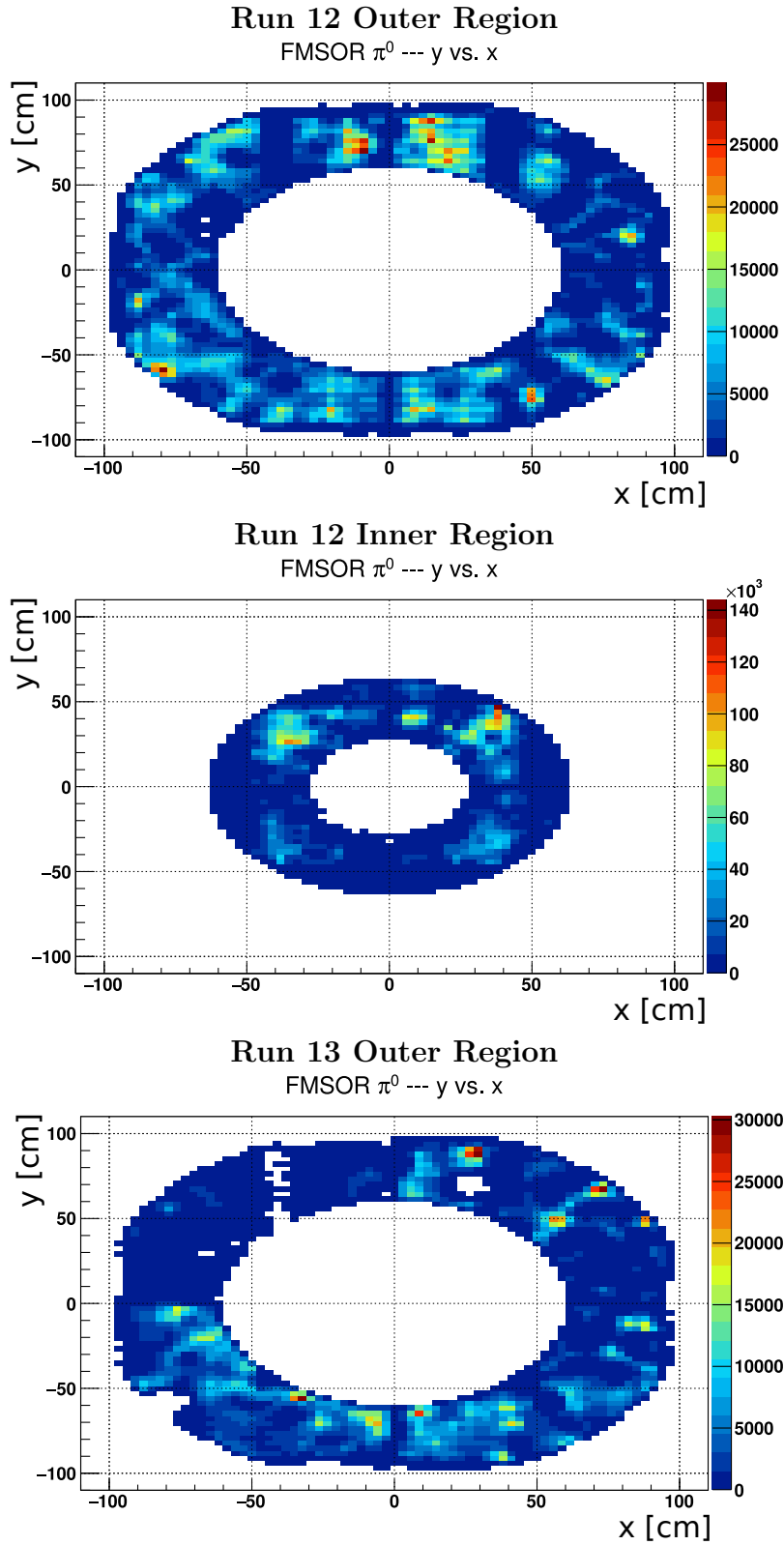


Figure 3.34: π^0 y -position vs x -position for Run 12 outer region (top), Run 12 inner region (middle) and Run 13 outer region (bottom).

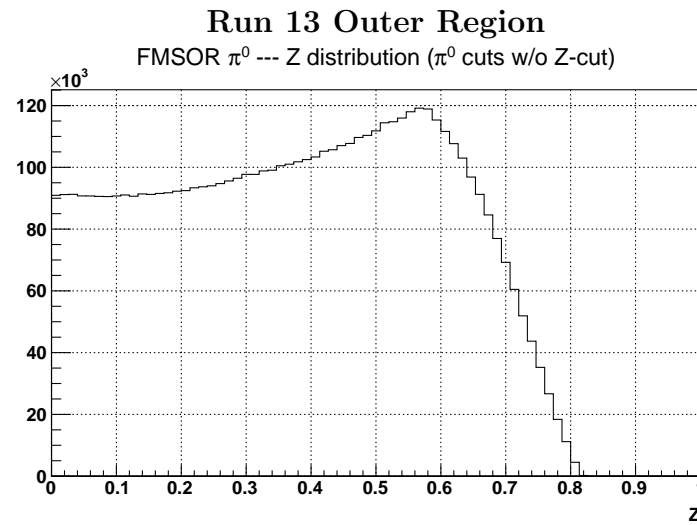
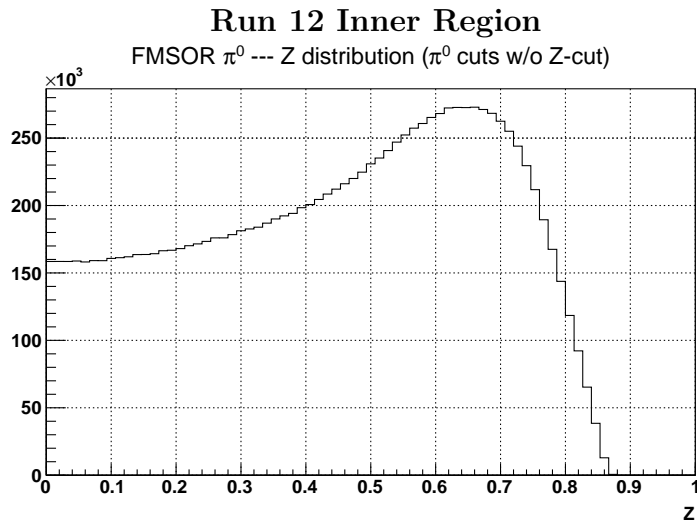
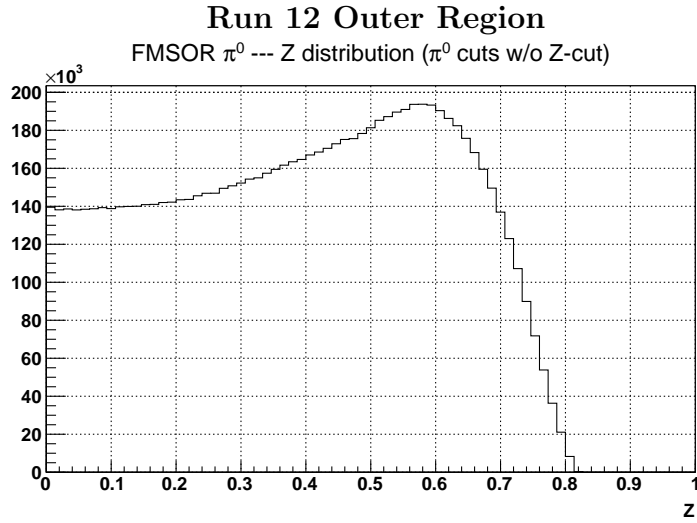


Figure 3.35: π^0 Z distribution ($Z < 0.8$ cut not applied) for Run 12 outer region (top), Run 12 inner region (middle) and Run 13 outer region (bottom).

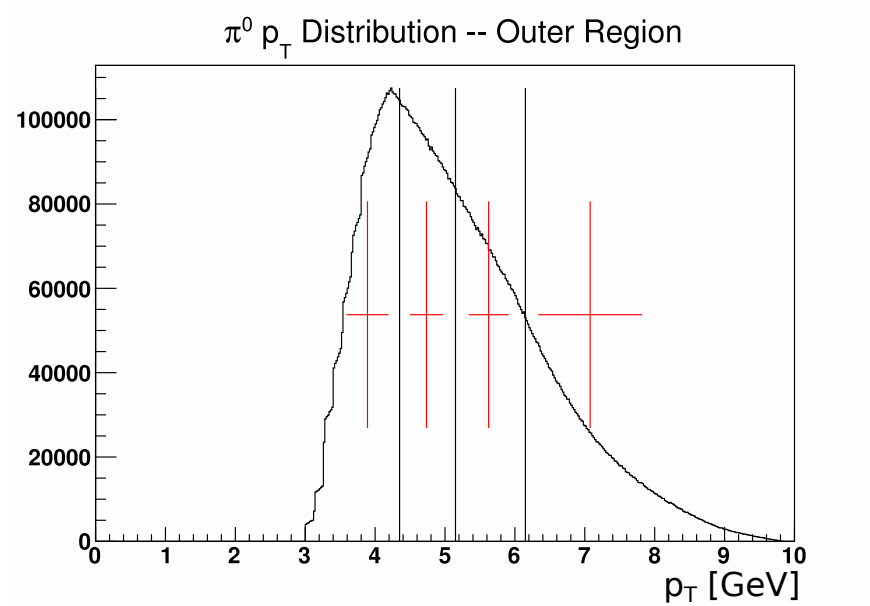


Figure 3.36: $\pi^0 p_T$ distribution for outer region. Tall black lines denote p_T bin boundaries. Horizontal positions of vertical red lines indicate p_T bin means. Lengths of horizontal red lines indicate bin RMS values. Note that this includes both Runs 12 and 13.

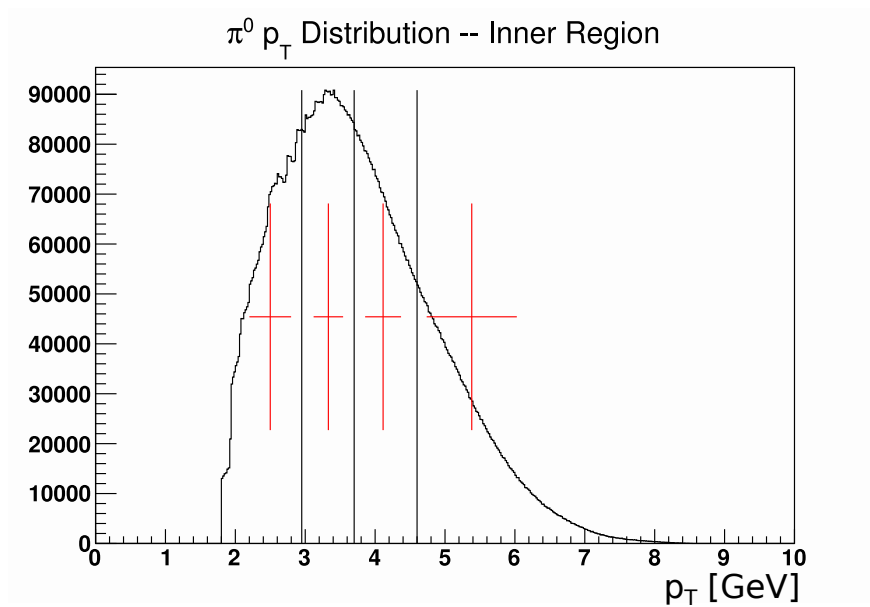


Figure 3.37: $\pi^0 p_T$ distribution for inner region. Note that this is for Run 12 only.

Chapter 4

Relative Luminosity

The relative luminosity is a ratio of luminosities for production from one set of spin states to another. For the longitudinal double-spin asymmetry, it is the ratio of luminosity from same-helicity bunch crossings to that from opposite-helicity bunch crossings:

$$R_3 = \frac{L_{++} + L_{--}}{L_{+-} + L_{-+}}. \quad (4.1)$$

Other relative luminosity ratios may be formed, which correspond to different kinds of asymmetries; see appendix B for the other combinations and associated details. This chapter presents the R_3 measurement as well as various diagnostics on its determination and consistency.

4.1 Basic Computation Algorithm

The relative luminosity is typically measured by high-rate scaler detectors, which were described in section 2.4. At STAR, the scaler detectors are the Beam-Beam Counter (BBC), the Vertex Position Detector (VPD), and the Zero Degree Calorimeter (ZDC). Hits in the scaler detectors, which satisfy certain conditions such as $\text{ADC} > \text{threshold}$, are read out for every bunch crossing via the scaler boards. Since luminosity is proportional to yield, the number of hits for each initial proton helicity combination $h_a h_b$ can then be taken as the values of $L_{h_a h_b}$ in equation 4.1, since proportionality factors such as efficiency and acceptance cancel in the ratio.

In both Runs 12 and 13, there was a designated luminosity scaler board used for such analyses. In Run 12, scaler board number 12 read out 24-bit streams for every bunch crossing, whereas in Run 13, board number 4 read out 32-bit streams. In both Runs, the last 7 bits represent a bunch crossing number with possible values 0–127, where a value of

0–119 represents a STAR bunch crossing. The proton beams at RHIC include 360 possible RF (radio frequency) buckets, each of which can hold a proton bunch with $\sim 10^{10}$ protons; these buckets are timed with the RF cavities of RHIC, which accelerate the protons as they pass through them. Typically only every third bucket is filled; furthermore, the last 9 of these 120 buckets are left empty. This empty region in the fill pattern is called the *abort gap*, and is very useful for many different purposes such as background studies and systematics, along with verifying the alignment of spin patterns with the observed collisions.

At PHENIX, the abort gaps from each beam are aligned, so that the abort gap from one beam “collides” with the abort gap of the other. At STAR, however, the abort gaps are not aligned, since the relative *cogging* between the beams depends on position within the RHIC rings. With the aforementioned crossing numbering, the abort gaps at STAR occupy bunch crossings 31–39, corresponding to the yellow beam abort gap, and 111–119, corresponding to the blue beam abort gap. Although the distinction between beam directions does not matter much for a double-spin asymmetry measurement, it is worth noting that the blue beam travels in the west direction, *toward* the FMS, while the yellow beam travels east, *away* from the FMS.

Figure 4.1 shows a sample spin pattern (RHIC fill number 16567) for the blue beam on the left and for the yellow beam on the right. The vertical axis is the bunch crossing number, starting from the bottom at bunch crossing 0. If a shaded box is drawn on the left (right), the bunch helicity is negative (positive), so for example, the blue beam pattern starts as $- - + +$. If a shaded box is drawn in the center, for example the last 9 bunches in the blue beam, the bunch is empty. Finally, yellow boxes indicate the helicities were the same, red indicates they were different, and cyan indicates no collision, *i.e.*, an abort gap.

Besides bunch crossing number, the scaler bits also indicate whether a certain scaler trigger fired. Most typically, for each scaler detector, there were two singles bits (one for the east scaler, denoted by e , and one for the west, denoted by w) which fire if the corresponding ADC counts are above a threshold, as well as one coincidence bit, denoted by x , which fires if the east and west scaler ADC counts were both above threshold and occurred within a short time window. These three bits were available for all three detector subsystems in both Runs 12 and 13, except for the VPD x bit in Run 13.

The three scaler bits can be considered as one 3-bit unit, a *triad*, written as $T = 4x + 2w + e$. In the most ideal setting, only one of four combinations of e, w, x should occur in each bunch crossing for each scaler detector: (1) only e fires, (2) only w fires, (3) all three e, w, x fire (since by definition, x only fires if both e and w fired), or (4) no bits fire. The first three of these triads are called *logical* bit combinations (the fourth is trivially the zero combination), as opposed to the other four possible triads, called *illogical* combinations,

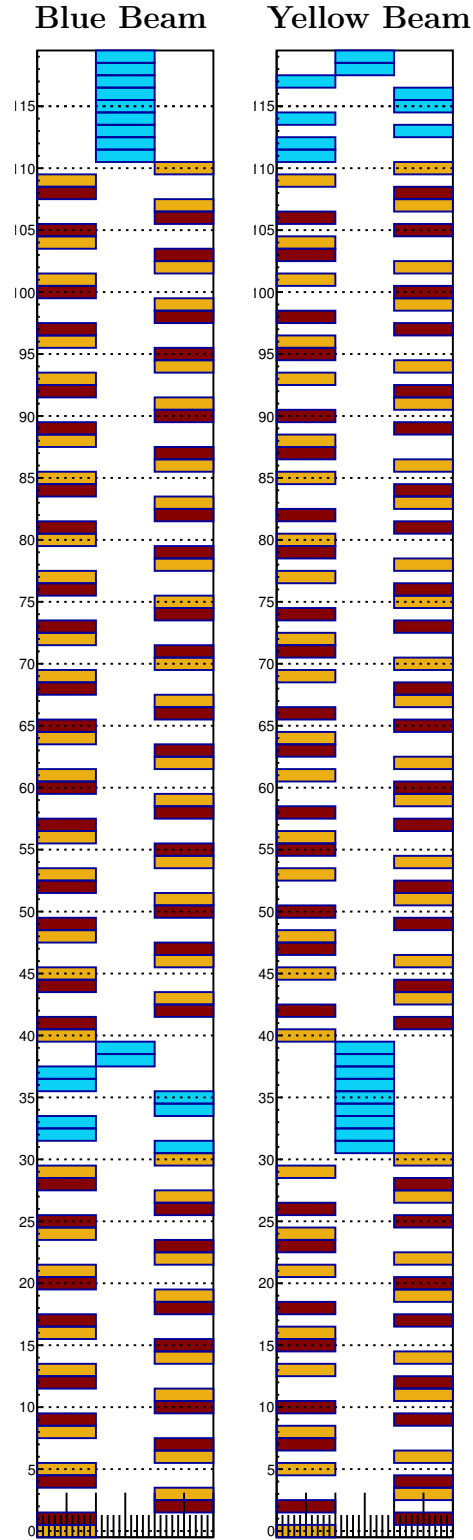


Figure 4.1: Example spin patterns for blue beam (left) and yellow beam (right). The vertical axis is the STAR bunch crossing number, and the horizontal axis is the helicity (left for $-$, right for $+$, and center for empty bunch).

Run 12 Scaler Bit Combinations

T	x	w	e	BBC			ZDC			VPD		
				E	W	X	E	W	X	E	W	X
1	0	0	1	•			•			•		
2	0	1	0		•			•			•	
7	1	1	1	•	•	•	•	•	•	•	•	•
3	0	1	1	•	•	•	•	•	•	•	•	•
4	1	0	0									
5	1	0	1	•			•			•		
6	1	1	0		•			•			•	

Run 13 Scaler Bit Combinations

T	x	w	e	BBC			ZDC			VPD		
				E	W	X	E	W	X	E	W	X
1	0	0	1	•			•			•		
2	0	1	0		•			•			•	
7	1	1	1	•	•	•	•	•	•	n/a	n/a	n/a
3	0	1	1	•	•	•	•	•	•	•	•	•
4	1	0	0							n/a	n/a	n/a
5	1	0	1	•			•			n/a	n/a	n/a
6	1	1	0		•			•		n/a	n/a	n/a

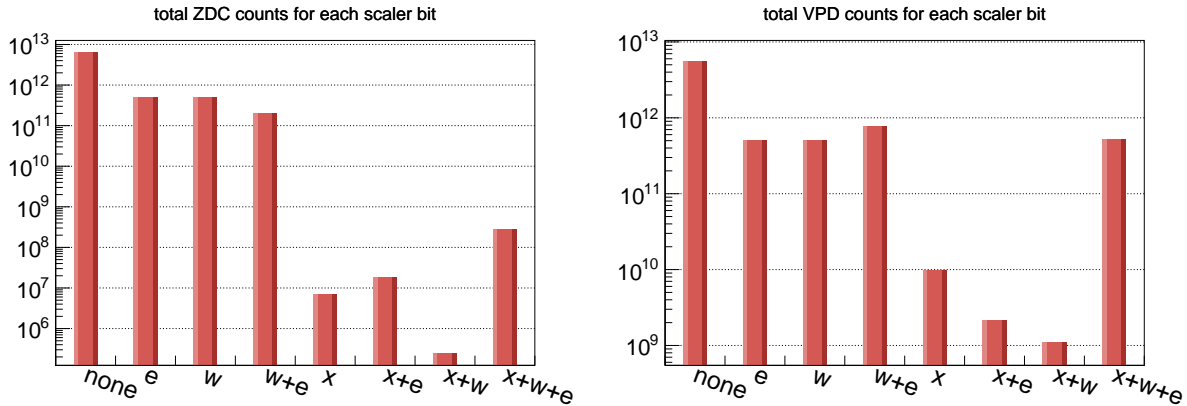
Table 4.1: Scaler bit recombinations. The left most column “ T ” is the decimal representation of the 7 combinations of the three scaler bits, x for coincidence, w and e for west and east singles. The logical bit combinations, $T \in \{1, 2, 7\}$, are bits which are expected to fire, *i.e.*, if the x bit fires, the e and w bits are also expected to fire; all other bit combinations are called illogical combinations: $T \in \{3, 4, 5, 6\}$. The E , W and X scale counts are then defined by ORing logical and illogical triads marked with •’s in each column. Note that in Run 13, there was no VPD x -bit, so for example, VPDE is defined as $T = 1$ OR $T = 3$.

which should not occur in an ideal setting. An example illogical combination is x firing, but not e or w .

The possible non-zero triads are given for Runs 12 and 13 in table 4.1. Triads $T \in \{1, 2, 7\}$ are logical bit combinations, whereas $T \in \{3, 4, 5, 6\}$ are illogical. The seven triads are then ORed together according to table 4.1 in order to form *raw scale counts* for each scaler detector for east singles, west singles, and coincidences; these raw scale counts are denoted with capital letters: E , W , and X , respectively. These ORs of triads follow from [93].

Figure 4.2 shows the relative number of scaler bit combinations which fired. More logical triads occurred than illigocal triads, except for the case where w and e fired, but not x , which is on the same order as the logical triads. From now on, only information on the ZDC and VPD will be shown for brevity, as the BBC had rather inconsistent relative luminosity

Run 12 Scaler Bit Counts



Run 13 Scaler Bit Counts

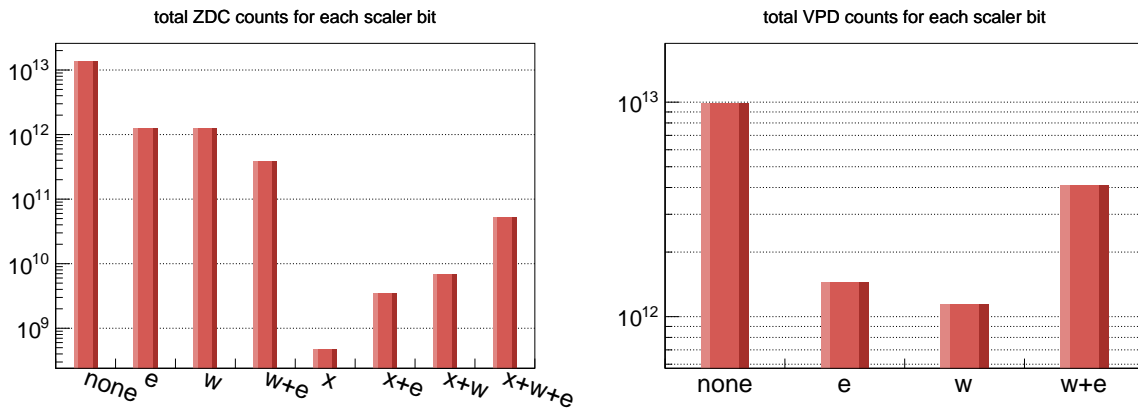


Figure 4.2: Scaler bit counts for ZDC (left) and VPD (right).

measurements with high systematic uncertainties.

4.2 Accidentals and Multiples Corrections

Figure 4.3 shows a schematic of the possible types of interactions which can cause scale counts. The vertical black lines represent east and west scaler detectors, and the blue cones represent particle production, which would fire the bits if they hit a detector. The top row shows a normal single event and a normal coincidence event. The bottom row shows a sample of an accidental coincidence of two separate interactions within the same bunch crossing, and of an under-counted multiple interaction in one bunch crossing. Given this viewpoint, the combined scaler counts E, W, and X need to be corrected for these cases where there were accidental coincidences and under-countings of multiple interactions in a

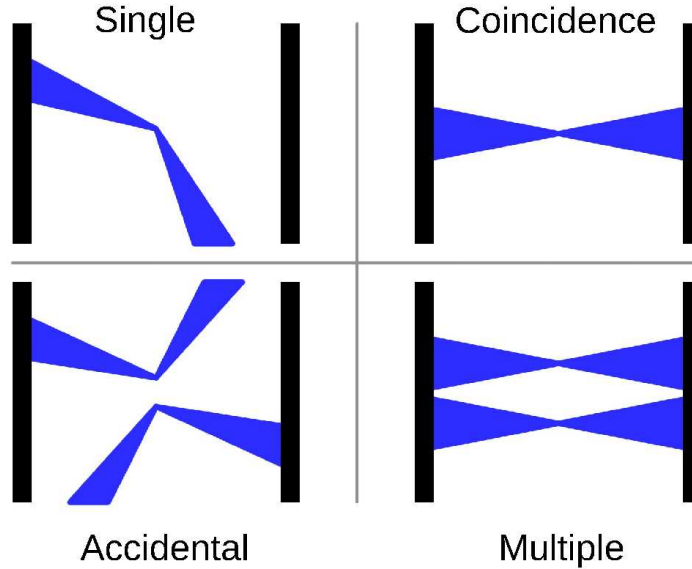


Figure 4.3: Types of events seen in scalers, showing the form of accidental coincidences and multiple interactions, to be corrected for in analysis. The vertical black lines represent scaler detectors (one for east and another for west) and the blue cones represent scaler count-producing particle trajectories.

single bunch crossing. Two forms of the accidentals and multiples corrections are presented in this section: the CDF corrections, developed by the Collider Detector at Fermilab (CDF) collaboration [94], and the rate-safe corrections, developed by PHENIX [95] (also sometimes called the pile-up correction method).

4.2.1 CDF Accidentals Correction

The CDF corrections are implemented by considering event probabilities. Let \mathcal{P}_S denote the physical probability of an event which should fire scaler bit combination $S \in \{E, W, X\}$. Let P_S be the *scale probability* of scaler S , *i.e.*, the probability that S actually fires. Note that $P_S = N_S/N_{bx}$, where N_S is the number of times S fired and N_{bx} is the total number of bunch crossings; N_S is a *raw* scale count, as opposed to a *corrected* scale count.

For the following argument, refer to figure 4.4. The scale probability P_E has contributions from physical probabilities \mathcal{P}_E and from \mathcal{P}_X , but we do not want to include the contribution where E and X would physically occur, that is, we omit the contribution of $\mathcal{P}_E \cap \mathcal{P}_X$ in P_E . Similarly for P_W , we include \mathcal{P}_W and \mathcal{P}_X , omitting $\mathcal{P}_W \cap \mathcal{P}_X$. For the coincidences, P_X naturally includes \mathcal{P}_X as well as the case $\mathcal{P}_E \cap \mathcal{P}_W$, but these two contributions are not disjoint: the case $\mathcal{P}_E \cap \mathcal{P}_W \cap \mathcal{P}_X$ is therefore omitted. In summary, by looking at the shaded regions of the Venn diagrams in figure 4.4, the scale probabilities may be written in

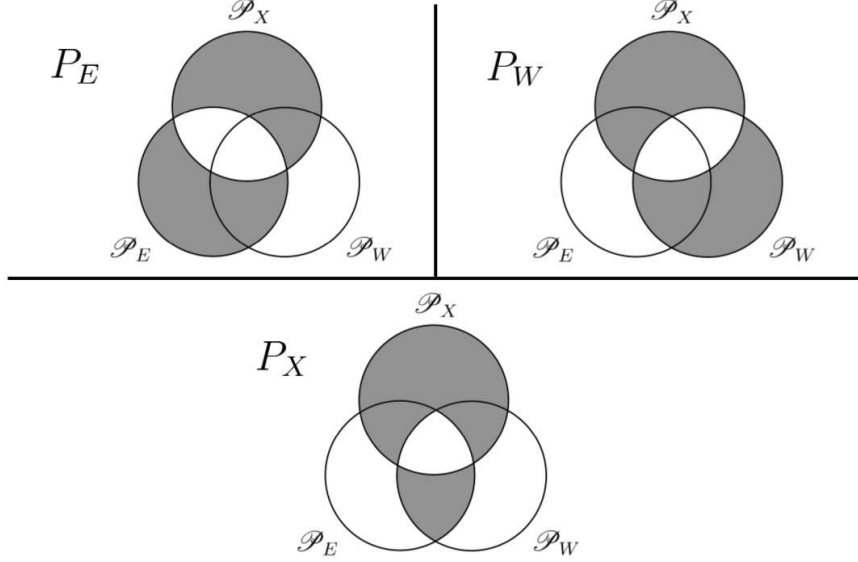


Figure 4.4: Scale probabilities as subsets of the union of physical process probabilities.

terms of the physical process probabilities as:

$$P_E = \mathcal{P}_E \cup \mathcal{P}_X \setminus (\mathcal{P}_E \cap \mathcal{P}_X) \Leftrightarrow \mathcal{P}_E + \mathcal{P}_X - \mathcal{P}_E \cdot \mathcal{P}_X, \quad (4.2)$$

$$P_W = \mathcal{P}_W \cup \mathcal{P}_X \setminus (\mathcal{P}_W \cap \mathcal{P}_X) \Leftrightarrow \mathcal{P}_W + \mathcal{P}_X - \mathcal{P}_W \cdot \mathcal{P}_X, \quad (4.3)$$

$$\begin{aligned} P_X &= \mathcal{P}_X \cup (\mathcal{P}_E \cap \mathcal{P}_W) \setminus (\mathcal{P}_E \cap \mathcal{P}_W \cap \mathcal{P}_X) \Leftrightarrow \\ &\Leftrightarrow \mathcal{P}_X + \mathcal{P}_E \cdot \mathcal{P}_W - \mathcal{P}_E \cdot \mathcal{P}_W \cdot \mathcal{P}_X. \end{aligned} \quad (4.4)$$

The physical process probabilities may then be written in terms of the scale probabilities and subsequently in terms of the scale counts as

$$\mathcal{P}_E = \frac{N_E - N_X}{N_{bx} - N_W}, \quad (4.5)$$

$$\mathcal{P}_W = \frac{N_W - N_X}{N_{bx} - N_E}, \quad (4.6)$$

$$\mathcal{P}_X = \frac{N_X - N_E N_W / N_{bx}}{N_{bx} + N_X - N_E - N_W}. \quad (4.7)$$

These are the accidentals-corrected probabilities; multiplying them by N_{bx} gives the accidentals-corrected scale counts.

4.2.2 CDF Multiple Interactions Correction

In order to correct for multiple interactions in a bunch crossing, the distribution of k interactions per bunch crossing, given λ as the “true” number of interactions in a bunch crossing, is modelled as a Poisson distribution:

$$\mathcal{P}(\lambda, k) = \frac{e^{-\lambda} \lambda^k}{k!}. \quad (4.8)$$

The Poisson distribution is used since the bunch crossings occur at a constant rate and independently of each other. The probability for no interactions in a bunch crossing is

$$\mathcal{P}(\lambda, k = 0) = e^{-\lambda} = 1 - \mathcal{P}(\lambda, k \neq 0). \quad (4.9)$$

Assuming that $\mathcal{P}(\lambda, k \neq 0)$ represents the accidentals-corrected probabilities in equations 4.5-4.7, which are independent of λ , the probability of no interactions provides access to the “true” number of interactions per bunch crossing:

$$\lambda = -\ln [1 - \mathcal{P}(k \neq 0)]. \quad (4.10)$$

The final CDF correction equations, which give the accidentals and multiples corrected counts \mathcal{N}_S in terms of the raw scale counts N_S , are therefore

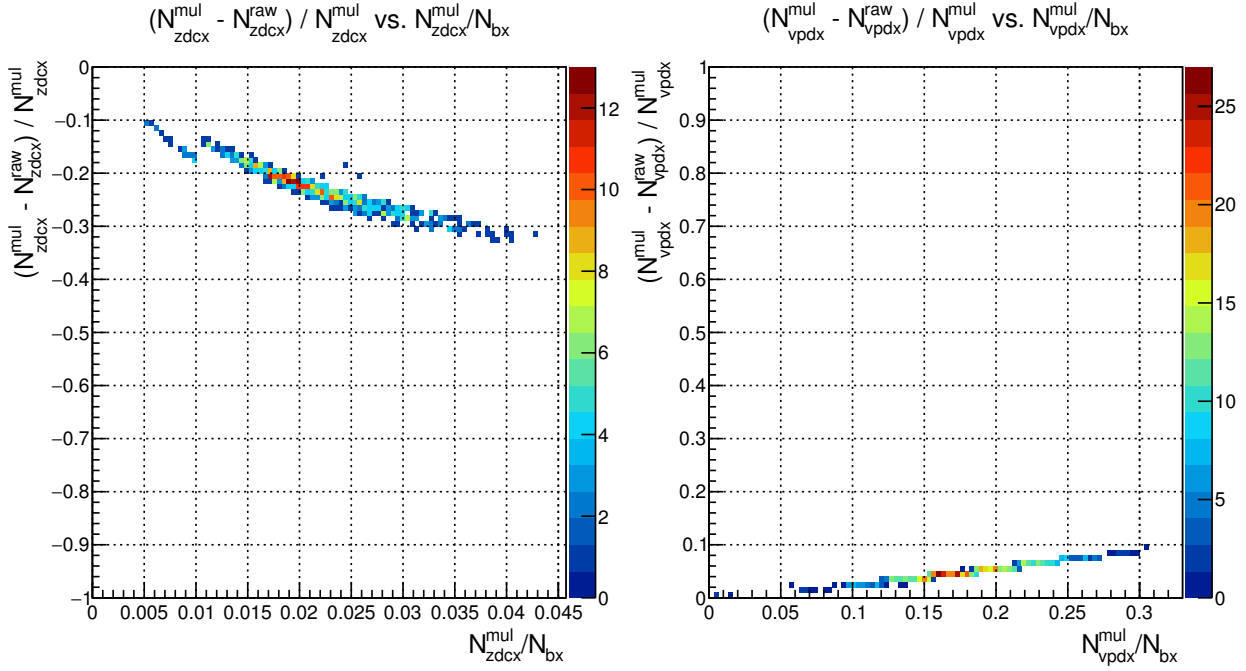
$$\mathcal{N}_E = -N_{bx} \cdot \ln \left(1 - \frac{N_E - N_X}{N_{bx} - N_W} \right), \quad (4.11)$$

$$\mathcal{N}_W = -N_{bx} \cdot \ln \left(1 - \frac{N_W - N_X}{N_{bx} - N_E} \right), \quad (4.12)$$

$$\mathcal{N}_X = -N_{bx} \cdot \ln \left(1 - \frac{N_X - N_E N_W / N_{bx}}{N_{bx} + N_X - N_E - N_W} \right). \quad (4.13)$$

Figure 4.5 shows the fractional deviation of the CDF corrected counts plotted vs. the corrected scale probability for coincidences. In other words, this is a plot of $(N_X^{CDF} - N_X^{raw}) / N_X^{CDF}$ vs. N_X^{CDF} / N_{bx} , where the superscript *CDF* indicates CDF-corrected counts and the superscript *raw* indicates the uncorrected counts. There is a strong dependence of this fractional deviation on the scale probability, which can be interpreted as a dependence of the correction on the rate.

Run 12 CDF Corrections



Run 13 CDF Corrections

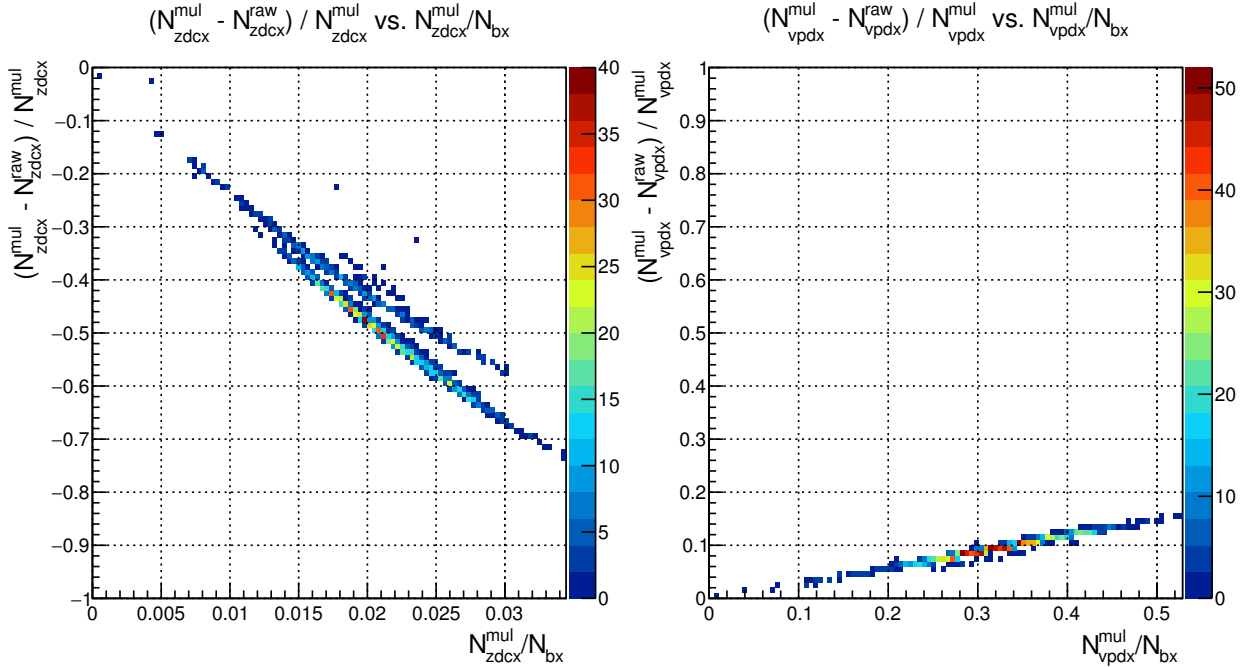


Figure 4.5: Fractional deviation of the CDF corrected counts vs. corrected scale probability for the ZDC (left) and VPD (right). Run 13 (bottom plots) shows stronger scale probability dependence than Run 12 (top plots).

4.2.3 Rate-Safe Accidentals and Multiples Corrections

PHENIX has developed an alternative method for applying scaler counts corrections for accidentals and multiples, called *rate-safe counting* (and sometimes also called the *pile-up correction*). Details may be found in section 4.3 of [95]. This section contains a terse description of the method and the final correction equations used; the full derivation has been reproduced in appendix G.

Three “event classes” are considered: east single-sided (ESS), west single-sided (WSS), and double-sided (DS). The average numbers of times these events occur in a bunch crossing are denoted λ_E , λ_W , and λ , respectively. Each event class has a detection probability of k events, given by a Poisson distribution. These distributions factor in the E and W detector efficiency \times acceptance, denoted by ε_E and ε_W .

One then considers the following three probabilities, in terms of event class probabilities (which are subscripted with the event class acronyms):

- Zero hits in E-scaler:

$$P(k_E = 0) = P_{DS}(k_E = 0) \cdot P_{ESS}(k_E = 0) = e^{-\varepsilon_E(\lambda + \lambda_E)} \quad (4.14)$$

- Zero hits in W-scaler:

$$P(k_W = 0) = P_{DS}(k_W = 0) \cdot P_{WSS}(k_W = 0) = e^{-\varepsilon_W(\lambda + \lambda_W)} \quad (4.15)$$

- Zero hits in either detector:

$$\begin{aligned} P(k_E = 0, k_W = 0) &= P_{DS}(k_E = 0, k_W = 0) \cdot P_{ESS}(k_E = 0) \cdot P_{WSS}(k_W = 0) = \\ &= e^{\varepsilon_W \varepsilon_E \lambda - \varepsilon_W \lambda - \varepsilon_E \lambda - \varepsilon_W \lambda_W - \varepsilon_E \lambda_E} \end{aligned} \quad (4.16)$$

These probabilities are combined into one expression by considering the probability that both detectors detect zero hits, given the condition that each of the single-sided detectors each detected zero hits. This probability, denoted P^* , is expressed as

$$P^* = \frac{P(k_E = 0, k_W = 0)}{P(k_E = 0) \cdot P(k_W = 0)} = e^{\Omega \lambda} \quad \text{where } \Omega := \varepsilon_W \varepsilon_E. \quad (4.17)$$

Taking the logarithm of each side and writing each probability of detecting zero hits as unity minus the probability of detecting nonzero hits yields

$$\Omega \lambda = \ln P^* = \ln \left[\frac{1 - P_X}{(1 - P_E)(1 - P_W)} \right]. \quad (4.18)$$

The probability of detecting a hit can be written as $P_S = \langle N_S \rangle / N_{bx}$, where $S \in \{E, W, X\}$. Finally, the rate-safe corrected counts N_{rsc} (times efficiency and acceptance Ω , which is factored out in any relative luminosity computation), is written as

$$\Omega N_{rsc} = N_{bx} \cdot \ln \left[\frac{1 - \langle N_X \rangle / N_{bx}}{(1 - \langle N_E \rangle / N_{bx})(1 - \langle N_W \rangle / N_{bx})} \right]. \quad (4.19)$$

Figure 4.6 shows the fractional deviation of the rate-safe corrected counts (times efficiency and acceptance) plotted versus the ratio of this corrected number of counts to the number of bunch crossings. Denoting the efficiency times acceptance as Ω , this is a plot of $(\Omega N^{RSC} - N_X^{raw}) / \Omega N^{RSC}$ vs. $\Omega N^{RSC} / N_{bx}$, where the superscript *RSC* is for the rate-safe corrected counts and the superscript *raw* is for the uncorrected number of counts. Comparing this to figure 4.5 and interpreting the horizontal axis as a surrogate for the scale rate, one sees that this correction method depends much less on rate, hence the nomenclature “rate-safe correction method” is appropriate.

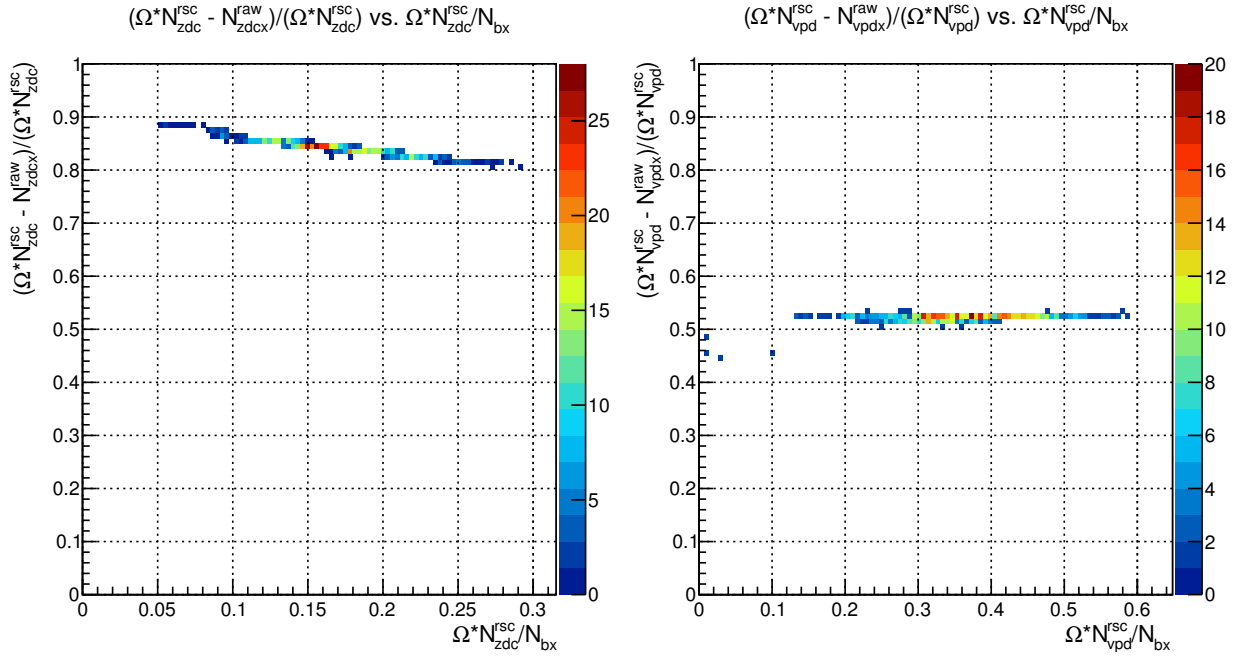
4.3 R_3 Results

Figures 4.7 and 4.8 show the R_3 values plotted vs. run index for the VPD for both Runs 12 and 13; measurements for the ZDC are in appendix F, figures F.1 and F.2. In each figure, four plots are shown. The first three use the CDF corrections equations and are, in order from top to bottom, R_3 for E, for W, and for X. The fourth plot is R_3 computed using the rate-safe corrections method, which makes use of all three E , W , and X raw counts.

The red lines in these figures show a constant fit and the fit results are quoted in the upper-right corner of each figure. The typical relative luminosity fluctuates between $\pm 4\%$ and remains approximately constant within each fill. Fluctuations up and down are from fill-to-fill and are due to the injected spin pattern. In Run 13, the first few fills had bunch crossings 69–70 empty, which caused the somewhat higher value of $|1 - R_3|$ up to about run index 300. Note that the χ^2 per degree of freedom for these fits is very high, because R_3 is not constant throughout the run; rather these fits indicate how well “balanced” the relative luminosity was for the Run as a whole.

Statistical uncertainty bars are also plotted on these figures, although they are too small to be seen at this scale; the uncertainty is typically $\lesssim 1 \times 10^{-4}$. For the CDF corrections method, the square root of the counts is used for the counts uncertainties; for the rate-safe method, the counts uncertainties are derived in appendix G.

Run 12 Rate-Safe Corrections



Run 13 Rate-Safe Corrections

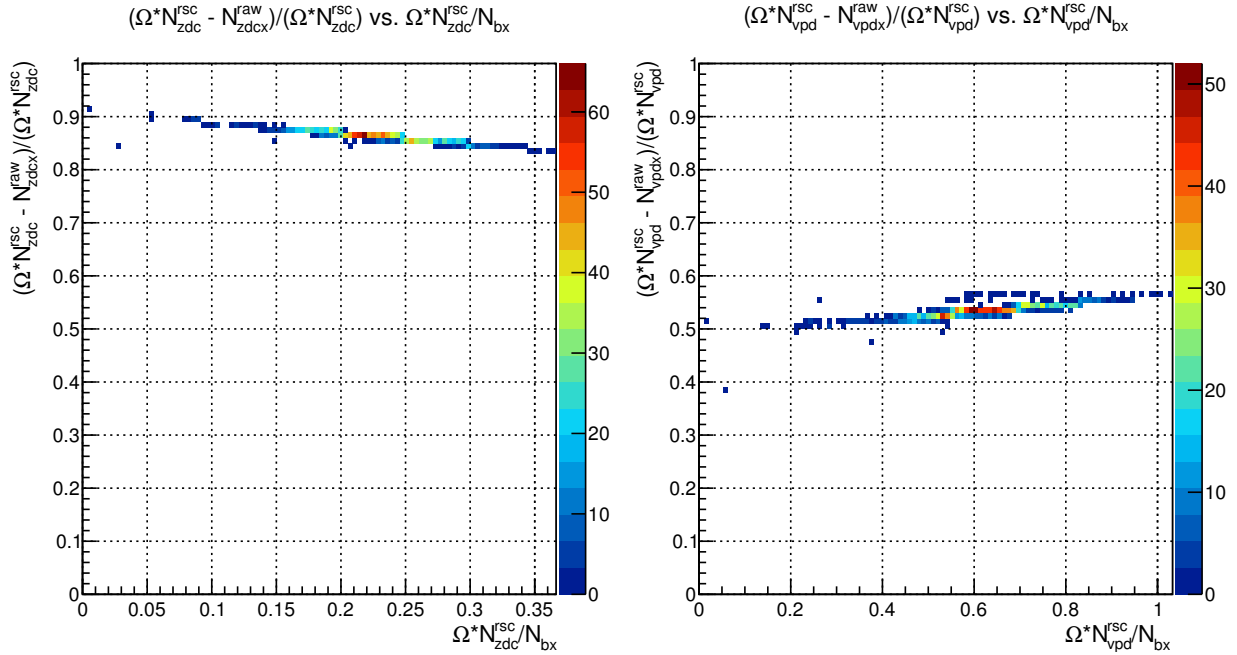


Figure 4.6: Fractional deviation of the rate-safe corrected counts vs. the ratio of the rate-safe counts (times efficiency and acceptance) to the number of bunch crossings for the ZDC (left) and VPD (right). This is a comparison to figure 4.5.

Run 12 VPD R_3 vs. Run Index

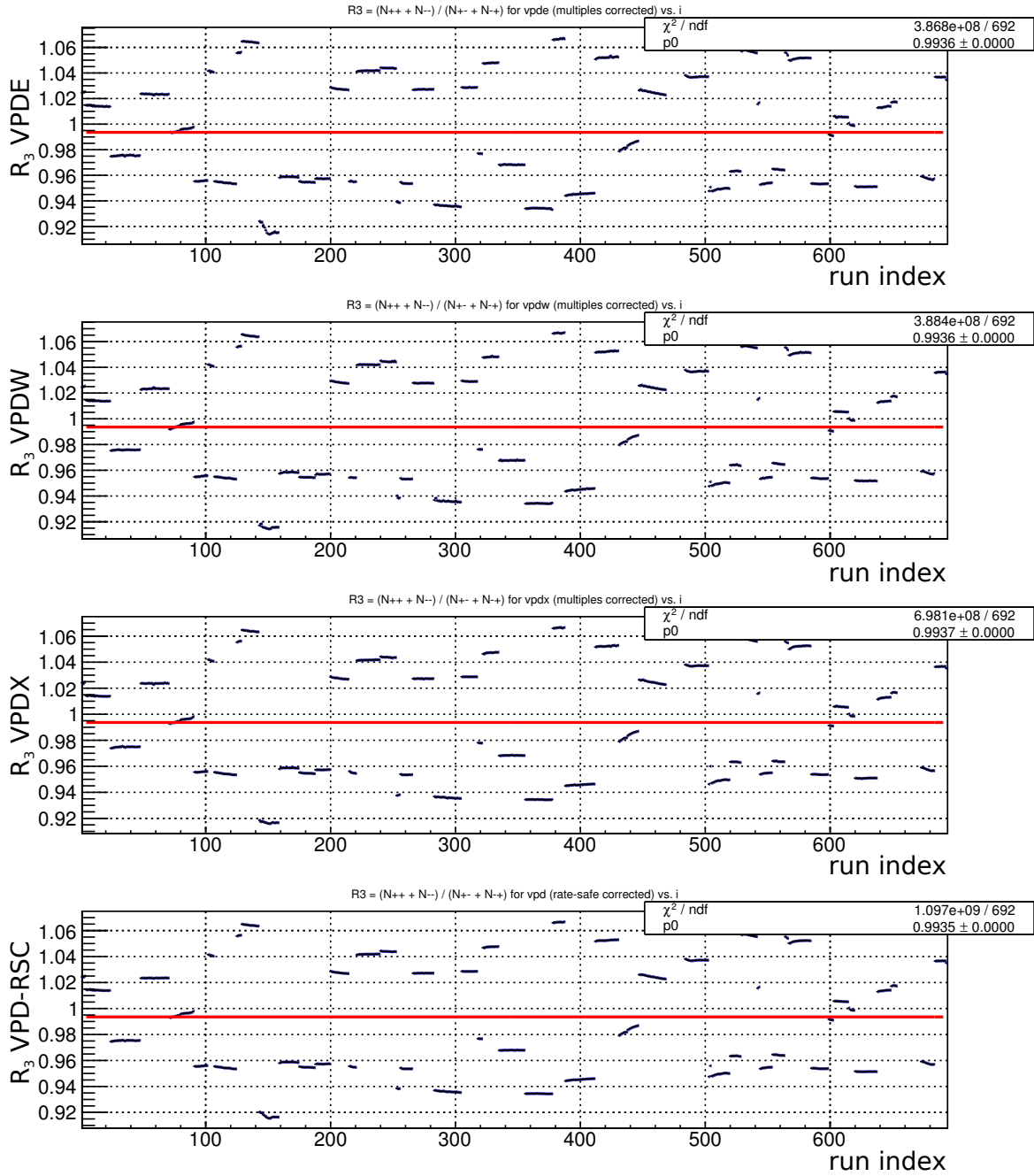


Figure 4.7: R_3 from VPD for Run 12; from top to bottom: CDE corrected E, CDE corrected W, CDE corrected X, rate-safe corrected.

Run 13 VPD R_3 vs. Run Index

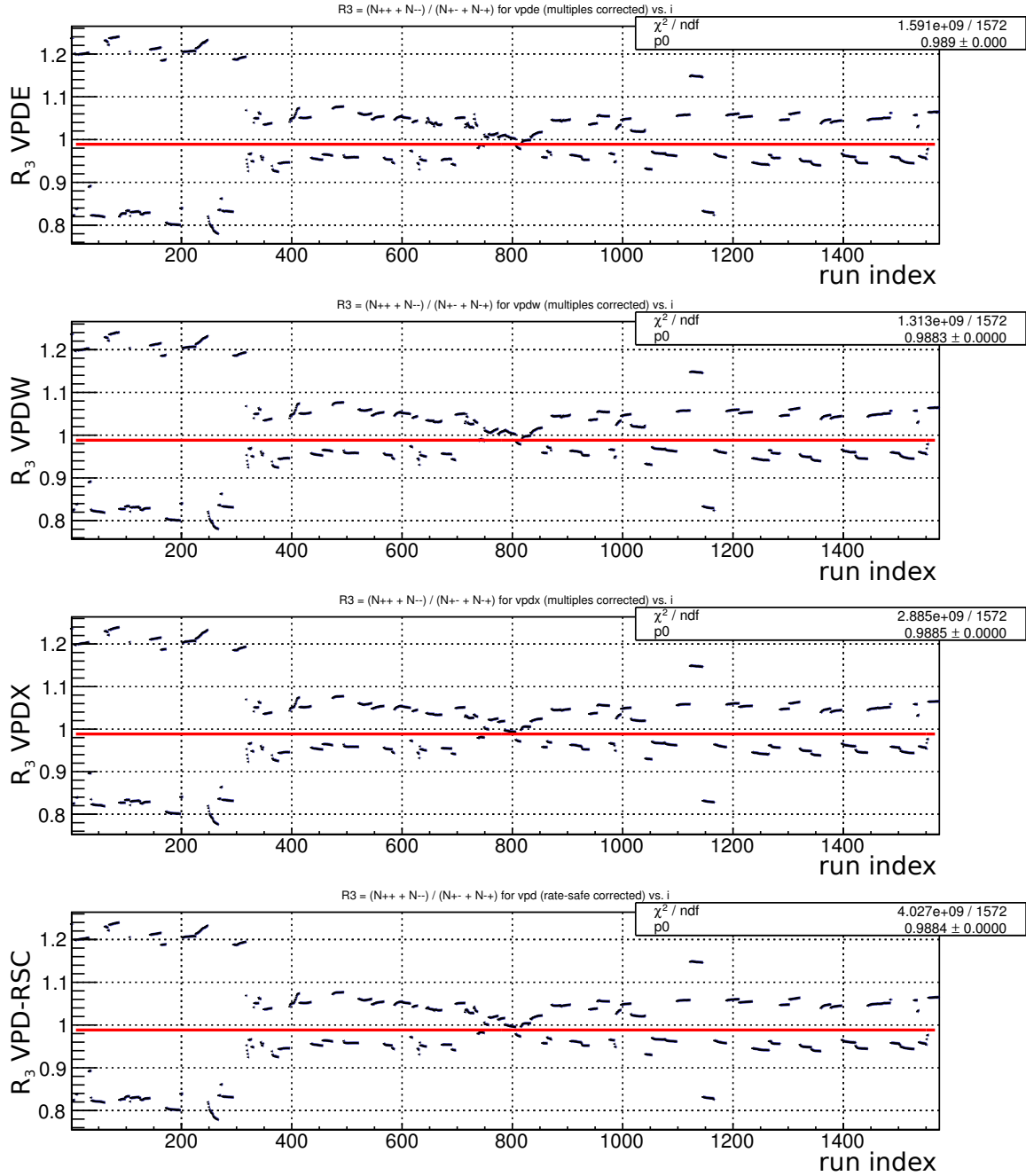


Figure 4.8: R_3 from VPD for Run 13.

4.4 R_3 Cross-Checks

The following cross-checks have been employed to test the consistency of the relative luminosity measurement between the ZDC and VPD, and to compare the two corrections methods:

- Rate-safe and CDF R_3 comparison (figures 4.9 and 4.10)
- ZDC and VPD R_3 comparison (figures 4.11 and 4.12)
- CDF-corrected E and W R_3 comparison (figures F.3 and F.4)
- CDF-corrected E and X R_3 comparison (figures F.5 and F.6)
- CDF-corrected W and X R_3 comparison (figures F.7 and F.8)

Some figures which are a bit superfluous are in appendix F.

One important observation is that, although the difference between the R_3 measurement via the CDF corrections and the rate-safe corrections is rather small, the difference of the R_3 measurement between the ZDC and VPD is about half as big for the rate-safe method as for the CDF corrections method (see figures 4.11 and 4.12, bottom plots). This observation motivates a preference toward the use of the rate-safe corrections method since it provides better consistency between the ZDC and VPD.

In all of the Run 13 cross-check figures, the fills around run index 800 tend to have differences which are larger than normal. An effect called *afterpulsing* is the likely culprit. The afterpulsing effect will be discussed more quantitatively in section 5.1.5, but can be thought of as a “ringing” of the signal pulse which may contribute to signals in subsequent bunch crossings. Consequently, the first few bunch crossings immediately following either abort gap tend to have lower-than-average counts, since there is no afterpulse ringing spilling into them; the number of counts in each subsequent bunch crossing quickly converges to the average as the ringing piles up to a maximum. For these abnormal Run 13 fills, the first bunch crossing coming out of each abort gap had about half of the average counts, and the subsequent crossing had about 80% of the average; on the other hand, a typical fill’s first post-abort-gap bunch crossing would have at least 95% of the average number of counts. We concluded the afterpulsing in these abnormal fills was significant, and ultimately they have been pruned from the $A_{LL}^{\pi^0}$ analysis.

Only runs which have “consistent” R_3 measurements are allowed in the full $A_{LL}^{\pi^0}$ analysis; the cross-check figures are used to define the cuts for such consistent measurements. Furthermore, the duration of the DAQ run, denoted by t , is compared to the ratio between the

total number of bunch crossings in the run and the bunch crossing rate; ideally t should be the same as this ratio, denoted by τ , however sometimes it could be a bit off, so we demand t/τ not be unreasonably high. The exact requirements for a consistent and good relative luminosity measurement are shown in table 4.2, which contains maximum allowed values of each metric given in the first column.

The BBC data have been included in some of these figures. Figures F.3-F.8 reveal that the consistency between the BBCE, BBCW, and BBCX is very poor compared to that for the ZDC and VPD. For reasons which will be discussed later, we have ultimately chosen to use the VPD rate-safe R_3 as the relative luminosity for the $A_{LL}^{\pi^0}$ measurement.

Comparison	Run 12	Run 13
$ R_3^{\text{VPDE}} - R_3^{\text{ZDCE}} $	0.005	0.006
$ R_3^{\text{VPDW}} - R_3^{\text{ZDCW}} $	0.005	0.004
$ R_3^{\text{VPDX}} - R_3^{\text{ZDCX}} $	0.005	0.008
$ R_3^{\text{VPDE}} - R_3^{\text{VPDW}} $	0.003	0.005
$ R_3^{\text{VPDE}} - R_3^{\text{VPDX}} $	0.002	0.006
$ R_3^{\text{VPDW}} - R_3^{\text{VPDX}} $	0.003	0.004
$ R_3^{\text{ZDCE}} - R_3^{\text{ZDCW}} $	0.002	0.002
$ R_3^{\text{ZDCE}} - R_3^{\text{ZDCX}} $	0.004	0.008
$ R_3^{\text{ZDCW}} - R_3^{\text{ZDCX}} $	0.004	0.007
t/τ	1.4	1.8

Table 4.2: Upper limits for various metrics for a DAQ run's R_3 measurement to be self-consistent; DAQ runs which do not satisfy all of these requirements are omitted from analysis.

Run 12 $R_3^{\text{rate-safe}} - R_3^{\text{CDF}}$ vs. Run Index

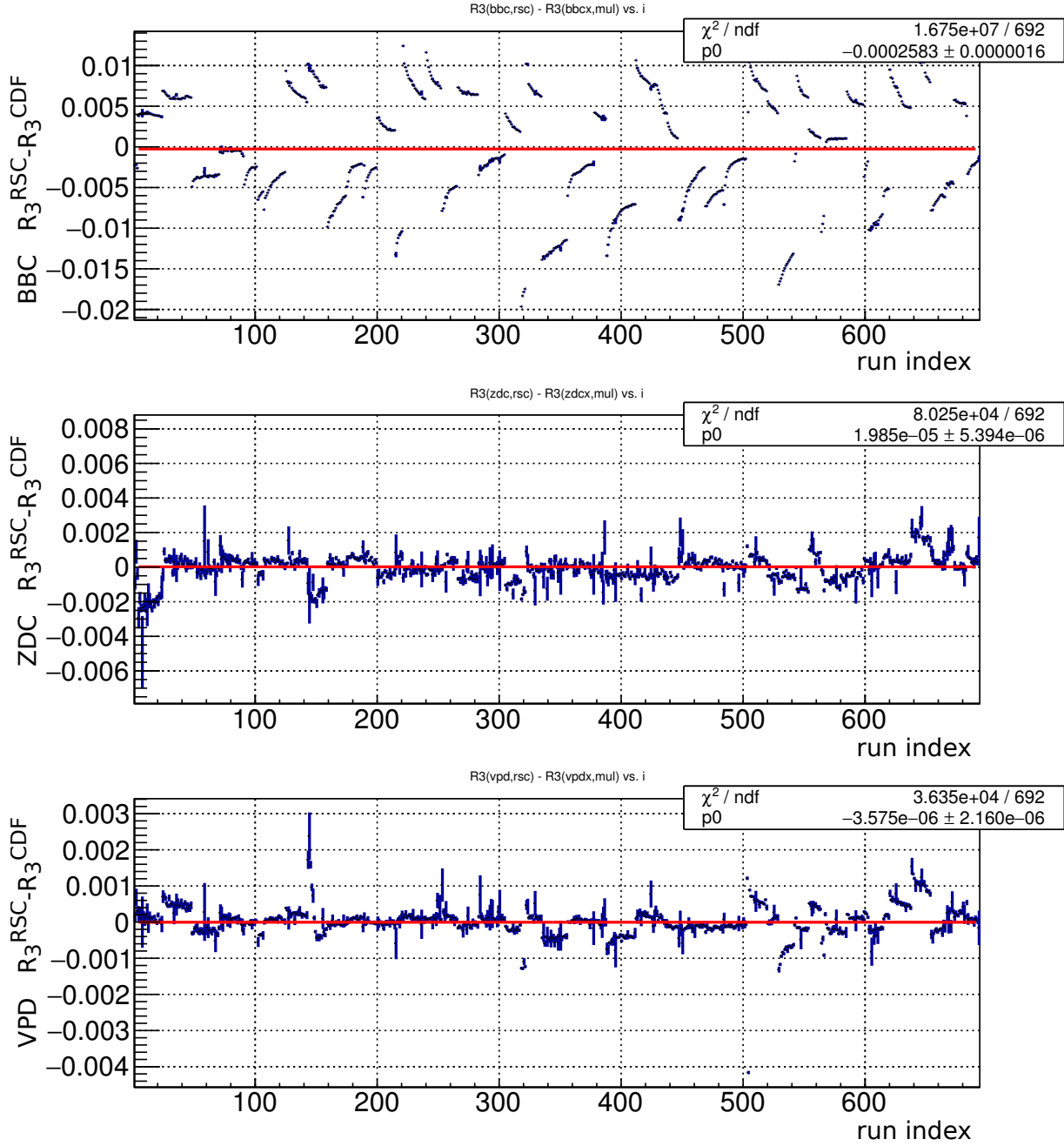


Figure 4.9: Run 12 R_3 from rate-safe corrections method minus R_3 from CDF corrections method vs. run index for BBC (top), ZDC (middle), and VPD (bottom).

Run 13 $R_3^{\text{rate-safe}} - R_3^{\text{CDF}}$ vs. Run Index

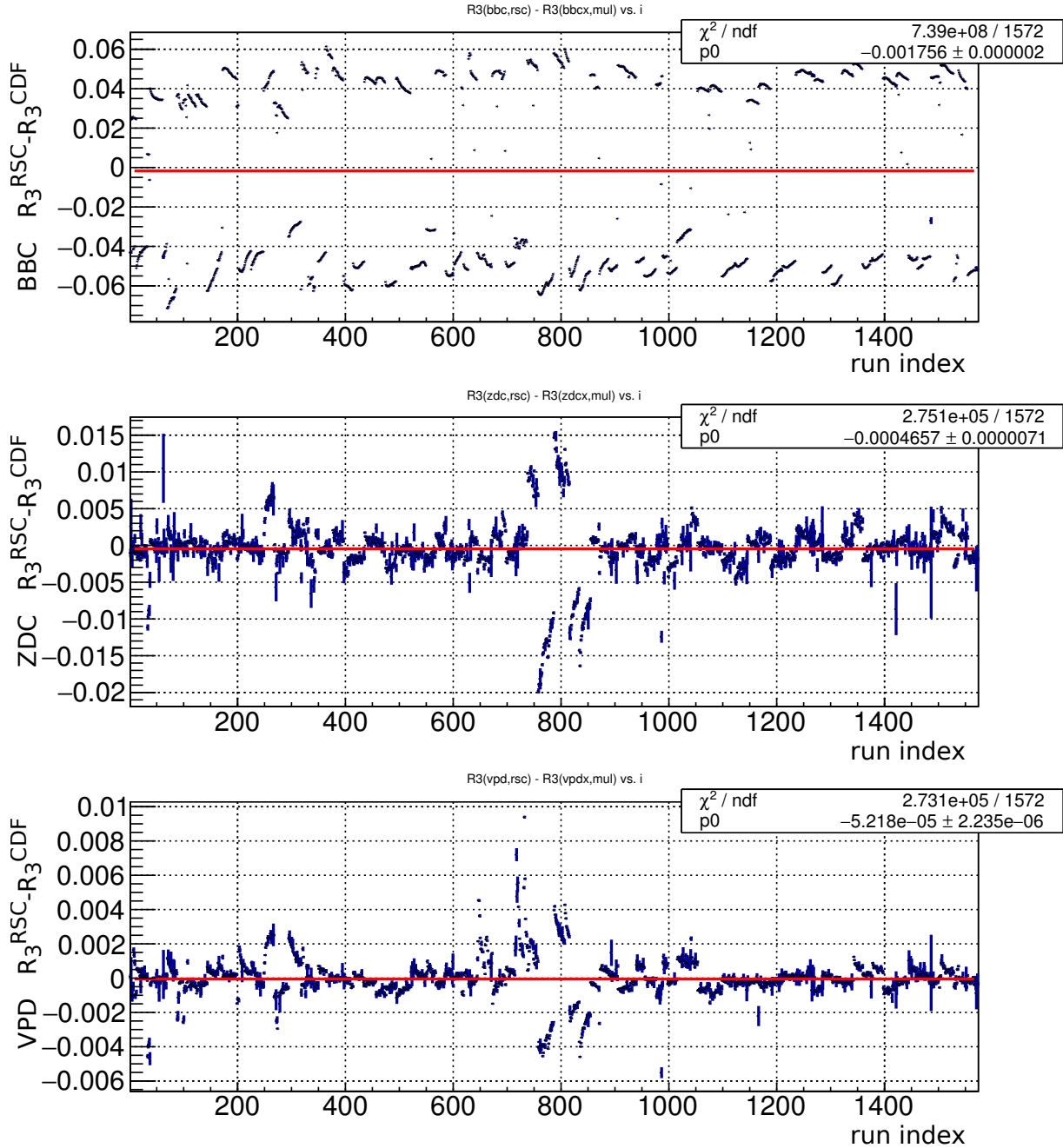


Figure 4.10: Run 13 R_3 from rate-safe corrections method minus R_3 from CDF corrections method vs. run index for BBC (top), ZDC (middle), and VPD (bottom).

Run 12 $R_3^{\text{ZDC}} - R_3^{\text{VPD}}$ vs. Run Index

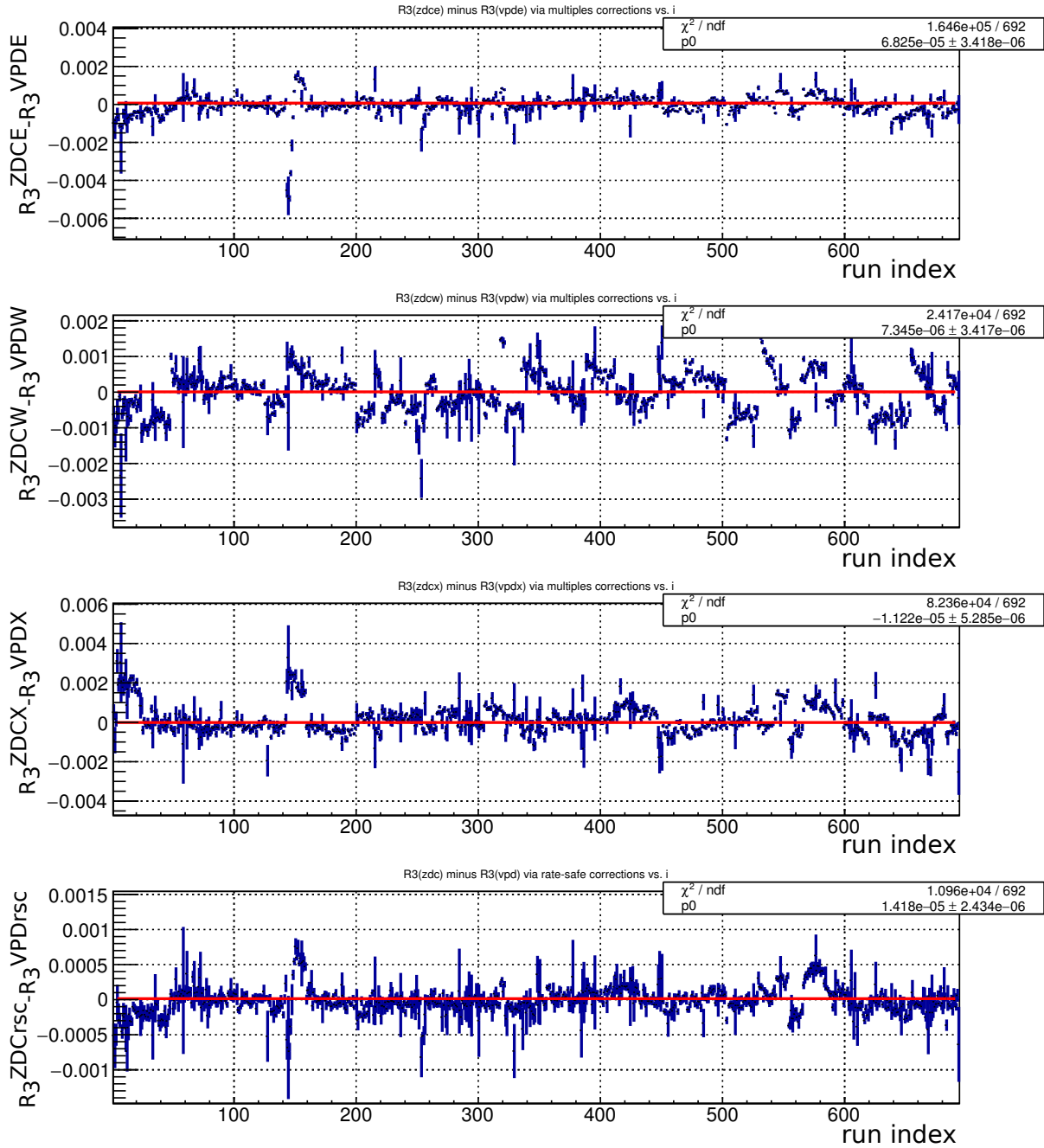


Figure 4.11: Run 12 R_3 from ZDC minus R_3 from VPD vs. run index; in order from top to bottom, the plots are for CDF corrected E, W, X, and rate-safe corrected.

Run 13 $R_3^{\text{ZDC}} - R_3^{\text{VPD}}$ vs. Run Index

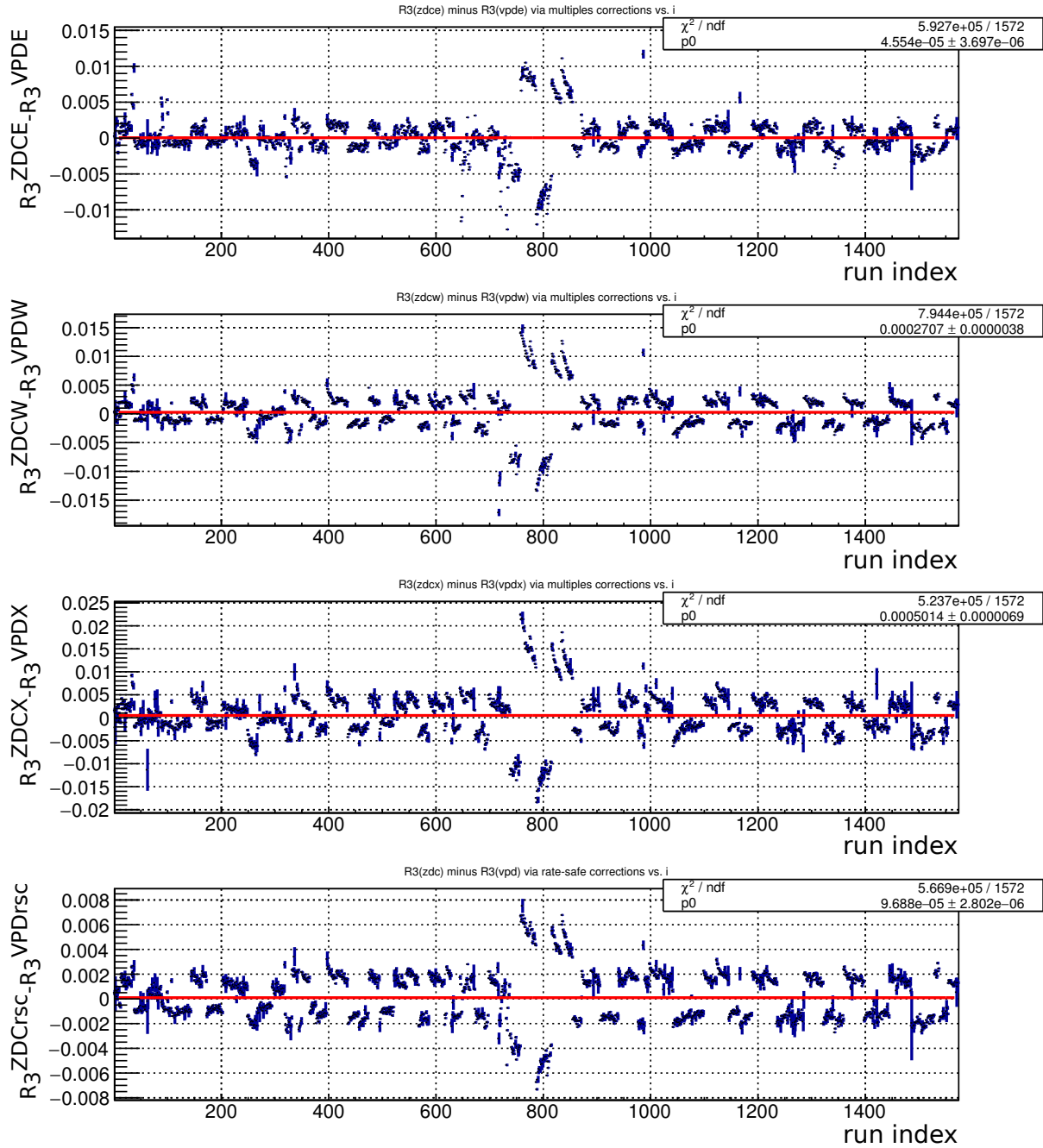


Figure 4.12: Run 13 R_3 from ZDC minus R_3 from VPD vs. run index; in order from top to bottom, the plots are for CDF corrected E, W, X, and rate-safe corrected.

4.5 Miscellaneous

Lastly, we mention a couple of additional details regarding the relative luminosity that do not fit into any of the above discussions.

4.5.1 Anomalous Bunch Crossings

For every fill, the numbers of corrected (and uncorrected) scaler counts were plotted as a function of bunch crossing number. Abort gaps were verified and any bunch crossings that had an anomalously low number of counts were omitted from the relative luminosity computation. Bunch crossings which had undefined spin were, by default, also omitted; this includes abort gaps as well as bunch crossings 69 and 70 for the first few fills analyzed in Run 13.

Furthermore, for Run 13 fills 17512–17520, the first two bunch crossings coming out of each abort gaps had somewhat lower counts. These bunches were not filled with the normal number of protons, according to the RHIC wall-current monitors, and were also removed from analysis. Any other bunch crossings which had abnormally low luminosities were also removed. Omitting bunch crossings from the relative luminosity analysis in turn omits their FMS π^0 s from the $A_{LL}^{\pi^0}$ analysis, while also greatly improving all of the aforementioned consistency metrics.

4.5.2 N_{bx} vs. Bunch Crossing

When plotting the number of bunch crossings N_{bx} as a function of bunch crossing number, an unexpected sigmoid-type function is observed. See figure 4.13 for an example, where for each bunch crossing, we plot the ratio of its N_{bx} to N_{bx} in bunch crossing zero. This effect is negligibly small in the context of a relative luminosity analysis; it is on the order of 2×10^{-4} and enters the relative luminosity analysis via the corrections equations (both CDF and rate-safe). It was finally solved near the beginning of Run 15: the issue was in the bunch counters as an “extra revolution tick reset.” After the fix, a typical plot shows a spike at bunch crossing 0 coincident with the start up time for the DAQ run, as well as a step of one count at the bunch crossing where the DAQ run ended. This issue is completely negligible for Runs 12 and 13, however.

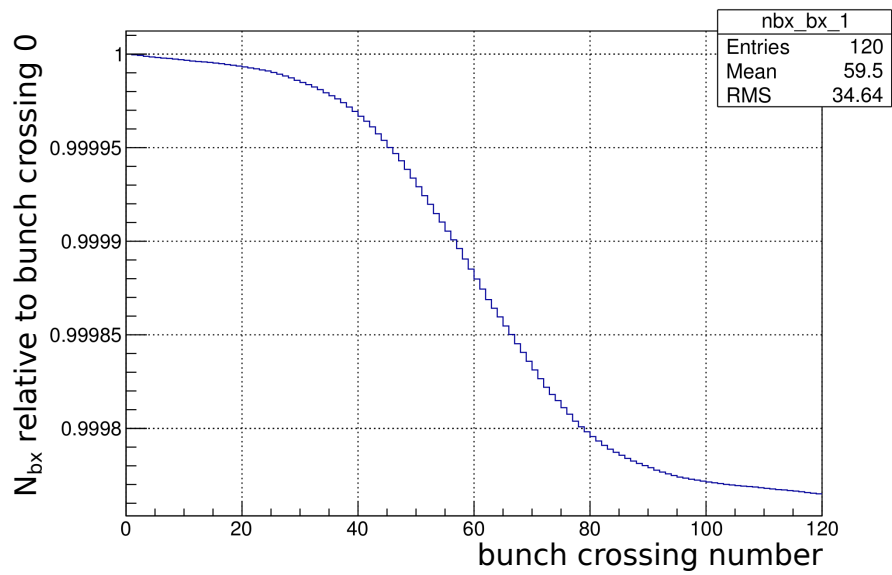


Figure 4.13: Relative N_{bx} vs. bunch crossing number for an example run, showing the typical sigmoid behavior.

Chapter 5

Systematic Uncertainties

The overall uncertainty on $A_{LL}^{\pi^0}$ and on p_T , the kinematic variable in terms of which the $A_{LL}^{\pi^0}$ measurement is presented, must be assessed. This chapter presents systematic uncertainties on $A_{LL}^{\pi^0}$ which come from the relative luminosity and from a nonzero transverse component in the polarization, followed by a determination of the overall systematic uncertainty on p_T , which comes from energy, position, and vertex uncertainties.

5.1 Relative Luminosity Systematic

The dominant systematic uncertainty on $A_{LL}^{\pi^0}$ comes from the relative luminosity determination.¹ Three schemes for determining this systematic have been explored: via direct comparison between VPD and ZDC, via scaler asymmetries from bunch fitting, and via scaler subsystem self-consistency through transverse single-spin asymmetries. Additionally, A_{LL} as determined using R_3 from the VPD was compared to that from the ZDC.

Given the representation of A_{LL} in terms of yield and relative luminosity R_3 as in equation 1.29, one can propagate the uncertainty of R_3 , denoted Δ_{R_3} , to an uncertainty on A_{LL} :

$$\Delta_{A_{LL}}^2 = \left(\frac{\partial A_{LL}}{\partial R_3} \right)^2 \Delta_{R_3}^2 = \left(\frac{2(N_{++} + N_{--})(N_{+-} + N_{-+})}{P_B P_Y [(N_{++} + N_{--}) + R_3(N_{+-} + N_{-+})]} \right)^2 \Delta_{R_3}^2. \quad (5.1)$$

With the approximation $N_{++} + N_{--} \approx R_3(N_{+-} + N_{-+})$, the systematic uncertainty becomes

$$\Delta_{A_{LL}} \approx \frac{1}{2} \cdot \frac{1}{P_B P_Y} \cdot \frac{\Delta_{R_3}}{R_3}. \quad (5.2)$$

¹This is a *shift* systematic uncertainty, which could additively shift the $A_{LL}^{\pi^0}$ values higher or lower. There is also a *scale* systematic uncertainty from the polarization, which affects $A_{LL}^{\pi^0}$ multiplicatively and will be discussed in section 6.2.1; however, since the measured $A_{LL}^{\pi^0}$ values are close to zero, this scale systematic does not matter as much as any shift systematic does.

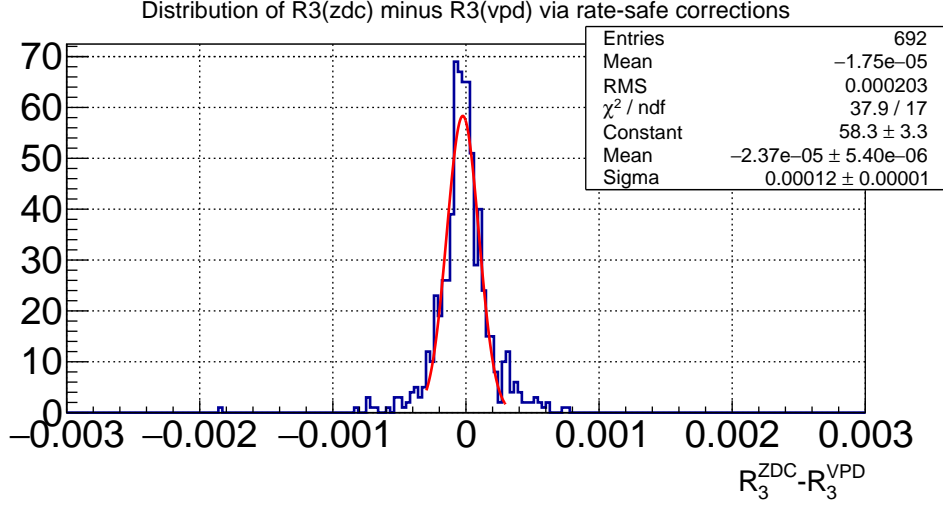


Figure 5.1: Run 12 rate-safe corrected $R_3^{\text{ZDC}} - R_3^{\text{VPD}}$ distribution with Gaussian fit.

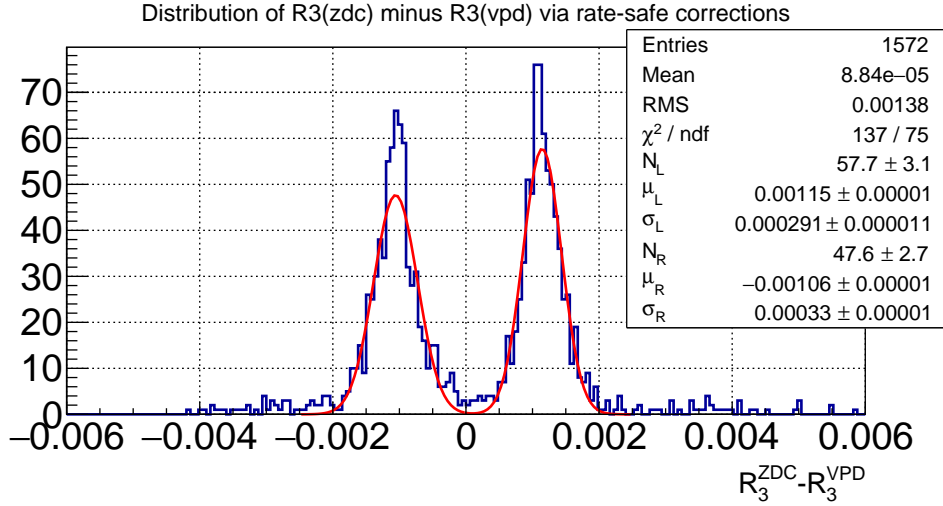


Figure 5.2: Run 13 rate-safe corrected $R_3^{\text{ZDC}} - R_3^{\text{VPD}}$ distribution with two Gaussian fits.

5.1.1 Direct VPD and ZDC Comparison: Δ_{R_3} Method

One way to obtain a systematic uncertainty is to simply compare the R_3 value obtained from the ZDC to that obtained from the VPD: we simply define Δ_{R_3} as $R_3^{\text{ZDC}} - R_3^{\text{VPD}}$. Figures 5.1 and 5.2 show the value of Δ_{R_3} for Runs 12 and 13, respectively. For Run 12, the RMS of the distribution is 2.0×10^{-4} and the standard deviation according to the Gaussian fit is 1.2×10^{-4} . Run 13, on the other hand, shows a bimodal distribution with standard deviations 2.9×10^{-4} for the lower peak and 3.3×10^{-4} for the higher peak and an overall RMS of 1.4×10^{-3} .

It turns out that the two separate Δ_{R_3} peaks in Run 13 correspond to two different

spin pattern sets (see section 5.1.3.2, figures 5.3 and 5.4 for the 8 overall spin patterns for each Run). From the perspective of double-spin asymmetries, there were two *classes* of spin patterns in each of Run 12 and 13. Denoting a same-helicity bunch crossing as “S” and an opposite-helicity crossing as “O”, the double-spin pattern classes can be represented by listing the double-spin states of the first 8 bunch crossings; we only need to list 8 because the spin of bunch n is equal to that of bunch $n \bmod 8$, for each beam. The pattern classes are listed in table 5.1.

Bunch Crossing # mod 8:	0	1	2	3	4	5	6	7
Run 12 Pattern Class A:	S	O	O	S	O	S	S	O
Run 12 Pattern Class B:	O	S	S	O	S	O	O	S
Run 13 Pattern Class A:	S	S	S	S	O	O	O	O
Run 13 Pattern Class B:	O	O	O	O	S	S	S	S

Table 5.1: Double-Spin Patterns, where “S” denotes same spins and “O” denotes opposite spins.

The main difference between the Runs is that Run 12 alternates between “SOOS” and “OSSO” whereas Run 13 alternates between “SSSS” and “OOOO.” The maximum number of consecutive bunch crossings which have the same double-spin state “S” or “O” is 2 for Run 12 and 4 for Run 13; consequently, any biases introduced by having multiple consecutive bunch crossings with same double-spin state will be enhanced in Run 13 with respect to Run 12. This enhancement would only be seen, however, if there was some information from one bunch crossing spilling over into subsequent bunch crossings. As will be discussed in section 5.1.5, afterpulsing in the scaler systems is a likely culprit and the bimodality of Δ_{R_3} is a consequence.

Equation 5.2 is used to convert Δ_{R_3} into a systematic uncertainty on $A_{LL}^{\pi^0}$. For the polarization, the overall average luminosity-weighted polarization (see section 6.2) from runs used in the $A_{LL}^{\pi^0}$ analysis was used: for Run 12 $P_B = 0.54$ and $P_Y = 0.56$ while for Run 13 $P_B = P_Y = 0.57$. The average VPD R_3 values, used for the denominator of equation 5.2, is 0.9967 for Run 12 and 1.002 for Run 13. For Run 12, we use the standard deviation (σ) from the Gaussian fit as an estimate of Δ_{R_3} ; for Run 13, the standard deviations (σ_L and σ_R) of the two Gaussian distributions are averaged together. The resulting systematic uncertainties are:

- Run 12: $\Delta_{ALL} [\Delta_{R_3}] = \frac{1}{2} \cdot \frac{1}{P_B P_Y} \cdot \frac{\sigma(\Delta_{R_3})}{\langle R_3 \rangle} = 2.1 \times 10^{-4}$
- Run 13: $\Delta_{ALL} [\Delta_{R_3}] = \frac{1}{2} \cdot \frac{1}{P_B P_Y} \cdot \frac{[\sigma_L(\Delta_{R_3}) + \sigma_R(\Delta_{R_3})]/2}{\langle R_3 \rangle} = 4.9 \times 10^{-4}$

5.1.2 Comparison of $A_{LL}^{\pi^0}$ via VPD and ZDC: δ_{ALL} Method

Another idea to obtain a systematic on $A_{LL}^{\pi^0}$ is to compare the nominal values of $A_{LL}^{\pi^0}$ computed using the relative luminosity from the VPD to those from the ZDC. Run 12 has a δ_{ALL} , defined as $A_{LL}^{\pi^0}$ with R_3 from the ZDC minus $A_{LL}^{\pi^0}$ with R_3 from the VPD, on the order of $5\text{--}8 \times 10^{-5}$ whereas Run 13 has a δ_{ALL} on the order of 1.5×10^{-4} . These differences are much smaller than any other method used to determine systematic uncertainties from relative luminosity.

The reason δ_{ALL} is smaller in comparison to the aforementioned systematic uncertainty is because δ_{ALL} is sensitive to the mean of Δ_{R_3} , not its standard deviation. To see this, consider using the maximum likelihood method for determining a value of δ_{ALL} . Following the same maximum likelihood method used for extracting $A_{LL}^{\pi^0}$ (appendix K), the maximum likely δ_{ALL} is

$$\bar{\delta}_{ALL} = \frac{\sum_{i=1}^N \delta_{ALLi} / \sigma_i^2}{\sum_{i=1}^N 1 / \sigma_i^2}, \quad (5.3)$$

where the sums run over DAQ runs and σ_i is the statistical uncertainty on the i th run's δ_{ALL} . Working out the details, one finds that the numerator terms are $\delta_{ALLi} / \sigma_i^2 \propto 1 / \Delta_{R_3}$ and the denominator terms are $1 / \sigma_i^2 \propto 1 / \Delta_{R_3}^2$. Since the numerator terms are proportional to $1 / \Delta_{R_3}$ and Δ_{R_3} is centered around zero, up to means of 1.8×10^{-5} in Run 12 and 9.6×10^{-5} in Run 13, the overall value of δ_{ALL} is expected to be within the same order of magnitude. Ultimately, this δ_{ALL} method has been abandoned as a systematic uncertainty for this analysis.

5.1.3 Intrinsic Scaler Double-Spin Asymmetries: Δ_{SLL} Method

One can also evaluate systematic biases of $A_{LL}^{\pi^0}$ due to the relative luminosity measurement by measuring a possible residual A_{LL} in one scaler detector while using another scaler detector to measure the relative luminosity. This method has been employed in various PHENIX analyses, e.g, as in chapter 4 of [95]. This *scaler asymmetry*, denoted here as S_{LL} , is extracted using the *bunch fitting* technique, which is summarized below; more details are in appendix H.

In order to relate S_{LL} to a systematic uncertainty on $A_{LL}^{\pi^0}$, one must propagate uncertainties on the number of counts in both scaler detectors used in extracting S_{LL} . Referring to the appendix of [33], the systematic uncertainty is simply

$$\Delta_{ALL} \approx \Delta_{SLL}. \quad (5.4)$$

5.1.3.1 Bunch Fitting Algorithm

Consider S_{LL} as an asymmetry in scaler subsystem S measured while using scaler system MB for a “minimum-biased” relative luminosity measurement (it does not have to truly be minimum-biased, it just needs to be another, independent scaler). It is written as

$$S_{LL} = \frac{1}{P_B P_Y} \varepsilon_3 = \frac{1}{P_B P_Y} \frac{(N_S^{++} + N_S^{--}) - R_3^{MB} (N_S^{+-} + N_S^{-+})}{(N_S^{++} + N_S^{--}) + R_3^{MB} (N_S^{+-} + N_S^{-+})}. \quad (5.5)$$

Writing out the relative luminosity R_3^{MB} in terms of yields in MB allows this asymmetry to be expressed as

$$S_{LL} = \frac{1}{P_B P_Y} \frac{(N_S^{++} + N_S^{--}) / (N_{MB}^{++} + N_{MB}^{--}) - (N_S^{+-} + N_S^{-+}) / (N_{MB}^{+-} + N_{MB}^{-+})}{(N_S^{++} + N_S^{--}) / (N_{MB}^{++} + N_{MB}^{--}) + (N_S^{+-} + N_S^{-+}) / (N_{MB}^{+-} + N_{MB}^{-+})}. \quad (5.6)$$

This is just an asymmetry of the ratios of scaler counts from S to MB ; the raw asymmetry can therefore be extracted by minimizing the χ^2 of the following fit ² to the ratio as a function of bunch crossing number:

$$\frac{N_S^i}{N_{MB}^i} = c_3 (1 + h_B^i h_Y^i \cdot \varepsilon_3), \quad (5.7)$$

where the superscripts i indicate a bunch crossing number, $h_B, h_Y \in \{-1, 1\}$ are the initial proton helicities, and $\{c_3, \varepsilon_3\}$ are the fit parameters. The raw asymmetry ε_3 is then divided by the polarization product to obtain S_{LL} , while the fit parameter c_3 is an overall scaling proportional to the overall yield.

5.1.3.2 Scaler Asymmetry Measurement

Because ultimately the $A_{LL}^{\pi^0}$ analysis uses the VPD relative luminosity measurement, this section presents the VPD scaler asymmetry S_{LL} while treating the ZDC as a relative luminosity measurement; in the language of the bunch fitting algorithm this is a bunch fit to the ratio VPD/ZDC yields. The rate-safe corrected data is presented here; it turns out that with the CDF corrections applied, the S_{LL} distribution is more than twice as wide as the distribution derived using rate-safe corrections.

The distribution of S_{LL} was analyzed for each spin pattern separately as well as for all spin patterns for an overall distribution. For each Run, there were 4 different spin patterns for each beam, numbered 1–4. Pattern 1 is the opposite of pattern 2, and pattern 3 is the

²This is another standard way to think about asymmetries. To see this, consider the raw double-spin asymmetry $\varepsilon_{LL} = (N_{++} + N_{--} - N_{+-} - N_{-+})/N$ and solve for a particular helicity’s yield in the form of $N_{h_B h_Y} = c(1 + h_B h_Y \varepsilon_{LL})$. Plugging in, for example $h_B = h_Y = +1$, we get $N_{++} = 2cN_{++}/N$, so the constant of proportionality is $c = N/2$. See appendix D for more on thinking about asymmetries in this way.

opposite of pattern 4. From these beam bunch patterns, 8 different combinations were used to form the bunch crossing patterns, for example, bunch pattern 1 colliding with pattern 3. Figures 5.3 and 5.4 show the 8 different bunch crossing spin patterns used in Runs 12 and 13, respectively, where the colors are used in the S_{LL} distributions presented below. The B and Y brackets represent the spin states of the first 8 bunch crossings, while the numerical subscript represents which of the 4 bunch patterns are used. The double-spin pattern classes in terms of Ss and Os is also given in parentheses; 4 bunch-crossing spin patterns are contained in each class, as mentioned in table 5.1.

Figures 5.5 and 5.6 show the S_{LL} distributions, where the overall distribution is in bold and the distributions for each spin pattern are colored according to figures 5.3 and 5.4. Run 12 shows a single-mode distribution and all spin patterns agree; it is therefore fit with a single Gaussian with normalization constant N , mean μ , and standard deviation σ . Run 13, on the other hand, shows a bimodal distribution, revealing that S_{LL} is correlated to spin pattern; this is the same correlation seen in the aforementioned Δ_{R_3} distribution. This distribution is fit to the sum of two Gaussian functions, where the parameters are given subscripts L and R for left and right. Pattern class OOOOSSSS tends to have positive S_{LL} (mean $\mu_R = 1.6 \times 10^{-3}$) while pattern class SSSSOOOO tends to have negative S_{LL} (mean $\mu_L = -1.6 \times 10^{-3}$). The widths of the two classes agree: $\sigma_L = 4.0 \times 10^{-4}$ and $\sigma_R = 3.9 \times 10^{-4}$.

The $A_{LL}^{\pi^0}$ systematic uncertainty is, according to equation 5.4, approximately equal to $\Delta_{S_{LL}}$. Because S_{LL} is basically a double-spin asymmetry in the VPD, which could contribute to the $A_{LL}^{\pi^0}$ measurement, the absolute value of the mean S_{LL} is added to the standard deviation (from the fit) as a conservative estimate for the overall $\Delta_{A_{LL}}$. As in the Δ_{R_3} method, the two standard deviations from Run 13 are averaged together. The resulting systematic uncertainties are:

- Run 12: $\Delta_{A_{LL}} [\Delta_{S_{LL}}] = \sigma (S_{LL}) + |\langle S_{LL} \rangle| = 1.9 \times 10^{-4}$
- Run 13: $\Delta_{A_{LL}} [\Delta_{S_{LL}}] = \frac{\sigma_L (S_{LL}) + \sigma_R (S_{LL})}{2} + |\langle S_{LL} \rangle| = 4.1 \times 10^{-4}$

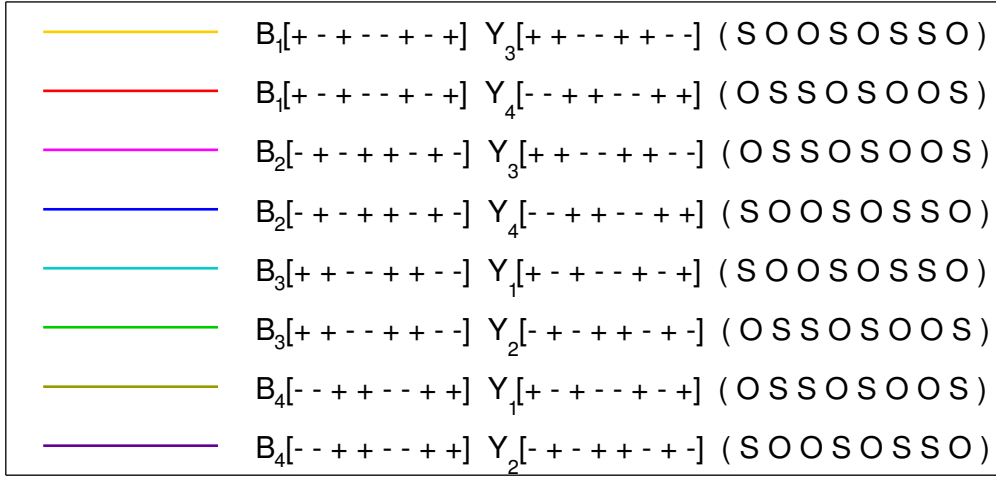


Figure 5.3: Run 12 spin patterns legend.

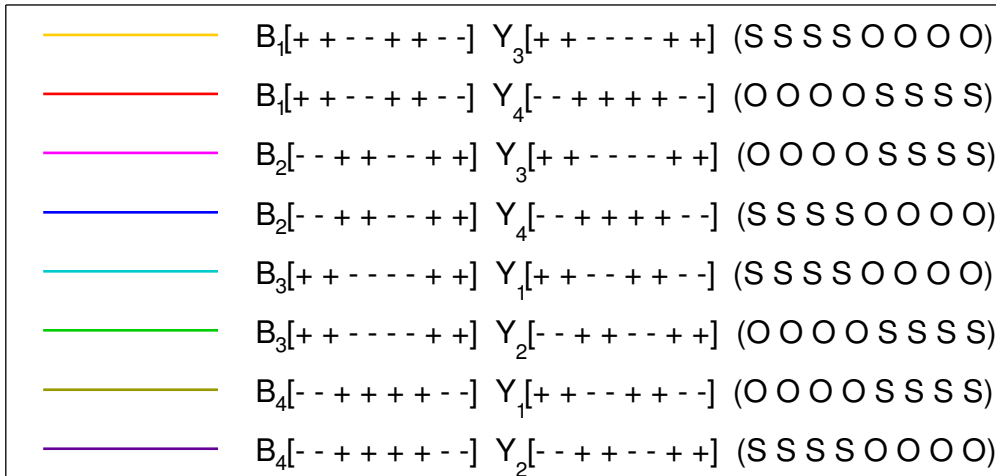


Figure 5.4: Run 13 spin patterns legend.

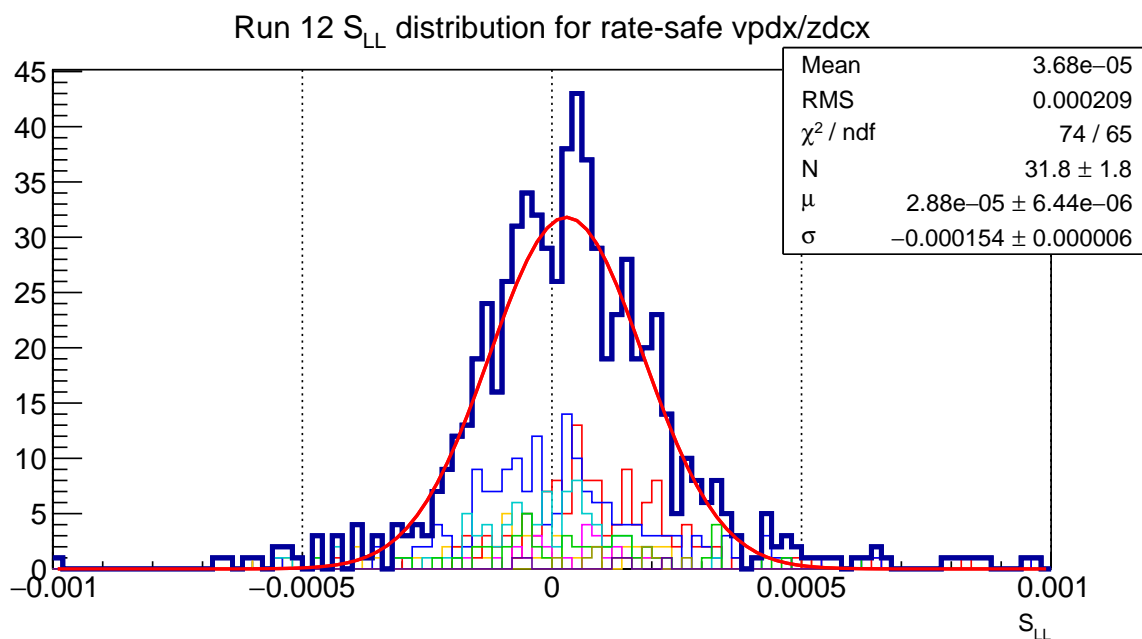


Figure 5.5: Run 12 S_{LL} for VPD while treating ZDC as a relative luminosity measurement.

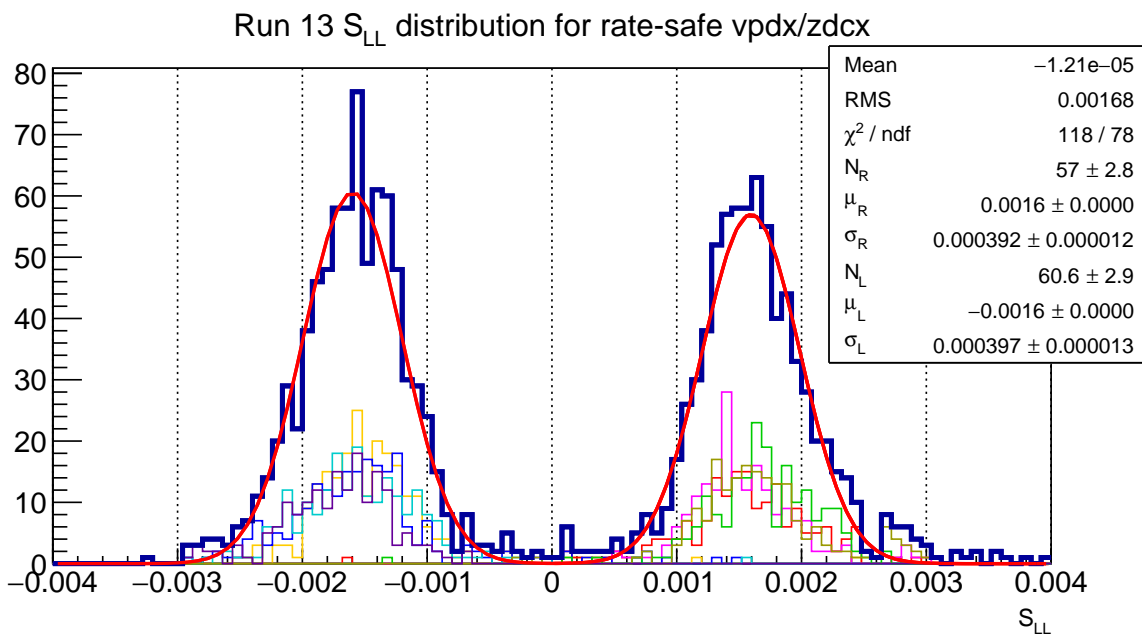


Figure 5.6: Run 13 S_{LL} for VPD while treating ZDC as a relative luminosity measurement.

5.1.4 Scaler Self-Consistency via A_N Cross Ratio: Δ_{D_N} Method

A completely alternative method to compute a systematic uncertainty from the relative luminosity is to measure the transverse single-spin asymmetry A_N in a scaler detector by two different methods: the *cross-ratio method*, which *does not* need a relative luminosity, and the standard method (similar to measuring A_{LL}), which *does* need a relative luminosity. The cross-ratio A_N can be compared to the A_N measured using the relative luminosity; a difference between the measurements indicates how much the asymmetry is biased by the relative luminosity.

The cross-ratio method (see, for example, [56]) exploits the following azimuthal symmetry in order to cancel out the need for a relative luminosity measurement; this technique cannot be done for any double-spin asymmetry. Let $N_{\uparrow(\downarrow)}$ be the π^0 yield for incoming spin-up(down) protons and let $\mathcal{L}_{\uparrow(\downarrow)}$ be the luminosity. Let Ω be the product of efficiency and acceptance for a detector. Now assume the detector is split left and right, and denote their yields, luminosities, and acceptance times efficiency by a superscript L for left and R for right. The assumed azimuthal symmetry is about a 180° rotation about the beam axis:

$$\frac{N_{\downarrow}^L}{\Omega^L \mathcal{L}_{\downarrow}} = \frac{N_{\uparrow}^R}{\Omega^R \mathcal{L}_{\uparrow}} \text{ and } \frac{N_{\uparrow}^L}{\Omega^L \mathcal{L}_{\uparrow}} = \frac{N_{\downarrow}^R}{\Omega^R \mathcal{L}_{\downarrow}}. \quad (5.8)$$

By writing out the expression for A_N for both the L and R halves of the detector and uniting them via this symmetry, one can express A_N as the so-called *cross-ratio*, which is independent of a relative luminosity:

$$A_N^{(\text{cross-ratio})} = \frac{1}{P} \cdot \frac{\sqrt{N_{\uparrow}^L N_{\downarrow}^R} - \sqrt{N_{\uparrow}^R N_{\downarrow}^L}}{\sqrt{N_{\uparrow}^L N_{\downarrow}^R} + \sqrt{N_{\uparrow}^R N_{\downarrow}^L}}, \quad (5.9)$$

where P is the polarization of the proton beam used to compute A_N .

A value of A_N can also be determined using the associated relative luminosity (R_1 for the yellow beam and R_2 for the blue beam, as defined in appendix B). Denoting the relative luminosity as $r \in \{R_1, R_2\}$, consider the difference of the A_N values:

$$D_N := A_N^{(\text{cross-ratio})} - \frac{1}{P} \cdot \frac{N_{\uparrow} - r N_{\downarrow}}{N_{\uparrow} + r N_{\downarrow}}. \quad (5.10)$$

The uncertainty on r propagates as

$$\Delta_{D_N} = \left| \frac{\partial D_N}{\partial r} \right| \cdot \Delta_r = \frac{1}{2} \cdot \frac{1}{P} \cdot \frac{\Delta_r}{r}. \quad (5.11)$$

The uncertainty on a measurement of D_N therefore is sensitive to a relative luminosity uncertainty, Δ_r/r ; however, this r is a relative luminosity used for a *single*-spin asymmetry. Since A_N is not sensitive to polarization, a measurement of Δ_{D_N} is sensitive to how well the relative luminosity is in general, and can be used for A_{LL} as well, which just uses different combinations of incoming spin-states than A_N does. To see this more a bit more clearly, consider the statistical uncertainties on the relative luminosity (see appendix B); they are

$$\begin{aligned}\Delta_{R_1} &= \sqrt{\frac{(\sigma_{-+}^2 + \sigma_{++}^2) (\mathcal{L}_{--} + \mathcal{L}_{+-})^2 + (\sigma_{--}^2 + \sigma_{+-}^2) (\mathcal{L}_{-+} + \mathcal{L}_{++})^2}{(\mathcal{L}_{--} + \mathcal{L}_{+-})^4}}, \\ \Delta_{R_2} &= \sqrt{\frac{(\sigma_{+-}^2 + \sigma_{++}^2) (\mathcal{L}_{--} + \mathcal{L}_{-+})^2 + (\sigma_{--}^2 + \sigma_{-+}^2) (\mathcal{L}_{+-} + \mathcal{L}_{++})^2}{(\mathcal{L}_{--} + \mathcal{L}_{-+})^4}}, \\ \Delta_{R_3} &= \sqrt{\frac{(\sigma_{--}^2 + \sigma_{++}^2) (\mathcal{L}_{-+} + \mathcal{L}_{+-})^2 + (\sigma_{-+}^2 + \sigma_{+-}^2) (\mathcal{L}_{--} + \mathcal{L}_{++})^2}{(\mathcal{L}_{-+} + \mathcal{L}_{+-})^4}},\end{aligned}$$

where σ_{ab} is the statistical error on \mathcal{L}_{ab} . If the four luminosities are equal, then although the relative luminosities would all be equal to one, their errors would be equal to each other. Under this assumption, we would therefore have $\Delta_r/r \approx \Delta_{R_3}/R_3$.

Using the above assumption, equation 5.11 is similar to equation 5.2. If we assume the polarization of each beam is the same, P , then comparing equation 5.11 and 5.2 reveals the approximating relation

$$\Delta_{A_{LL}} \approx \frac{1}{P} \Delta_{D_N}. \quad (5.12)$$

For extracting A_{LL} , the VPD is used for a relative luminosity; therefore, D_N is measured in the VPD. The yields which go into the computation of D_N were taken from the VPD PMT scaler boards, which provide the azimuthal (and pseudorapidity) segmentation needed to compute an A_N . The R_1 and R_2 relative luminosity values appropriate for east and west were taken from the VPD rate-safe corrected counts. The ZDC-SMD detector, which has hodoscope-like segmentation (described in section 5.2), was also used to extract a value of D_N ; the D_N distributions in the ZDC are much wider than those in the VPD, however. The VPD is ultimately more self-consistent than the ZDC, and this is the primary reason the VPD is used for the relative luminosity in the overall $A_{LL}^{\pi^0}$ analysis.

In Run 12, the VPD PMTs were not read-out in any scaler system; only the overall VPD scaler counts were read-out. In Run 13, however, VPD PMT scaler counts were read-out, and thus the focus of this self-consistency analysis is constrained to the Run 13 VPD. Figure 5.7 shows D_N distributions for the east and west VPD systems. The dependence of D_N on spin patterns was also assessed by plotting the distributions for each spin pattern listed in figure 5.4, where the pattern number here is defined as 10 times the blue pattern number

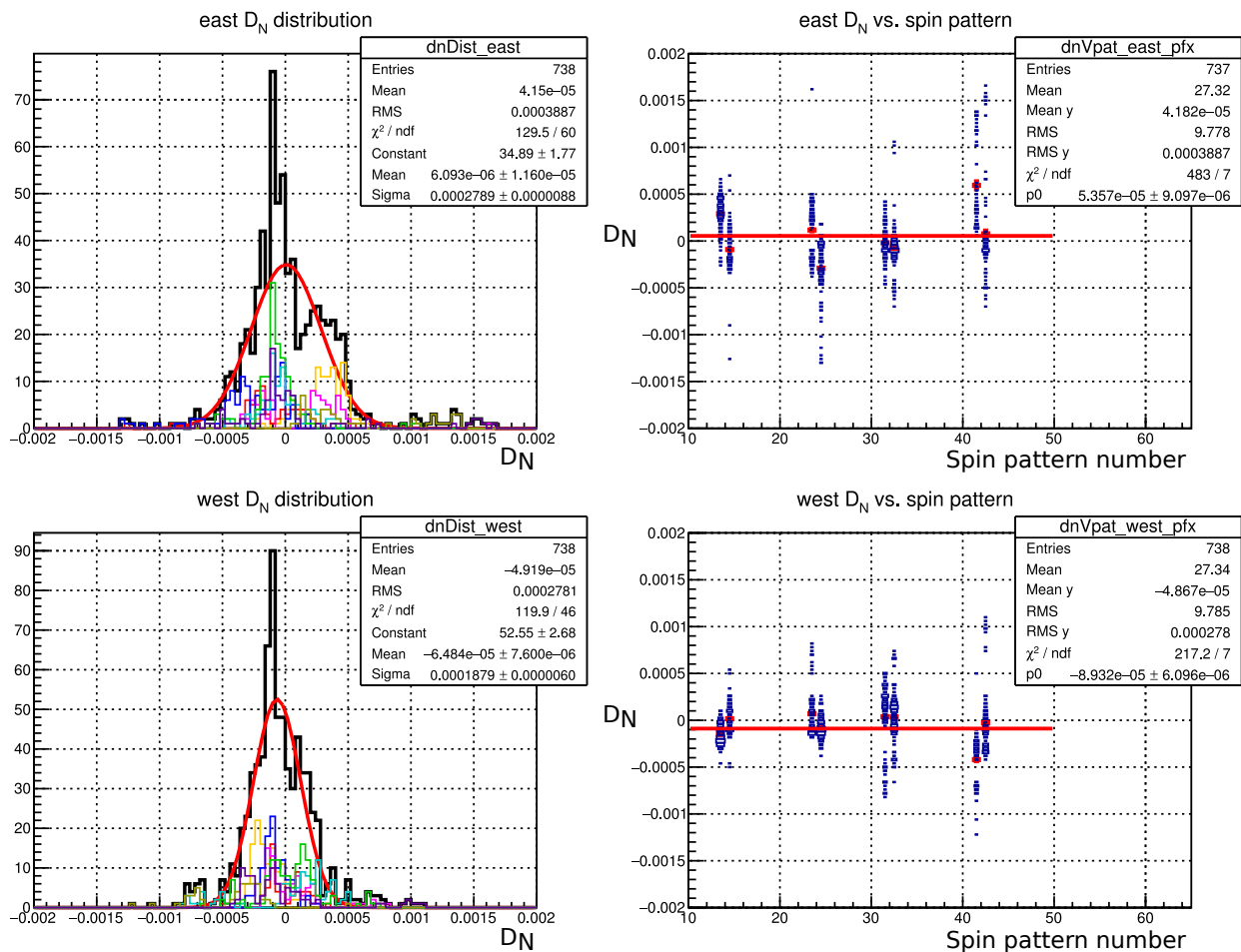


Figure 5.7: Top row is east VPD D_N data and bottom row is west VPD. Left column: D_N distribution; black is full distribution and the colors are for each spin pattern (legend in figure 5.4). A Gaussian fit to the total distribution is also drawn. Right column: D_N vs. spin pattern number; red crosses within each spin pattern indicate the pattern's D_N means and errors, and the red horizontal line is an overall fit to those means.

plus the yellow pattern number. In the east VPD, one can observe some mild correlation with spin patterns; this correlation is not nearly as strong in the west VPD, however.

The RMS of the east VPD D_N is 3.9×10^{-4} and for the west is 2.8×10^{-4} . The standard deviations from the Gaussian fits are 2.8×10^{-4} and 1.9×10^{-4} for the east and west, respectively; the higher width in the east VPD is attributed to its mild spin pattern correlation.

From equation 5.12, in order to obtain a systematic on $A_{LL}^{\pi^0}$ one needs to multiply by an additional factor of $1/P_B$ or $1/P_Y$; the correct factor is the polarization which is *not* already multiplied in D_N , e.g., use Δ_{D_N}/P_B for the east systematic since $D_N^{\text{east}} \propto 1/P_Y$. By using standard deviation from the fit as Δ_{D_N} , we have

- East: $\Delta_{ALL} [\Delta_{DN}] = \frac{\Delta_{DN}^{\text{east}}}{P_B} = \frac{2.8 \times 10^{-4}}{0.57} = 4.9 \times 10^{-4}$
- West: $\Delta_{ALL} [\Delta_{DN}] = \frac{\Delta_{DN}^{\text{west}}}{P_Y} = \frac{1.9 \times 10^{-4}}{0.57} = 3.3 \times 10^{-4}$
- Average over East and West: $\langle \Delta_{ALL} [D_N] \rangle = 4.1 \times 10^{-4}$

5.1.5 Correlations of Run 13 Δ_{R_3} and S_{LL} with Spin Patterns

The exact origin of the Run 13 dependence of Δ_{R_3} and S_{LL} on spin patterns remains under investigation. One possible cause of a correlation with spin patterns is scaler afterpulsing. Afterpulsing was introduced in section 4.4, and to look for it, we consider bunch crossing distributions, defined as the number of (rate-safe corrected) scaler counts for each bunch crossing. We take a true bunch crossing distribution from scaler data and assume it is the convolution of a scaler signal pulse with an ideal bunch crossing distribution (the kernel). Applying a deconvolution algorithm reveals the true signal pulse shape, including any afterpulsing.

Figure 5.8 shows bunch crossing distributions for all data in Run 13, normalized over all bunch crossings. The two usual abort gaps appear in bunch crossings 31–39 and 111–119; the nonzero number of counts in the abort gaps is likely from beam background, as well as some residual afterpulsing. Furthermore, about 25% of the data had bunch crossings 69 and 70 empty, creating a divot in the distributions. The ideal bunch crossing distribution is drawn in the bottom right panel of figure 5.8, and it assumes that each bunch crossing had a single collision and the bunches were also filled ideally. This ideal bunch crossing distribution will be referred to as the kernel distribution; its abort gaps have zero counts and its divot at bunch crossings 69–70 is set at 75% of the typical filled bunch crossing.

The first few bunch crossings after each abort gap, denoted as the *post-abort* bunch crossings, show a slow rise in the number of counts; this is much more evident in the BBC than in the ZDC or VPD. Furthermore, the BBC shows a complementary fall-off of the number of counts in the abort gaps (this is also seen in the ZDC and VPD, but there the abort gap counts are down by a factor of 10,000 from the nominal number of counts). These abort gap and post-abort features are also seen in and after the 69–70 divot.

The most likely reason for this post-abort gap bunch crossing behavior is claimed to be afterpulsing somewhere in the scaler systems. In order to explore a possible afterpulsing effect, first let the pulse seen by scaler phototubes be $P(t)$, where t represents time and can be mapped to bunch crossing number b by multiplying by the bunch crossing rate (RHIC clock frequency). Let the pulse shape be defined by a single pulse confined to one bunch

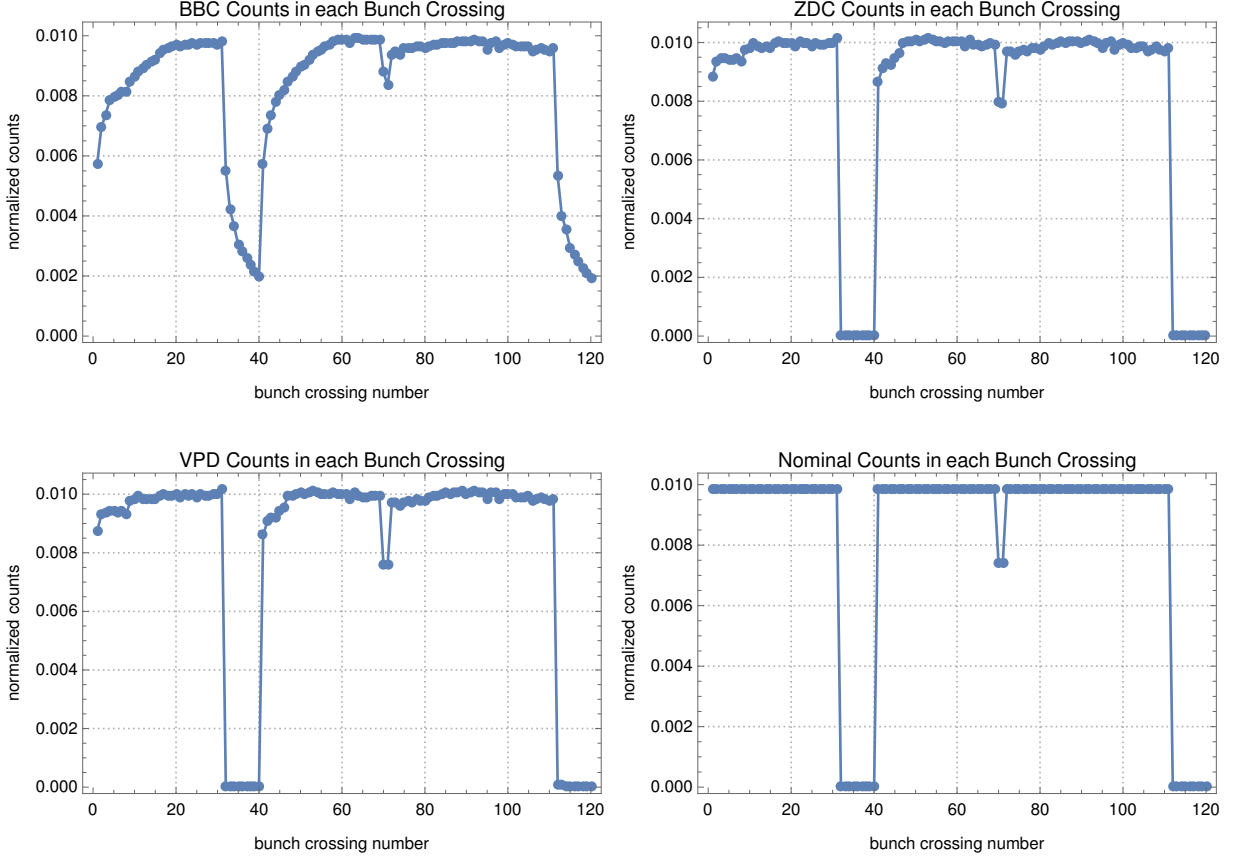


Figure 5.8: Rate-safe corrected number of counts vs. bunch crossing number for the BBC (top left), ZDC (top right), VPD (bottom left), and for an ideal scaler (bottom right). All plots are normalized.

crossing, plus an afterpulse $A(b)$:

$$P(b) = \frac{1}{\sigma_P \sqrt{2\pi}} \cdot e^{-b^2/2\sigma_P^2} + A(b), \quad (5.13)$$

where σ_P is sufficiently small for the pulse to be confined to within one bunch crossing. Let $K(b)$ be the kernel distribution as defined above; this is the distribution one would see if $P(t)$ were ideal and there was no afterpulsing. The number of scaler counts per bunch crossing, denoted $N(b)$, is then modelled as a convolution of the pulse shape and the kernel distribution:

$$N(b) = (K * P)(b) = \int_{-\infty}^{\infty} d\beta K(\beta)P(b - \beta). \quad (5.14)$$

In an attempt to determine what might have been the original $P(b)$ for a given $N(b)$, several different deconvolution algorithms were tried. Most of them returned similar results, but with varying levels of noise and artifacts coming from noise in the $N(b)$ data, from the

assumption of $K(b)$ and its comparison to the actual bunch filling quality, and from the deconvolution algorithm itself. The algorithm which resulted with $P(t)$ shapes with the least amount of noise was the Tikhonov regularization method in Mathematica; more details can be found in the Mathematica documentation for the functions `ListDeconvolve` [96] and `ImageDeconvolve` [97].

The deconvolved $P(b)$ results are shown in figure 5.9 for each of the three scaler systems, along with the deconvolved nominal pulse in order to test the algorithm. The horizontal axis is bunch crossing number, but the pulse begins at bunch crossing number 60; this is just a consequence of the deconvolution algorithm and hence the horizontal axis numbers can be interpreted as the number of bunch crossings after the pulse, plus 60. Figure 5.10 shows a zoom in of the noise level on the deconvolved nominal pulse, which is at the 1% level. Clearly the BBC shows some afterpulsing effect, since $P(b)$ takes ~ 15 bunch crossings to settle to zero; the ZDC and VPD pulses decay to zero after 1 or 2 bunch crossings. The nominal pulse is as expected: a narrow pulse within bunch crossing 61, plus noise.

The bunch crossings with the least amount of afterpulsing effects are those which are just after the abort gaps, since they feel little-to-no afterpulsing from the preceding abort gap bunch crossings; however, these post-abort bunch crossings show a strong dependence on how far they are from the previous abort gap end. After sufficiently many post-abort gap bunch crossings, the afterpulsing effect is saturated and no more increase in the number of scaler counts per bunch crossing is observed. Because we are searching for a dependence on the relative luminosity systematics on spin patterns, we now turn our attention to spin patterns in the post-abort gap regions.

Table 5.2 shows the absolute value of the difference in the number of S crossings (N_S) and the number of O crossings (N_O) within N_{pa} bunch crossings after each abort gap; note that the spin pattern coming out of each abort gap is the same, since it is a pattern which repeats every 8 bunch crossings and the post-abort regions begin at bunch crossing 0 and at bunch crossing 40. In Run 12, the number of S crossings and O crossings balances out every other bunch crossing. In Run 13, however, the number of S crossings exceeds the number of O crossings by as much as 4 (and vice versa); if the observed afterpulsing effect occurs for ~ 4 bunch crossings, then we could see a bias in R_3 values which correlates to spin pattern classes A and B. For example, if the first four post-abort gap crossings are OOOO, then we have *less-than-nominal* O scaler counts which would consequently bias R_3 toward higher values. If the effect is stronger in the ZDC with respect to the VPD (or vice versa), then the difference in their R_3 values becomes biased by spin pattern class; consequently so does the $A_{LL}^{\pi^0}$ systematic uncertainty from R_3 uncertainty.

The above ideas can be tested by omitting the first few post-abort gap bunch crossings

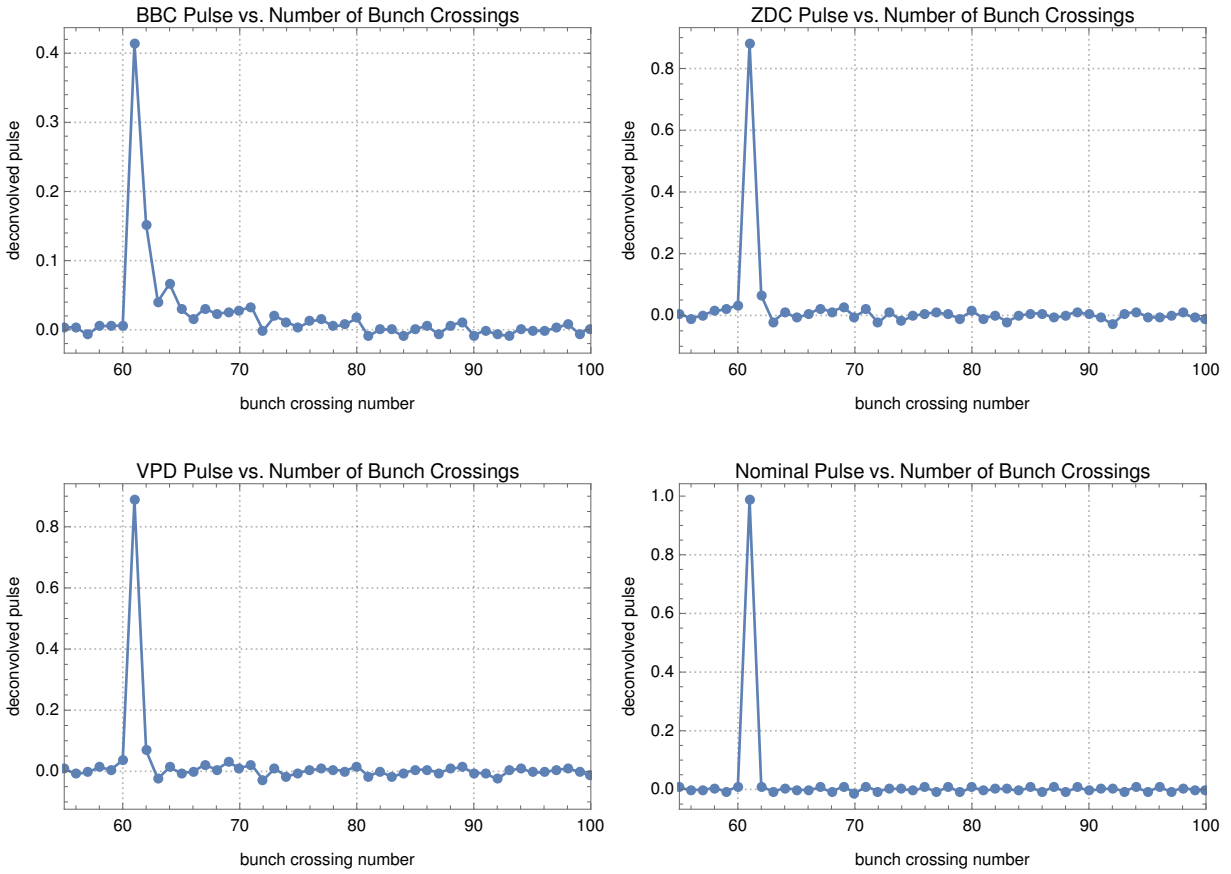


Figure 5.9: Deconvolved pulse $P(b)$ vs. bunch crossing number for the BBC (top left), ZDC (top right), VPD (bottom left), and for an ideal scaler (bottom right). The pulse is centered at bunch crossing 61.

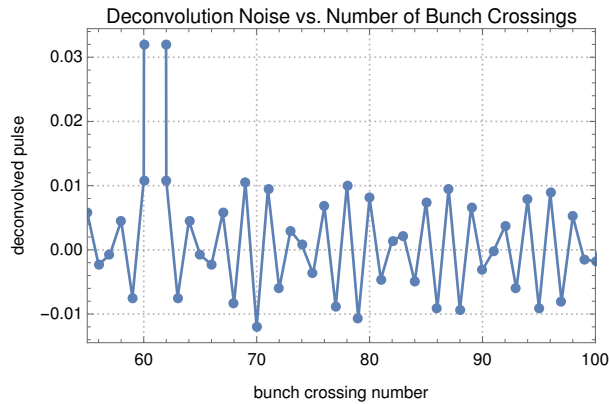


Figure 5.10: Deconvolved nominal pulse $P(b)$ vs. bunch crossing number, zoomed in to show the noise.

N_{pa}	Run 12	Run 13
1	1	1
2	0	2
3	1	3
4	0	4
5	1	3
6	0	2
7	1	1
8	0	0
9	1	1
10	0	2
11	1	3
12	0	4

Table 5.2: Double-spin state differences $|N_S - N_O|$ within N_{pa} bunch crossings after an abort gap.

and recomputing Δ_{R_3} . Figure 5.11 shows the Gaussian fit results of Δ_{R_3} distributions for the omission of N_{pa} post-abort gap bunch crossings, from 0 omitted up to 40. The blue points indicate two Gaussian fits were used to fit two separate peaks and the green points indicate one Gaussian fit to one peak. The open magenta points indicate a single Gaussian fit to what may actually be two peaks, but the two peak fit was too difficult to implement. The following features in this oscillation are observed:

- Nodes at approximately $N_{pa} \in \{4, 12, 20, 28, 36\}$ and anti-nodes in between
- The largest splitting of the peaks is in the $N_{pa} = 0$ case, that is, in the full data set
- Slight damping, which is likely due to afterpulsing saturating the number of scaler counts
- The period is 8 bunch crossings, which is the same as that of the spin patterns
- The distance between any node and its nearest anti-node is 4, which is related to the pattern of 4 “S” bunch crossings followed by 4 “O” bunch crossings
- The amplitude is anti-correlated with the value of $|N_S - N_O|$ from table 5.2

As a complementary study, removal of N_{pa} pre-abort gap bunch crossings was tested. Figure 5.12 shows the result of the distribution fits. All distributions are bimodal, however, there is still sinusoidal behavior of the distribution means, with respect to N_{pa} . There is no value of omitted N_{pa} pre-abort gap bunch crossings for which the distributions merge;

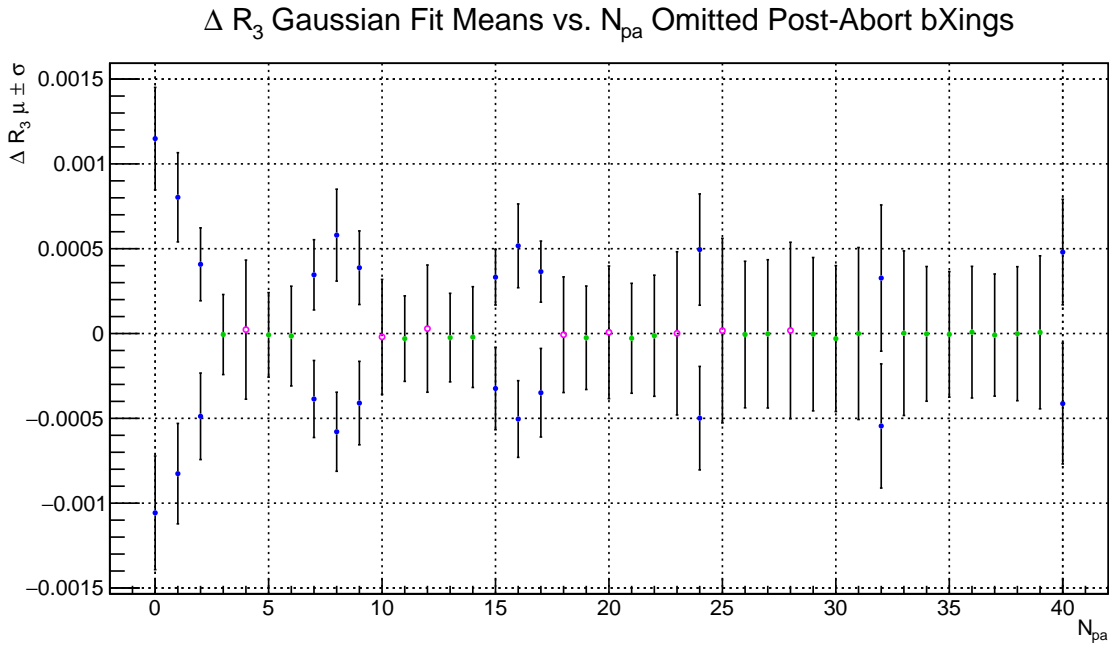


Figure 5.11: Gaussian fit results for Δ_{R_3} distributions as a function of number of omitted post-abortion gap bunch crossings, N_{pa} . Blue: 2 peaks and 2 Gaussians; Green: 1 peak and 1 Gaussian; Open Magenta: possibly 2 peaks but 1 Gaussian.

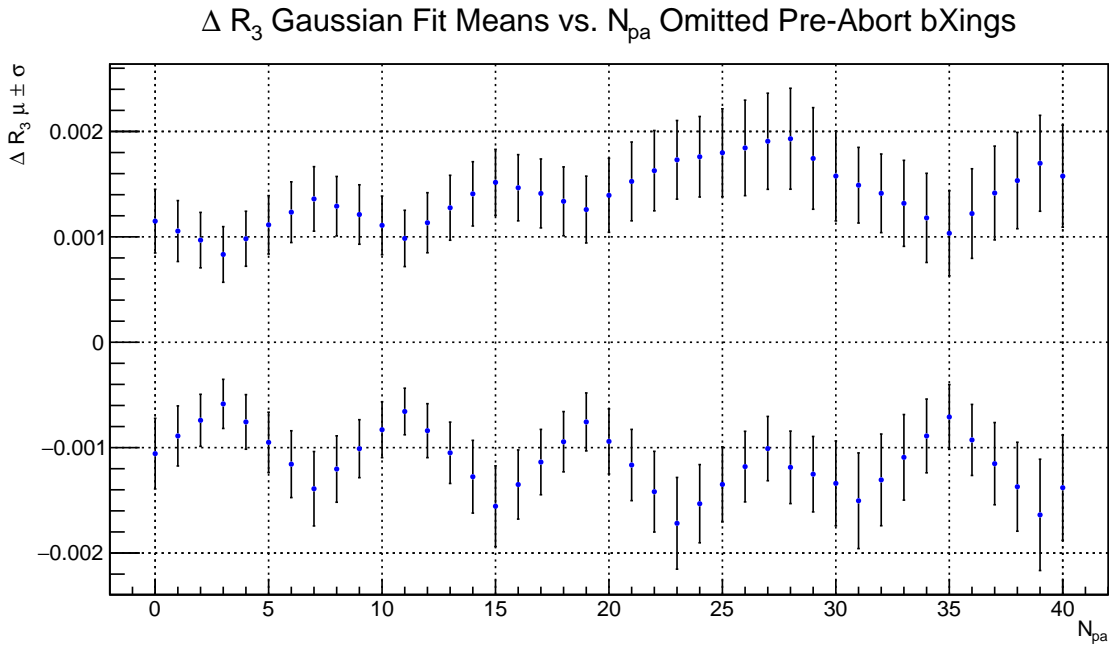


Figure 5.12: Gaussian fit results for Δ_{R_3} distributions as a function of number of omitted pre-abortion gap bunch crossings, N_{pa} . In this case, all distributions were bimodal.

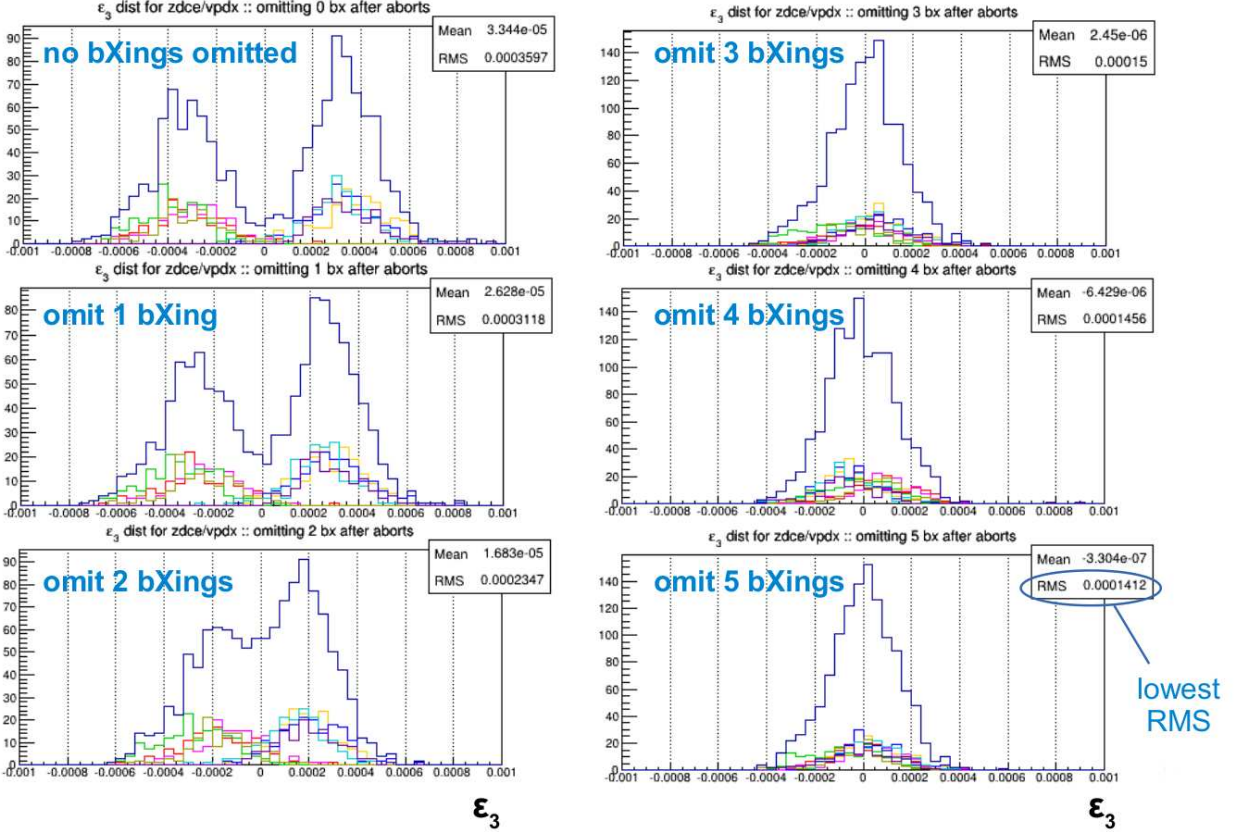


Figure 5.13: Raw ZDCE scaler asymmetry distributions with VPDx as relative luminosity; Run 13. Each panel is for a different number of bunch crossings after each abort gap omitted (0–5).

this property verifies that the observed bimodal structure is sensitive to only post-abort gap bunch crossings.

This test of omitting post-abort gap bunch crossings was also performed on S_{LL} , although only up to $N_{pa} = 8$. The results are similar and are given in figures 5.13-5.14; note that although the ZDCE/VPDX raw asymmetry with CDF corrections is shown here, the general result holds for the rate-safe corrected VPD/ZDC S_{LL} as well.

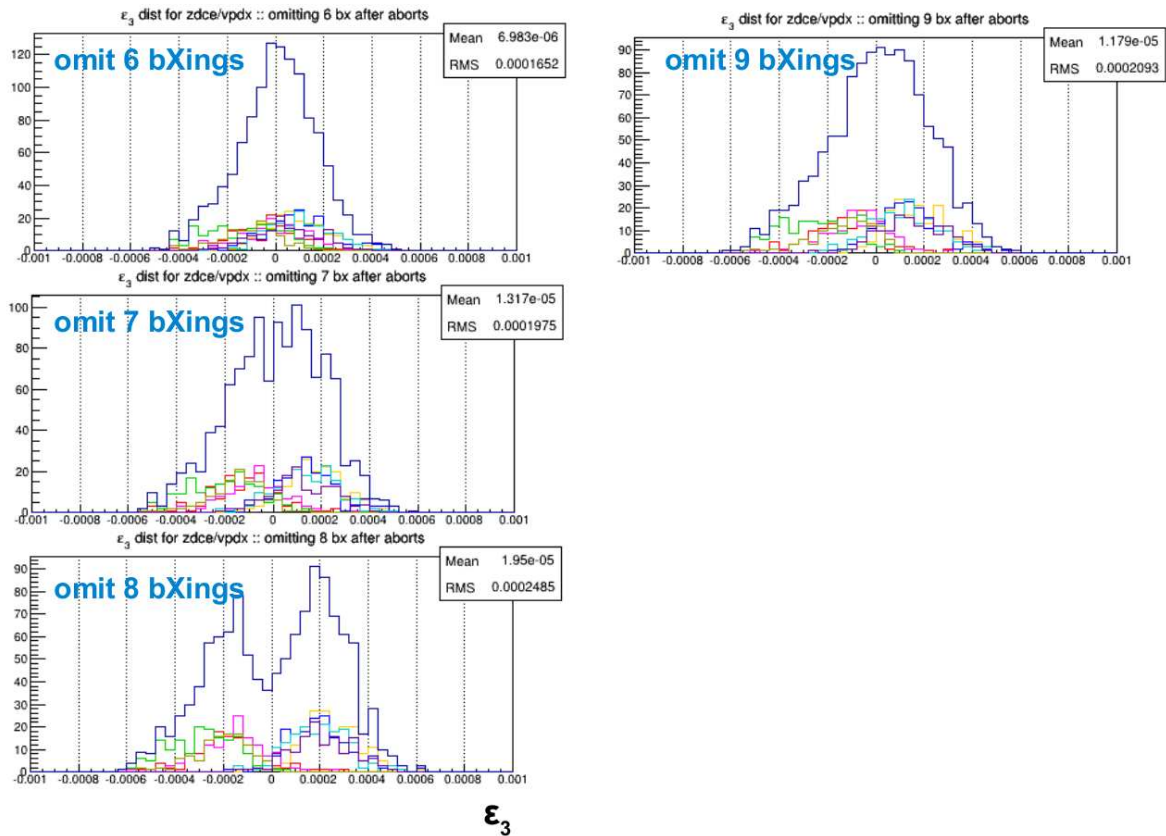


Figure 5.14: Raw ZDCE scaler asymmetry distributions with VPDX as relative luminosity; Run 13. Each panel is for a different number of bunch crossings after each abort gap omitted (6–9).

5.1.6 Summary of Relative Luminosity Systematics

Table 5.3 shows a summary of the systematic uncertainties on $A_{LL}^{\pi^0}$ from relative luminosity. While they are mostly consistent with each other, we have ultimately decided to use the $\Delta_{ALL} [\Delta_{R_3}]$ values in order to be conservative and because it is the method with the simplest implementation and interpretation.

Method	Run 12	Run 13
$\Delta_{ALL} [\Delta_{R_3}]$	2.1×10^{-4}	4.9×10^{-4}
$\Delta_{ALL} [\Delta_{SLL}]$	1.9×10^{-4}	4.1×10^{-4}
$\Delta_{ALL} [\Delta_{DN}]$	N/A	4.1×10^{-4}

Table 5.3: Summary of $A_{LL}^{\pi^0}$ systematic uncertainties from relative luminosity.

This systematic uncertainty is the dominant shift systematic uncertainty on $A_{LL}^{\pi^0}$. It is still smaller than the statistical uncertainty, however, which is on the order of 10^{-3} for this analysis.

5.2 Polarization Transverse Component Systematic

While the protons are circulating through RHIC, a transverse polarization is maintained. In order to achieve collisions with longitudinal polarizations, the spin rotators are used to rotate the spin states from transverse to longitudinal when the protons enter the STAR hall, and back to transverse when they exit. This spin rotation may be imperfect, however. A nonzero transverse component of the polarization just before collision propagates as an additional systematic to any A_{LL} measurement.

The ZDC has a hodoscopic scintillator layer with 8 horizontal slats and 7 vertical slats. This layer is called the Shower Maximum Detector (SMD) layer of the ZDC, or ZDC-SMD [98, 99], and for Run 12 and 13 was used as the main local polarimeter at STAR. Transverse single-spin asymmetries A_N measured during a longitudinally polarized data-taking period can be compared to expected A_N values with transversely polarized collisions. The ratio between these asymmetries for each beam, along with an estimate of the transverse double-spin asymmetry, are all factors of the associated A_{LL} systematic. See appendix C for a discussion of local polarimetry in general, along with a derivation of the $A_{LL}^{\pi^0}$ systematic uncertainty from residual transverse polarization; for a more in-depth discussion of local polarimetry and asymmetries from a quantum mechanical point of view, see appendix D.

Let ε_T and ε_L denote the raw transverse single-spin asymmetries, taken during transverse (T) and longitudinal (L) data-taking periods, respectively. These asymmetries are measured

in the ZDC-SMD. Let A_{NN} be the transverse double spin asymmetry, measured for π^0 s in the FMS and defined as a function of ϕ , the pion azimuth, as

$$A_{NN} = A_{\Sigma} + A_{TT} \cos 2\phi. \quad (5.15)$$

A_{Σ} is the overall offset double-spin asymmetry, and A_{TT} is the amplitude of the azimuthal modulation. Letting B and Y denote the blue and yellow beams, the systematic uncertainty on $A_{LL}^{\pi^0}$ due to residual transverse polarization is

$$\Delta_{A_{LL}} [P^{\perp}] = \frac{\varepsilon_L^B}{\varepsilon_T^B} \cdot \frac{\varepsilon_L^Y}{\varepsilon_T^Y} \cdot A_{NN}. \quad (5.16)$$

Figures 5.15-5.17 show the ZDC-SMD raw transverse single-spin asymmetries, for each beam, plotted versus a run index. Transverse period asymmetries ε_T are from two transverse fills' worth of data taken at $\sqrt{s} = 510$ GeV during the Run 12 longitudinal startup running period; longitudinal period asymmetries ε_L are from Runs 12 and 13 longitudinal. Constant fit lines are shown, which indicate the maximum-likely values of these asymmetries and are used in equation 5.16.

For the transverse double-spin asymmetry A_{NN} , both A_{Σ} and A_{TT} can be measured from Run 11 $\sqrt{s} = 500$ GeV transverse data, using a similar technique to extracting A_{LL} by making use of a relative luminosity. The relative luminosity measurement for Run 11 is very similar to that in Runs 12 and 13. The raw double spin asymmetry is then extracted for bins in p_T using the same Maximum Likelihood Method (MLM) as was used for A_{LL} ; however, this raw asymmetry must also be binned in azimuth. The azimuthal-dependence of the raw asymmetry is then scaled by polarization and fit to the functional form $A_{\Sigma} + A_{TT} \cos 2\phi$.

Regarding the systematic uncertainty on A_{LL} , only A_{Σ} matters since A_{TT} vanishes upon averaging over azimuth. Figure 5.18 shows the A_{Σ} result, where vertical error bars are statistical and horizontal error bars are the RMSs of the p_T bins. The p_T binning and η boundaries approximately match those in the $A_{LL}^{\pi^0}$ analysis. Because the transverse polarization component systematic is a sub-dominant systematic on $A_{LL}^{\pi^0}$, this rough estimate of A_{Σ} is sufficient; a conservative upper bound of $A_{\Sigma} < 0.008$ is used.

Using the mean raw asymmetries from the 3 datasets in equation 5.16, the systematic uncertainty from each Run is:

$$\text{Run 12: } \Delta_{A_{LL}} [P^{\perp}] = \frac{0.0023}{0.055} \cdot \frac{0.0025}{0.048} \cdot 0.008 = 1.7 \times 10^{-5} \quad (5.17)$$

$$\text{Run 13: } \Delta_{A_{LL}} [P^{\perp}] = \frac{0.0020}{0.055} \cdot \frac{0.0019}{0.048} \cdot 0.008 = 1.2 \times 10^{-5} \quad (5.18)$$

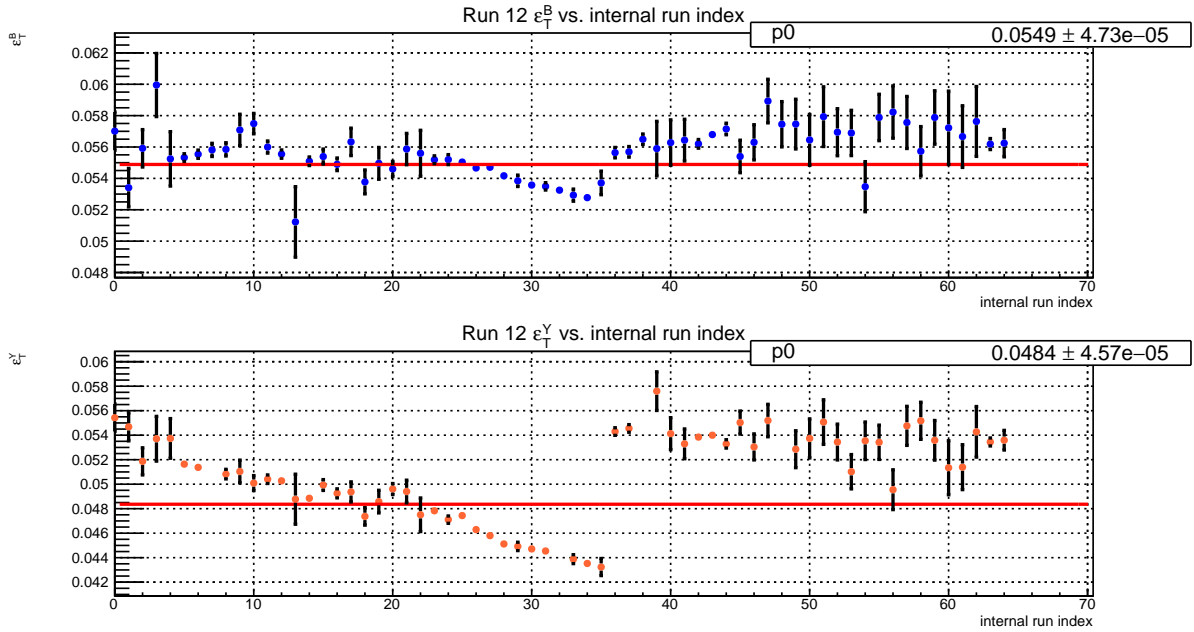


Figure 5.15: Raw transverse single-spin asymmetries in the ZDC-SMD for fills 16570 and 16578, which had transversely polarized collisions at STAR during Run 12 ($\sqrt{s} = 510$ GeV), vs. an internal run index. The jump in asymmetries around run index 35 represents the separation between the two fills. The top panel is for the blue beam and the bottom panel is for the yellow beam.

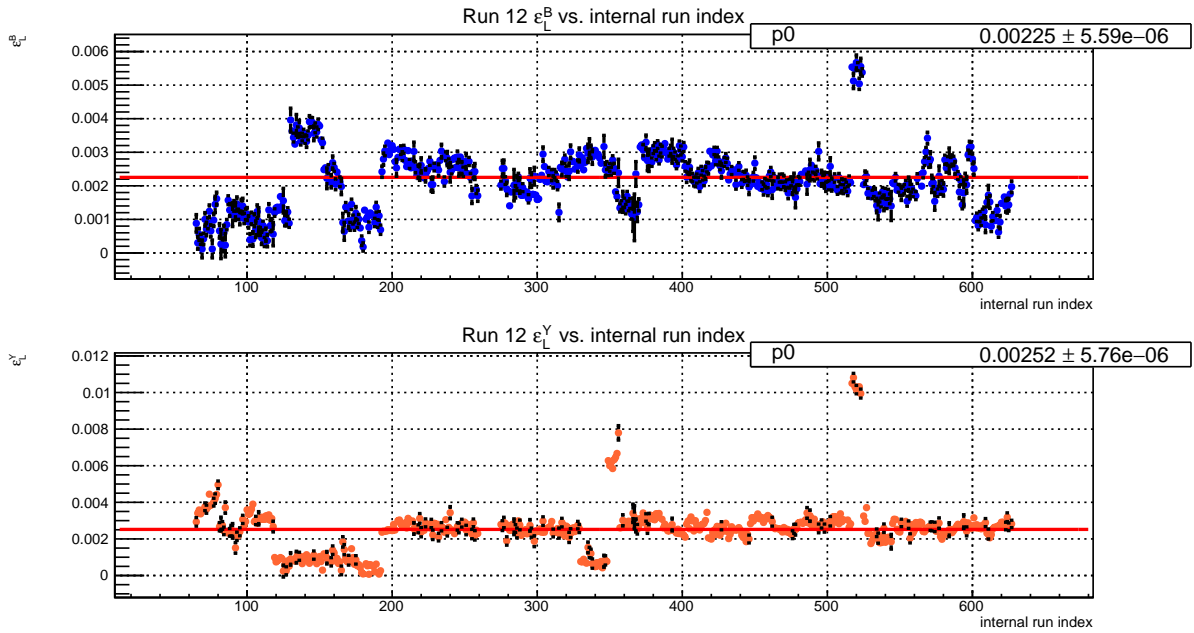


Figure 5.16: Raw transverse single-spin asymmetries in the ZDC-SMD for all fills during Run 12 longitudinal data-taking, vs. an internal run index.

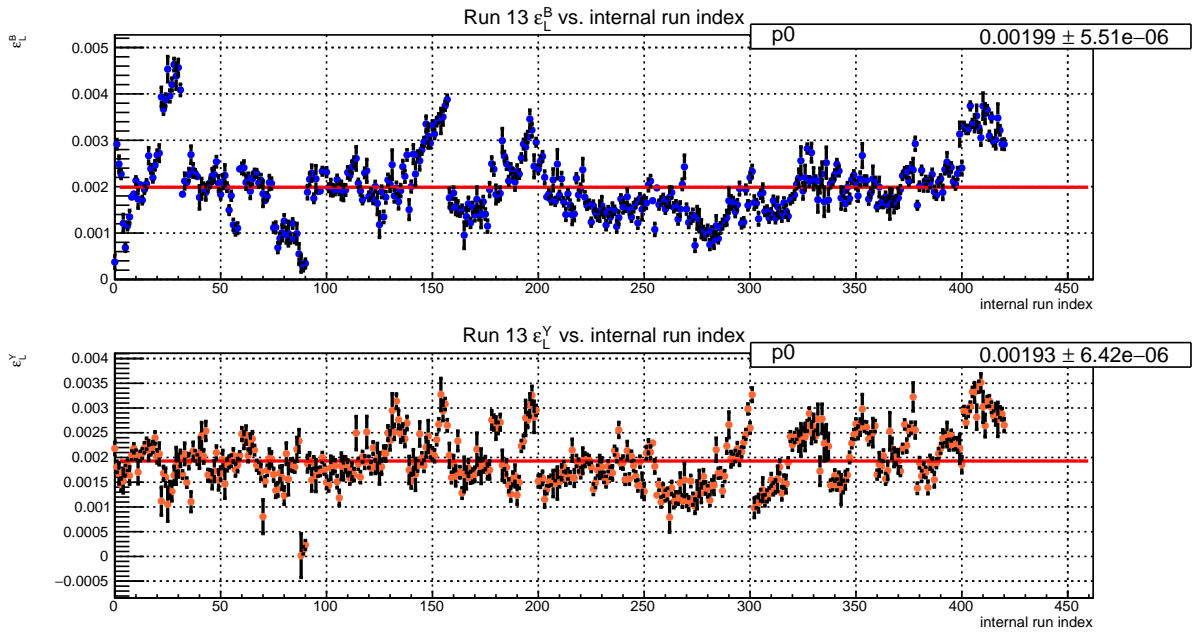


Figure 5.17: Raw transverse single-spin asymmetries in the ZDC-SMD for all fills during Run 13 longitudinal data-taking, vs. an internal run index.

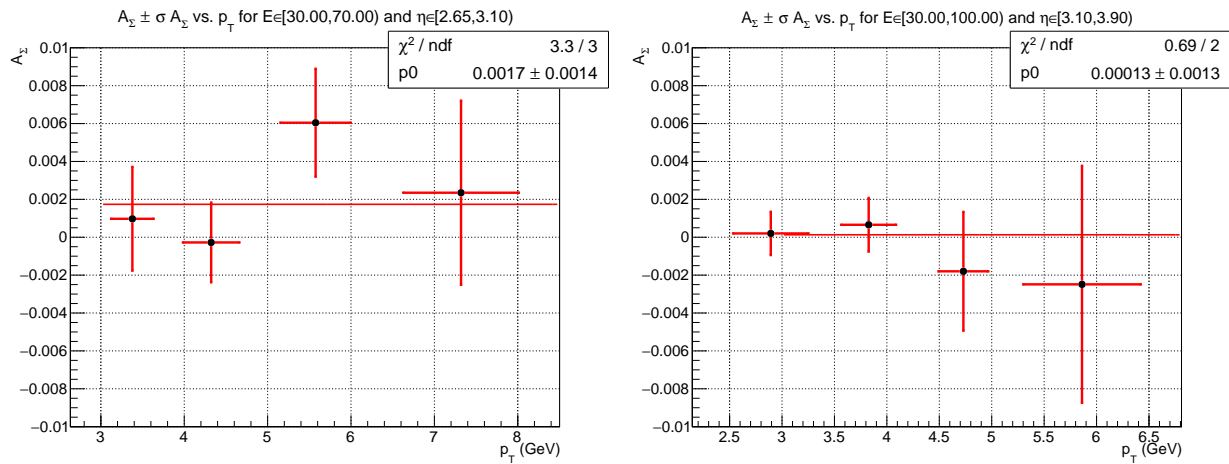


Figure 5.18: Transverse double-spin asymmetries A_Σ from Run 11 transverse data, binned in p_T , for outer η region on the left and inner η region on the right. Vertical error bars are statistical uncertainties and horizontal error bars are p_T bin RMSs.

In comparison to the relative luminosity systematic ($\sim 10^{-4}$) and statistical uncertainties, this is a rather small contribution to the overall $A_{LL}^{\pi^0}$ uncertainty; it is an order of magnitude smaller than the relative luminosity systematic and is basically negligible, but it is still included in the final $A_{LL}^{\pi^0}$ measurement for completion.

5.3 p_T Uncertainty

The final $A_{LL}^{\pi^0}$ values will be plotted as a function of π^0 p_T , thus an estimate of the overall p_T uncertainty for each p_T bin must be assessed. This uncertainty has several contributions: energy uncertainty, vertex uncertainty, position uncertainty, and other systematic uncertainties arising from calibration studies. This section shows how the p_T uncertainty is composed of the different contributions, followed by a discussion of each.

Consider a π^0 with 4-momentum

$$p_{\pi^0} = (E, p_T \cos \phi, p_T \sin \phi, p_T \cot \theta), \quad (5.19)$$

which represents a π^0 scattered at polar angle θ and azimuth ϕ . Assume the longitudinal momentum is approximately equal to the energy, *i.e.*, $p_T \approx E \tan \theta$; this approximation is acceptable for the forward η range which the FMS occupies. Now consider the π^0 decay photons hitting the FMS a transverse distance of h from the beam, as in figure 5.19 (*i.e.*, h is defined using the position of the centroid of the photons). Let R_z be the distance between the shower max plane and the nominal vertex, so that $\tan \theta = h/R_z$. Putting these relations together,

$$p_T(E, h, R_z) \approx \frac{Eh}{R_z}. \quad (5.20)$$

The uncertainties on E and $\theta(h, R_z)$ propagate as

$$\frac{\sigma_{p_T}}{p_T} \approx \frac{\sigma_E}{E} \oplus \frac{\sigma_h}{h} \oplus \frac{\sigma_{R_z}}{R_z}, \quad (5.21)$$

where the symbol “ \oplus ” denotes quadrature summation: $A \oplus B = \sqrt{A^2 + B^2}$. Thus σ_{p_T} is linear with respect to p_T . Energy resolution, nonlinear PMT response, and calibration uncertainties give σ_E , position uncertainty gives σ_h , and vertex uncertainty gives σ_{R_z} .

A more accurate determination of the p_T uncertainty can be made by making use of invariant mass and taking into account uncertainties on photon separation and energy imbalance; however, extra terms which correct equation 5.21, arising from considering the two photons’ kinematics, are negligibly small (see appendix J).

One could also consider correlation terms in the p_T uncertainty. Because there are three

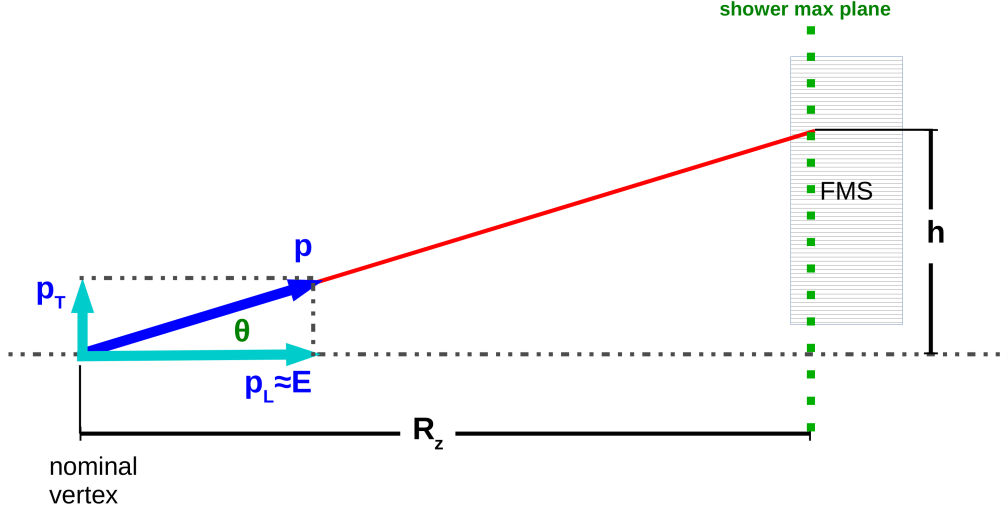


Figure 5.19: Diagram of geometry used to determine p_T uncertainty.

uncertainty terms in equation 5.21, there are three possible correlation terms: energy with position, energy with vertex, and position with vertex. These terms are not included in the final p_T uncertainty calculation, for reasons which will be discussed in section 5.3.4.

For every π^0 which is used for determining $A_{LL}^{\pi^0}$, we know all quantities in equation 5.21 and consequently have a value of σ_{p_T} for each π^0 . For each p_T bin, we can assemble a distribution of σ_{p_T} values and from there determine an overall p_T uncertainty on each $A_{LL}^{\pi^0}$ vs. p_T point. The following sections will now discuss in detail the contributing uncertainties: σ_E , σ_h , and σ_{R_z} .

5.3.1 Energy Uncertainty

The energy uncertainty can be broken into three contributions: energy resolution, nonlinear response of the PMTs, and calibration uncertainty. By far the most dominant contribution is from the nonlinear response and the calibration; furthermore, these contributions are dominant in the overall p_T uncertainty. Letting Q represent the energy resolution, G the uncertainty from nonlinear response, and C the uncertainty from calibration, the energy uncertainty is decomposed as

$$\frac{\sigma_E}{E} = \frac{Q}{\sqrt{E}} \oplus G \oplus C. \quad (5.22)$$

5.3.1.1 Energy Resolution

The measured energy in a calorimeter is proportional to the number of particles in the electromagnetic shower, denoted N , which follows a Poisson distribution. Since the mean

value of N is equal to its variance σ_N^2 , we have

$$\frac{\sigma_N}{N} = \frac{\sqrt{N}}{N} \propto \frac{1}{\sqrt{E}}. \quad (5.23)$$

Thus energy resolution is typically quoted in terms of \sqrt{E} :

$$\frac{\sigma_E}{E} = \frac{Q}{\sqrt{E}} \quad (5.24)$$

for $Q \in (0, 1)$, which depends on the calorimeter material, setup, and energy measurement.

While the energy of a pion is the sum of energies of its decay photons, the energy resolution of the pions is the same as that of the decay photons, because, given $E = \sum_i E_i$, we have

$$\sigma_E^2 = \sum_i \left(\frac{\partial E}{\partial E_i} \right)^2 \sigma_{E_i}^2 = \sum_i \sigma_{E_i}^2 = \sum_i Q^2 E_i = Q^2 E. \quad (5.25)$$

An attempt to measure an estimated energy resolution for a single FMS cell was made at Fermilab, by making use of an electron beam which was being used for another test experiment for STAR calorimetry, experiment T-1018 [100]. A single large FMS cell was wrapped in mylar and coupled to a PMT (radius 1.4 cm, *i.e.*, small cell sized), such that the coupling could be easily adjusted; the original purpose of this test was to determine the dependence of photo-electron yield and energy resolution on the optical coupling between the PMT and the Pb-glass, with the goal to select an optimal coupling for a proposed refurbishment of the FMS. The cell and coupled PMT were made light-tight, mounted on a remotely-controllable stage, and the setup was moved into electron beams with energies of 8 GeV and 16 GeV. Data were then acquired for several different PMT-Pb-glass couplings, in coincidence with several other monitoring detectors, such as a Cherenkov detector, beam hodoscope, and scaler counters.

The criteria used for event selection included a hodoscope geometry cut, which ensured centered electron incidence, as well as minimum ADC cuts on associated Cherenkov and scintillator detectors. The momentum spread of the beam was measured to be about 1.8%, however the cell's energy resolution measurement was heavily dominated by light leakage out of the sides of the cell; it would have been better to test a matrix of cells for an energy resolution measurement. We have therefore chosen to be conservative and to not try to deconvolve the “true” energy resolution from the beam momentum spread.

Because this test at Fermilab was not designed to measure the energy resolution and was focused more on optical couplings, it is not a good measurement of the energy resolution of the FMS; nonetheless, it is the only measurement available at the time of this analysis.

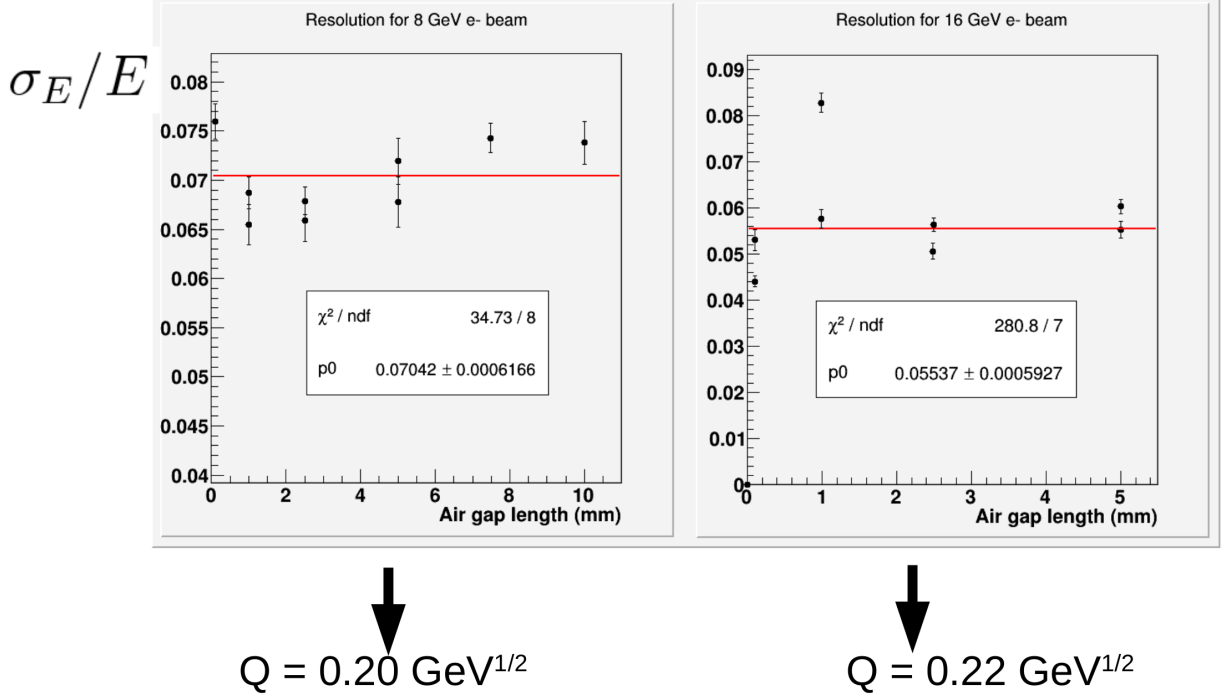


Figure 5.20: σ_E/E vs. PMT-to-Pb-glass air gap length for two different e^- beams; data from test conducted during beam time at Fermilab test experiment T-1018.

Additionally, it was only done for a large cell and no tests were performed with a small cell. Fortunately, this p_T systematic contribution is sub-dominant when compared to the G and C terms in the overall energy uncertainty.

Figure 5.20 shows a plot of the measured energy resolution as a function of various air-gap sizes between the Pb-glass and PMT; an air-gap size of 0.1 mm actually represents a test where the PMT and the Pb-glass were coupled with optical grease. No substantial dependence on optical coupling was observed in the energy resolution, therefore a fit to a constant is shown in order to estimate a value of $Q \sim 0.2$. The resolution is slightly better for an air gap of 1–2 mm for the 8 GeV beam case, which motivated us to add air gaps between the glass and the PMTs during the FMS refurbishment after Run 13; simulations confirmed this idea.

This estimate of $Q \sim 0.2$ is likely an overestimate, given the light leakage out of the sides of the cell as well as the momentum spread of the electron beam. Even at the estimated scale of Q , it represents a sub-dominant systematic uncertainty compared to the other contributions to the energy uncertainty. Furthermore, it is measuring an event-by-event smearing of the energy, not a bias, and therefore gets averaged out in the overall $A_{LL}^{\pi^0}$ measurement. Ultimately it was decided to *drop* this contribution to the p_T systematic uncertainty.

5.3.1.2 Calibration Anchor Point

The fit algorithm for π^0 s has a tendency to overestimate the 2-photon opening angle at higher π^0 energies, as described in section 3.4.5. Because of this overestimation of opening angles, the reconstructed invariant two-photon mass depends on the total energy: a monotonic increase of the mass as a function of energy is observed. Calibration involves the adjustment of PMT gains (during RHIC running periods) and gain corrections (after RHIC running) to shift the π^0 mass peaks to be as close as possible to the real π^0 mass, uniformly over all regions of the FMS. Since the mass has a dependence on energy, the calibration result depends heavily on what range of π^0 energies are selected to calibrate with; this choice of energy range is known as the *calibration anchor point*.

The anchor point range was 28 ± 10 GeV for the large cells and 40 ± 10 GeV for the small cells; most of the π^0 s are found within these energy ranges. If a different calibration anchor point energy were chosen, the overall calibration would shift. For relevant changes in the anchor point, the overall energies could change up to about 5%, which represents another possible systematic bias in p_T . Therefore, a value of $C = 5\%$ was adopted as a contribution to the p_T uncertainty, arising from the overall choice of calibration. This is the most dominant contribution to the p_T systematic uncertainty.

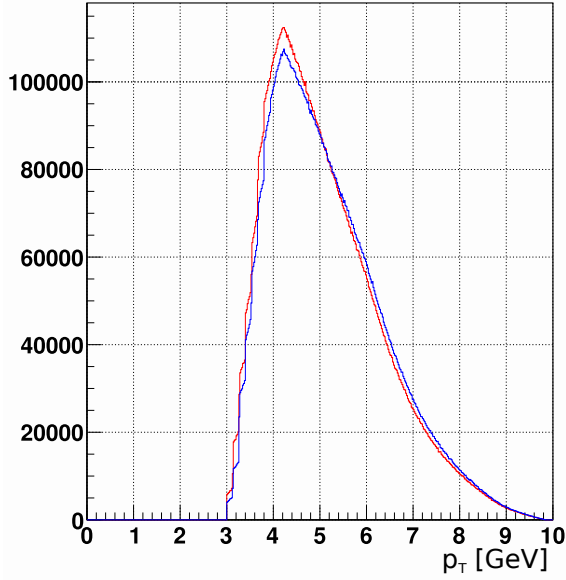
5.3.1.3 Nonlinear Response

The overall $A_{LL}^{\pi^0}$ analysis is performed with an implementation of the day-0 nonlinear gain $g(E)$ correction applied (see section 3.5.2). The result is compared to a parallel analysis of the data with the day-D corrections applied, as well as a *control* analysis with the corrections disabled altogether. By comparing the p_T means, i.e., the plotted positions of the final $A_{LL}^{\pi^0}$ data points, for the day-0 case with the day-D case, the p_T systematic uncertainty contribution G is determined. The value of G is interpreted as the additional shift in p_T that would incur had we taken into account the increased nonlinearity caused by the radiation damage. The day-0 model is better understood as a basic nonlinear E -dependent gain correction, whereas the day-D model as an extension to include radiation damage effects is not as well-vetted; therefore, we have decided to assign the fractional difference between the day-0 and day-D p_T means as a value of G :

$$G = \frac{\langle p_{T_i}^{\text{day-D}} \rangle - \langle p_{T_i}^{\text{day-0}} \rangle}{\langle p_{T_i}^{\text{day-0}} \rangle}. \quad (5.26)$$

Figure 5.21 shows a comparison of the day-0 p_T distribution in blue to the day-D distribution in red. The overall shape looks the same, hence the p_T means do not change by much.

Outer Region



Inner Region

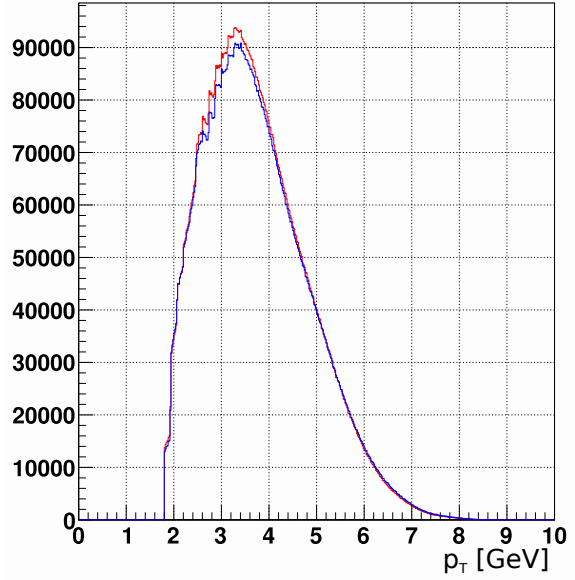


Figure 5.21: Comparison of p_T distributions between day-0 in blue and day- D in red. The day- D distribution has slightly more events, as explained in the text.

There are some additional events in the p_T peak region from the day- D model compared to the day-0 model; this is because all of the kinematics cuts apply to the $g(E)$ -corrected values (*i.e.*, not the uncorrected, observed values), which differ between the day- D and day-0 models. Some events which satisfy kinematic cuts after day- D corrections may not satisfy them after day-0 corrections. In fact, more events satisfy kinematic cuts for either day-0 or day- D corrections than for the case where no nonlinear correction is applied; this is because, in general, the $g(E)$ corrections tend to reduce E and p_T , and this reduction is stronger for higher values of E and p_T (see figures 3.18 and 3.19). More events near the upper limits of the cuts are being brought down in E and p_T into the accepted kinematic region; fewer events near the lower limits of the cuts are “falling” out of the accepted region. Thus overall, applying $g(E)$ corrections tends to increase the overall number of events which pass all cuts.

Table 5.4 lists the p_T means for each p_T bin in the $A_{LL}^{\pi^0}$ analysis for each of the three parallel analyses. The value of G is also listed; this contribution to the overall p_T systematic uncertainty is very small. Note that the fractional differences in p_T means from the control analysis are not very high either; this indicates that the net effect of the $g(E)$ correction on the p_T means is effectively washed out.

p_T Bin		No $g(E)$	Day-0 $g(E)$	Day-D $g(E)$	G
Outer Region	$p_T^{\text{thresh}}-4.35$	3.91	3.91	3.89	-0.41%
	4.35-5.15	4.73	4.73	4.73	-0.07%
	5.15-6.15	5.62	5.62	5.62	-0.09%
	6.15- p_T^{max}	7.08	7.08	7.07	-0.06%
Inner Region	$p_T^{\text{thresh}}-2.95$	2.50	2.50	2.50	0.17%
	2.95-3.70	3.33	3.33	3.33	-0.04%
	3.70-4.60	4.11	4.11	4.11	-0.01%
	4.60- p_T^{max}	5.37	5.37	5.36	-0.29%

Table 5.4: Mean p_T values for each bin and for the cases of no $g(E)$ correction, day-0 $g(E)$, and day-D $g(E)$; the p_T systematic uncertainty contribution G is also given, which compares day-0 $g(E)$ to day-D $g(E)$ p_T means. Note that while not many significant figures are printed in the table (because the p_T uncertainty is *already* at least 5% from the calibration uncertainty), the calculation of G used all available digits, verifying how little G contributes to the overall p_T systematic uncertainty.

5.3.2 Position Uncertainty

Although position uncertainty is expected to be a sub-dominant contribution to the p_T uncertainty, it is nonetheless important to estimate its magnitude. Consider a single photon cluster in the FMS. Let E_i denote the energy of the i th tower in the cluster and let (x_i, y_i) be the coordinates of that tower. Following [101], consider the photon position (\bar{x}, \bar{y}) as approximated by the energy-weighted mean of the towers:

$$\bar{x} = \frac{\sum_i x_i E_i}{\sum_i E_i}. \quad (5.27)$$

Derivatives of \bar{x} with respect to each tower energy E_j are $(x_j - \bar{x})/E$. Given that the energy resolution is $\sigma_{E_j} = Q^2 E_j$, the uncertainty on the centroid is

$$\sigma_{\bar{x}}^2 = \frac{Q^2 \hat{\sigma}_x^2}{E}, \quad (5.28)$$

where $\hat{\sigma}_x^2$ is the energy-weighted variance,

$$\hat{\sigma}_x^2 := \sum_i \frac{E_i (x_i - \bar{x})^2}{E}. \quad (5.29)$$

Therefore the error on the photon position, approximated here by the cluster centroid, is proportional to $1/\sqrt{E}$, where the constant of proportionality will be henceforth denoted $W := Q\hat{\sigma}_x$.

In addition to the photon centroid, the penetration of the photon into the glass before the shower initializes must also be taken into account. If the photon has a polar angle θ from the vertex, then the projection of one radiation length X_0 to the front plane of the FMS is $X_0 \sin \theta$. This amount represents another possible uncertainty in the reconstructed transverse position of the photon, especially if the incident angle is high.

A value for W was determined in the RADPHI calorimeter at Jefferson Lab [102], which is an array of FMS small cells. This value can be extended to the large cells as well, by multiplying by a factor 6 cm / 4 cm, which is the approximate ratio of large to small cell transverse sizes. Radiation lengths were measured in other Pb-glass arrays which utilized the same glass; see [76] for large cells and [77] for small cells. Values of W and X_0 are given in table 5.5.

	Large Cell	Small Cell
W	1.065 cm · GeV ^{1/2}	0.71 cm · GeV ^{1/2}
X_0	3.2 cm	2.5 cm

Table 5.5: W and X_0 values for FMS Pb-glass, measured by RADPHI for small cells and extrapolated to large cells.

Another contribution to the systematic uncertainty is due to the choice of shower shape model. As mentioned before in section 3.4.2, one can use an asymmetric shower shape model, which takes into account corrections from the incident photon angle. The symmetric shower shape model, which is independent of incident angle, is employed in this $A_{LL}^{\pi^0}$ analysis, therefore the possible bias from having not applied incident angle corrections must be taken into account.

At the highest angle of incidence accepted in the FMS, using the asymmetric shower shape returns a photon position a distance of, at the most, 0.5 cm from the position returned from the symmetric shower shape. This bias has been confirmed in simulations. Furthermore, as was mentioned in section 3.4.2, the bias is much more sensitive to the choice of z plane onto which the photon trajectories are projected, rather than on the transverse shower shape. Nonetheless, the bias represents another contribution to the overall position uncertainty, and is denoted as $A = 0.5$ cm.

Putting everything together, the full position uncertainty is

$$\sigma_h = \frac{W}{\sqrt{E}} \oplus X_0 \sin \theta \oplus A. \quad (5.30)$$

Given typical values of E and θ , the typical contribution to the p_T systematic is $\sigma_h/h \sim 1\%$, which is sub-dominant, but not negligible.

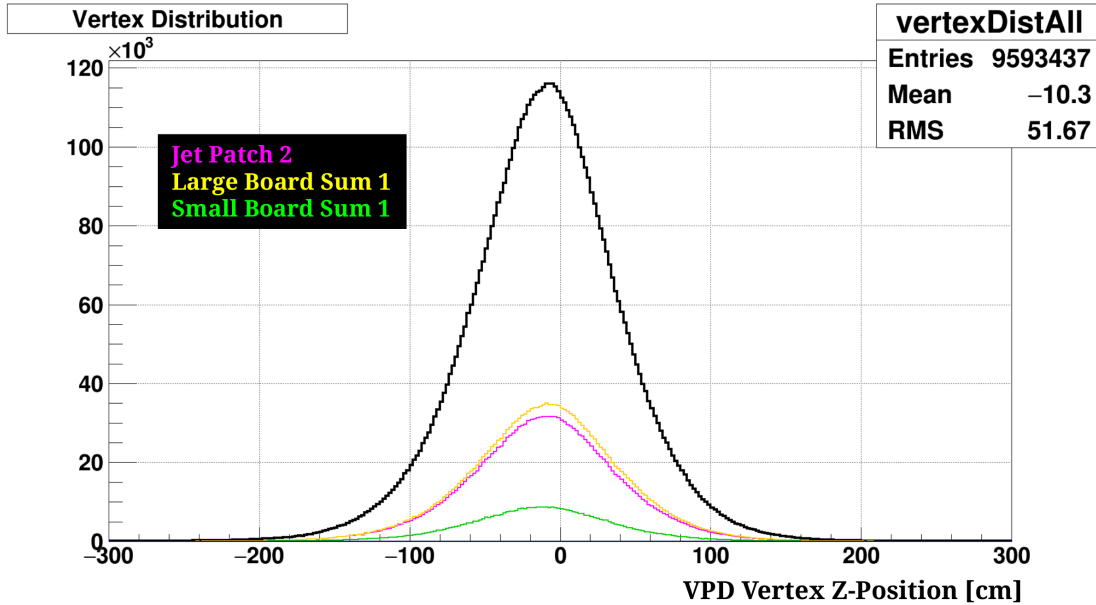


Figure 5.22: Vertex distribution, in particular, the z -position of the vertex as determined by the VPD. The black distribution is for all events, magenta is for FMS-JP2, yellow for FMS-LgBS1, and green for FMS-SmBS1.

5.3.3 Vertex Uncertainty

The offset in the vertex is another possible bias in the overall p_T of events seen in the FMS. This offset, denoted σ_{R_z} , contributes to the p_T systematic as σ_{R_z}/R_z , where R_z is the distance between the FMS and the nominal vertex position, 7.2 m. Figure 5.22 shows the vertex distribution in Run 13, along with distributions filtered by FMS trigger.

Since in Run 13 only the large cells were ultimately analyzed, the LgBS1 trigger is the most unbiased trigger selection on the vertex distribution, which would give a reasonable estimate of the vertex offset in the $A_{LL}^{\tau^0}$ data set. The mean of the LgBS1-filtered vertex distribution is about 9.8 cm, which gives a value of $\sigma_{R_z}/R_z = 1.4\%$; other trigger-filtered distributions give a very similar mean, so this choice of trigger is of little impact. Furthermore, the Run 12 distribution was similar, and therefore this value of 1.4% is used as an overall value for this p_T systematic contribution.

5.3.4 Correlation Terms in p_T Uncertainty

We now return to the question of including correlation terms: energy with position, energy with vertex, and position with vertex. The measured energy is physically not correlated with the vertex offset, therefore the energy and vertex term vanishes. The position uncertainty and vertex offset could be correlated, however this correlation term also includes factors

for the position and vertex uncertainties themselves, both of which are small with respect to correlations involving energy uncertainty. Therefore, the position and vertex correlation term is omitted as negligible. Finally, regarding the energy with position term, the dominant energy uncertainty contribution, C , is from the calibration anchor point and is not correlated with position. The sub-dominant contribution, G , from including radiation damage considerations for the nonlinear gain correction, can be correlated with position and needs some careful thought.

Consider the case where the energy of a shower is underestimated, that is, $E_o < E_t$. This case occurs because the initial part of the shower was not detected, since it was effectively blocked by attenuation due to properties of the Pb-glass as well as radiation damage. The part of the shower that is detected, however, averages out in the transverse plane to a greater value of h than it would have had the entire shower been observed. Therefore, underestimating E leads to an overestimate of h and vice versa; the energy and position uncertainties are thus anti-correlated. The derivatives of $p_T(E, h, R_z)$ with respect to E and h are both positive, so the anti-correlation therefore makes the overall energy and position correlation term negative and would serve to reduce the overall p_T uncertainty. Because this correlation is based on the sub-dominant p_T uncertainty contribution G , it is expected to be small. Therefore, neglecting this term altogether returns an overall p_T uncertainty which is a slight overestimate. Ultimately, the more-conservative path was chosen and this correlation term was omitted altogether as well.

5.3.5 p_T Uncertainty Result

To summarize the above discussions, the full p_T systematic uncertainty is

$$\frac{\sigma_{p_T}}{p_T} = [G \oplus C] \oplus \frac{1}{h} \left[\frac{W}{\sqrt{E}} \oplus X_0 \sin \theta \oplus A \right] \oplus \left[\frac{\sigma_{R_z}}{R_z} \right], \quad (5.31)$$

where the contributions from energy, position, and vertex uncertainties have been respectively bracketed. The overall contribution from energy uncertainty ranges around 5–6%, and is dominant and also dependent on which p_T bin is considered. The position and vertex uncertainties contribute about 1% and 1.5%, respectively, and when added in quadrature with the energy uncertainty, give an overall σ_{p_T}/p_T of approximately 5–6%.

The σ_{p_T} value is plotted in figure 5.23 as a function of p_T , for all π^0 events in the $A_{LL}^{\pi^0}$ analysis. The p_T binning can be seen in the small discontinuities at the p_T bin boundaries, where the slope increases slightly when proceeding to higher p_T . The overall value of σ_{p_T}/p_T is 5.3% for both the outer and inner regions.

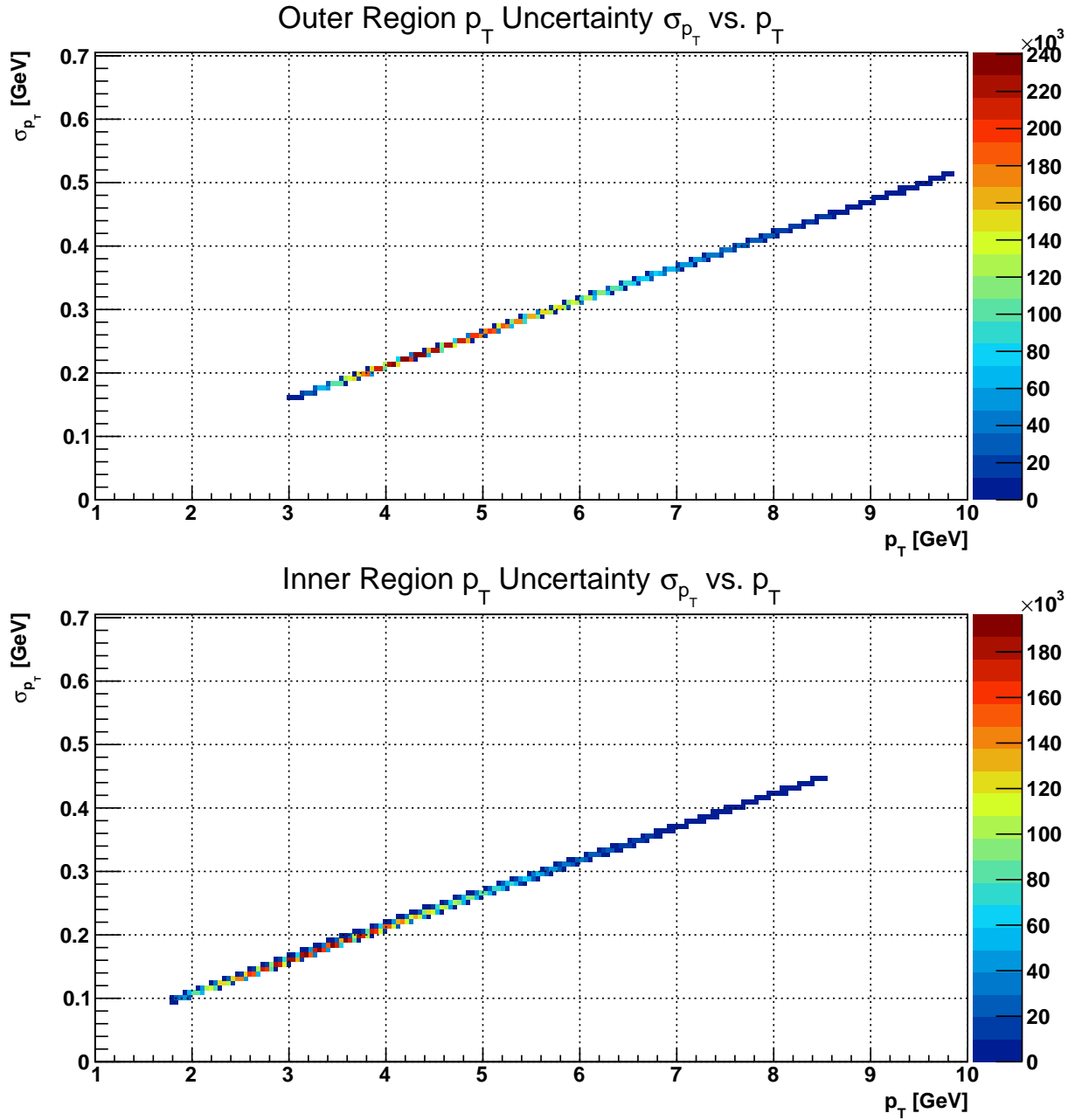


Figure 5.23: Full p_T uncertainty vs. p_T for outer region (top) and inner region (bottom).

5.4 Summary of Systematic Uncertainties

Table 5.6 shows a summary of all of the systematic uncertainties which are included in the $A_{LL}^{\pi^0}$ analysis. They are organized by type and origin, indicated in the classification column; approximate typical values for each uncertainty are given in the rightmost column.

Uncertainty	Symbol	Classification	Typical Value
Relative Luminosity	$\Delta_{A_{LL}} [\Delta_{R_3}]$	$A_{LL}^{\pi^0}$ Shift	$2-5 \times 10^{-4}$
Polarization Transverse Component	$\Delta_{A_{LL}} [P^\perp]$	$A_{LL}^{\pi^0}$ Shift	$1-2 \times 10^{-5}$
Overall Polarization	$\sigma_{\mathbb{P}_B \mathbb{P}_Y} / \mathbb{P}_B \mathbb{P}_Y$	$A_{LL}^{\pi^0}$ Scale	6.7%
Calibration Bias	C	p_T Bias	5%
Nonlinear Gain Correction	G	p_T Bias	< 0.4%
Energy Bias in Position	$W/h\sqrt{E}$	p_T Bias	< 0.5%
Position Bias from Shower Depth	$X_0 \sin \theta/h$	p_T Bias	< 0.5%
Position Bias from Shower Shapes	A/h	p_T Bias	< 1%
Vertex Offset	σ_{R_z}/R_z	p_T Bias	1.4%

Table 5.6: Summary of $A_{LL}^{\pi^0}$ systematic uncertainties.

Chapter 6

$A_{LL}^{\pi^0}$ Analysis Procedure

So far we have discussed the π^0 event selection in chapter 3, the relative luminosity in chapter 4, and systematic uncertainties on $A_{LL}^{\pi^0}$ and on π^0 transverse momentum in chapter 5. This chapter shows how these components are combined into the final $A_{LL}^{\pi^0}$ measurement. The kinematic binning will be discussed first, followed by the Run 12 and 13 polarization measurements from the RHIC Polarimetry Group. After that is a discussion of how the π^0 yields, relative luminosities, and polarizations are combined for the entire data set into an $A_{LL}^{\pi^0}$ measurement for each kinematic bin. This is followed by a study of the π^0 signal and background fractions, which are used to correct for a possible background A_{LL} contribution to $A_{LL}^{\pi^0}$. The full, background-corrected $A_{LL}^{\pi^0}$ measurement as a function of p_T will be presented in the next chapter.

6.1 Kinematic Binning and Means

Table 6.1 shows the kinematic bins used in the $A_{LL}^{\pi^0}$ analysis. Two η regions are defined: an outer region which has mostly large cells and an inner region with mostly small cells. The η -ring between the regions is set at 3.15 as a rounded value which appropriately separates the large cells and small cells calibration schemes, as presented in the M vs. η plot back in figure 3.6. For the outer region, both Runs 12 and 13 are analyzed, whereas only Run 12 is analyzed for the inner region, because the small cells were heavily radiation-damaged during Run 13. Furthermore, only the first half of Run 13 data was ultimately analyzed, because we determined the radiation damage to be too severe in the second half.

Four p_T bins are defined separately within the two η regions. Their boundaries were determined by approximately equalizing the π^0 yields within each bin, given the full p_T distribution of the π^0 s considered in $A_{LL}^{\pi^0}$. The value p_T^{thresh} is a time-dependent p_T threshold, which was discussed in section 3.7.2; the lowest kinematically-allowed value of p_T , given by

η Region	p_T Bin	p_T Range (GeV)	E Range (GeV)	η Range
Outer Region	1	$p_T^{\text{thresh}}-4.35$	30–70	2.65–3.15
	2	4.35–5.15		
	3	5.15–6.15		
	4	6.15– p_T^{max}		
Inner Region	1	$p_T^{\text{thresh}}-2.95$	30–100	3.15–3.90
	2	2.95–3.70		
	3	3.70–4.60		
	4	4.60– p_T^{max}		

Table 6.1: Kinematic bin ranges for the $A_{LL}^{\pi^0}$ analysis. Two η regions were used, each divided into four p_T bins.

η Region	p_T Bin	$\langle p_T \rangle$ (GeV)	$\langle E \rangle$ (GeV)	$\langle \eta \rangle$
Outer Region	1	3.91	36.8	2.92
	2	4.73	42.7	2.88
	3	5.62	49.9	2.87
	4	7.08	58.6	2.80
Inner Region	1	2.50	41.2	3.49
	2	3.33	52.7	3.44
	3	4.11	63.8	3.42
	4	5.37	79.2	3.38

Table 6.2: Kinematic bin means for the $A_{LL}^{\pi^0}$ analysis.

$p_T^{\text{min}} \approx E^{\text{min}}/\cosh \eta^{\text{max}}$, is less than p_T^{thresh} for both η regions. The upper limit of p_T is $p_T^{\text{max}} \approx E^{\text{max}}/\cosh \eta^{\text{min}}$, which gives a value of $p_T^{\text{max}} = 9.8$ GeV for the outer region and 8.6 GeV for the inner region.

Table 6.2 lists the means of the kinematic variables p_T , E , and η for each of the p_T bins. Note that the p_T means quoted here are the values at which the $A_{LL}^{\pi^0}$ data points are plotted; these p_T means are background corrected (see section 6.4.1), but they are negligibly different from the uncorrected values. The E and η values are not background-corrected. These kinematic means are needed in the forthcoming global analysis of $\Delta g(x)$, the polarized gluon distribution function, for which this $A_{LL}^{\pi^0}$ measurement is a key piece.

6.2 Polarization

An A_{LL} measurement requires three ingredients: particle yields, relative luminosity, and polarization. The first two ingredients are obtained from STAR detectors and have been discussed, however the polarization of the proton bunches is measured by an independent set

of polarimeters which are located in the RHIC ring diametrically opposite STAR. They are maintained by the RHIC Polarimetry Group at RHIC. For further details of the polarimetry measurement, see [103] and references therein.

For each fill, the polarimetry group provides two numbers along with their uncertainties: the initial polarization at the beginning of a fill, P_0 , and the time dependence of the polarization, $P_1 = dP/dt$. For a given DAQ run which occurs T seconds after the beginning of a fill, the polarization is

$$P(T) = P_0 + P_1 T. \quad (6.1)$$

The value of T for each run in this analysis is taken from the *middle* of the run. Typically a few polarization measurements are taken per fill.

These polarization measurements are then taken together within each fill and combined into a luminosity-weighted average, returning one value of the polarization for each fill; the FMS JP2 trigger was used for the luminosity measurement. Statistical and systematic errors were also propagated on a run-by-run and fill-by-fill basis; details can be found in appendix I as well as the polarimetry group’s analysis note, [103].

Figures 6.1 and 6.2 show the polarizations for the blue and yellow beams as well as the polarization product, as a function of a run index. Both the time-dependent polarization $P(t)$ (in blue) and the luminosity-weighted average $P(t)$ (in magenta) are plotted. The data shown in these figures are limited to the runs which are used in the $A_{LL}^{\pi^0}$ analysis. For scaling the raw double-helicity asymmetry to $A_{LL}^{\pi^0}$, the luminosity-weighted average polarizations are used on a fill-by-fill basis. The overall luminosity-weighted polarizations and their errors were also computed for both Runs 12 and 13; these numbers are given in table 6.3.

	Run 12	Run 13	Runs 12+13
\mathbb{P}_B	0.54 ± 0.019	0.57 ± 0.019	0.55 ± 0.019
\mathbb{P}_Y	0.56 ± 0.019	0.57 ± 0.019	0.56 ± 0.020
$\mathbb{P}_B \mathbb{P}_Y$	0.31 ± 0.020	0.32 ± 0.021	0.31 ± 0.021
L_{int}	57.4 pb^{-1}	6.0 pb^{-1}	63.4 pb^{-1}

Table 6.3: Overall luminosity-weighted average polarizations with uncertainties; blue beam, yellow beam, and product polarizations are shown, as well as the overall integrated luminosity. See appendix I for details.

6.2.1 Scale Systematic on $A_{LL}^{\pi^0}$

The final value of A_{LL} is a measured raw double-spin asymmetry ε_{LL} scaled by the polarization product: $A_{LL} = \varepsilon_{LL} / \mathbb{P}_B \mathbb{P}_Y$. Because of this scaling, an additional scale systematic on $A_{LL}^{\pi^0}$ is assigned. Table 6.3 indicates this scale systematic for Runs 12 and 13 combined is

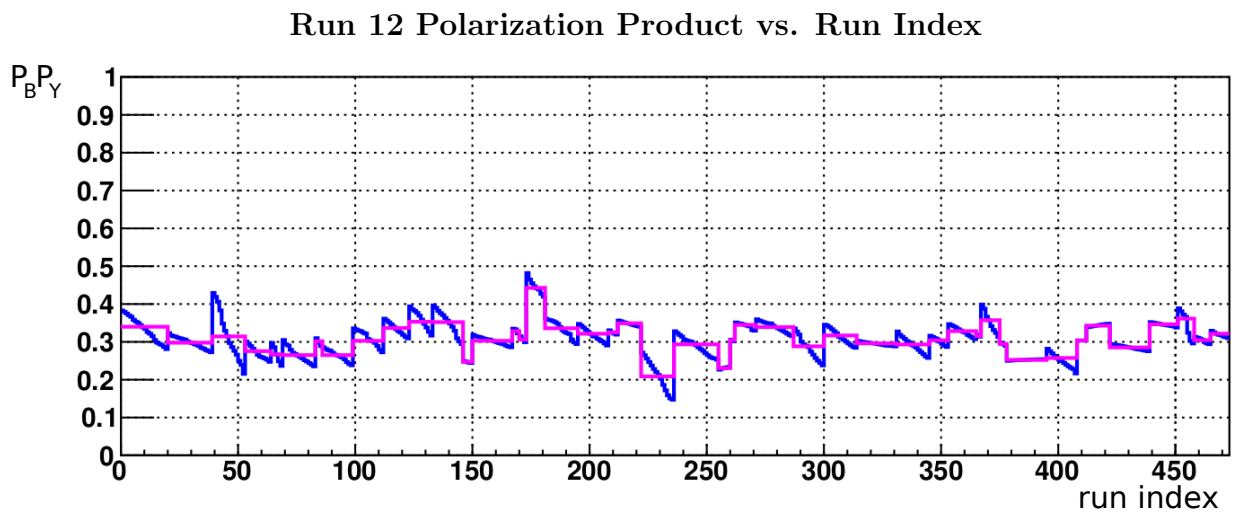
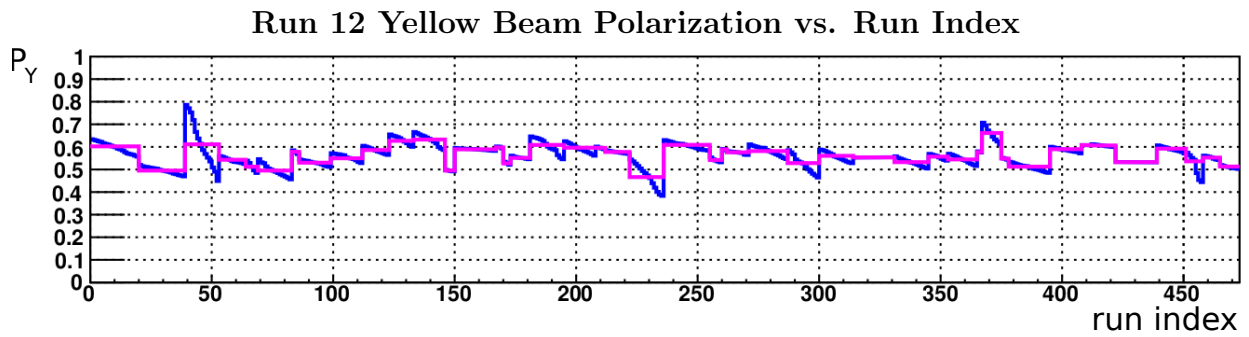
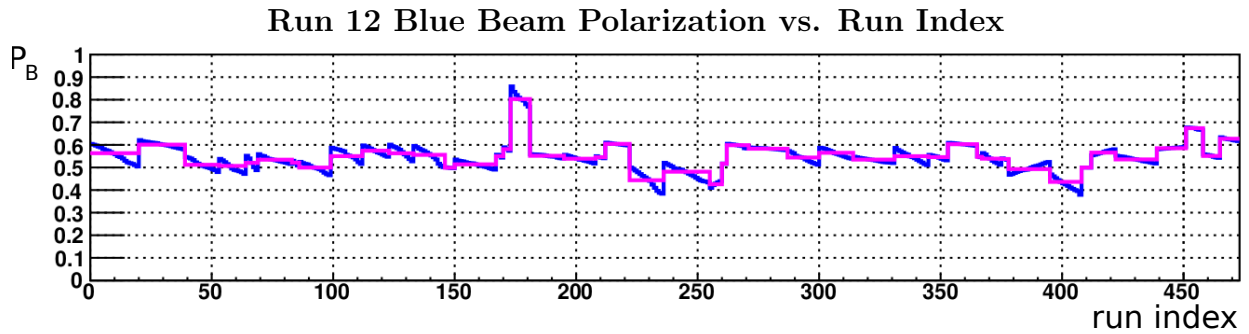


Figure 6.1: Polarizations vs. run index for Run 12; blue line is $P(t)$ and magenta line is the luminosity-weighted average of $P(t)$ within each fill.

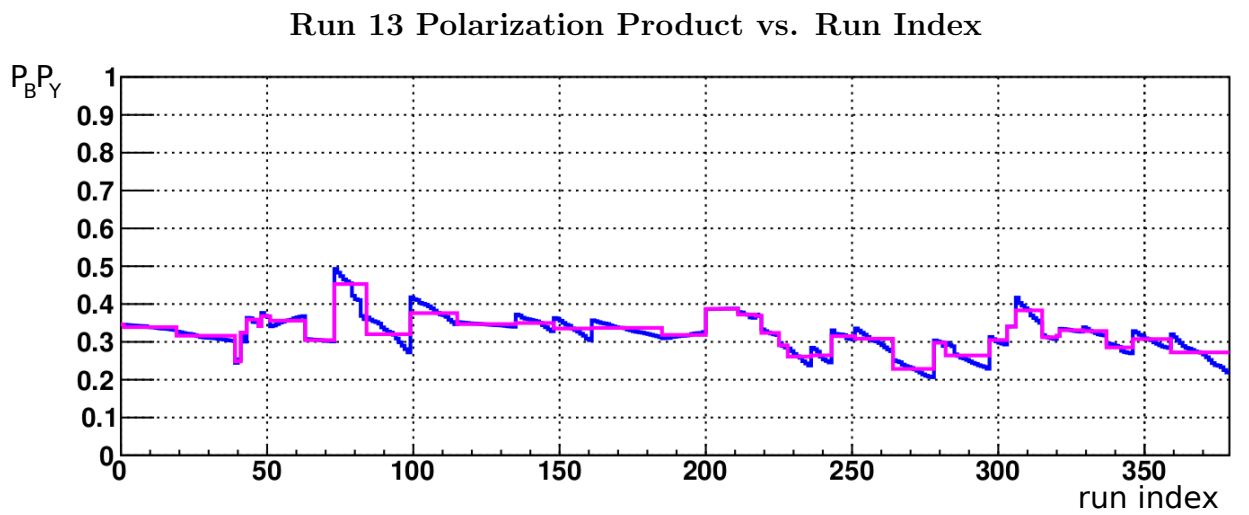
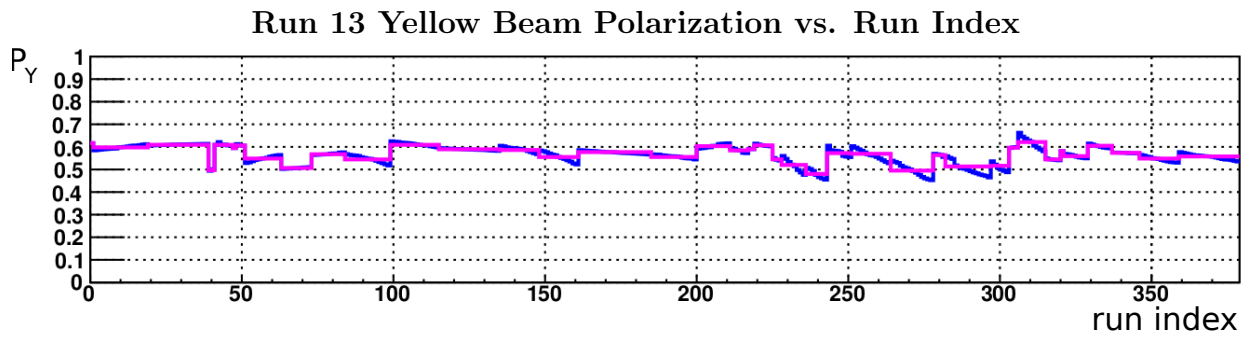
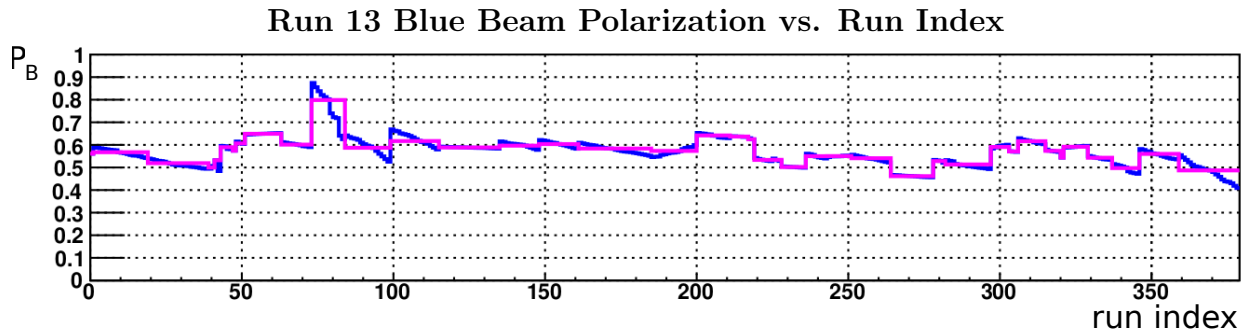


Figure 6.2: Polarizations vs. run index for Run 13; blue line is $P(t)$ and magenta line is the luminosity-weighted average of $P(t)$ within each fill.

$\sigma_{\mathbb{P}^B\mathbb{P}^Y}/\mathbb{P}^B\mathbb{P}^Y = 6.7\%$. This is a systematic uncertainty on $A_{LL}^{\pi^0}$ that is independent of all the aforementioned shift systematic uncertainties. Furthermore, the aforementioned shift systematic uncertainties define an uncertainty of the overall offset from zero; on the other hand, the polarization scale systematic uncertainty defines an uncertainty in the overall multiplicative scale of the asymmetry.

6.3 Maximum Likelihood Method A_{LL} Computation

Data at STAR are typically taken in half-hour segments, called DAQ runs. In order to combine the data from all DAQ runs into a single measurement, a Maximum Likelihood Method (MLM) is employed. See appendix K for the full derivation; only the final formulae are presented in this section.

Recalling equation 1.29, the asymmetry for a single run i is expressed as

$$A_{LLi} = \frac{1}{P_{f(i)}^B P_{f(i)}^Y} \frac{(N_i^{++} + N_i^{--}) - R_{3_i} (N_i^{+-} + N_i^{-+})}{(N_i^{++} + N_i^{--}) + R_{3_i} (N_i^{+-} + N_i^{-+})}, \quad (6.2)$$

where $f(i)$ is the fill which contains run i . Instead of measuring A_{LLi} for each run, we combine the yields, relative luminosities, and polarizations into a single formula which gives the overall maximum likely A_{LL} , denoted by \bar{A}_{LL} :

$$\bar{A}_{LL} = \frac{\sum_i P_{f(i)}^B P_{f(i)}^Y [(N_i^{++} + N_i^{--}) - R_{3_i} (N_i^{+-} + N_i^{-+})]}{\sum_i (P_{f(i)}^B P_{f(i)}^Y)^2 [(N_i^{++} + N_i^{--}) + R_{3_i} (N_i^{+-} + N_i^{-+})]}. \quad (6.3)$$

While this expression looks similar to equation 6.2, it is a summation over a summation. Moreover, the numerator summands are weighted by the polarization product, whereas those in the denominator are weighted by the polarization product *squared*.

With $\mathbb{P}^B\mathbb{P}^Y$ the average polarization product and $N = \sum_i (N_i^{++} + N_i^{--} + N_i^{+-} + N_i^{-+})$ the total yield, the simplified statistical uncertainty is

$$\sigma_{\bar{A}_{LL}} \approx \frac{1}{\mathbb{P}^B\mathbb{P}^Y \sqrt{N}}. \quad (6.4)$$

The more-exact statistical uncertainty is given in appendix K, which is what is actually used in the calculation, but the result is extremely close to this approximation.

6.4 Background Corrections

Any measured asymmetry of any signal could be influenced by a possible nonzero asymmetry in the background under the signal. Given measurements of both the signal+background asymmetry and the background asymmetry alone, the signal asymmetry can be extracted from the signal+background asymmetry. Such a procedure is called the *background correction* to the asymmetry and it is applied to $A_{LL}^{\pi^0}$, given a background A_{LL} measurement from the mass window sideband region, which was discussed in section 3.7.3.

6.4.1 Implementation

Let A_M be a measured asymmetry in some mass signal window, with a nonzero background; A_M includes both the signal and background contributions. Let A_B be the asymmetry of the background and let A_S be the signal asymmetry, which we are trying to extract. Let F be the signal purity, defined as the fraction of the events within the mass window that are the true signal events; thus $1 - F$ is the fraction of events which are from the background. The measured asymmetry is then decomposed as

$$A_M = FA_S + (1 - F)A_B. \quad (6.5)$$

The signal asymmetry, corrected by the background asymmetry, is therefore

$$A_S = \frac{1}{F}A_M - \frac{1 - F}{F}A_B. \quad (6.6)$$

The uncertainties of A_M , A_B , and F , written σ_{A_M} , σ_{A_B} , and σ_F , propagate to the uncertainty of A_S as

$$\sigma_{A_S}^2 = \left(\frac{1}{F}\right)^2 \sigma_{A_M}^2 + \left(\frac{F - 1}{F}\right)^2 \sigma_{A_B}^2 + \left(\frac{A_B - A_M}{F^2}\right)^2 \sigma_F^2. \quad (6.7)$$

Typically asymmetries are measured as a function of a kinematic variable $v \in \{\eta, p_T, E\}$ or a set of such variables. The mean v in each measurement bin, denoted by $\langle v \rangle$, also needs to be corrected by the background. Its correction and uncertainty can easily be obtained by replacing the A s in equations 6.6 and 6.7 by $\langle v \rangle$ s. The final asymmetry plot is of $A_{LL}^{\pi^0}$ vs. p_T and we use $A_{LL}^{\pi^0} = A_S$, $A_{LL}^{\text{Tot}} = A_M$, and $A_{LL}^{\text{BG}} = A_B$, as well as similar notation for the mean p_T values. The background correction is then

$$A_{LL}^{\pi^0} = \frac{1}{F} \cdot A_{LL}^{\text{Tot}} - \frac{1 - F}{F} \cdot A_{LL}^{\text{BG}}, \quad (6.8)$$

$$\langle p_T^{\pi^0} \rangle = \frac{1}{F} \cdot \langle p_T^{\text{Tot}} \rangle - \frac{1-F}{F} \cdot \langle p_T^{\text{BG}} \rangle. \quad (6.9)$$

In practice, the shift in asymmetry due to the background correction is smaller than the statistical uncertainty, but it is sometimes larger than the systematic uncertainty; the shift in $\langle p_T \rangle$ is typically smaller than 0.01 GeV and is negligible, but nonetheless implemented. A correction on the p_T uncertainty is not implemented here, since the correction itself is negligible and the final p_T uncertainty given in the $A_{LL}^{\pi^0}$ measurement plots represents an overall systematic uncertainty anyway.

Regarding the background-corrected uncertainty, σ_{A_S} from equation 6.7, one can gain an understanding of how large the increase in statistical uncertainty will be, which arises from including the lower-statistics background asymmetry A_B determination along with the higher-statistics A_M in order to produce A_S , which has less statistics than A_M . Let N_M and N_B be the number of events used for A_M and A_B , respectively. Then, with P the polarization product,

$$\sigma_{A_B} = \frac{1}{P\sqrt{N_B}} = \frac{1}{P\sqrt{N_M(1-F)}} = \sigma_{A_M} \frac{1}{\sqrt{1-F}}. \quad (6.10)$$

Inserting this relation into equation 6.7 and assuming $A_B \approx A_M$ gives the ratio of background-corrected uncertainty to the original uncertainty as

$$\frac{\sigma_{A_S}}{\sigma_{A_M}} \approx \frac{\sqrt{2-F}}{F}, \quad (6.11)$$

which falls toward 1 as F increases; for $F > 0.75$, the gain in uncertainty is less than a factor of 1.5.

For each runset, which is a set of 5–10 consecutive (good) runs, contributions to A_{LL}^{Tot} and to A_{LL}^{BG} are included in separate MLM sums of equation 6.3. The final maximum likely values of these asymmetries are those which are used in equation 6.6 and equation 6.7 is used as the corrected statistical uncertainty. We now turn to a determination of the signal purity, F .

6.4.2 Signal and Background Fitting

Let m be invariant mass. The π^0 (or η) signal is modelled by a skewed Gaussian,

$$G(m) = \exp \left[-\frac{1}{2} \left(\frac{m - \mu}{\omega} \right)^2 \right] \times \left\{ 1 + \text{erf} \left[\frac{\alpha}{\sqrt{2}} \cdot \frac{m - \mu}{\omega} \right] \right\}, \quad (6.12)$$

where the fit parameters are μ , the expected and un-skewed signal mass, ω , the signal width, and α , which is related to the skewness. The background is modelled with a linear

combination of Chebyshev polynomials of the first kind:

$$B(m) = 1 + \sum_{k=1}^n b_k T_k(m), \quad \text{where } T_k(\cos \theta) = \cos(k\theta). \quad (6.13)$$

The degree used here is $n = 3$ and the coefficients $\{b_k\}$ are the fit parameters. Written explicitly,

$$B(m) = 1 + b_1 m + b_2 (2m^2 - 1) + b_3 (4m^3 - 3m). \quad (6.14)$$

Typical values of $\{b_1, b_2, b_3\}$ obtained from fitting are around

$$\begin{aligned} &\{1.5 \text{ to } 2, \quad -0.5 \text{ to } 0.5, \quad 1 \text{ to } 1.5\} \text{ for the outer region,} \\ &\{-1.5 \text{ to } -1, \quad -3 \text{ to } -0.5, \quad 1 \text{ to } 1.5\} \text{ for the inner region.} \end{aligned}$$

Now define the following additional fit parameters: the estimated number of pions N_π , η -mesons N_η , and background events N_B . Letting $G_\pi(m)$ and $G_\eta(m)$ be the skewed Gaussians for the pions and η -mesons, respectively, the full fit model $M(m)$ is

$$M(m) = N_\pi G_\pi(m) + N_\eta G_\eta(m) + N_B B(m). \quad (6.15)$$

The fit functions $\{G_\pi, G_\eta, B\}$ are considered as probability density functions and are normalized over the full mass range of 0 to 1 GeV. Consequently, the total number of events as determined by the fit algorithm is

$$\int_0^1 M(m) dm = N_\pi + N_\eta + N_B. \quad (6.16)$$

The signal range, S_π , over which the purity is calculated is determined using an algorithm similar to that used in determining the E -dependent π^0 mass window, described in section 3.7.3. The same idea of starting from the fit maximum and sliding left and right of the peak to a fraction of the maximum is used in order to establish a similarly defined signal range. The endpoints of S_π are used as boundaries of integrals used to calculate the π^0 purity.

Using the mass histogram $H(m)$, the pion purity F , defined as the fraction of events in the signal range S_π which are pions, is

$$F = N_\pi \cdot \frac{I_{G_\pi}}{I_H}, \quad (6.17)$$

where I_f , given a function of mass $f(m)$, is defined as

$$I_f := \int_{S_\pi} f(m) dm. \quad (6.18)$$

Note that for the case of I_H , the integral over S_π is replaced by a sum over the corresponding mass bins of $H(m)$, a histogram. In practice, it is better to use the background fit $B(m)$ compared to the data histogram $H(m)$ to determine the pion purity:

$$F = 1 - N_B \cdot \frac{I_B}{I_H} - N_\eta \cdot \frac{I_{G_\eta}}{I_H}. \quad (6.19)$$

Note that the η -meson contribution is included in case S_π , the window corresponding to $G_\eta(m)$, overlaps into the signal region S_π ; this usually does not happen and for the purpose of discussion can be ignored.

The propagated uncertainty on F is

$$\sigma_F^2 = \left(\frac{\partial F}{\partial N_B} \right)^2 \sigma_{N_B}^2 + \left(\frac{\partial F}{\partial I_H} \right)^2 \sigma_{I_H}^2 + \sum_{j=1}^3 \sum_{k=1}^3 \frac{\partial F}{\partial b_j} \frac{\partial F}{\partial b_k} \sigma_{b_j b_k} + 2 \sum_{k=1}^3 \frac{\partial F}{\partial N_B} \frac{\partial F}{\partial b_k} \sigma_{b_k N_B}, \quad (6.20)$$

where the covariances $\sigma_{f_1 f_2}$ can be written in terms of correlation coefficients $\rho_{f_1 f_2}$ via $\sigma_{f_1 f_2} = \rho_{f_1 f_2} \sigma_{f_1} \sigma_{f_2}$. The uncertainties $\{\sigma_{N_B}, \sigma_{b_k}\}$ and correlation coefficients may all be determined from the fit, and $\sigma_{I_H} = \sqrt{I_H}$. Putting everything together, the uncertainty is

$$\sigma_F^2 = \frac{1}{I_H^2} \left[I_B^2 \sigma_{N_B}^2 + \frac{N_B^2 I_B^2}{I_H} + \sum_{j=1}^3 \sum_{k=1}^3 N_B^2 I_{T_j} I_{T_k} \rho_{b_j b_k} \sigma_{b_j} \sigma_{b_k} + 2 \sum_{k=1}^3 I_B N_B I_{T_k} \rho_{b_k N_B} \sigma_{b_k} \sigma_{N_B} \right]. \quad (6.21)$$

This uncertainty is useful for determining the fit quality, but it does not impact $A_{LL}^{\pi^0}$ significantly, since σ_F is scaled by a factor of $(A_B - A_M)/F^2$ in equation 6.7, which is typically small.

The signal+background fitting is performed with an extended maximum likelihood fit algorithm by RooFit [104]. Figures 6.3 and 6.4 show sample fits for the outer and inner regions, respectively. The fit algorithm was performed runset-by-runset for all p_T bins used in $A_{LL}^{\pi^0}$. The fits were to data in a *fit window*, defined between a lower mass bound of typically 0.06–0.1 GeV up to an upper bound of 0.6–0.75 GeV. The exact boundaries chosen depended on the shape of the mass distribution and the performance of the fit algorithm; the algorithm would tend to be successful for various fit window boundaries, but after a relative

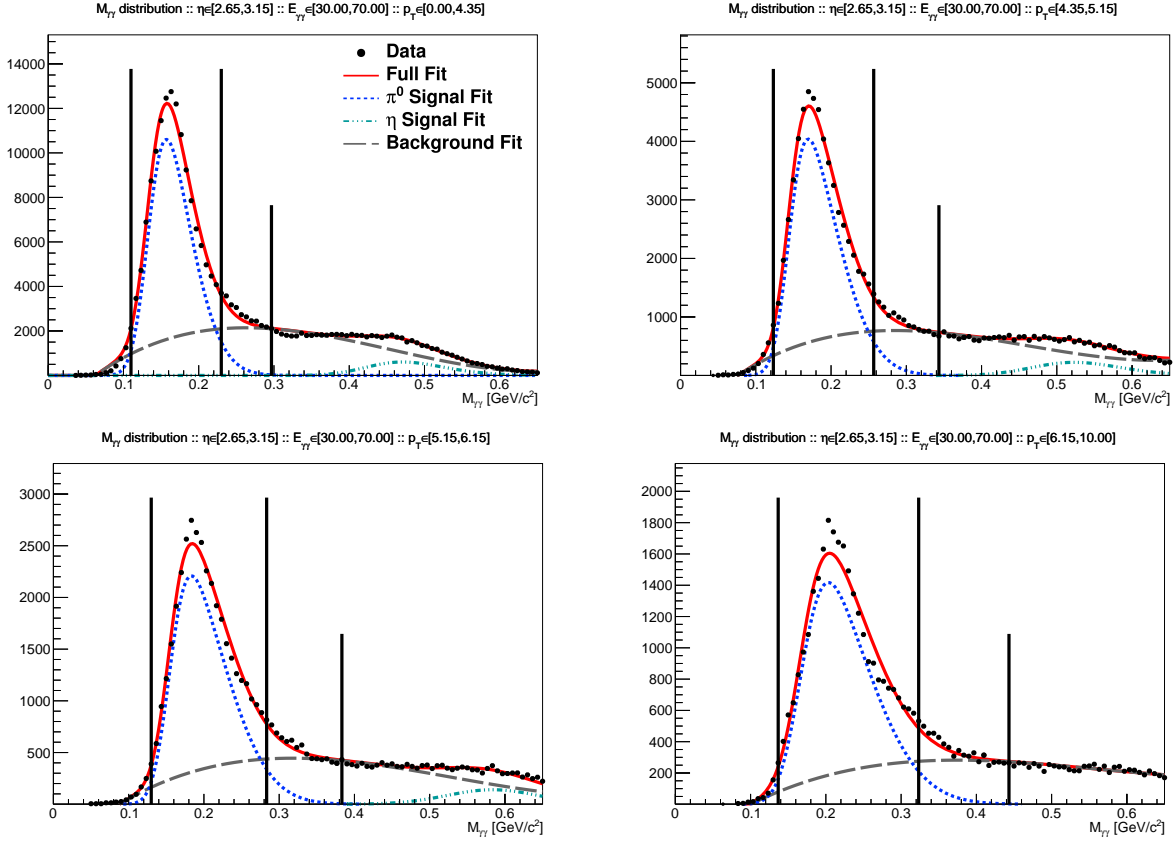


Figure 6.3: Sample fit results for each of the four p_T bins of the outer region. The fit legend is in the first panel. Tall vertical lines denote signal window S_π boundaries, and the short vertical line indicates the upper boundary of the sideband region (which is not used in the fit or calculation of F).

limit, the fit would fail if the window was too wide. Consequently, the fit window boundaries were chosen to push toward that limit, in order to maximize the subset of data considered in the fit. The lowest three p_T bins of the outer region included an η -meson fit; all other p_T bins did not show enough of an η -signal to warrant an η -meson fit attempt.

The signal peak fit height does not match the data peak height as well as one would hope, especially at higher p_T . This weakness justifies the preference toward using the background fit and data histogram integrals to calculate F (via equation 6.19), rather than making use of the signal fit integral. The sideband regions, along with the η -meson, seem to be reasonably well-fit for almost all of the runsets, therefore the background fit is more reliable than the signal fit for providing a measurement of F .

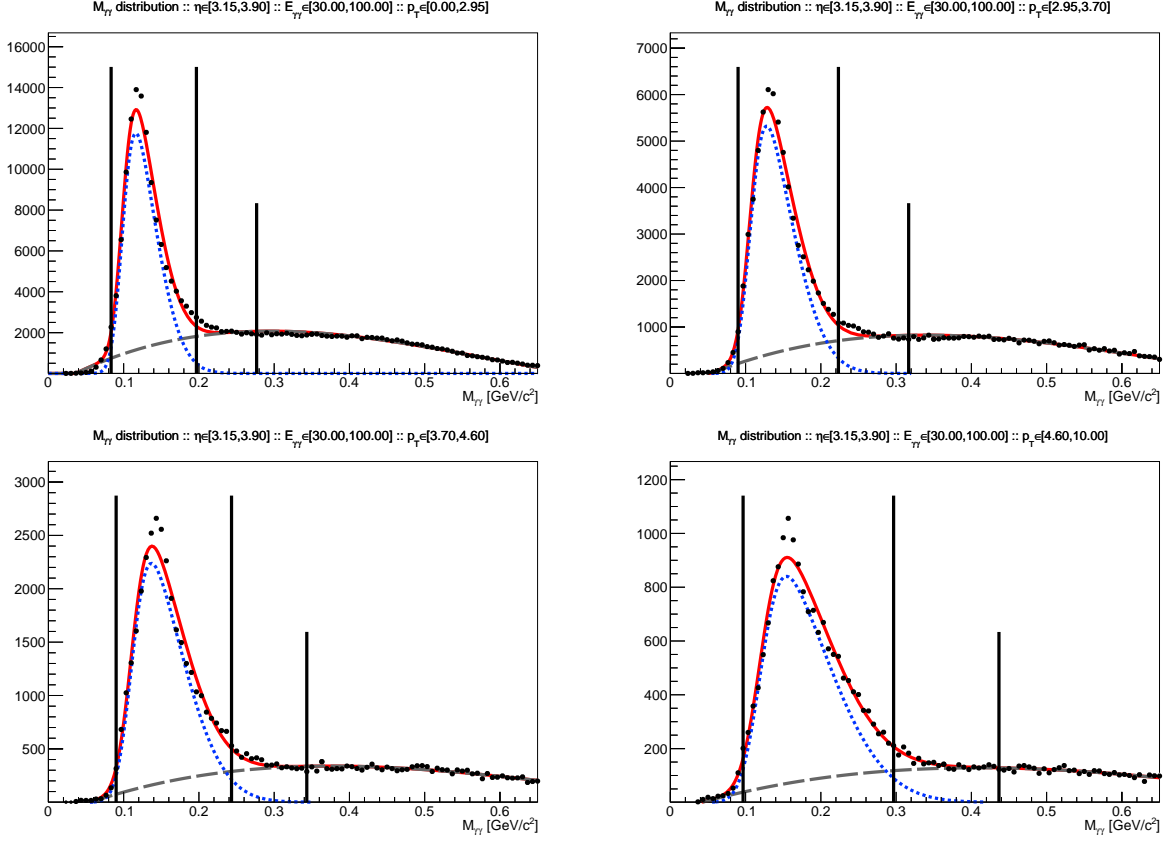


Figure 6.4: Sample fit results for each of the four p_T bins of the inner region.

6.4.3 Purity Results

Figures 6.5-6.8 show plots of pion purity F as a function of runset as well as a distribution, for each p_T bin for both η regions. The error bars are from equation 6.21. There is some slight time-dependence observed in some of the F values. In practice, one could background-correct each runset's $A_{LL}^{\pi^0}$ value, use each runset's value of F , and form an enhanced MLM sum; however, this would require a good measurement of the background asymmetry for each runset, which is not available since the background (sideband) sample size is much smaller than the signal sample size. Therefore, a single maximum-likely value of F for each p_T bin used in $A_{LL}^{\pi^0}$ is obtained instead; correcting for time-dependent F would not improve the $A_{LL}^{\pi^0}$ result much, given the context of the error bars on F .

These maximum likely purity values are indicated by the red constant fit lines. Figure 6.9 shows a plot of these values for each of the p_T bins used in $A_{LL}^{\pi^0}$. The error bars are from equation 6.7. The background level is 20–25% for the outer region and 10–15% for the inner region.

One might ask if there is a systematic uncertainty on $A_{LL}^{\pi^0}$ associated to this background

correction. Already, according to equation 6.7, there is an increase in statistical uncertainties from making this correction. On the other hand, it is reasonable to investigate the $A_{LL}^{\pi^0}$ values for different choices of F . It turns out that for changes in F within its uncertainty, changes in $A_{LL}^{\pi^0}$ are no more than 3×10^{-4} , which is comparable to the relative luminosity systematic uncertainty and well below the gain in statistical uncertainties. We have therefore left the uncertainty associated to the background correction to be taken into account via the increased statistical uncertainties.

The application of the background correction is shown in figures 6.10 and 6.11. The top-left panel of each figure shows a comparison of signal+background asymmetry A_{LL}^{Tot} in red, to the background asymmetry A_{LL}^{BG} in blue. These asymmetries are plotted versus their p_T bin means; the vertical uncertainties are statistical and the horizontal uncertainties are p_T bin RMS values. The bottom-left panel shows the difference $A_{LL}^{\text{Tot}} - A_{LL}^{\text{BG}}$ versus corrected p_T means, with error bars representing their propagated uncertainties (since A_{LL}^{Tot} and A_{LL}^{BG} are taken from separate parts of the M distribution, the uncertainty on their difference is the quadrature sum of their uncertainties). A fit line is drawn, showing the difference between A_{LL}^{Tot} and A_{LL}^{BG} is no more than one standard deviation. The top-right panel shows the extracted, background-corrected signal asymmetry $A_{LL}^{\pi^0}$ in green compared to A_{LL}^{Tot} in red. The bottom-right panel shows $A_{LL}^{\pi^0} - A_{LL}^{\text{Tot}}$ on the vertical axis versus $\langle p_T^{\pi^0} \rangle - \langle p_T^{\text{Tot}} \rangle$ on the horizontal axis; vertical error bars are not uncertainties, but differences in the uncertainties of the asymmetries, $\sigma_{A_{LL}^{\pi^0}} - \sigma_{A_{LL}^{\text{Tot}}}$. Differences between $A_{LL}^{\pi^0}$ and A_{LL}^{Tot} range from 2×10^{-4} to 1.5×10^{-3} .

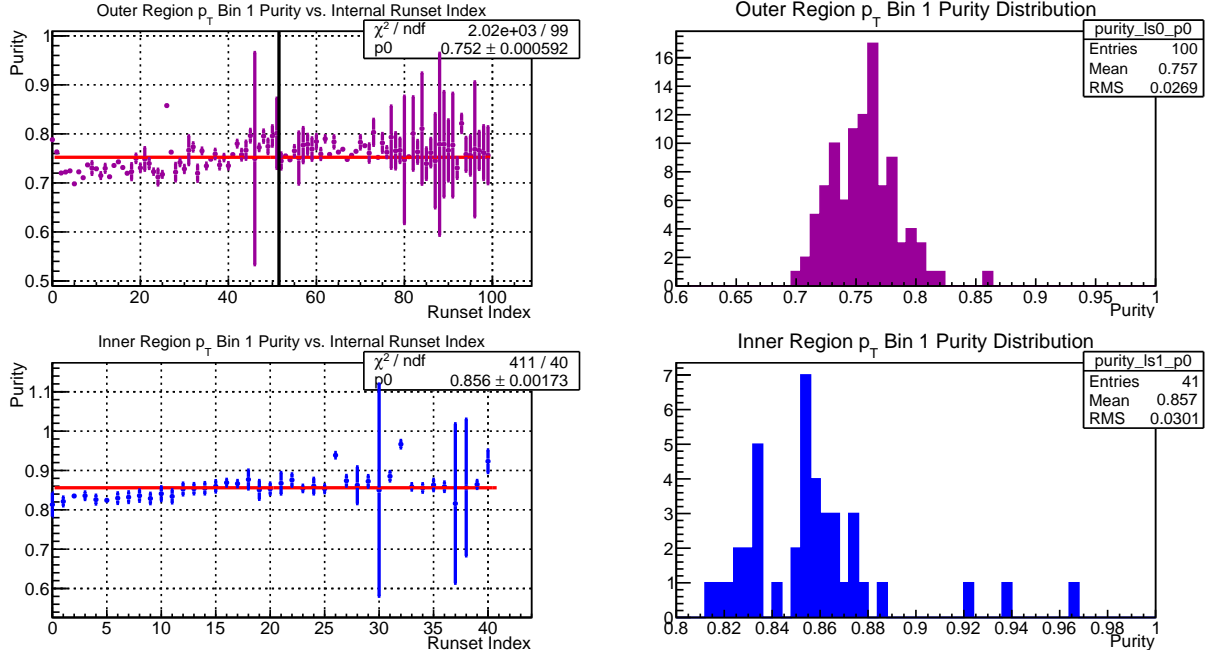


Figure 6.5: Left plots show the π^0 purity vs. a runset index, and right plots show the distributions of purities. The outer region (top plots) includes both Runs 12 and 13, and there is a vertical black line in the top-left plot showing the boundary between the Runs. The inner region (bottom plots) does not include Run 13. This is for p_T bin 1.

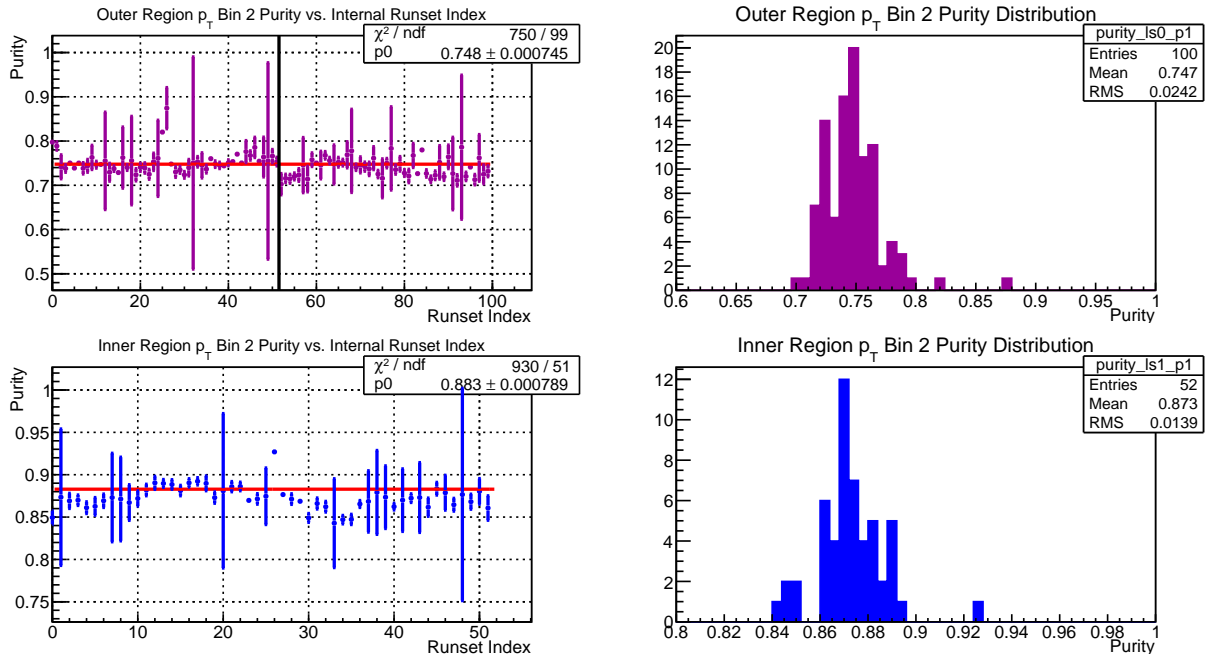


Figure 6.6: π^0 purities for p_T bin 2. Note that for p_T bins 2–4, there are more runsets plotted; this is because a few later runsets are completely cut out of p_T bin 1 via the time-dependent p_T threshold cut.

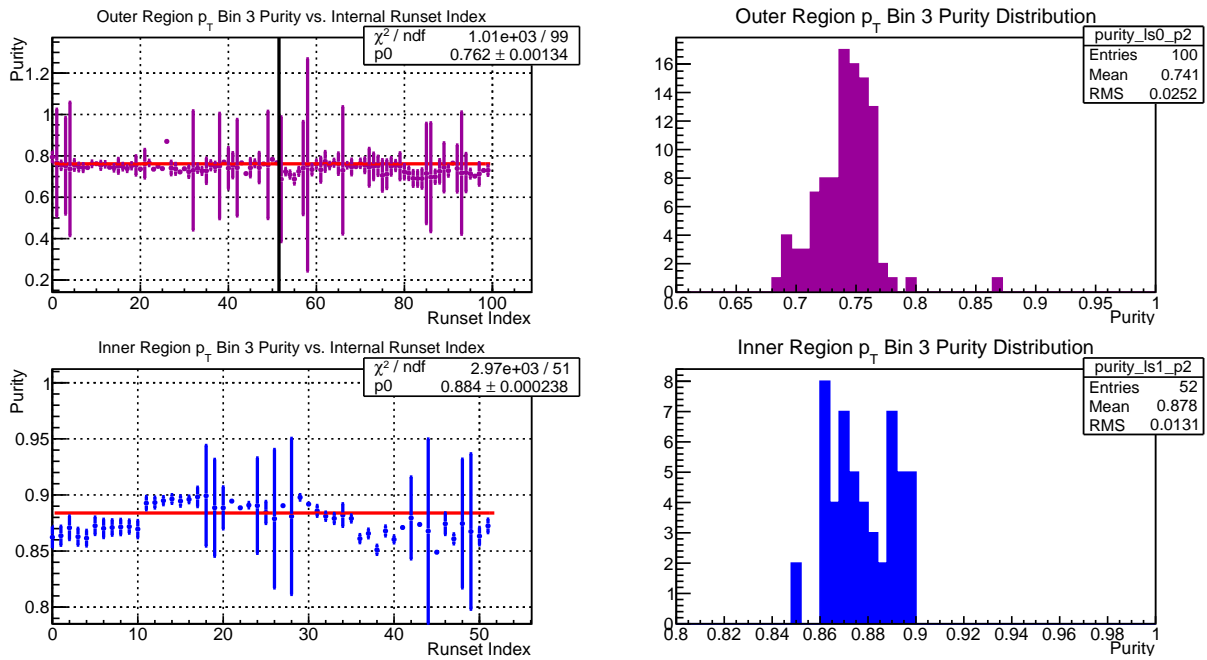


Figure 6.7: π^0 purities for p_T bin 3.

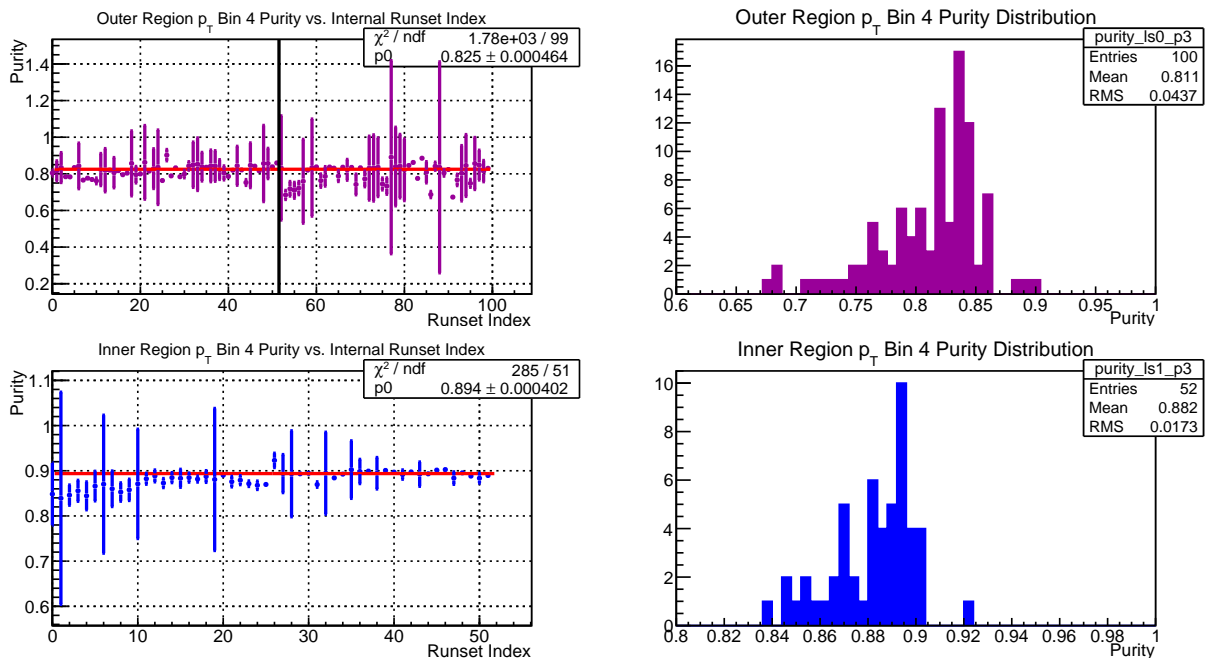


Figure 6.8: π^0 purities for p_T bin 4.

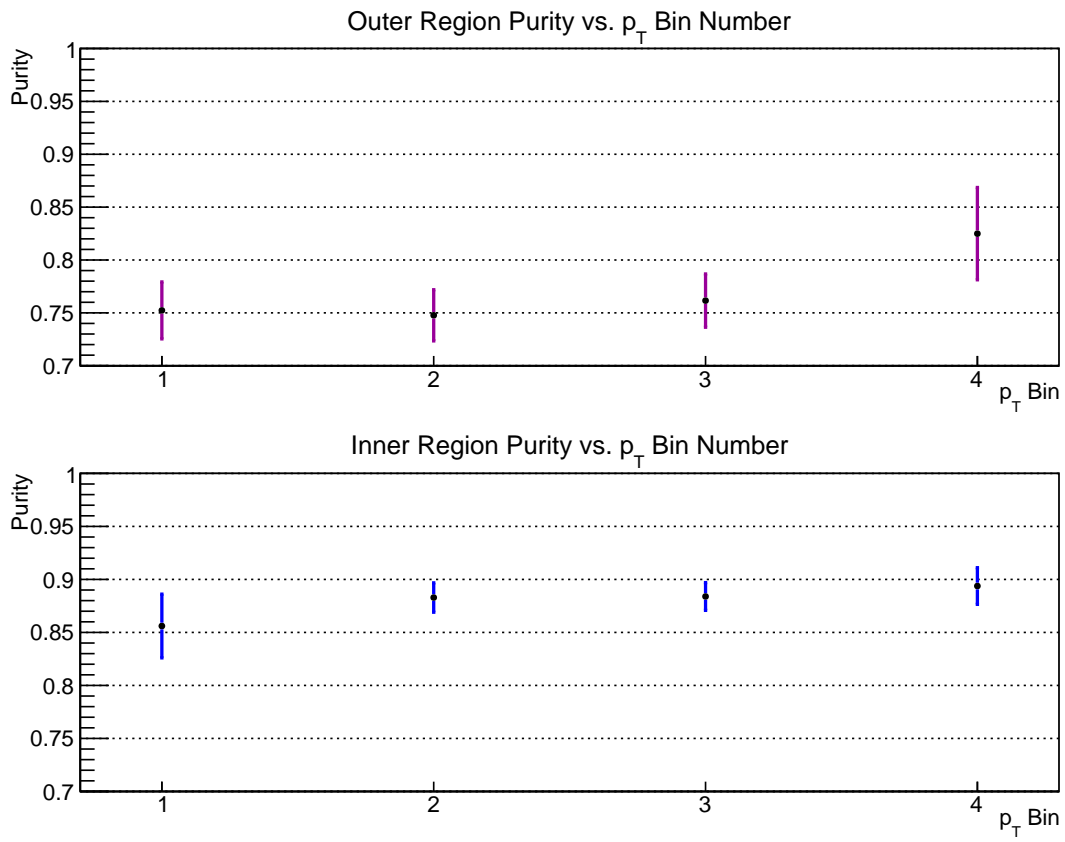


Figure 6.9: π^0 purities F for each p_T bin used in $A_{LL}^{\pi^0}$ for outer region (top) and inner region (bottom).

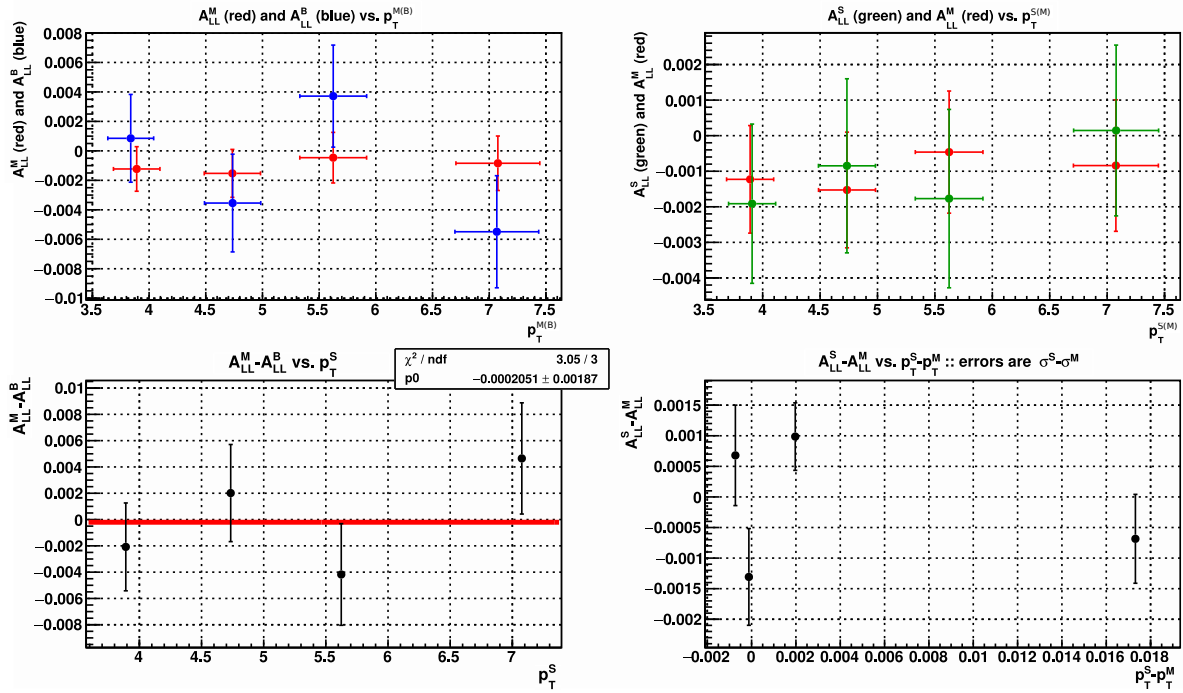


Figure 6.10: Background corrections implementation for outer region; see text for description of plots.

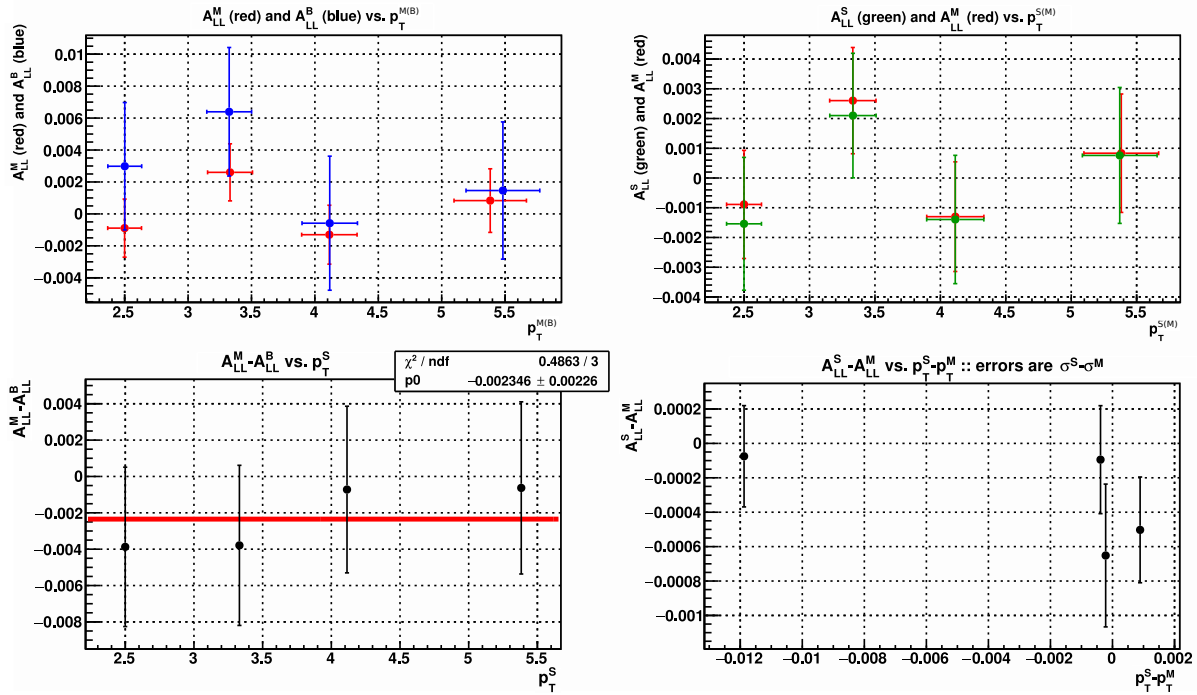


Figure 6.11: Background corrections implementation for inner region; see text for description of plots.

Chapter 7

$A_{LL}^{\pi^0}$ Measurement Result

We are now prepared to discuss the $A_{LL}^{\pi^0}$ measurement result. This measurement has been released first in 2014 [105], as a *preliminary* measurement, meaning that some corrections and systematics were not yet studied. Four years later, it has been published as a *final* measurement [15], which includes everything discussed in this dissertation. This chapter presents both of these versions, along with a discussion of the impact of the result.

7.1 Preliminary $A_{LL}^{\pi^0}$ Measurement

Measurements at STAR are typically released to the public twice: the first release is a preliminary release, and is an early look at a particular measurement; typically a preliminary measurement is in a state where further analysis is unlikely to change its story much. After further detailed analysis, when a particular measurement is mature enough and well-vetted within the collaboration, it is published as a final result. The preliminary measurement of $A_{LL}^{\pi^0}$ was released in 2014 [105], and does not include many of the topics that have been discussed, such as the p_T systematic uncertainty.

Most of the π^0 selection cuts were somewhat less-restrictive than they are for the final measurement. The inner and outer regions were both analyzed together, and the asymmetry was determined for 6 bins in energy, integrating over p_T , as well as for 6 bins in p_T , integrating over energy. The π^0 selection cuts were the following:

- $2.5 < \eta < 4$
- $2.5 < p_T < 10$ GeV for Run 12 and $2.0 < p_T < 10$ GeV for Run 13
- $30 < E < 100$ GeV
- $Z < 0.8$

- Similar E -dependent mass cut, but it was not yet time-dependent

The time-dependent p_T threshold cut was also not yet implemented, meaning a fraction of sub-threshold π^0 s were included in the analysis (see figures 3.25-3.27).

Two π^0 isolation cones sizes were used (see section 3.4.4): 35 mrad and 100 mrad, inspired by the dependence of $A_N^{\pi^0}$ on π^0 isolation, where higher $A_N^{\pi^0}$ is observed for more-isolated π^0 s [58]. The relative luminosity used for the preliminary plots was measured by averaging the R_3 values obtained from the VPDE, VPDW, and VPDX using the CDF corrections, since the preliminary plots were released before the rate-safe corrections were implemented. Finally, the beam-current fill-by-fill polarization measurements were used, rather than the luminosity-weighted averages of the time-dependent polarizations; the impact of this change on $A_{LL}^{\pi^0}$ is negligibly small, however the RHIC polarimetry group prefers the use of luminosity-weighted average polarizations for any asymmetry analysis.

Figures 7.1 and 7.2 show $A_{LL}^{\pi^0}$ plotted vs. E and p_T , respectively. The vertical lines are statistical uncertainties, the horizontal lines are E and p_T bin RMSs, and the vertical size of the shaded boxes represents the systematic uncertainty from the relative luminosity. For the relative luminosity systematic, the widths of the S_{LL} distributions were used (for Run 13, the distribution was bimodal, and the width of the wider distribution was used), plus the distribution mean. For Run 12, the systematic uncertainty on $A_{LL}^{\pi^0}$ was 2.8×10^{-4} and for Run 13 it was 6.2×10^{-4} . These uncertainties were averaged together, weighted by π^0 statistics for each bin.

The red markers are for 35 mrad π^0 isolation, and the blue markers are for 100 mrad isolation. For visibility, the 100 mrad points are offset to the right by 1 GeV in energy in figure 7.1 and by 0.1 GeV in p_T in figure 7.2. Unlike $A_N^{\pi^0}$, which depends on π^0 isolation, no such dependence is observed in $A_{LL}^{\pi^0}$. Given the statistical and systematic uncertainties, this measurement does not show any significant nonzero asymmetry; the highest p_T point in figure 7.2 is an outlier, being almost two standard deviations from the zero line, however it was later found that hot towers were contributing to this point's anomalously high asymmetry. The statistical and systematic uncertainties therefore represent overall bounds on the size of $A_{LL}^{\pi^0}$ for these forward kinematics.

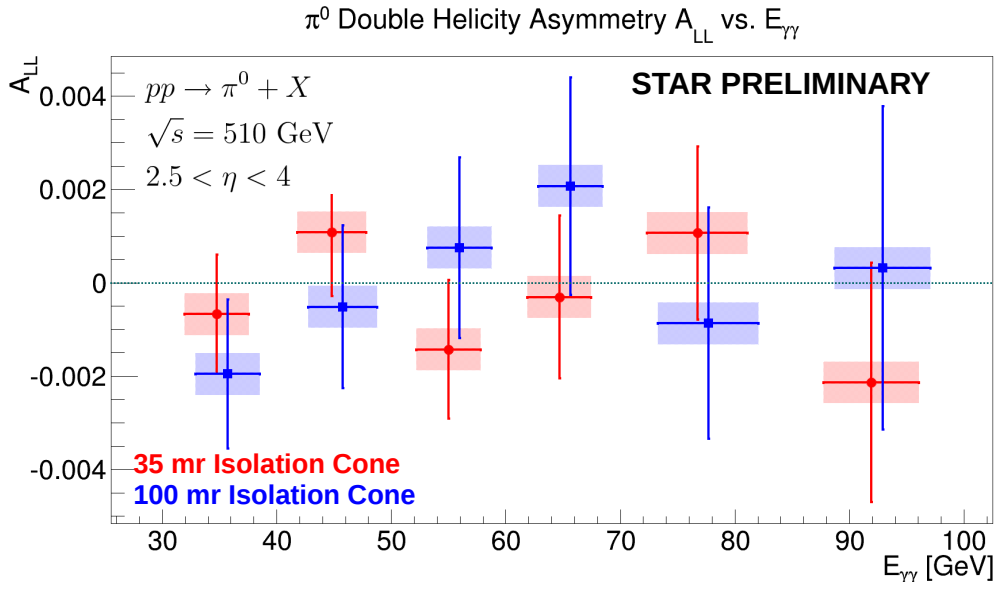


Figure 7.1: Preliminary measurement of $A_{LL}^{\pi^0}$ vs. E ; see text for details.

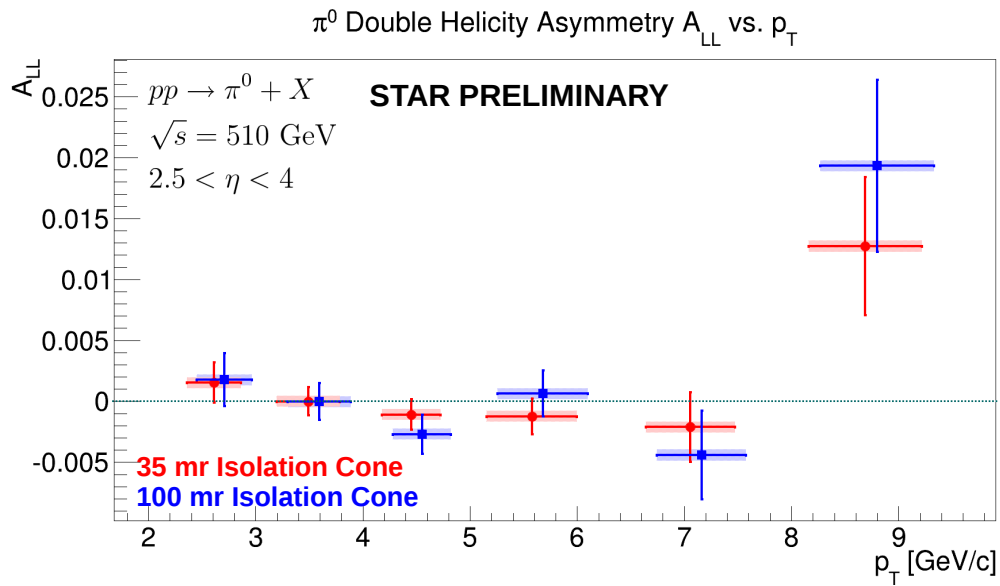


Figure 7.2: Preliminary measurement of $A_{LL}^{\pi^0}$ vs. p_T ; see text for details.

7.2 Final $A_{LL}^{\pi^0}$ Measurement

Figure 7.3 shows the final version of the $A_{LL}^{\pi^0}$ measurement [15], as a function of p_T , for the outer and inner η regions (see table 6.1 for the binning). Numerical values for the points and errors are provided in table 7.1. The vertical error bars represent the statistical uncertainty on $A_{LL}^{\pi^0}$, and the vertical extent of the shaded boxes represents the $A_{LL}^{\pi^0}$ shift systematic uncertainty from relative luminosity and polarization transverse component. The horizontal extent of the shaded boxes represents the p_T systematic uncertainty. The polarization scale systematic uncertainty of 6.7% is not included in the plot.

Extrapolations of the present theoretical models of $A_{LL}^{\pi^0}(p_T)$ to these kinematics have been plotted as well; the measured $A_{LL}^{\pi^0}$ is in agreement with both of them. These extrapolations were determined from next-to-leading order calculations from [106, 107] and the following PDF and polarized PDF sets were supplied to the algorithms used to generate these predictions:

- NNPDFpol1.1 polarized PDF [13] with NNPDF2.3 PDF [108]
- DSSV14 polarized PDF [14] with CTEQ6M PDF [109]

For both of these, the DSS fragmentation functions were used [110].

The uncertainty band on the theoretical $A_{LL}^{\pi^0}(p_T)$ extrapolation is that for the NNPDF prediction. The NNPDF collaboration trains a neural network based fit on Monte Carlo generated copies of the data, called replicas, which take into account the data nominal values, errors, and correlations. Given 100 replicas, the variance in the neural network parameterized $\Delta g(x, Q^2)$ was determined, along with the central value; this was done for the possible values of x and Q^2 corresponding to the pion transverse momenta. The next-to-leading order calculation of $A_{LL}^{\pi^0}$ was performed for the variations of $\Delta g(x, Q^2)$ within one standard deviation, providing the error band. It is worth mentioning that this is an uncertainty band on an *extrapolation*, which is somewhat open to interpretation.

We have also fit the $A_{LL}^{\pi^0}$ measurement data points to a constant, which gives an overall maximum likely value for each pseudorapidity region, denoted $\bar{A}_{LL}^{\pi^0}$; note that the fit result is not plotted. For the fit, the $A_{LL}^{\pi^0}$ statistical and shift systematic uncertainties are added in quadrature for each point, but the polarization scale systematic uncertainty is not included. The constant fit results, along with the χ -squared per number of degrees of freedom are:

- Outer Region: $\bar{A}_{LL}^{\pi^0} = -0.0011 \pm 0.0012$, with $\chi^2/\text{NDF} = 0.47/3$
- Inner Region: $\bar{A}_{LL}^{\pi^0} = +0.000018 \pm 0.0011$, with $\chi^2/\text{NDF} = 2.0/3$

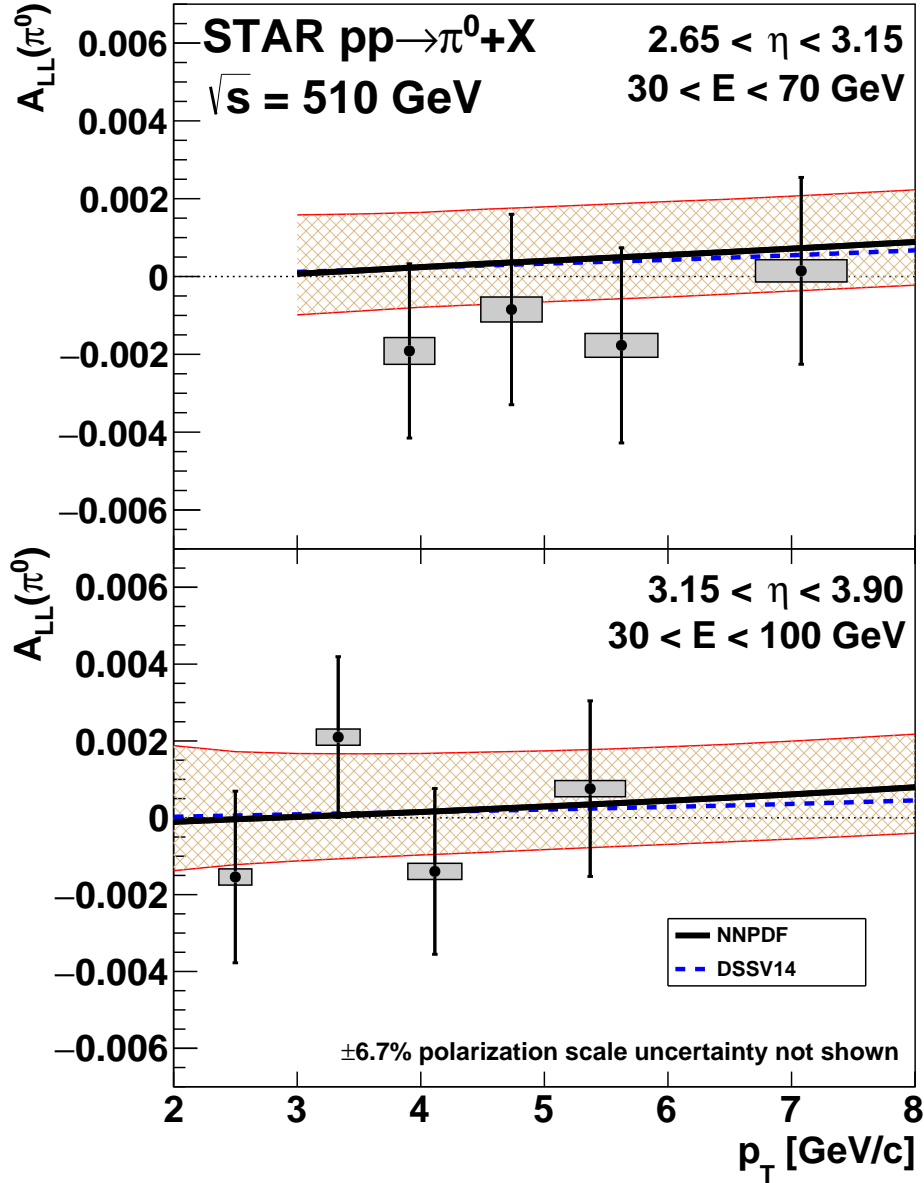


Figure 7.3: Final measurement of FMS $A_{LL}^{\pi^0}$ vs. p_T for the outer region (top) and inner region (bottom). The vertical error bars are statistical uncertainties, the vertical extent of the shaded boxes is the shift systematic uncertainty, and the horizontal extent is the p_T systematic uncertainty. Extrapolations of model calculations for $A_{LL}^{\pi^0}(p_T)$ to these kinematics are also plotted, where the dashed blue curve is that from DSSV14 [14] and the solid black curve that from NNPDF [13]. The hatched band represents the uncertainty on the NNPDF extrapolation, as described in the text.

p_T Bin	$\langle p_T \rangle$	$A_{LL}^{\pi^0}$	$A_{LL}^{\pi^0}$ Stat. Unc.	$A_{LL}^{\pi^0}$ Sys. Unc.	p_T Sys. Unc.
Outer Pseudorapidity Region: $2.65 < \eta < 3.15, 30 < E < 70$ GeV					
1	3.91	-0.00191	0.0022	0.00034	0.21
2	4.73	-0.00085	0.0024	0.00032	0.25
3	5.62	-0.00177	0.0025	0.00031	0.29
4	7.08	+0.00015	0.0024	0.00029	0.37
Inner Pseudorapidity Region: $3.15 < \eta < 3.90, 30 < E < 100$ GeV					
1	2.50	-0.00154	0.0022	0.00021	0.13
2	3.33	+0.00210	0.0021	0.00021	0.18
3	4.11	-0.00140	0.0022	0.00021	0.22
4	5.37	+0.00076	0.0023	0.00021	0.29

Table 7.1: $A_{LL}^{\pi^0}$ measurement numerical values. The columns are p_T bin number, mean p_T (GeV) of the point, $A_{LL}^{\pi^0}$ measurement in that p_T bin, $A_{LL}^{\pi^0}$ statistical uncertainty, $A_{LL}^{\pi^0}$ shift systematic uncertainty, and p_T systematic uncertainty (GeV).

7.3 Discussion and Outlook

The measured $A_{LL}^{\pi^0}$ is consistent with both theoretical extrapolations. While the gluon polarization models, represented by $\Delta g(x)$, are rather unconstrained in the low- x region ($x < 0.05$), these extrapolations essentially assume the central $\Delta g(x)$ fit, which is nearly zero at low x . Although all of the $A_{LL}^{\pi^0}$ data points' error bars cross the zero line, this measurement presents *upper bounds* on $A_{LL}^{\pi^0}$ for these forward π^0 kinematics. This is the first time $A_{LL}^{\pi^0}$ has been assessed for forward π^0 kinematics to such a high sensitivity (*cf.*, for example, figure 1.17, [60]). Our measurement is sensitive to gluons down to $x \sim 10^{-3}$ (see figure 1.15), a region that is *abundant* with soft gluons. A new global analysis combining other recent results is needed in order to constrain the true size of $\Delta g(x)$ for these low- x gluons, as well as the shape of $\Delta g(x)$ at higher x .

Along with this measurement, several other recent A_{LL} measurements from RHIC will be included in the next global analysis [111]. In particular, some recent measurements at STAR include inclusive jets and dijets at central pseudorapidity ($|\eta| < 1$) [64, 65, 112], as well as inclusive dijets at intermediate pseudorapidity ($0.8 < \eta < 2$) [62]. Figure 7.4 gives a sense of the impact these new data will have on the upcoming global analyses. It defines the contributions to the proton spin from the gluons and the quarks as *running integrals*, where the integrals are taken over the polarized PDFs from a minimum x value, x_{\min} , up to 1:

$$\Delta G|_{x_{\min}}^1 := \int_{x_{\min}}^1 dx \Delta g(x), \quad (7.1)$$

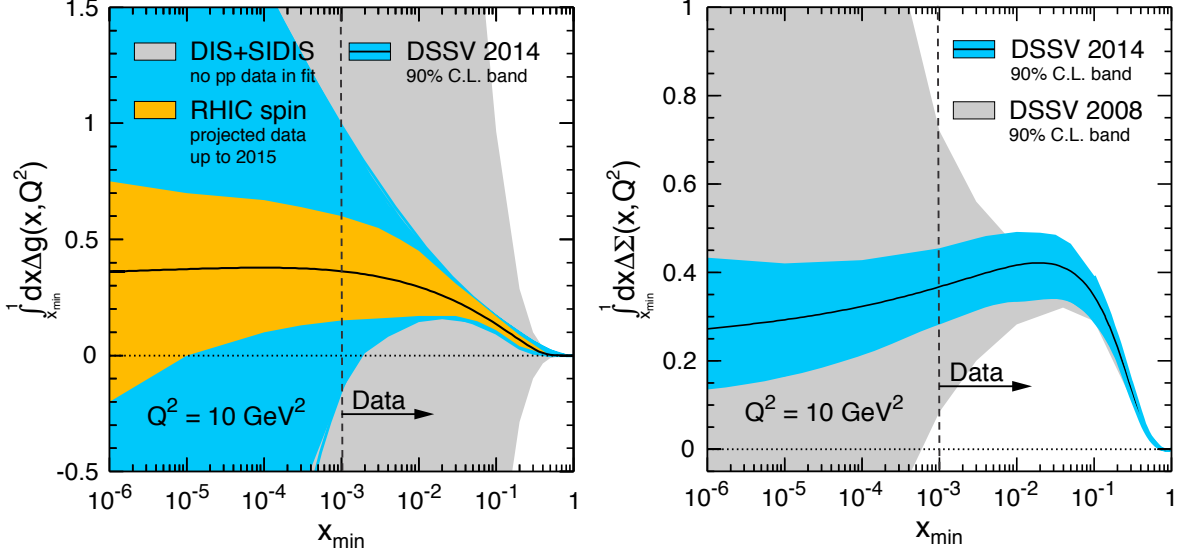


Figure 7.4: Running integrals $\Delta G|_{x_{\min}}^1$ (left) and $\Delta \Sigma|_{x_{\min}}^1$ (right), indicated by the solid black curves. The gray and blue bands are for the DSSV08 [5] and DSSV14 [14] global analyses, respectively. The yellow band indicates the projected uncertainties for the upcoming global analysis. Figure adapted from [113].

$$\Delta \Sigma|_{x_{\min}}^1 := \int_{x_{\min}}^1 dx \Delta \Sigma(x) = \sum_{f \in \{q, \bar{q}\}} \int_{x_{\min}}^1 dx \Delta f(x). \quad (7.2)$$

The lower x_{\min} is, the better understood ΔG and $\Delta \Sigma$ are; some say that these running integrals may converge to a central value after x_{\min} is low enough, but that remains to be investigated.

The solid black curves in figure 7.4 represent $\Delta G|_{x_{\min}}^1$ and $\Delta \Sigma|_{x_{\min}}^1$ from the DSSV14 global analysis [14]; their uncertainty bands are given by the blue shaded regions. The gray bands represent the uncertainties from the previous DSSV08 global analysis [5]. The yellow band represents projected uncertainties for the upcoming global analysis, which will be based on data for $x > 10^{-3}$, indicated by the vertical dashed line. While these plots are rather open to interpretation, they provide some sense of the impact that the recent RHIC pp data will have on our understanding of ΔG , with the largest improvements to be seen in the region $10^{-3} < x < 10^{-2}$.

One might ask if the analyzed π^0 s are primarily originating from the QCD hard scattering, or if a substantial fraction of them are coming from proton remnants or other multi-parton interactions. $A_{LL}^{\pi^0}$ could be diluted by π^0 s which do not come from the hard-scattering. Typically NLO calculations fold in these additional π^0 sources, as does Pythia (provided we do not try to simulate gluons which are *too* soft). One could instead look at forward dijet

asymmetries, which are guaranteed to originate from the hard scattering. In this channel, the asymmetry will not be diluted, however dijets represent a rather small fraction of the overall cross section.

Measuring A_{LL} for forward dijets in an upgraded forward calorimetry system at STAR, where both jets are in the range $2.8 < \eta < 3.7$ (and $\sqrt{s} = 500$ GeV), could push sensitivity down to $x \sim 10^{-5}$ [114]. This is one of the many motivations for an upgrade to the forward calorimetry at STAR, which includes a tracking system in the STAR barrel, along with a new electromagnetic calorimeter and a new hadronic calorimeter, both to be installed in place of the FMS [115]. The FMS was dismantled in 2018, allowing for the installation of these new systems to begin, opening the door to many exciting new measurements. Moreover, the upcoming Electron Ion Collider (EIC), which will collide polarized electron beams with polarized proton beams, will provide many more precise measurements, further pushing the boundaries of our understanding of the proton and of QCD in general into new frontiers [113].

Appendices

Appendix A

Decay Kinematics of $\pi^0 \rightarrow \gamma + \gamma$

A.1 Invariant Mass

Consider the decay of a π^0 with momentum along the z axis into two photons spanning the xz plane with 4-momenta

$$k_1 = (E_1, E_1 \sin \alpha_1, 0, E_1 \cos \alpha_1), \quad (\text{A.1})$$

$$k_2 = (E_2, -E_2 \sin \alpha_2, 0, E_2 \cos \alpha_2). \quad (\text{A.2})$$

The invariant mass squared is

$$M^2 = (k_1 + k_2)^2 = 2k_1 k_2 = 4E_1 E_2 \sin^2 \frac{\alpha}{2}, \quad (\text{A.3})$$

where $\alpha = \alpha_1 + \alpha_2$ is the photon decay opening angle. Let $E = E_1 + E_2$ be the total energy and let $Z = |E_1 - E_2|/E$ be the energy imbalance. The invariant mass is then

$$M = 2\sqrt{E_1 E_2} \cdot \sin \frac{\alpha}{2} \approx \sqrt{E_1 E_2} \cdot \alpha \quad (\text{A.4})$$

$$= E\sqrt{1 - Z^2} \cdot \sin \frac{\alpha}{2} \approx \frac{E}{2}\sqrt{1 - Z^2} \cdot \alpha. \quad (\text{A.5})$$

The mass can be thought of as a function of E_1 and E_2 or of E and Z , given a fixed value of α . Solving for the opening angle gives

$$\alpha = 2 \arcsin \left(\frac{M}{2\sqrt{E_1 E_2}} \right) \approx \frac{M}{\sqrt{E_1 E_2}} \quad (\text{A.6})$$

$$= 2 \arcsin \left(\frac{M}{E\sqrt{1 - Z^2}} \right) \approx \frac{2M}{E\sqrt{1 - Z^2}}. \quad (\text{A.7})$$

Note that the opening angle spans approximately $z\alpha/w$ cells, where z is the distance to the interaction point and w is the cell width. For $z = 7$ m, a 10 mrad opening angle spans 7 cm, which is just over 1 large cell width or just under 2 small cell widths.

In order to explore the inter-dependencies of the kinematic variables, the next few pages show various planes cut from the $M(E, Z, \alpha)$ and $M(E_1, E_2, \alpha)$ hypersurfaces.

- Figure A.1 shows M -contours in the α vs. E plane for fixed values of Z , as described by equation A.7. These plots show the energy-dependence of the opening angle: higher energy pions ($M = 0.135$ GeV) have smaller opening angles than those with lower energy, and the more massive η -mesons ($M = 0.55$ GeV) have much larger opening angles than pions.
- Figure A.2 shows α -contours in the M vs. E plane for fixed values of Z , as described by equation A.5. For constant opening angles, the invariant mass rises as a function of energy. If the opening angle as a function of energy is overestimated, then data will tend to show an increase in the mass as a function of energy. In other words, the observation of a positive linear dependence of the invariant mass on the energy is evidence of an overestimation of the photon separation at higher energies.
- Figure A.3 shows α -contours in the M vs. Z plane for fixed values of E . At higher Z , the mass decreases for fixed values of α . This decrease is more extreme at higher energies. Note that the uncertainty on Z becomes much greater as the photon separation decreases and approaches the region where it is difficult to distinguish 1-photon clusters from those with 2 photons.
- Figures A.4 and A.5 show contours of $\alpha(E_1, E_2)$ and $\alpha(E, Z)$ given M fixed at the π^0 mass and at the η mass. Placing an upper limit on a π^0 opening angle, a consequence of an isolation cone, helps reduce contributions from low energy *soft* photons.

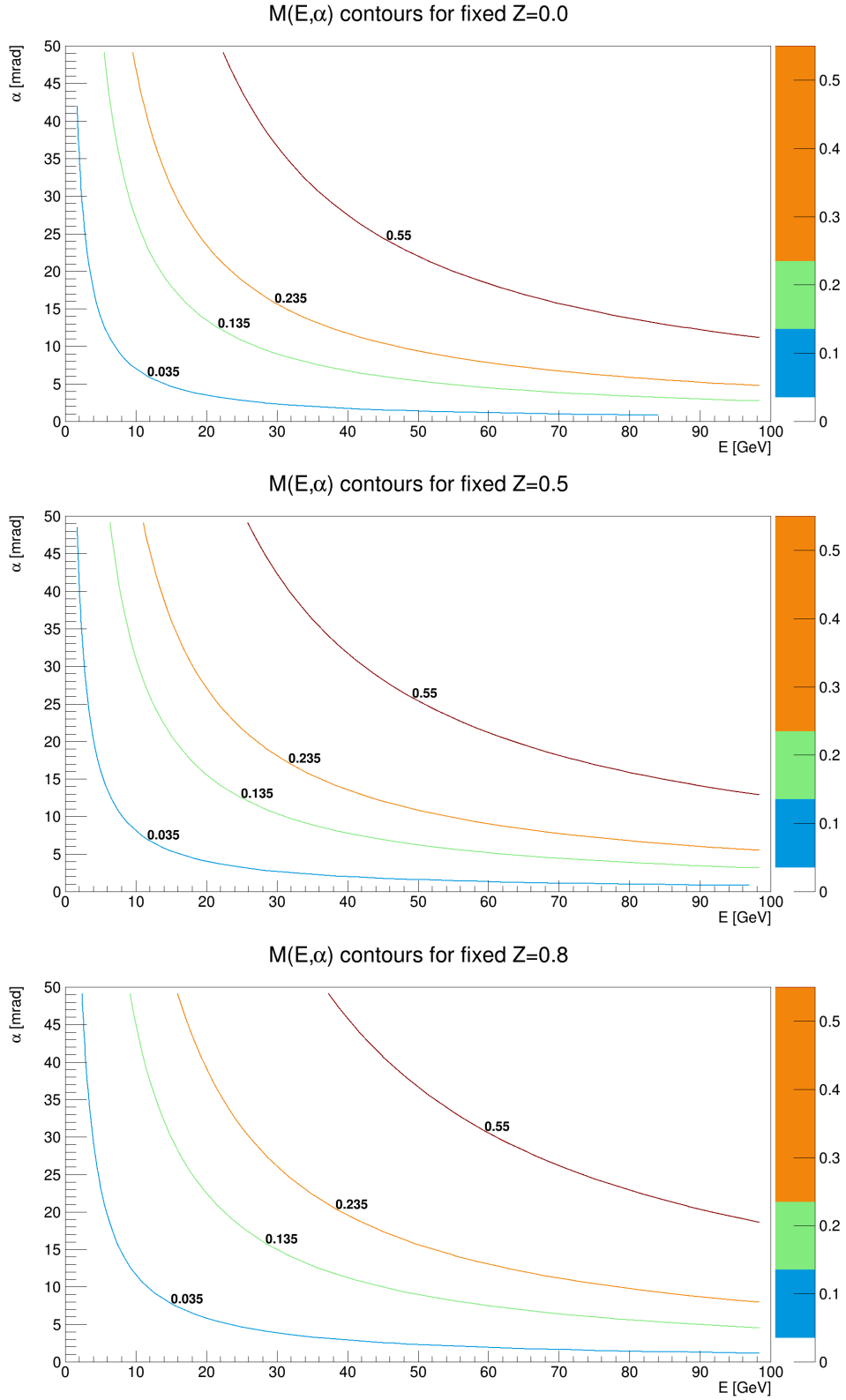


Figure A.1: α vs. E plane with M contours for fixed $Z = 0$ (top), $Z = 0.5$ (middle), and $Z = 0.8$ (bottom).

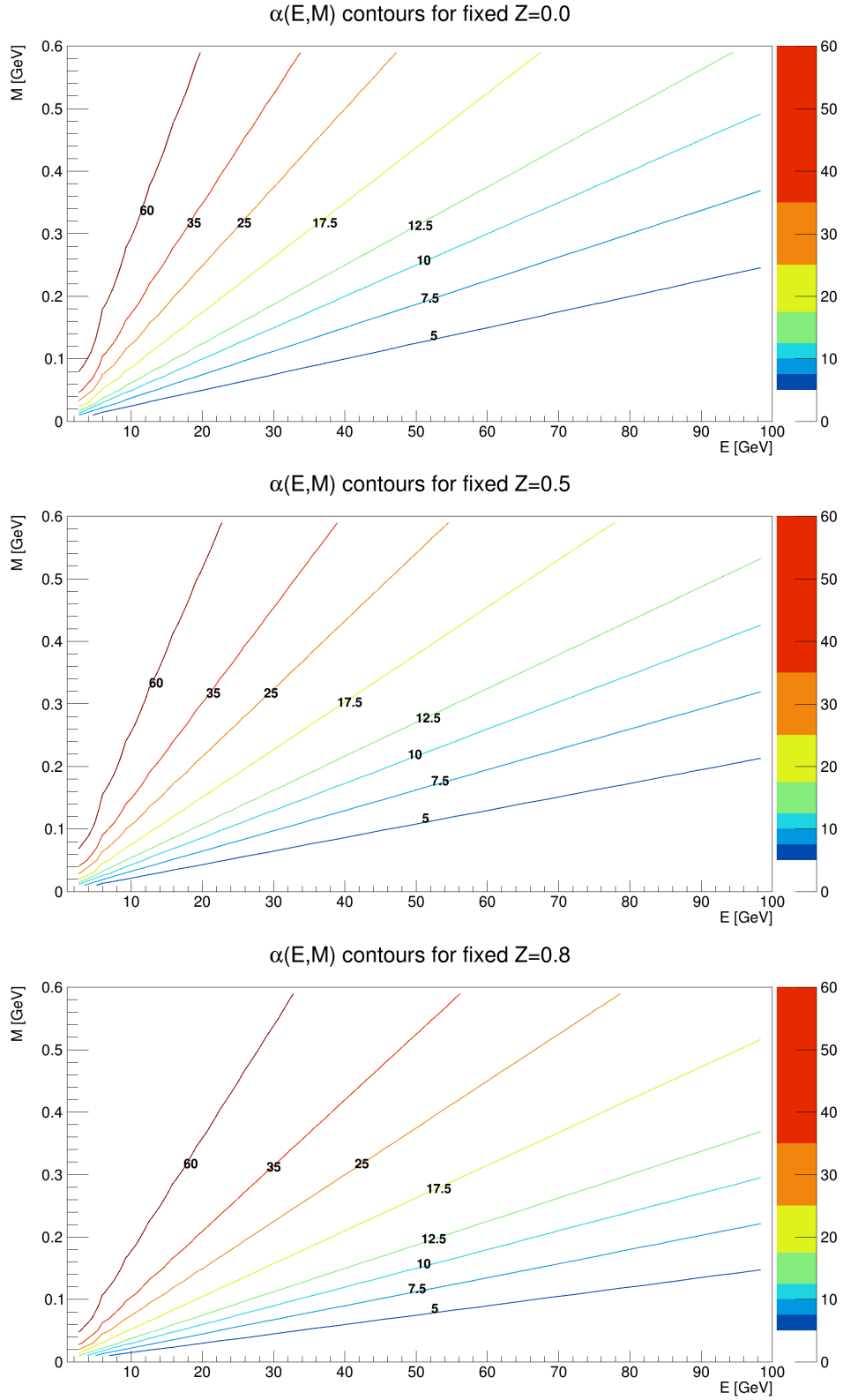


Figure A.2: M vs. E plane with α contours for fixed $Z = 0$ (top), $Z = 0.5$ (middle), and $Z = 0.8$ (bottom).

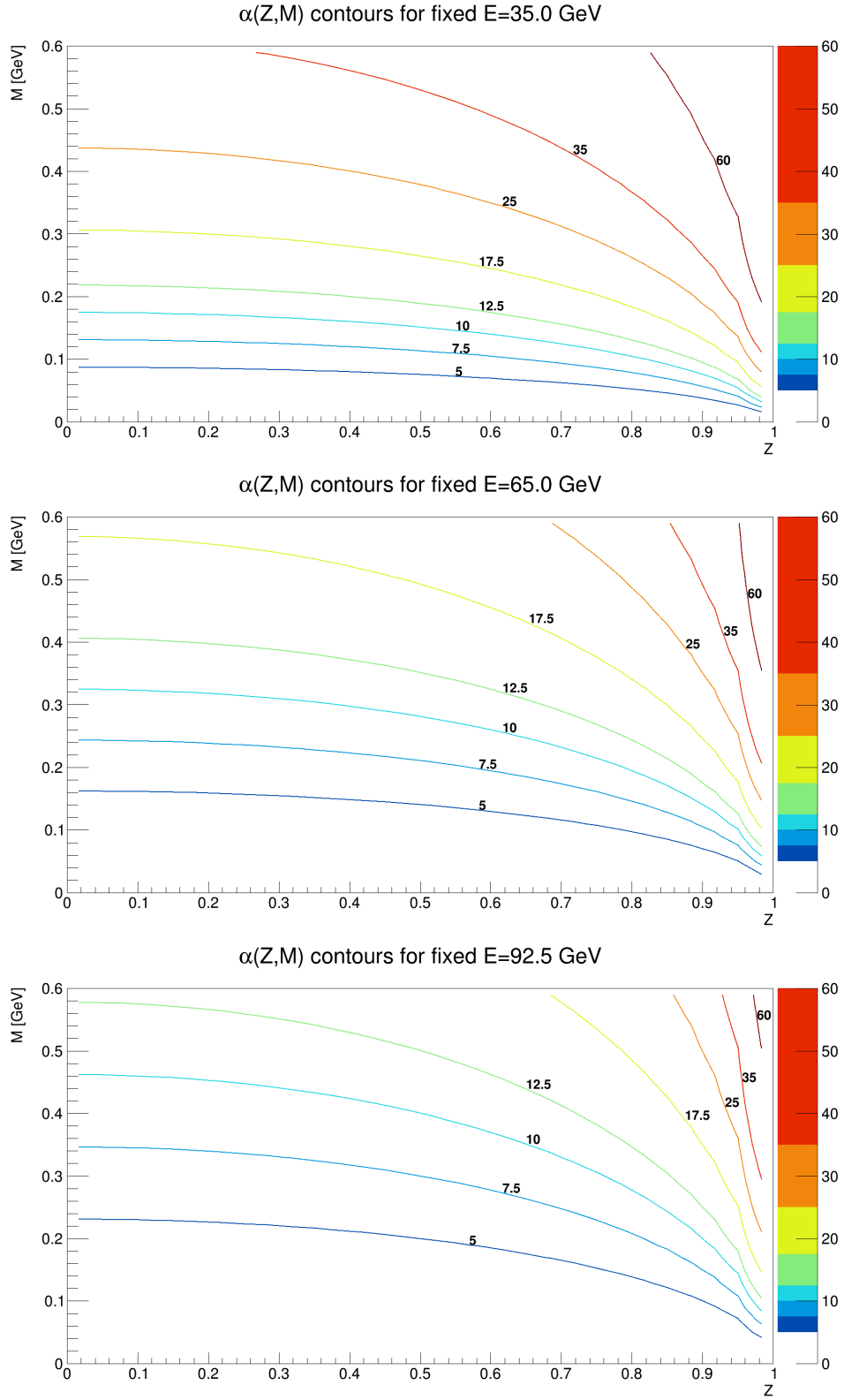


Figure A.3: M vs. Z plane with α contours for fixed $E = 35$ GeV (top), $E = 65$ GeV (middle), and $E = 92.5$ GeV (bottom).

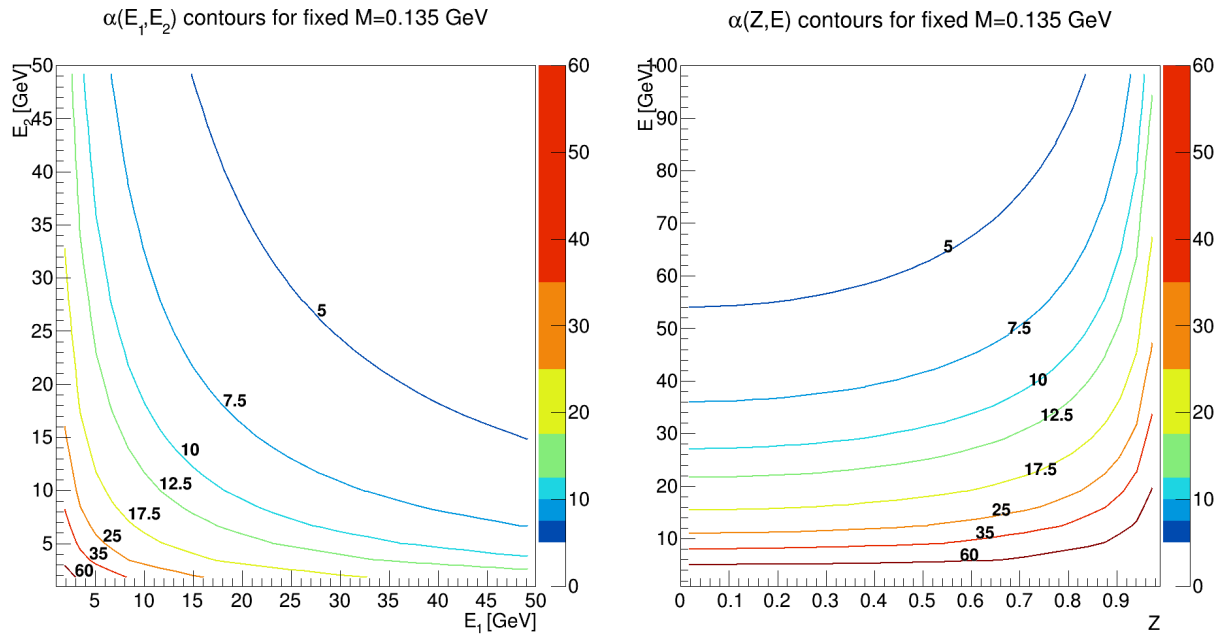


Figure A.4: E_2 vs. E_1 plane (left) and E vs. Z plane (right) with α contours for M fixed at the π^0 mass.

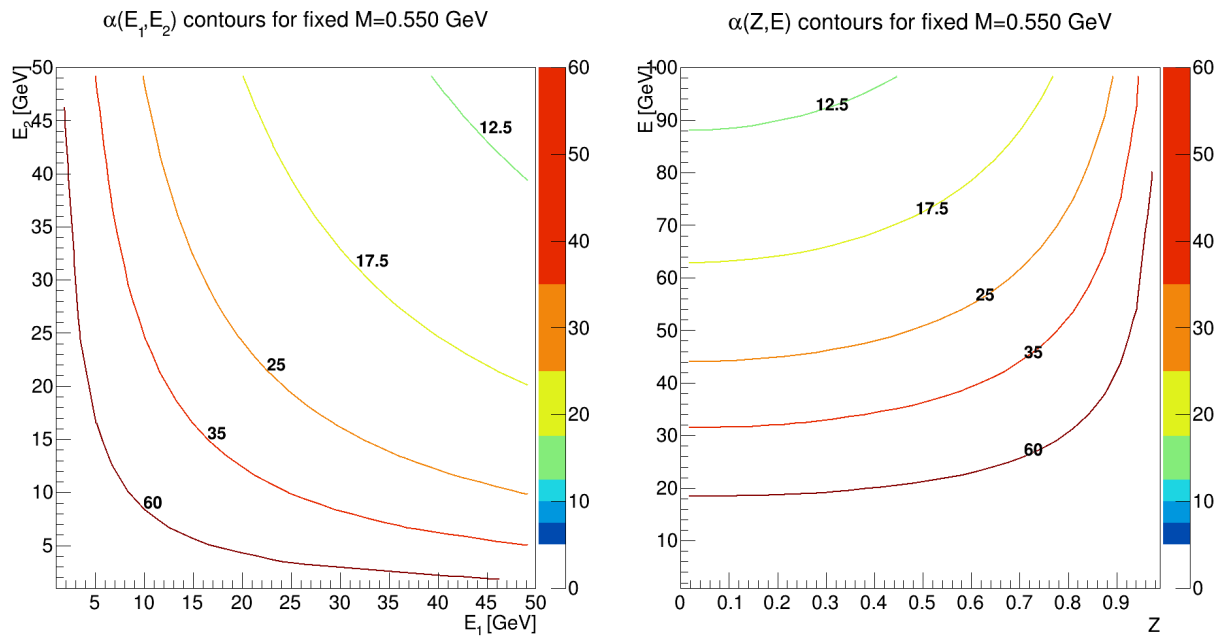


Figure A.5: E_2 vs. E_1 plane (left) and E vs. Z plane (right) with α contours for M fixed at the η -meson mass.

A.2 Note on Small Angles from π^0 Decay Cones

Consider a 30 GeV π^0 decaying toward the FMS. Typically it will decay into a pair of photons with an opening angle of 10 mrad. Assuming the decay can happen with any azimuthal orientation, the space of possible photon trajectories forms a 10 mrad cone, which intersects the FMS front plane in an ellipse, since the cone axis is at an angle with respect to the normal vector of the FMS front plane. The question is whether we can just use the transverse separation between the photons as a simple approximation to get α (which assumes the cone intersects the FMS plane as a circle), or if we need to correct for slight ellipticity.

Let the angle between the cone axis and the FMS plane's normal vector, which is equivalent to the π^0 scattering angle θ , be 70 mrad, corresponding to photon hits detected 0.5 m away from where the beam pipe intersects the FMS front plane. The eccentricity of the projected ellipse is then

$$\varepsilon = \frac{\sin 0.070}{\cos 0.010/2} = 0.07. \quad (\text{A.8})$$

The ratio of the ellipse's minor axis length to the major axis length is then $\sqrt{1 - \varepsilon^2} = 0.9975$, which is too small to be noticeable with respect to the position resolution of the FMS. Thus ellipticity corrections are not needed in the determination of opening angles based solely on distance between photon hits.

Appendix B

Spin Asymmetries and their Relative Luminosities

This appendix lists the 9 possible spin asymmetries and their associated relative luminosities, defined using a notation which is commonly used at STAR and PHENIX. Their relations to the spin asymmetries defined in physics literature, such as A_{LL} and A_N , are listed at the end.

B.1 Notation

a = asymmetry number (following STAR relative luminosity convention)

h_B = blue (west) beam proton helicity

h_Y = yellow (east) beam proton helicity

ε_a = raw asymmetry

$d\sigma^{\text{sign}(h_B)\text{sign}(h_Y)}$ = proton helicity-dependent differential cross section

R_a = relative luminosity

$L^{\text{sign}(h_B)\text{sign}(h_Y)}$ = proton helicity-dependent integrated luminosity

H_a = helicity factor (see appendix [H](#))

$H_a = +1$ for helicity combo in R_a numerator

$H_a = -1$ for helicity combo in R_a denominator

a	ε_a	R_a	H_a	Description
1	$\frac{(d\sigma^{++} + d\sigma^{-+}) - (d\sigma^{+-} + d\sigma^{--})}{(d\sigma^{++} + d\sigma^{-+}) + (d\sigma^{+-} + d\sigma^{--})}$	$\frac{L^{++} + L^{-+}}{L^{+-} + L^{--}}$	h_Y	yellow SSA
2	$\frac{(d\sigma^{++} + d\sigma^{+-}) - (d\sigma^{-+} + d\sigma^{--})}{(d\sigma^{++} + d\sigma^{+-}) + (d\sigma^{-+} + d\sigma^{--})}$	$\frac{L^{++} + L^{+-}}{L^{-+} + L^{--}}$	h_B	blue SSA
3	$\frac{(d\sigma^{++} + d\sigma^{--}) - (d\sigma^{+-} + d\sigma^{-+})}{(d\sigma^{++} + d\sigma^{--}) + (d\sigma^{+-} + d\sigma^{-+})}$	$\frac{L^{++} + L^{--}}{L^{+-} + L^{-+}}$	$h_B h_Y$	DSA
4	$\frac{d\sigma^{++} - d\sigma^{--}}{d\sigma^{++} + d\sigma^{--}}$	$\frac{L^{++}}{L^{--}}$	$\frac{h_B + h_Y}{2}$	like sign asym
5	$\frac{d\sigma^{-+} - d\sigma^{--}}{d\sigma^{-+} + d\sigma^{--}}$	$\frac{L^{-+}}{L^{--}}$	$\frac{(1 - h_B) h_Y}{2}$	yellow SSA, $h_B = -1$
6	$\frac{d\sigma^{+-} - d\sigma^{--}}{d\sigma^{+-} + d\sigma^{--}}$	$\frac{L^{+-}}{L^{--}}$	$\frac{(1 - h_Y) h_B}{2}$	blue SSA, $h_Y = -1$
7	$\frac{d\sigma^{++} - d\sigma^{+-}}{d\sigma^{++} + d\sigma^{+-}}$	$\frac{L^{++}}{L^{+-}}$	$\frac{(1 + h_B) h_Y}{2}$	yellow SSA, $h_B = +1$
8	$\frac{d\sigma^{-+} - d\sigma^{+-}}{d\sigma^{-+} + d\sigma^{+-}}$	$\frac{L^{-+}}{L^{+-}}$	$\frac{h_Y - h_B}{2}$	unlike sign asym
9	$\frac{d\sigma^{++} - d\sigma^{-+}}{d\sigma^{++} + d\sigma^{-+}}$	$\frac{L^{++}}{L^{-+}}$	$\frac{(1 + h_Y) h_B}{2}$	blue SSA, $h_Y = +1$

Table B.1: The nine asymmetries and their relative luminosities.

B.2 Nine Asymmetries and Relative Luminosities

Table B.1 lists the 9 asymmetries defined at RHIC, along with their corresponding relative luminosities. While these asymmetries are longitudinal asymmetries, they can also be defined for transverse polarized collisions as well, however they gain a dependence on azimuth, ϕ . The naming conventions for physics asymmetries are usually as follows (given $a = 1$ corresponds to the RHIC yellow beam and $a = 2$ to blue):

- Single-Spin Asymmetries (SSAs):

$$- \text{ Longitudinal: } A_L^Y = \frac{1}{P_Y} \varepsilon_1 \quad \text{ Transverse: } A_N^Y \cos \phi = \frac{1}{P_Y} \varepsilon_1$$

$$- \text{ Longitudinal: } A_L^B = \frac{1}{P_B} \varepsilon_2 \quad \text{ Transverse: } A_N^B \cos \phi = \frac{1}{P_B} \varepsilon_2$$

- Double-Spin Asymmetries (DSAs):

$$- \text{ Longitudinal: } A_{LL} = \frac{1}{P_B P_Y} \varepsilon_3 \quad \text{ Transverse: } A_{NN} = A_{TT} + A_{\Sigma} \cos 2\phi = \frac{1}{P_B P_Y} \varepsilon_3$$

Assuming the luminosity uncertainties (*i.e.*, statistical uncertainties of scaler counts) of $L_{h_B h_Y}$ are $\Delta_{h_B h_Y}$, the relative luminosity uncertainties are:

$$\Delta_{R_1} = \sqrt{\frac{(\Delta_{-+}^2 + \Delta_{++}^2) (L_{--} + L_{+-})^2 + (\Delta_{--}^2 + \Delta_{+-}^2) (L_{-+} + L_{++})^2}{(L_{--} + L_{+-})^4}}$$

$$\Delta_{R_2} = \sqrt{\frac{(\Delta_{+-}^2 + \Delta_{++}^2) (L_{--} + L_{-+})^2 + (\Delta_{--}^2 + \Delta_{+-}^2) (L_{+-} + L_{++})^2}{(L_{--} + L_{-+})^4}}$$

$$\Delta_{R_3} = \sqrt{\frac{(\Delta_{--}^2 + \Delta_{++}^2) (L_{-+} + L_{+-})^2 + (\Delta_{-+}^2 + \Delta_{+-}^2) (L_{--} + L_{++})^2}{(L_{-+} + L_{+-})^4}}$$

$$\Delta_{R_4} = \sqrt{\frac{\Delta_{++}^2 L_{--}^2 + \Delta_{--}^2 L_{++}^2}{L_{--}^4}}$$

$$\Delta_{R_5} = \sqrt{\frac{\Delta_{-+}^2 L_{--}^2 + \Delta_{--}^2 L_{-+}^2}{L_{--}^4}}$$

$$\Delta_{R_6} = \sqrt{\frac{\Delta_{+-}^2 L_{--}^2 + \Delta_{--}^2 L_{+-}^2}{L_{--}^4}}$$

$$\Delta_{R_7} = \sqrt{\frac{\Delta_{++}^2 L_{+-}^2 + \Delta_{+-}^2 L_{++}^2}{L_{+-}^4}}$$

$$\Delta_{R_8} = \sqrt{\frac{\Delta_{-+}^2 L_{+-}^2 + \Delta_{+-}^2 L_{-+}^2}{L_{+-}^4}}$$

$$\Delta_{R_9} = \sqrt{\frac{\Delta_{++}^2 L_{-+}^2 + \Delta_{-+}^2 L_{++}^2}{L_{-+}^4}}$$

Appendix C

Local Polarimetry and Residual Transverse Component Systematic

Here we discuss polarization measurements at STAR, obtained by the ZDC-SMD [98, 99]. Measuring polarization at STAR provides an independent verification that the beams are polarized transversely, during a transverse running period, by measuring transverse single-spin asymmetries (TSSAs) in the ZDC-SMD. During a longitudinal running period, the TSSA should be very close to zero; if so, the spin rotators are appropriately rotating the proton bunch spin states to longitudinal, since any residual transverse component of the polarization would appear in the ZDC-SMD as a nonzero TSSA. This appendix outlines measurements of these asymmetries and their application to a measurement of the systematic uncertainty on $A_{LL}^{\pi^0}$ due to possible nonzero transverse polarization components.

C.1 Local Polarimetry

Consider a beam of protons, accelerated by a synchrotron, entering a local coordinate system such that the beam is along the z axis, with the y axis vertical and the x axis parallel to the synchrotron radius. During a transverse polarization running period, let the incoming proton polarization vector be

$$\vec{P}_T = (0, P_T, 0), \quad (\text{C.1})$$

assuming that longitudinal components are zero (*i.e.*, negligible Thomas precession). During a longitudinal polarization running period, let the polarization vector be

$$\vec{P}_L = (P_x, P_y, P_z), \quad (\text{C.2})$$

where $P_z \gg P_x, P_y$.

During a transverse run, the raw left/right TSSA is

$$\varepsilon_T = P_T A_N = \frac{\sqrt{N_L^\uparrow N_R^\downarrow} - \sqrt{N_R^\uparrow N_L^\downarrow}}{\sqrt{N_L^\uparrow N_R^\downarrow} + \sqrt{N_R^\uparrow N_L^\downarrow}}, \quad (\text{C.3})$$

where A_N is the TSSA (analyzing power), and $N_{L,R}^{\uparrow,\downarrow}$ is the number of hits (*viz.* ZDC-SMD, but this could be done with any appropriately segmented detector) which scatter to the left (L) or right (R) for incoming proton spin up (\uparrow) or down (\downarrow). This is the cross-ratio formula for a TSSA, which does not require a measurement of the relative luminosity [56].

During a longitudinal run, given that the polarization vector can have arbitrary nonzero transverse components, one can look at two asymmetries: the raw left/right asymmetry

$$\varepsilon_{LR} = P_y A_N = \frac{\sqrt{N_L^+ N_R^-} - \sqrt{N_R^+ N_L^-}}{\sqrt{N_L^+ N_R^-} + \sqrt{N_R^+ N_L^-}}, \quad (\text{C.4})$$

and the raw up/down asymmetry

$$\varepsilon_{UD} = P_x A_N = \frac{\sqrt{N_U^+ N_D^-} - \sqrt{N_D^+ N_U^-}}{\sqrt{N_U^+ N_D^-} + \sqrt{N_D^+ N_U^-}}. \quad (\text{C.5})$$

For the longitudinal running period, the notation for yields $N_{L,R,U,D}^{+,-}$ is a bit different: L and R again denote scattering left or right, U and D denote scattering up and down, but since the beam is ideally polarized along the beam axis, the notational superscripts $+$ and $-$ are used to indicate incoming polarization aligned and anti-aligned along the beam axis, respectively. If there is a nonzero transverse component to the polarization, either $+$ will select the transverse component *up* protons and $-$ will select the transverse component *down* protons or vice versa. Therefore the signs of ε_{LR} and ε_{UD} will depend on the azimuth of the polarization vector's transverse component; however, it turns out that this sign ambiguity does not matter in the determination of the final polarization vector angles.

Converting to polar coordinates, the longitudinal polarization vector becomes

$$P_x = P_L \sin \theta \cos \phi, \quad (\text{C.6})$$

$$P_y = P_L \sin \theta \sin \phi, \quad (\text{C.7})$$

where $P_L = \sqrt{P_x^2 + P_y^2 + P_z^2}$ can be measured by the RHIC polarimetry group by, for example, by their pC polarimeters.

Inserting equations C.6 and C.7 into equations C.4 and C.5 and using the value of A_N from equation C.3 yields

$$\varepsilon_{LR} = \frac{P_L}{P_T} \varepsilon_T \sin \theta \sin \phi, \quad (\text{C.8})$$

$$\varepsilon_{UD} = \frac{P_L}{P_T} \varepsilon_T \sin \theta \cos \phi, \quad (\text{C.9})$$

the solution of which gives the polarization polar angle and azimuth:

$$\sin \theta = \frac{P_T \sqrt{\varepsilon_{LR}^2 + \varepsilon_{UD}^2}}{P_L \varepsilon_T}, \quad (\text{C.10})$$

$$\tan \phi = \frac{\varepsilon_{LR}}{\varepsilon_{UD}}. \quad (\text{C.11})$$

Instead of measuring ε_{LR} and ε_{UD} , one can fit the TSSA cross-ratio as a function of ϕ to the form $\varepsilon_L \sin(\phi + \phi_0)$, with fit parameters ε_L , the asymmetry, and ϕ_0 , a phase angle related to the azimuth of the transverse component of the polarization. This ‘‘overall’’ TSSA is related to the U/D and L/R asymmetries via

$$\varepsilon_L = P_L^\perp A_N = \sqrt{P_x^2 + P_y^2} A_N = \sqrt{\varepsilon_{LR}^2 + \varepsilon_{UD}^2}.$$

Since A_N is independent of polarization, we have

$$A_N = \frac{\varepsilon_T}{P_T} = \frac{\varepsilon_L}{P_L^\perp}, \quad (\text{C.12})$$

which implies

$$\frac{\varepsilon_L}{\varepsilon_T} = \frac{P_L^\perp}{P_T}. \quad (\text{C.13})$$

Note that by equation C.10 this verifies $\sin \theta = P_L^\perp / P_L$.

C.2 Relating Local Polarimetry to A_{LL} Systematic

Let P_B and P_Y be the polarization vectors for two colliding longitudinally-polarized proton bunches. Define their product as $\rho = P_B P_Y$ as well as the products of their transverse and longitudinal components as $\rho^\perp = P_B^\perp P_Y^\perp$ and $\rho^\parallel = P_B^\parallel P_Y^\parallel$.

In the ZDC-SMD, we can measure the raw TSSA during longitudinal running, ε_L , and compare it to ε_T , the raw TSSA during a period of transverse polarization with polarization P_T , with the same conditions under which ε_L was measured, such that $P_T^2 \approx P^\parallel{}^2 + P^\perp{}^2 = P^2$

(*e.g.*, by disabling spin rotators for a few fills during a longitudinal running period). Following equations C.12 and C.13, we have for each beam

$$\frac{\varepsilon_L}{P^\perp} = \frac{\varepsilon_T}{P}. \quad (\text{C.14})$$

Letting $N^{h_B h_Y}$ be the yield, given proton spin states $h_B, h_Y \in \{+, -\}$, and R_3 be the relative luminosity, the measured overall double-spin asymmetry (DSA), denoted \mathbb{A} , may be decomposed into contributions from A_{LL} and from the transverse DSA $A_{NN} = A_\Sigma + A_{TT} \cos 2\phi$ as

$$\mathbb{A} = \frac{1}{\rho} \cdot \frac{N^{++} + N^{--} - R_3(N^{+-} + N^{-+})}{N^{++} + N^{--} + R_3(N^{+-} + N^{-+})} = A'_{LL} + A'_{NN}, \quad (\text{C.15})$$

where $A'_{LL} = \varepsilon_{LL}/\rho$ is the measured longitudinal DSA, and $A'_{NN} = \varepsilon_{NN}/\rho$ is the measured transverse DSA (see appendix D for details). The primes denote that these asymmetries are measured with respect to the overall polarization; they can be compared to the “true” DSAs, $A_{LL} = \varepsilon_{LL}/\rho^\parallel$ and $A_{NN} = \varepsilon_{NN}/\rho^\perp$, allowing \mathbb{A} to be expressed as

$$\mathbb{A} = \frac{\rho^\parallel}{\rho} A_{LL} + \frac{\rho^\perp}{\rho} A_{NN}. \quad (\text{C.16})$$

By assuming $P^\perp \ll P$, we expand the factors of the first term:

$$\frac{\rho^\parallel}{\rho} = \sqrt{\frac{P^2 - P^{\perp 2}}{P^2}} = \sqrt{1 - \left(\frac{P^\perp}{P}\right)^2} = 1 + O\left[\left(\frac{P^\perp}{P}\right)^2\right]. \quad (\text{C.17})$$

In the context of small asymmetries, the higher order terms can be ignored and we may safely assume $\rho^\parallel/\rho \approx 1$.

The systematic uncertainty then is just the difference between the measured asymmetry and extracted “true” asymmetry:

$$\Delta_{A_{LL}} [P^\perp] := \mathbb{A} - A_{LL} = \frac{P^\perp}{P_B} \cdot \frac{P_Y^\perp}{P_Y} \cdot A_{NN} = \frac{\varepsilon_L^B}{\varepsilon_B^B} \cdot \frac{\varepsilon_L^Y}{\varepsilon_T^Y} \cdot A_{NN}, \quad (\text{C.18})$$

where equation C.14 was used to write the fractional transverse polarization components as ratios of asymmetries measured in the ZDC-SMD.

Appendix D

Decomposing Cross Sections in terms of Spin Asymmetries

This section illustrates how cross sections can be decomposed into the longitudinal and transverse spin asymmetries. It essentially follows appendix A.3 of [33], and is meant to show another interpretation of spin asymmetries in general.

D.1 Longitudinal Components

Consider a particle, described by the state $|\psi\rangle$, heading in the z direction. Let its spin be in the xz plane, such that it makes an angle α with the z axis. That is, the spin vector is

$$\vec{P} = (P \sin \alpha, 0, P \cos \alpha) \quad (\text{D.1})$$

(the label P stands for polarization, which is more properly defined for an ensemble of particles, but P is chosen instead of S to avoid confusion with spin operators). If $\alpha = 0$, then the spin of $|\psi\rangle$ is aligned with its momentum.

Consider the two helicity states: spin along the $+z$ axis, described by $|+\rangle$, and spin along the $-z$ axis, described by $|-\rangle$. These states form a basis

$$\left\{ |+\rangle = \begin{pmatrix} 1 \\ 0 \end{pmatrix}, |-\rangle = \begin{pmatrix} 0 \\ 1 \end{pmatrix} \right\}, \quad (\text{D.2})$$

which spans the spinor space on which the spin-1/2 representation of the spin operators act. The matrices corresponding to the spin operators S_x , S_y , and S_z in this representation can

be expanded as follows:

$$S_x = \frac{1}{2} \begin{pmatrix} 0 & 1 \\ 1 & 0 \end{pmatrix} = \frac{1}{2} \left(|+\rangle\langle-| + |-\rangle\langle+| \right), \quad (\text{D.3})$$

$$S_y = \frac{1}{2} \begin{pmatrix} 0 & -i \\ i & 0 \end{pmatrix} = \frac{i}{2} \left(|-\rangle\langle+| - |+\rangle\langle-| \right), \quad (\text{D.4})$$

$$S_z = \frac{1}{2} \begin{pmatrix} 1 & 0 \\ 0 & -1 \end{pmatrix} = \frac{1}{2} \left(|+\rangle\langle+| - |-\rangle\langle-| \right). \quad (\text{D.5})$$

With the spin vector of $|\psi\rangle$ defined via equation D.1, the expectation values of the spin operators must be

$$\langle\psi|S_x|\psi\rangle = \frac{1}{2} \sin \alpha, \quad (\text{D.6})$$

$$\langle\psi|S_y|\psi\rangle = 0, \quad (\text{D.7})$$

$$\langle\psi|S_z|\psi\rangle = \frac{1}{2} \cos \alpha. \quad (\text{D.8})$$

We expand $|\psi\rangle$ in the $\{|+\rangle, |-\rangle\}$ basis as $|\psi\rangle = c_+|+\rangle + c_-|-\rangle$. Acting with S_z yields

$$S_z|\psi\rangle = \frac{1}{2}c_+|+\rangle - \frac{1}{2}c_-|-\rangle$$

and hence the expectation value,

$$\langle\psi|S_z|\psi\rangle = \left(c_+^*\langle+| + c_-^*\langle-| \right) \left(\frac{1}{2}c_+|+\rangle - \frac{1}{2}c_-|-\rangle \right) = \frac{1}{2} (c_+^2 - c_-^2),$$

together with equation D.8, implies the relation

$$c_+^2 - c_-^2 = \cos \alpha. \quad (\text{D.9})$$

The S_x operator yields a similar relation:

$$\langle\psi|S_x|\psi\rangle = \left(c_+^*\langle+| + c_-^*\langle-| \right) \left(\frac{1}{2}c_+|-\rangle + \frac{1}{2}c_-|+\rangle \right) = c_+c_-,$$

and thus

$$2c_+c_- = \sin \alpha. \quad (\text{D.10})$$

Simultaneously solving equations D.9 and D.10 for c_{\pm} allows us to express the state in terms

of its spin vector angle:

$$|\psi\rangle = \sqrt{\frac{1 + \cos \alpha}{2}} |+\rangle + \sqrt{\frac{1 - \cos \alpha}{2}} |-\rangle. \quad (\text{D.11})$$

Now consider two colliding particles a and b with spin vector angles α and β , described as:

$$|a\rangle = \sqrt{\frac{1 + \cos \alpha}{2}} |a_+\rangle + \sqrt{\frac{1 - \cos \alpha}{2}} |a_-\rangle, \quad (\text{D.12})$$

$$|b\rangle = \sqrt{\frac{1 + \cos \beta}{2}} |b_+\rangle + \sqrt{\frac{1 - \cos \beta}{2}} |b_-\rangle. \quad (\text{D.13})$$

The scattering cross section may be written as:

$$\begin{aligned} 4\sigma_{ab} = 4 \cdot \langle ab | \sigma | ab \rangle &= (1 + \cos \alpha)(1 + \cos \beta) \sigma_{++} + (1 + \cos \alpha)(1 - \cos \beta) \sigma_{+-} + \\ &\quad (1 - \cos \alpha)(1 + \cos \beta) \sigma_{-+} + (1 - \cos \alpha)(1 - \cos \beta) \sigma_{--} \\ &= (\sigma_{++} + \sigma_{+-} + \sigma_{-+} + \sigma_{--}) + \cos \alpha (\sigma_{++} + \sigma_{+-} - \sigma_{-+} - \sigma_{--}) + \\ &\quad \cos \beta (\sigma_{++} - \sigma_{+-} + \sigma_{-+} - \sigma_{--}) + \cos \alpha \cos \beta (\sigma_{++} - \sigma_{+-} - \sigma_{-+} + \sigma_{--}), \end{aligned}$$

where

$$\sigma_{\pm\pm} := \langle a_{\pm} b_{\pm} | \sigma | a_{\pm} b_{\pm} \rangle$$

and

$$\sigma = \sigma_{++} + \sigma_{+-} + \sigma_{-+} + \sigma_{--}.$$

Defining the following asymmetries

$$\begin{aligned} A_L^a &= \frac{(\sigma_{++} + \sigma_{+-} - \sigma_{-+} - \sigma_{--})}{\sigma}, \\ A_L^b &= \frac{(\sigma_{++} + \sigma_{-+} - \sigma_{+-} - \sigma_{--})}{\sigma}, \\ A_{LL} &= \frac{(\sigma_{++} + \sigma_{--} - \sigma_{+-} - \sigma_{-+})}{\sigma}, \end{aligned}$$

allows us to write the cross section as

$$\sigma_{ab} = \frac{\sigma}{4} (1 + A_L^a \cos \alpha + A_L^b \cos \beta + A_{LL} \cos \alpha \cos \beta). \quad (\text{D.14})$$

D.2 Transverse Components

We can easily move to the transverse basis $\{|\uparrow\rangle, |\downarrow\rangle\}$ with the following transformation:

$$\begin{aligned} |+\rangle &= \frac{1}{\sqrt{2}} \left(|\uparrow\rangle + |\downarrow\rangle \right), \\ |-\rangle &= \frac{1}{\sqrt{2}} \left(|\uparrow\rangle - |\downarrow\rangle \right). \end{aligned}$$

The spin operators become

$$\begin{aligned} S_x &= \frac{1}{2} \left(|\uparrow\rangle\langle\uparrow| - |\downarrow\rangle\langle\downarrow| \right), \\ S_y &= \frac{i}{2} \left(|\uparrow\rangle\langle\downarrow| - |\downarrow\rangle\langle\uparrow| \right), \\ S_z &= \frac{1}{2} \left(|\uparrow\rangle\langle\downarrow| + |\downarrow\rangle\langle\uparrow| \right), \end{aligned}$$

and the state is expanded as

$$|\psi\rangle = c_\uparrow |\uparrow\rangle + c_\downarrow |\downarrow\rangle.$$

Expectation values give rise to the following relations:

$$\begin{aligned} \langle\psi|S_x|\psi\rangle &= \frac{1}{2} (c_\uparrow^2 - c_\downarrow^2) = \frac{1}{2} \sin \alpha, \\ \langle\psi|S_z|\psi\rangle &= c_\uparrow c_\downarrow = \frac{1}{2} \cos \alpha. \end{aligned}$$

Solving this system yields

$$|\psi\rangle = \sqrt{\frac{1 + \sin \alpha}{2}} |\uparrow\rangle + \sqrt{\frac{1 - \sin \alpha}{2}} |\downarrow\rangle. \quad (\text{D.15})$$

Similar to the longitudinal case, one can define the following asymmetries, which are azimuthally modulated:

$$\begin{aligned} A_P^a &= \frac{\sigma_{\uparrow\uparrow} + \sigma_{\uparrow\downarrow} - \sigma_{\downarrow\uparrow} - \sigma_{\downarrow\downarrow}}{\sigma} = R^a + A_N^a \cos \phi, \\ A_P^b &= \frac{\sigma_{\uparrow\uparrow} + \sigma_{\downarrow\uparrow} - \sigma_{\uparrow\downarrow} - \sigma_{\downarrow\downarrow}}{\sigma} = R^b + A_N^b \cos \phi, \\ A_{PP} &= \frac{\sigma_{\uparrow\uparrow} + \sigma_{\downarrow\downarrow} - \sigma_{\uparrow\downarrow} - \sigma_{\downarrow\uparrow}}{\sigma} = A_\Sigma + A_{TT} \cos(2\phi), \end{aligned}$$

where ϕ is the azimuth of the measured particle or jet and R is related to the relative luminosity. The cross ratio single-spin asymmetry can be used for A_P , negating the need for

the offsets R , and hence we can assume $R = 0$ if A_N is properly measured. Finally, the cross section may be written as

$$\sigma_{ab} = \frac{\sigma}{4} \left\{ 1 + A_N^a \sin \alpha \cos \phi + A_N^b \sin \beta \cos \phi + [A_\Sigma + A_{TT} \cos(2\phi)] \sin \alpha \sin \beta \right\}. \quad (\text{D.16})$$

D.3 Application: Systematic Uncertainty on A_{LL} due to Nonzero Transverse Polarization

The full cross section, after averaging over azimuth, assuming parity conservation ($A_L = 0$), and assuming $\cos \alpha = \cos \beta \approx 1$ is

$$\begin{aligned} \sigma_{ab} &\propto 1 + A_{LL} \cos \alpha \cos \beta + A_\Sigma \sin \alpha \sin \beta \\ &\approx 1 + A_{LL} + A_\Sigma \sin \alpha \sin \beta. \end{aligned}$$

The systematic uncertainty on A_{LL} from a nonzero transverse polarization component is just the extra term:

$$\delta A_{LL} = |A_\Sigma \cdot \sin \alpha \cdot \sin \beta|. \quad (\text{D.17})$$

This is the same as equation C.18 when we average that over azimuth (so $A_{NN} = A_\Sigma$) and use $\sin \theta = P^\perp/P$, where $\theta \in \{\alpha, \beta\}$. If we allow a and b to have a nonzero azimuth, equation D.17 becomes

$$\delta A_{LL} = |A_\Sigma \cdot \sin \alpha \cdot \sin \beta \cdot \cos(\phi_a - \phi_b)|, \quad (\text{D.18})$$

but since ϕ_a and ϕ_b are typically difficult to measure, the most conservative estimate of $\cos(\phi_a - \phi_b) = 1$, which gives equation D.17, suffices.

Appendix E

Shower Shape Derivation and Incident Angle Corrections

This appendix presents a derivation and a possible physical motivation for the shower shape model used for reconstructing photon positions from contiguous regions of energy deposition (clusters) in the FMS cells. The derivation begins with the simpler 1-dimensional version, followed by an extension to 2 dimensions in application to the FMS; this method allows for the physical motivation for the model to become clear. Finally, some ideas for correcting the shower shape for nonzero incident angles are presented. The original reference upon which the shower shape model is based is [90].

Some attempts of incident angle corrections involve taking the original model and applying it to six longitudinal slices. Each slice is a copy of the model in [90], fit to a simulated transverse profile. Each slice's fit result is then weighted by the longitudinal shower profile. For details on this method, see [91] and [92]. This appendix, however, presents progress toward a much simpler alternative.

E.1 Derivation of the Symmetric Shower Shape

We begin by deriving the symmetric shower shape, as used in [90]. It is called “symmetric” because it assumes the incoming photon which starts the shower is at *normal* incidence to the detector, causing a transverse profile which is symmetric about the photon's trajectory. Correcting for nonzero incidence angles would skew the shower shape.

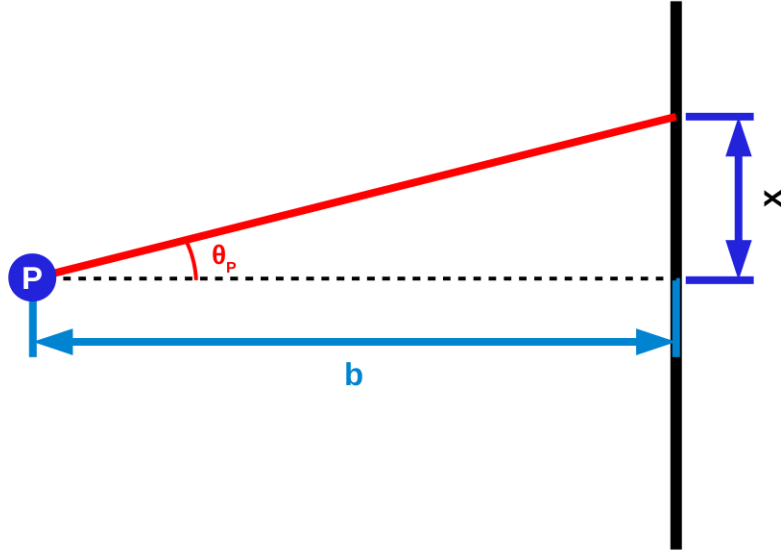


Figure E.1: 1-dimensional Cauchy distribution physical picture.

E.1.1 1-Dimensional Shower Shape

The shower shape, whether skewed by incident angles or not, is modelled by a sum of 2-dimensional Cauchy distributions, thus it is important to first understand a simple, but relevant physical scenario in which a Cauchy distribution appears. We begin with a physics question which forms the motivation for the use of a 1-dimensional Cauchy distribution, and later show how it extends to 2 dimensions and applies to the shower shape model used in FMS photon reconstruction.

E.1.1.1 The Cauchy Distribution

Consider a point P from which photons are emitted, uniformly in all angles. Let P be a distance b from a line, as shown in figure E.1. Given that photons have a uniform probability of being emitted at any angle θ , what is the probability distribution of photons hitting the line, as a function of source distance b and of position x on the line?

The probability distribution of photons being emitted as a function of θ , denoted $f(\theta)$, is constant but must be normalized. If the line is infinitely long, it will detect photons for all $\theta \in (-\pi/2, \pi/2)$, thus for $f(\theta)$ to be normalized over this range, we have $f(\theta) = 1/\pi$.

The angular coordinate θ from the source is related to those of the plane, x and b , by

$$\theta = \arctan\left(\frac{x}{b}\right). \quad (\text{E.1})$$

This relation can be used to transform the distribution $f(\theta)$ to $f(x)$. The probability of a

photon being emitted within a small angle $\Delta\theta$ is equal to the probability of observing it in a small interval of the line Δx , which is determined by $\Delta\theta$ and θ . The transformation of probability distributions is then

$$\int dx f(x) = \int d\theta f(\theta) \implies f(x) = \left| \frac{d\theta}{dx} \right| f(\theta). \quad (\text{E.2})$$

Differentiating equation E.1 shows that

$$f(x) = \frac{1}{\pi} \frac{b}{b^2 + x^2}, \quad (\text{E.3})$$

which is the 1-dimensional Cauchy distribution. It is a function of x , for a given parameter b , which is proportional to the width of the distribution. When b is small, that is the photon source is close to the line, $f(x)$ is peaked sharply at $x = 0$; on the other hand, when the source is distant from the plane, $f(x)$ is much more spread out over x .

E.1.1.2 Segmenting the Line into Cells

Now imagine that the line is *segmented*, as a 1-dimensional detector might be: it is composed of cells, which are segments each of length d , where only the total number of photons which strike each cell is read out (more correctly, the ADC counts). If we draw a straight line from P to the detector such that this line is perpendicular to the detector, it will intersect a particular cell which will see the highest relative number of photons; this cell is called the *high tower*, and let the point at which the line intersects it be denoted by p .

Define x_c as the transverse distance between p and the center of a particular cell; any cell works, but it should either be the high tower or one nearby. Let this cell be denoted by C . What is the probability distribution over x_c , in other words, what is the relative number of photons seen in the cell C , as compared to its neighboring cells?

Cumulative distribution functions (CDFs) of a given probability distribution can be used to determine probabilities within ranges; this assumes the probability distribution is integrable. In this case, CDF of $f(x)$ is:

$$F(x) = \int_{-\infty}^x d\hat{x} f(\hat{x}) = \frac{1}{2} + \frac{1}{\pi} \arctan\left(\frac{x}{b}\right). \quad (\text{E.4})$$

To obtain the fraction of light detected in cell C , we consider the probability of observing the photon in a range $[x_c - d/2, x_c + d/2]$. This probability, denoted $G(x_c)$, is then the difference

of two CDFs evaluated at the range endpoints:

$$G(x_c) = F\left(x_c + \frac{d}{2}\right) - F\left(x_c - \frac{d}{2}\right). \quad (\text{E.5})$$

E.1.1.3 Multiple Photon Sources

Instead of just considering one source P at a distance b , one can consider a set of sources $\{P_i\}$, with each P_i a distance b_i from the line detector. The overall probability distribution seen at the line would just be a sum of Cauchy distributions for each i (this ignores interference). If we consider N sources, all along a straight line perpendicular to the detector line, then the probability distribution on the detector is:

$$f(x) = \frac{1}{\pi} \sum_{i=1}^N \frac{a_i b_i}{b_i^2 + x^2}. \quad (\text{E.6})$$

The parameters (weights) a_i represent relative photon emission rates of the sources, and in order to maintain normalization, the sum of all a_i s must be 1. The CDF of this weighted sum is the weighted sum of Cauchy distribution CDFs, and consequently the $G(x_c)$ for N sources is easy to derive. The FMS shower shape model from [90], which is 2-dimensional, considers 3 P_i s all along a straight line perpendicular to the FMS plane.

If the sources are along a line which is not perpendicular to the detector line, then we must account for the x position of each source. To do so, the terms in equation E.6 just need to be shifted by $x \mapsto x + x_i$, where x_i is the transverse distance of P_i from some central axis through $x = 0$. This consideration will be our motivation for the simpler incident angle corrections idea.

E.1.2 2-Dimensional Shower Shape

Now consider a source P at a distance b from a *plane*. The source emits a uniform distribution of photons with respect to a polar angle θ and an azimuthal angle ϕ , as shown in figure E.2. The uniform probability distribution must be normalized over $\theta \in [0, \pi/2)$ and $\phi \in [0, 2\pi)$, thus $f(\theta, \phi) = 1/2\pi$.

The detector plane coordinates x, y are related to the source coordinates by

$$\theta = \arctan\left(\frac{\sqrt{x^2 + y^2}}{b}\right), \quad (\text{E.7})$$

$$\phi = \arctan\left(\frac{y}{x}\right). \quad (\text{E.8})$$

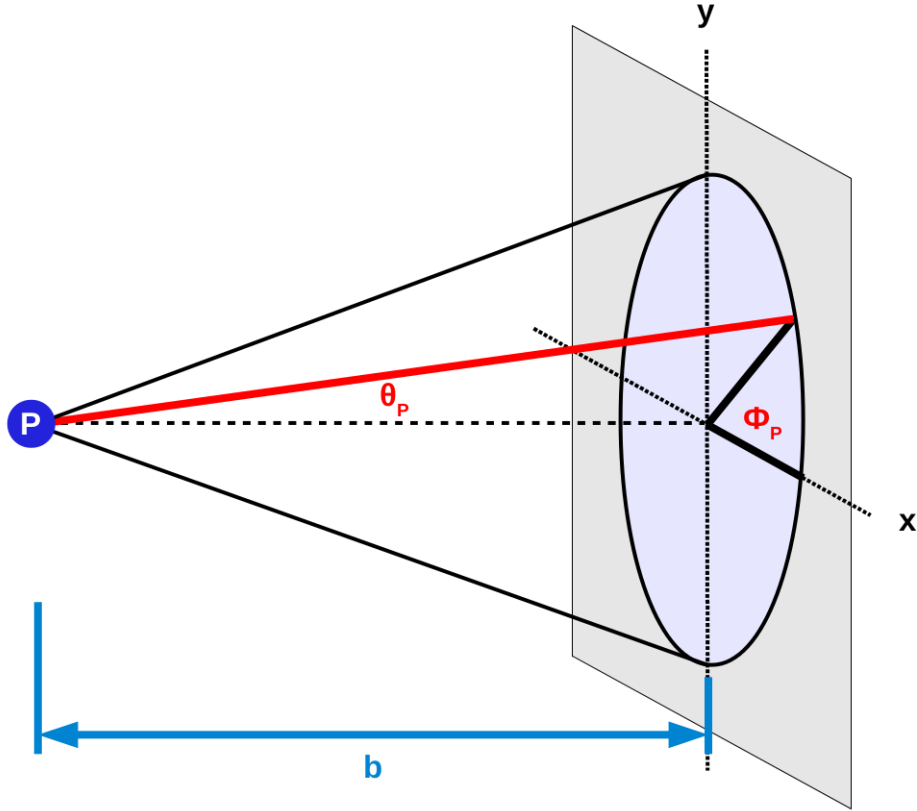


Figure E.2: 2-dimensional Cauchy distribution physical picture.

The transformation of the source emission probability distribution is again achieved by equating integrals, bearing in mind the necessity of Jacobian factor in the source's integrand:

$$\int dx dy f(x, y) = \int d\phi d\theta \cdot \sin \theta \cdot f(\theta, \phi). \quad (\text{E.9})$$

Differentiating each side returns

$$f(x, y) = \left| \frac{\partial(\theta, \phi)}{\partial(x, y)} \right| \cdot \sin \theta \cdot f(\theta, \phi), \quad (\text{E.10})$$

where the second Jacobian factor comes from the generalized chain rule. Writing out the Jacobian and extending the result to an arbitrary number of sources (in a perpendicular line) gives the expression

$$f(x, y) = \frac{1}{2\pi} \cdot \sum_{i=1}^N \frac{a_i b_i}{(b_i^2 + x^2 + y^2)^{3/2}}. \quad (\text{E.11})$$

This equation is the sum of N 2-dimensional Cauchy distributions; it matches the shower shape model given by equation 10 in [90].

We now extend this model to a plane which is segmented into squares, each with side lengths d ; this segmentation is that of the FMS with the squares representing the Pb-glass cells. The CDF of equation E.11 is

$$\begin{aligned} F(x, y) &= \int_{-\infty}^x \int_{-\infty}^y d\hat{x}d\hat{y}f(\hat{x}, \hat{y}) = \\ &= \frac{1}{4} + \frac{1}{2\pi} \sum_{i=1}^N a_i \left[\arctan\left(\frac{x}{b_i}\right) + \arctan\left(\frac{y}{b_i}\right) + \arctan\left(\frac{xy}{b_i\sqrt{b_i^2 + x^2 + y^2}}\right) \right] \end{aligned} \quad (\text{E.12})$$

and the segmented distribution (*cf.* equation 5 in [90]) is

$$\begin{aligned} G(x_c, y_c) &= F\left(x_c + \frac{d}{2}, y_c + \frac{d}{2}\right) - F\left(x_c - \frac{d}{2}, y_c + \frac{d}{2}\right) - \\ &\quad - F\left(x_c + \frac{d}{2}, y_c - \frac{d}{2}\right) + F\left(x_c - \frac{d}{2}, y_c - \frac{d}{2}\right), \end{aligned} \quad (\text{E.13})$$

which is the sum of two corners' CDFs, minus the sum of the opposite two.

E.1.2.1 The FMS Shower Shape Parameterization

The symmetric shower shape for the FMS is modelled by 3 sources along a straight line. The default parameter values, as determined from a fit in [90], are:

- $a_1 = 0.8$, $b_1 = 0.8$ cm
- $a_2 = 0.3$, $b_2 = 0.2$ cm
- $a_3 = -0.1$, $b_3 = 7.6$ cm
- (given $N = 3$ and $d = 4$ cm)

The biggest contributions come from P_1 and P_2 , which are close to the FMS plane and are thus sharply peaked at $x = y = 0$. The distant source P_3 “anti-contributes” to the shower shape. The fit may not have been constrained by the aforementioned physical picture, where we would likely prefer all $a_i > 0$; nonetheless, this parameterization has been used in many analyses of FMS data.

It is worth noting that the longitudinal position of the plane here is a bit ambiguous: while it definitely should not be the front plane of the FMS glass, it could be the shower max plane (where the electromagnetic shower is at maximum), the PMT plane, or something

else. Whatever the plane may be, the transverse position of reconstructed photons is *highly* sensitive to the choice of plane, which only really matters when we take into account incident angle corrections.

E.2 Incident Angle Corrections

When the angle of incidence is nonzero, the electromagnetic shower is no longer symmetric. To correct for the nonzero skewness, we must use an *asymmetric* shower shape. Recalling section 5.3.2, however, the effect of correcting for the incident angle imparts only a maximum of a 0.5 cm change in the photon position; the energy uncertainty from the calibration (5%) completely eclipses this effect. Nonetheless, incident angle corrections are still worth considering if one desires higher accuracy in the photon position reconstruction

E.2.1 Longitudinal Slices of Symmetric Shower Shapes

One attempt at incident angle corrections simply takes the symmetric shower shape model (with $N = 3$) and uses it for each of six (or any reasonable number) longitudinal slices. Each slice k has its own set of parameters $\{a_{k1}, a_{k2}, a_{k3}, b_{k1}, b_{k2}, b_{k3}\}$. The shower shapes for each slice are centered along a line which represents the incident photon's trajectory, which may not be at normal incidence. The transverse position-dependence of each slice is injected into the x_c and y_c variables for each slice (see [92, 91] for details). Simulations were performed to determine the shower shape slice-by-slice, and fits were done for each slice. Each slice was also weighted according to the longitudinal shower profile. Ultimately, there are 42 parameters in this model: 6 slices, each with 6 shower shape parameters and 1 longitudinal weight (although the longitudinal weights could have been absorbed into the a_{ki} parameters, giving 36 free parameters overall). Altogether, this is a linear combination of 18 2-dimensional Cauchy distributions.

Because there are so many parameters involved, this shower shape model is rather complicated for practical matters, where millions of photons need to be reconstructed. The model begins to break down as the incidence angle is increased (beyond FMS acceptance); furthermore, it is not valid for all incident photon energies, since the longitudinal position of the shower max plane is dependent on incident energy *and* angle. The slicing procedure overlooks the *already present* longitudinal dependence of the Cauchy distributions: the b_i parameters. Instead, a computer algorithm was used to determine the values of a_{ki} and b_{ki} , and many of them have become nonsensical, even though the overall sum of the 18 Cauchy distributions looks reasonable even at the highest scattering angles within the FMS

acceptance.

E.2.2 Simpler Alternative: Cherenkov Parameterization

We now attempt an alternative model: making use of physical intuition to try to simplify the incident angle-dependent shower shape. Since the default shower shape parameters do not seem to be physically motivated, one can try to re-parameterize the shower shape according to a simplified physical model of the shower development. The model presented here is an unfinished endeavor.

The idea here, which is based on photon sources that come from shower particles, is to re-parameterize the shower shape with a_i s and b_i s chosen such that we have a “path” of sources approaching a detector plane; this path depends on the incident angle of the photon which starts the electromagnetic (EM) shower. The weight a_i of each source could be determined by a property of the shower, such as the number of shower particles per radiation length X_0 , which is assumed to double after each X_0 .

Cherenkov Shower Model

Consider a charged particle moving through a medium with a velocity faster than the phase velocity of light in that medium. This particle will leave behind a trail of spherical EM waves which will add together to form a phase-front, shaped like a cone, which trails behind the charged particle. This radiation, called Cherenkov radiation, is typically within the visible part of the EM spectrum, and well within the photo-sensitivity range of the FMS PMTs. If we assume that most of the photons that the PMTs detect are Cherenkov photons, we first consider modelling the Cherenkov part of the EM shower.

Consider the simplified model of an EM shower, where after every radiation length either pair-production $\gamma \rightarrow e^+e^-$ or bremsstrahlung $e^\pm \rightarrow e^\pm\gamma$ occurs. Assume that after each radiation length, the number of shower particles doubles while the energy per particle halves. A simple shower re-parameterization is to have a source P_i at each radiation length (up to a limit, called “shower max”), and have the weights double as $a_i = 2a_{i-1}$. These sources are physically analogous to the “trail” of spherical EM waves which form the addends of the Cherenkov cone. The next few sections show how to modify the parameters of the current shower shape in order to model this Cherenkov shower development.

Parameter N

We would like N to be the number of radiation lengths to consider. Since at every radiation length t , the energy per shower particle $E(t)$ halves, eventually $E(t)$ will be less than a critical

energy value E_0 , where pair-production and bremsstrahlung will cease to be the dominant energy-loss mechanism. At this point in the shower development, the number of particles will be maximized, which gives rise to its name: shower max.

Let δ represent the depth of a shower into the Pb-glass; the number of radiation lengths is $t = \delta/X_0$. Given an incident photon energy of E_γ , the energy for particles at a depth of t radiation lengths is approximately

$$E(t) = \frac{E_\gamma}{2^t}. \quad (\text{E.14})$$

Define the shower max position t_m to occur at a depth such that $E(t_m) = E_0$. Solving for t_m returns the value

$$t_m(E_\gamma) = \frac{\ln(E_\gamma/E_0)}{\ln 2}. \quad (\text{E.15})$$

We may then define N to be t_m , truncated to an integer, that is, let

$$N(E_\gamma) = \lfloor t_m(E_\gamma) \rfloor. \quad (\text{E.16})$$

Parameters a_i

We assume the sources are positioned at each radiation length t , so that the i th source's weight parameter a_i is proportional to 2^i . Since the sum of all a_i s must be 1, we have a normalization factor, which depends on $N(E_\gamma)$, times 2^i :

$$a_i(E_\gamma) = \frac{1}{\sum_{i=0}^{N(E_\gamma)} 2^i} \cdot 2^i = \frac{2^i}{2^{N(E_\gamma)+1} - 1}. \quad (\text{E.17})$$

One caveat to this idea is that only the electrons and positrons in the shower will contribute to the Cherenkov shower; in the first radiation length there are 0 leptons, then in the second there are 2. In the third length there are still 2 leptons, plus two bremsstrahlung photons. In the fourth length, the two photons pair produce, giving a total of 6 leptons. Continuing this process and letting n_i denote the number of leptons in layer i of the shower, we have a recurrence relation which can be used to determine n_i for each i :

$$n_i = 2n_{i-2} + n_{i-1} = \frac{2}{3} [2^i - (-1)^i]. \quad (\text{E.18})$$

To determine a_i using this recurrence relation, one divides each n_i by the total number of leptons after $N(E_\gamma)$ layers, which returns

$$a_i(E_\gamma) = \frac{2^{i+1} - 2(-1)^k}{2^{N(E_\gamma)+2} - (-1)^{N(E_\gamma)} - 3}. \quad (\text{E.19})$$

It turns out that equation E.19 is approximately the same as equation E.17, with the difference between the two decreasing as $N(E_\gamma)$ increases. For $N(E_\gamma) = 10$, the difference is of order 10^{-4} , thus for simplicity equation E.17 will be used for $a_i(E_\gamma)$.

Parameters b_i

At this point, it is unclear exactly where the “detector plane” should be, relative to the path of sources. One idea is to let the detector plane be a distance of L radiation lengths from source P_N , with the distance measured along the path of sources P_i . Let r_i be the distance of source P_i to the detector plane, with r_i measured along the path of P_i :

$$r_i(E_\gamma, L) = [N(E_\gamma) - i + L] \cdot X_0. \quad (\text{E.20})$$

Given an angle of incidence θ_γ of the incident photon, the distance between any source P_i and the plane is then

$$b_i(E_\gamma, L, \theta_\gamma) = r_i(E_\gamma, L) \cdot \cos \theta_\gamma. \quad (\text{E.21})$$

The distance L is left as a free parameter of the re-parameterized shower shape.

Parameters (x_i, y_i)

Now define (x_i, y_i) to be the transverse position of the source P_i , such that $(x = 0, y = 0)$ corresponds to the point at which the path of sources intersects the detector plane. If the photon enters the Pb-glass with an azimuthal angle ϕ_γ , we then have

$$x_i(\theta_\gamma, \phi_\gamma) = r_i(E_\gamma, L) \cdot \sin \theta_\gamma \cdot \cos \phi_\gamma, \quad (\text{E.22})$$

$$y_i(\theta_\gamma, \phi_\gamma) = r_i(E_\gamma, L) \cdot \sin \theta_\gamma \cdot \sin \phi_\gamma. \quad (\text{E.23})$$

Re-parameterized Shower Shape

Putting all of the above together using equation E.11, the probability distribution becomes

$$f(x, y; E_\gamma, \theta_\gamma, \phi_\gamma) = \frac{1}{2\pi} \cdot \sum_{i=0}^{N(E_\gamma)} \frac{a_i(E_\gamma) \cdot b_i(E_\gamma, L, \theta_\gamma)}{\{b_i(E_\gamma, L, \theta_\gamma)^2 + [x - x_i(\theta_\gamma, \phi_\gamma)]^2 + [y - y_i(\theta_\gamma, \phi_\gamma)]^2\}^{3/2}}. \quad (\text{E.24})$$

Note that all the old parameters a_i and b_i are now in terms of the incident photon properties, and that the only free parameter of this shape is L , the distance between P_N and the detector plane.

The CDF is then the same as equation [E.12](#), but with the following substitutions:

$$N \rightarrow N(E_\gamma) \tag{E.25}$$

$$a_i \rightarrow a_i(E_\gamma) \tag{E.26}$$

$$b_i \rightarrow b_i(E_\gamma, L, \theta_\gamma) \tag{E.27}$$

$$x \mapsto x - x_i(\theta_\gamma, \phi_\gamma) \tag{E.28}$$

$$y \mapsto y - y_i(\theta_\gamma, \phi_\gamma) \tag{E.29}$$

This parameterization has shown potential of getting us closer to a proper incident angle correction, and is certainly worthy of further exploration, for those who wish to improve photon position reconstruction accuracy. Improving photon position accuracy may ultimately improve 2-photon invariant mass resolution for π^0 and η -meson reconstruction.

Figure [E.3](#) shows one of the fit attempts of this shower shape to simulation data. It uses a similar parameterization, although there is certainly room for improvement and further exploration:

$$a_i(E_\gamma) = \frac{2^i}{2^{N(E_\gamma)+1} - 1} \tag{E.30}$$

$$b_i = \frac{X_0}{W} [L + N(E_\gamma) - i \cos \theta_\gamma] \tag{E.31}$$

$$x \mapsto x - iX_0 \sin \theta_\gamma \tag{E.32}$$

$$y \mapsto y \tag{E.33}$$

$$G(x_c, y_c) \mapsto V \cdot G(Hx_c + S \tan \theta_\gamma, 0) \tag{E.34}$$

With $N(E_\gamma)$ fixed at 10, W fixed at $4X_0$ and H fixed at -1 , the remaining fit parameters are L , V (a vertical scale), and S (an additional horizontal shift). This is a 1-dimensional model, so y is not changed. Figure [E.3](#) is the best parameterization we have been able to do so far, but clearly needs work.

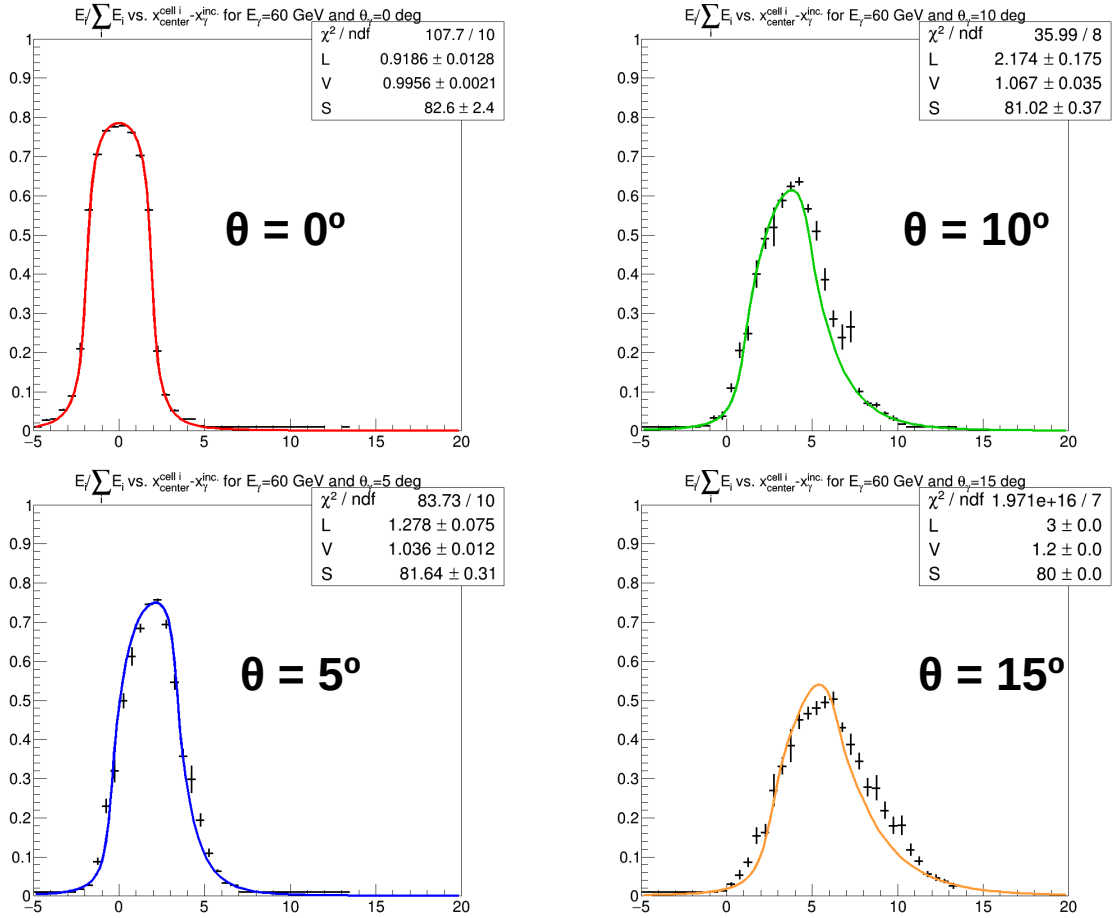


Figure E.3: New shower shape parameterization result. FMS Geant4 simulation data are plotted as black points, and the shower shapes are drawn; parameters L , V , and S are written in the upper right corner of each plot. Four angles of incidence are plotted, and E_γ is fixed at 60 GeV.

Appendix F

Additional Relative Luminosity Figures

This appendix contains extra figures for relative luminosity measurements and cross checks, as discussed in chapter 4:

- ZDC R_3 measurements: figures [F.1](#) and [F.2](#)
- CDF-corrected E and W R_3 comparison: figures [F.3](#) and [F.4](#)
- CDF-corrected E and X R_3 comparison: figures [F.5](#) and [F.6](#)
- CDF-corrected W and X R_3 comparison: figures [F.7](#) and [F.8](#)

Run 12 ZDC R_3 vs. Run Index

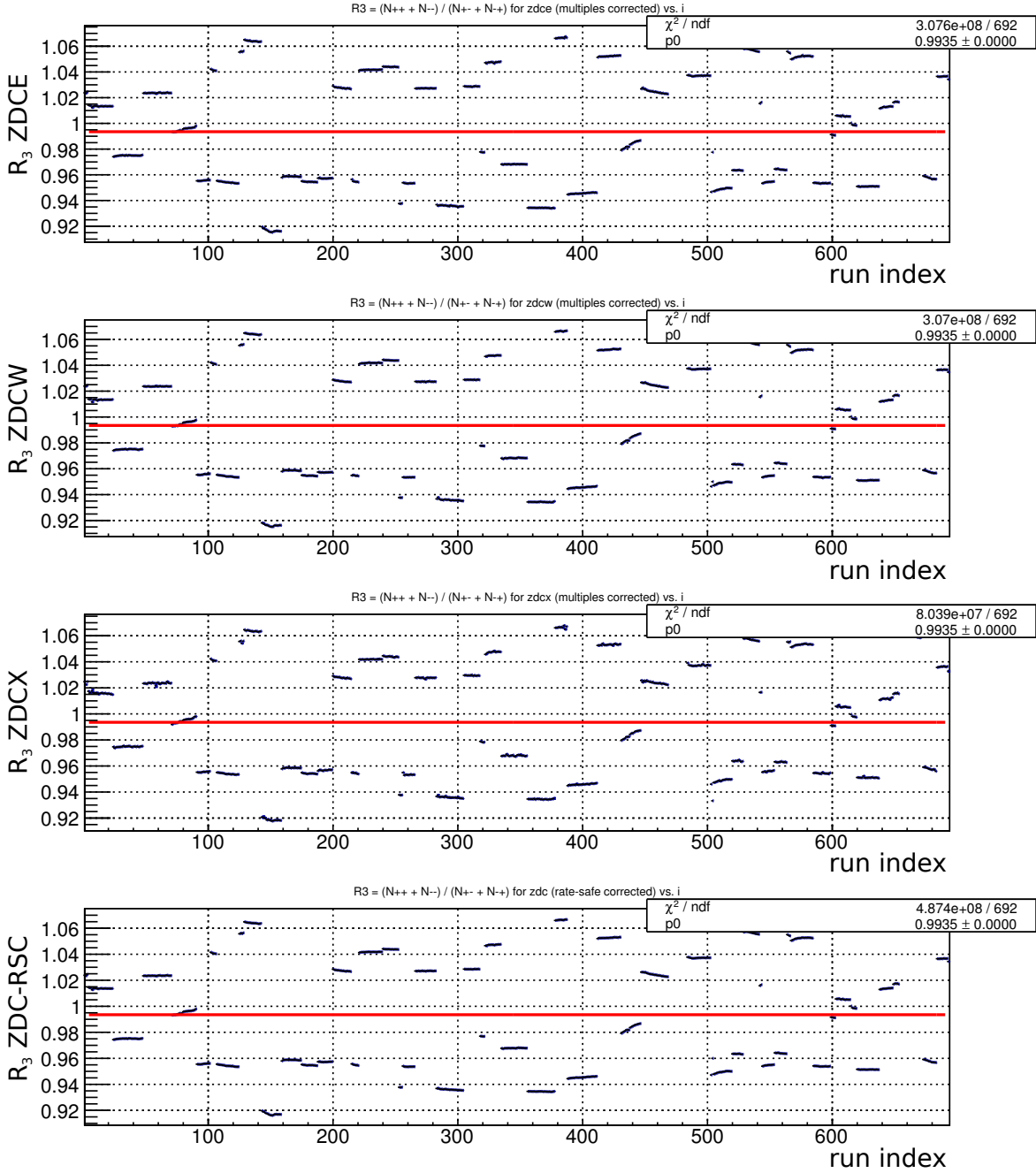


Figure F.1: R_3 from ZDC for Run 12; from top to bottom: CDF corrected E, CDF corrected W, CDF corrected X, rate-safe corrected.

Run 13 ZDC R_3 vs. Run Index

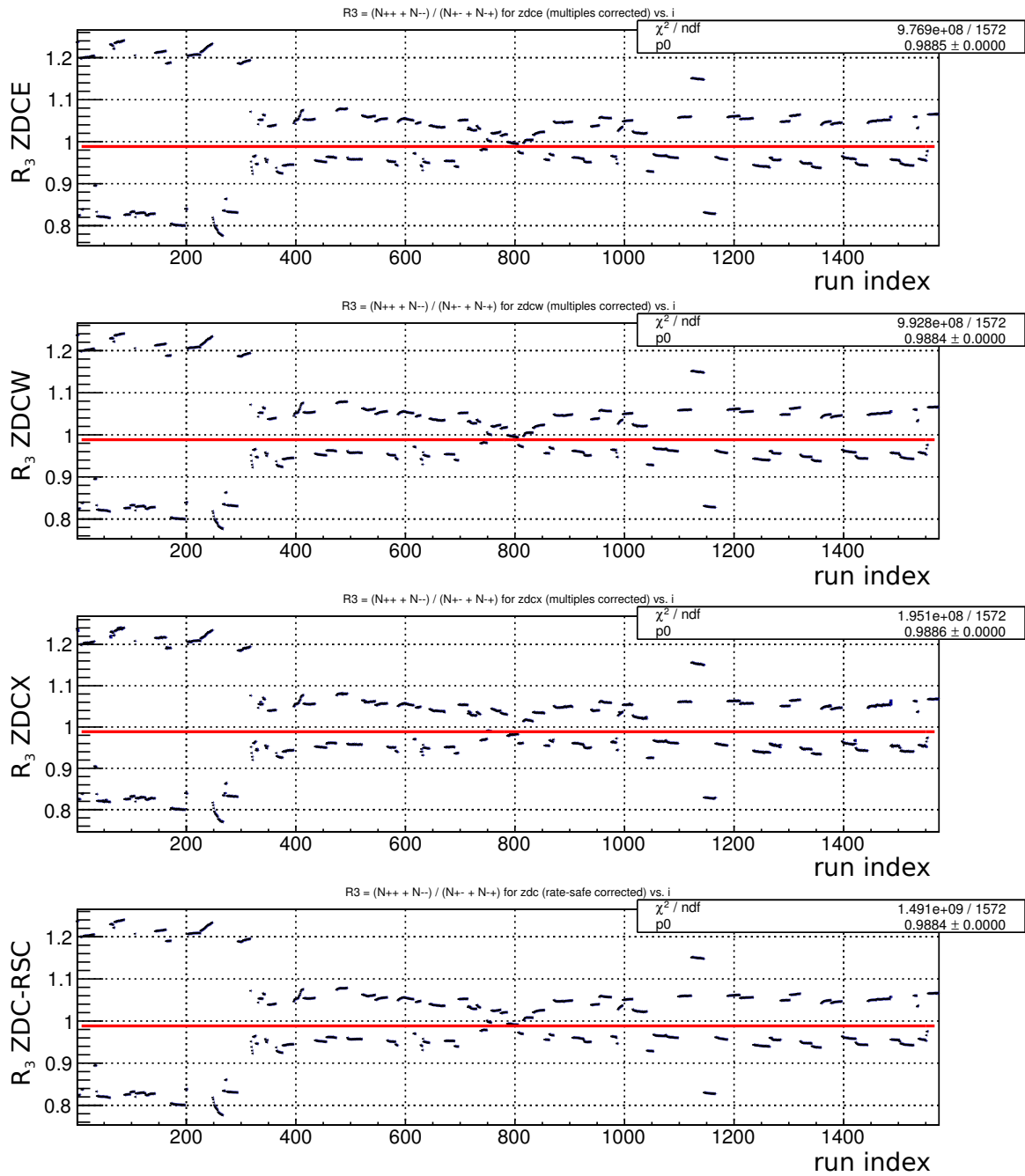


Figure F.2: R_3 from ZDC for Run 13.

Run 12 $R_3^E - R_3^W$ vs. Run Index

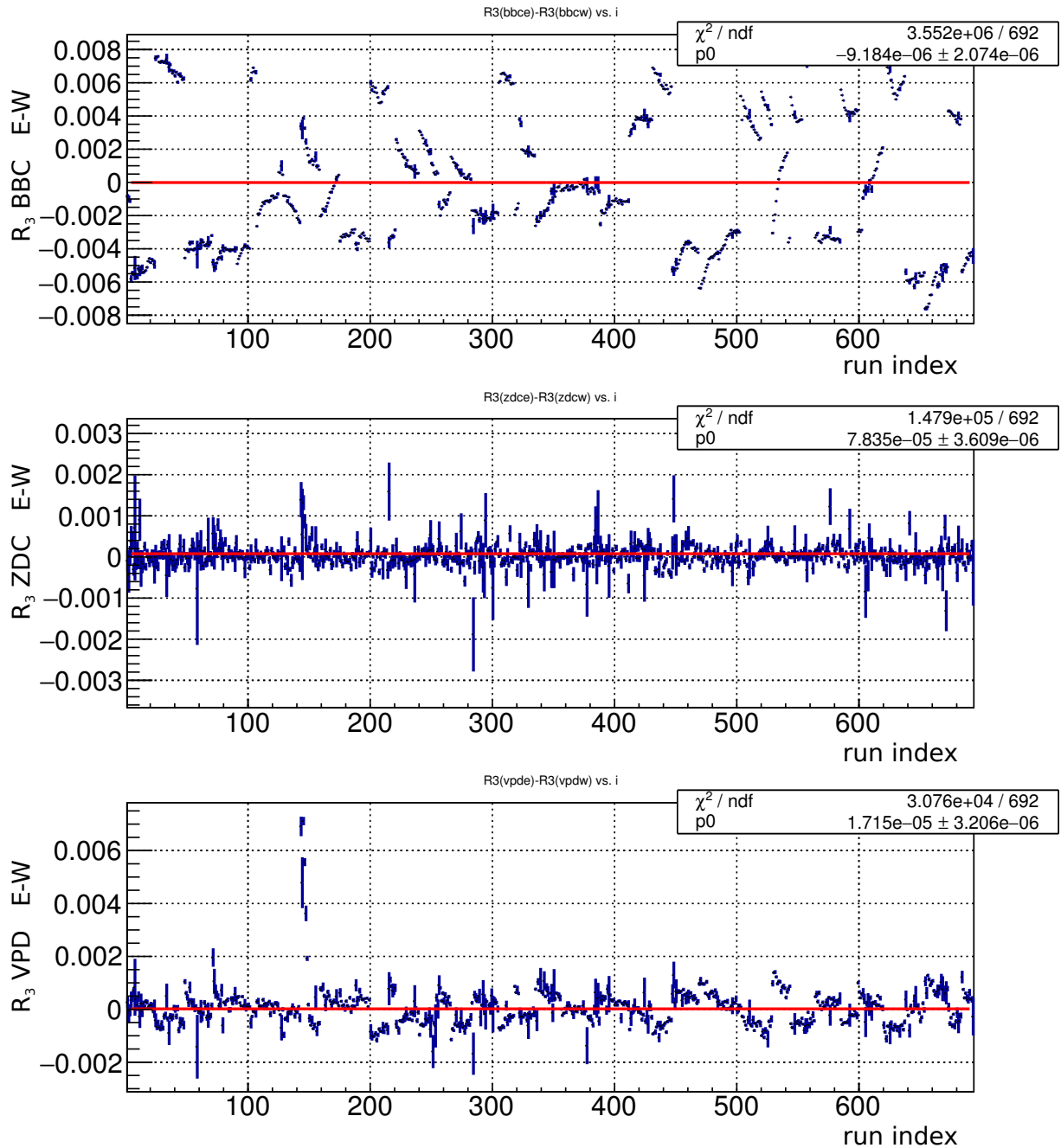


Figure F.3: Run 12 R_3 from E minus R_3 from W vs. run index; in order from top to bottom, the plots are for CDF corrected BBC, ZDC, and VPD.

Run 13 $R_3^E - R_3^W$ vs. Run Index

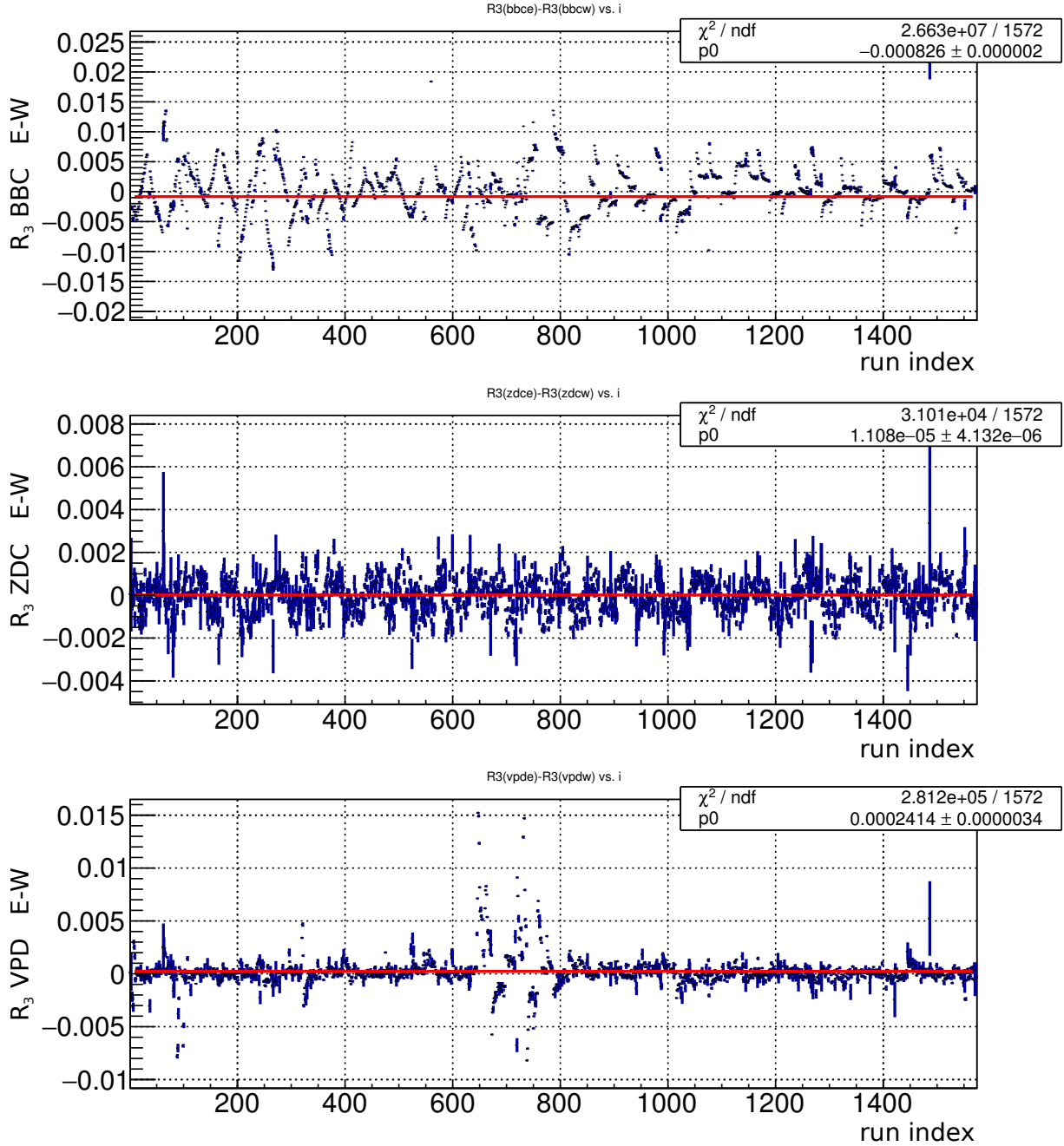


Figure F.4: Run 13 R_3 from E minus R_3 from W vs. run index; in order from top to bottom, the plots are for CDF corrected BBC, ZDC, and VPD.

Run 12 $R_3^E - R_3^X$ vs. Run Index

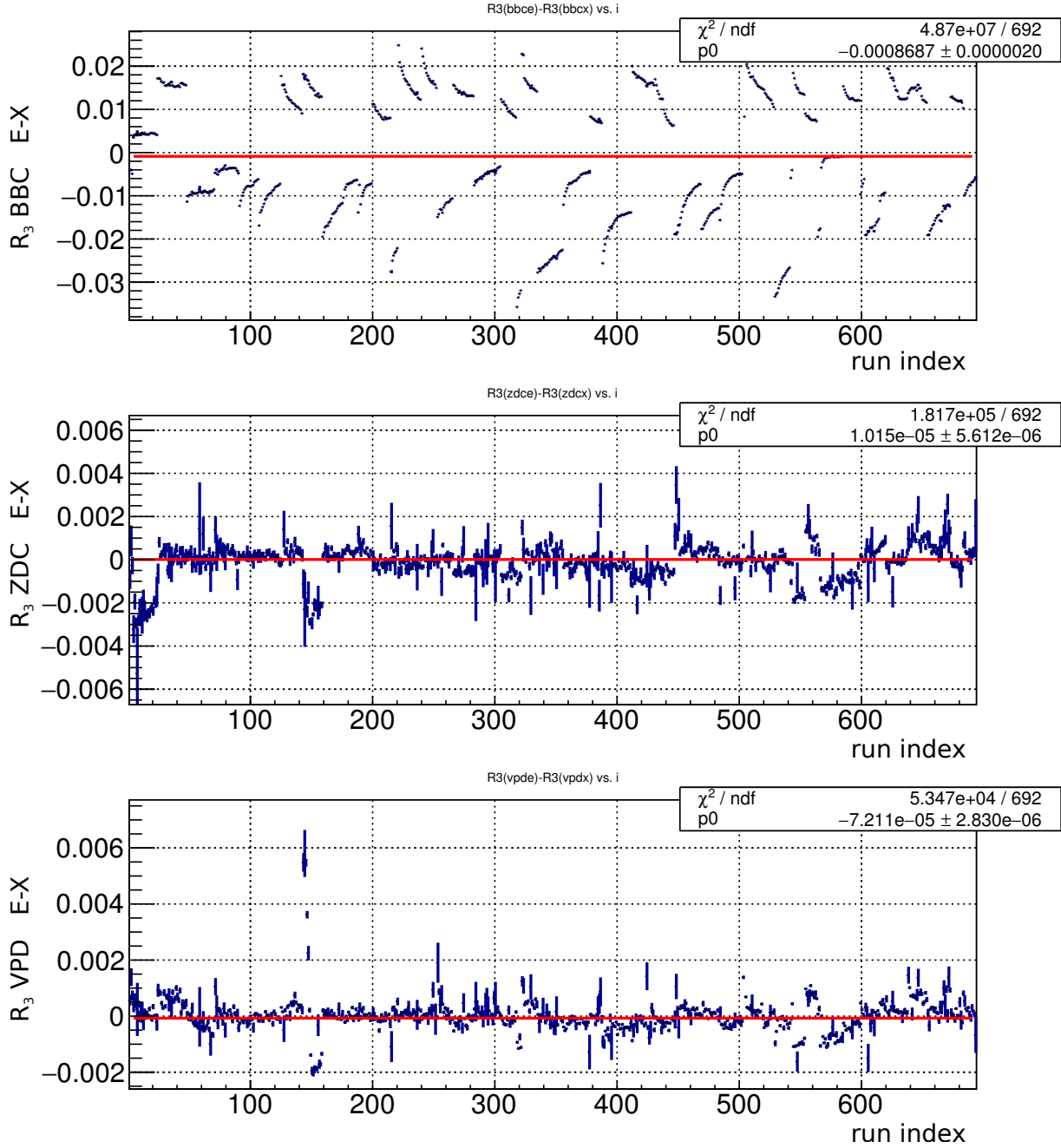


Figure F.5: Run 12 R_3 from E minus R_3 from X vs. run index; in order from top to bottom, the plots are for CDF corrected BBC, ZDC, and VPD.

Run 13 $R_3^E - R_3^X$ vs. Run Index

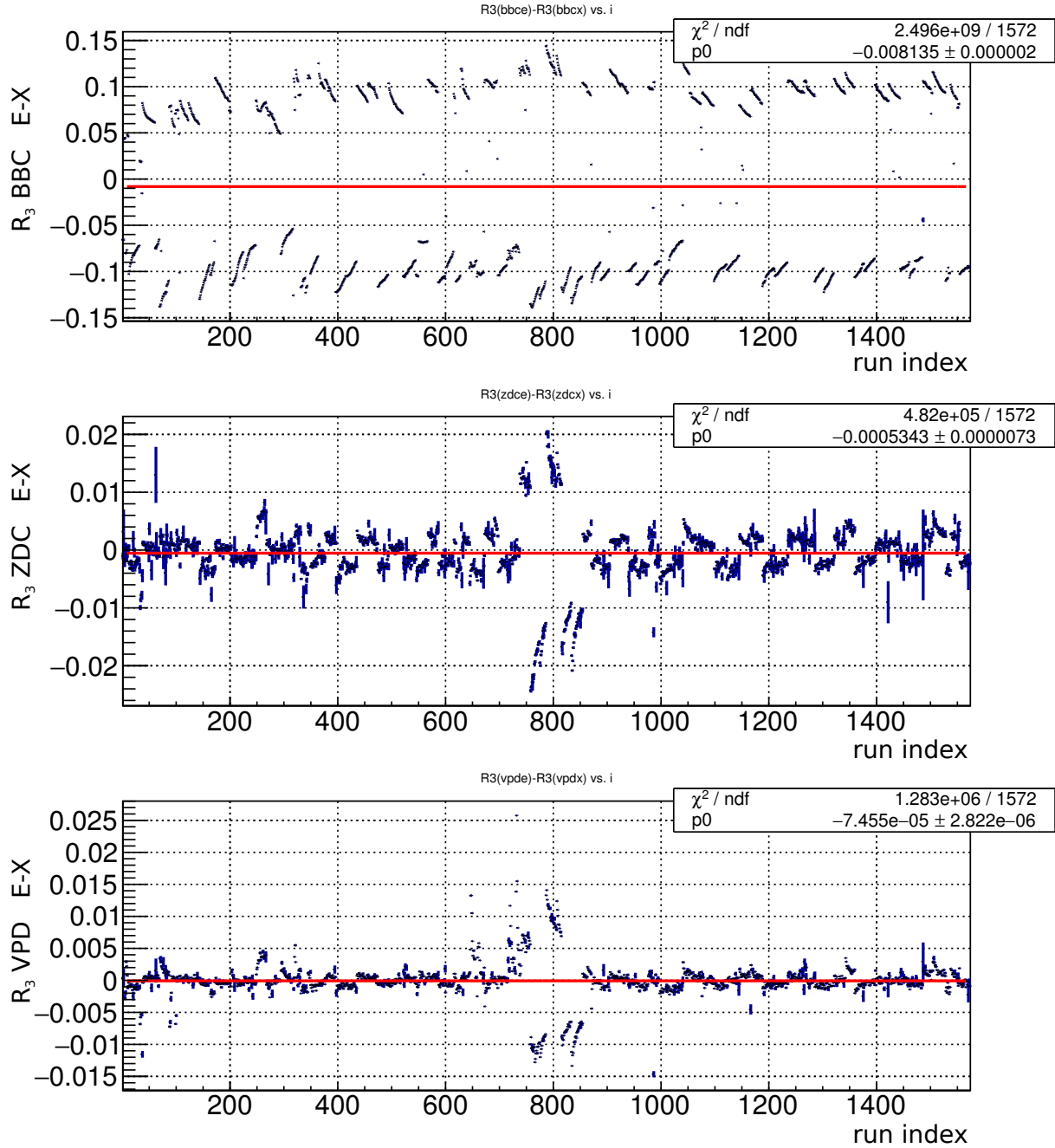


Figure F.6: Run 13 R_3 from E minus R_3 from X vs. run index; in order from top to bottom, the plots are for CDF corrected BBC, ZDC, and VPD.

Run 12 $R_3^W - R_3^X$ vs. Run Index

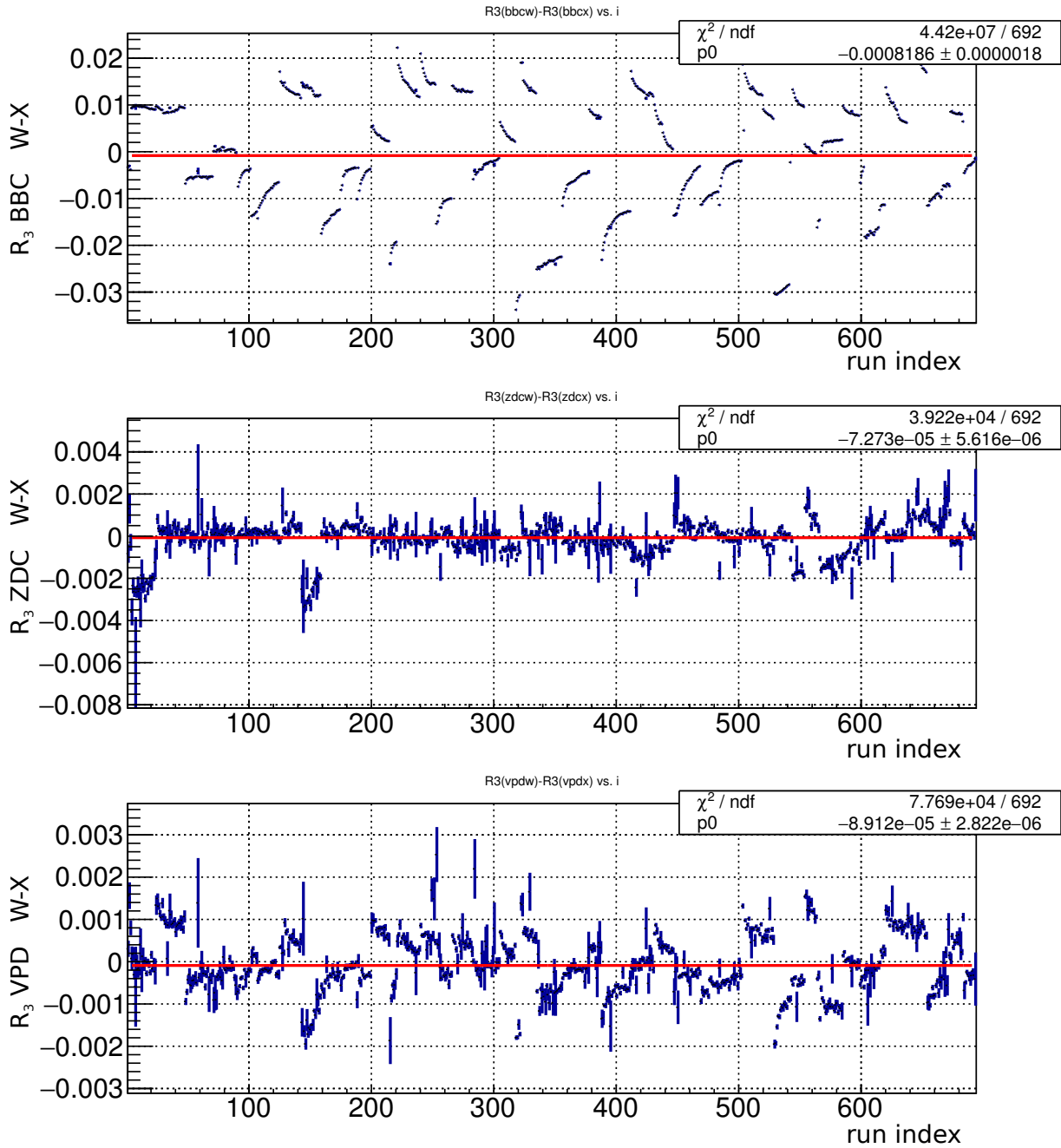


Figure F.7: Run 12 R_3 from W minus R_3 from X vs. run index; in order from top to bottom, the plots are for CDF corrected BBC, ZDC, and VPD.

Run 13 $R_3^W - R_3^X$ vs. Run Index

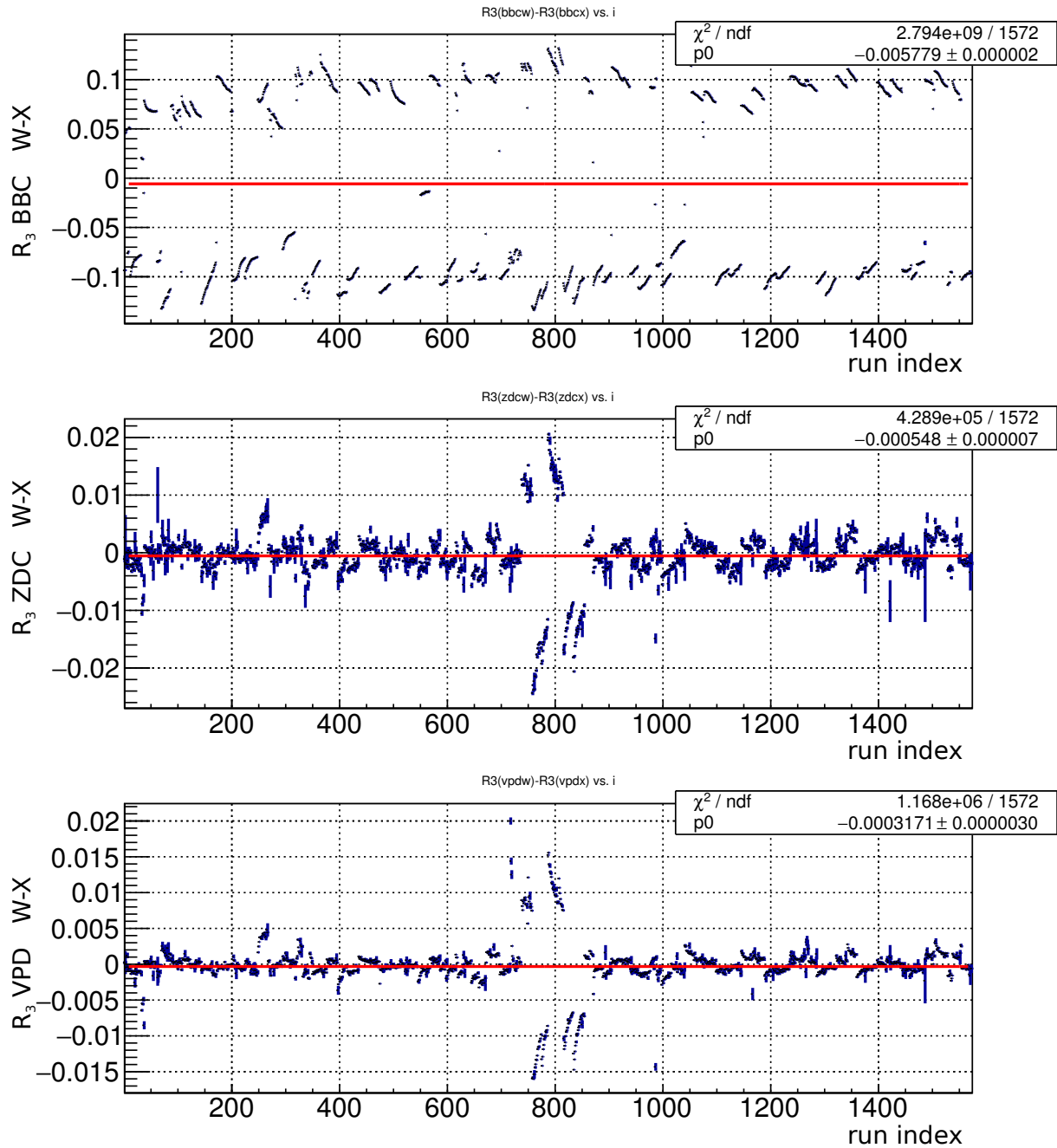


Figure F.8: Run 13 R_3 from W minus R_3 from X vs. run index; in order from top to bottom, the plots are for CDF corrected BBC, ZDC, and VPD.

Appendix G

Rate-Safe Counting Derivation

This derivation is a summary of that in [95]. This is a method for correcting scaler counts for accidental coincidences and multiple collisions, and is the method used for computing the relative luminosities used for $A_{LL}^{\pi^0}$. It is called the rate-safe counting method, or also sometimes the pile-up correction method.

G.1 Rate-Safe-Corrected Scaler Counts

Event Classes

Assume that there can be multiple collisions per bunch crossing; typically there are ~ 1 collisions / bunch crossing. We define two classes of collisions, called “event classes”:

1. Double-sided events (DS): collisions which will trigger a coincidence
 - DS events occur an average of λ_X times / bunch crossing
2. Single-sided events (SS): collisions which will trigger a single hit, but not a coincidence
 - East Single-sided events (ESS) occur an average of λ_E times / bunch crossing
 - West Single-sided events (WSS) occur an average of λ_W times / bunch crossing

Hit Probabilities

– DS events

The probability for detecting k_E hits in the E-scaler from DS events, given that the E-scaler has efficiency \times acceptance = ε_E is

$$P_{DS}(k_E) = \frac{(\varepsilon_E \lambda_X)^{k_E} e^{-\varepsilon_E \lambda_X}}{k_E!}. \quad (\text{G.1})$$

Likewise, the probability for detecting k_W hits in the W-scaler from DS events, given that the W-scaler has efficiency \times acceptance = ε_W is

$$P_{DS}(k_W) = \frac{(\varepsilon_W \lambda_X)^{k_W} e^{-\varepsilon_W \lambda_X}}{k_W!}. \quad (\text{G.2})$$

The joint probability that the E-scaler detects k_E hits and the W-scaler detects k_W hits from DS events is

$$P_{DS}(k_E, k_W) = P_{DS}(k_W|k_E) \cdot P_{DS}(k_E), \quad (\text{G.3})$$

where $P_{DS}(k_W|k_E)$ is the probability that the W-scaler detected k_W hits, given that the E-scaler detected k_E hits.

Let i denote the number of collisions in the bunch crossing. After a bit of effort (see [95]), one can show that this joint probability distribution may be written as

$$P_{DS}(k_E, k_W) = \sum_{i \geq \max(k_E, k_W)} \binom{i}{k_W} \binom{i}{k_E} \varepsilon_W^{k_W} \varepsilon_E^{k_E} (1 - \varepsilon_W)^{i - k_W} (1 - \varepsilon_E)^{i - k_E} \frac{\lambda_X^i e^{-\lambda_X}}{i!}. \quad (\text{G.4})$$

– SS events

The probability for detecting k_E hits in the E-scaler from SS events is

$$P_{ESS}(k_E) = \frac{(\varepsilon_E \lambda_E)^{k_E} e^{-\varepsilon_E \lambda_E}}{k_E!}. \quad (\text{G.5})$$

Likewise, the probability for detecting k_W hits in the W-scaler from SS events is

$$P_{WSS}(k_W) = \frac{(\varepsilon_W \lambda_W)^{k_W} e^{-\varepsilon_W \lambda_W}}{k_W!}. \quad (\text{G.6})$$

Probabilities for Detecting Zero Hits

Consider the following three probability distributions:

1. Zero hits in E-scaler

$$P(k_E = 0) = P_{DS}(k_E = 0) \cdot P_{ESS}(k_E = 0) = e^{-\varepsilon_E(\lambda_X + \lambda_E)} \quad (\text{G.7})$$

2. Zero hits in W-scaler

$$P(k_W = 0) = P_{DS}(k_W = 0) \cdot P_{WSS}(k_W = 0) = e^{-\varepsilon_W(\lambda_X + \lambda_W)} \quad (\text{G.8})$$

3. Zero hits in both E and W scalers

$$\begin{aligned} P(k_E = 0, k_W = 0) &= P_{DS}(k_E = 0, k_W = 0) \cdot P_{ESS}(k_E = 0) \cdot P_{WSS}(k_W = 0) = \\ &= e^{\varepsilon_W \varepsilon_E \lambda_X - \varepsilon_W \lambda_X - \varepsilon_E \lambda_X - \varepsilon_W \lambda_W - \varepsilon_E \lambda_E} \end{aligned} \quad (\text{G.9})$$

Let P^* denote the probability that we detect zero hits in both E and W scalers, given the condition that both the E and W scalers also detected zero hits. Using the Kolmogorov definition of conditional probability, P^* is expressed as

$$P^* = \frac{P(k_E = 0, k_W = 0)}{P(k_E = 0) \cdot P(k_W = 0)} = e^{\Omega \lambda_X}, \quad \text{where } \Omega := \varepsilon_W \varepsilon_E. \quad (\text{G.10})$$

Let $P_{E(W)}$ be the probability of detecting at least 1 E(W)-scaler single, and P_X be the probability of detecting at least 1 coincidence. These probabilities are used to rewrite the above three probability distributions for detecting zero hits in the form of

$$(\text{probability of zero hits}) = 1 - (\text{probability of at least 1 hit}).$$

Rate-Safe Correction Equation

Take the logarithm of P^* to obtain

$$\Omega \lambda_X = \ln P^* = \ln \left[\frac{1 - P_X}{(1 - P_E)(1 - P_W)} \right]. \quad (\text{G.11})$$

Assume the probability distributions of detecting $N_{E(W)}$ hits in the E(W)-scaler and N_X coincidences are all binomial, given a total of N_{bx} bunch crossings. Binomial distributions are

needed, since the probability of a trigger is significant for all filled bunch crossings. Denoting the mean of these binomial distributions by $\langle \cdot \rangle$, we thus have

$$P_S = \frac{\langle N_S \rangle}{N_{bx}}, \quad \text{where } S \in \{E, W, X\}. \quad (\text{G.12})$$

Finally, the product of E and W acceptances and efficiencies times the rate-safe counts N_{rsc} is written in terms of the raw scaler counts $\{N_E, N_W, N_X\}$ and total number of bunch crossings N_{bx} as

$$\Omega N_{rsc} = N_{bx} \cdot \ln \left[\frac{1 - \langle N_X \rangle / N_{bx}}{(1 - \langle N_E \rangle / N_{bx})(1 - \langle N_W \rangle / N_{bx})} \right], \quad (\text{G.13})$$

where the subscript ‘‘rsc’’ stands for ‘‘rate-safe correction’’. Because the relative luminosities are computed as ratios of corrected counts, for different spin combinations, the Ω factor may be left here, since it will cancel out in any relative luminosity computation.

G.2 A Note on Accidental Coincidences

1. For bunch crossings with 1 collision, we either have a true coincidence from a DS-event or a single hit from a SS-event
 - No accidental coincidences can occur in this case
2. For bunch crossings with more than 1 collision, we have the following possibilities:
 - Detection of coincidence event: either one or both of the following cases must occur:
 - At least 1 DS-collision – occurs an average of λ_X times / bunch crossing
 - At least 1 ESS-collision and 1 WSS-collision – occurs an average of λ_E and λ_W times / bunch crossing, respectively
 - Detection of single event
 - DS-event contribution
 - All SS-events in the bunch crossing are toward one detector – occurs an average of λ_E or λ_W times / bunch crossing

Since P^* only depends on λ_X , but not on λ_E or λ_W , equation G.13 for N_{rsc} only counts ‘‘true coincidences,’’ eliminating the need to consider ‘‘accidental coincidences.’’

G.3 Corrected Statistical Uncertainty

Define the function f , through which the counts uncertainties will be propagated:

$$f(N_X, N_E, N_W) := \Omega \cdot N_{rsc}(N_X, N_E, N_W). \quad (\text{G.14})$$

The uncertainties in $\{N_X, N_E, N_W\}$ propagate to an uncertainty in $\Omega \cdot N_{rsc}$ as

$$\begin{aligned} \sigma_{\Omega \cdot N_{rsc}}^2 = & \left(\frac{\partial f}{\partial N_X} \right)^2 \sigma_{N_X}^2 + \left(\frac{\partial f}{\partial N_E} \right)^2 \sigma_{N_E}^2 + \left(\frac{\partial f}{\partial N_W} \right)^2 \sigma_{N_W}^2 + \\ & + 2 \left[\frac{\partial f}{\partial N_X} \frac{\partial f}{\partial N_E} \sigma_{N_X N_E} + \frac{\partial f}{\partial N_X} \frac{\partial f}{\partial N_W} \sigma_{N_X N_W} + \frac{\partial f}{\partial N_E} \frac{\partial f}{\partial N_W} \sigma_{N_E N_W} \right], \end{aligned} \quad (\text{G.15})$$

where σ_A is the uncertainty (variance) of A and σ_{AB} is the covariance of A and B . All derivatives are evaluated at $N_S = \langle N_S \rangle$, with $S \in \{X, E, W\}$. Since the scalar counts $\{N_S\}$ are given by binomial distributions, the variances are

$$\begin{aligned} \sigma_{N_S}^2 &= N_{bx} P_S (1 - P_S) \\ &= \langle N_S \rangle \left(1 - \frac{\langle N_S \rangle}{N_{bx}} \right) \\ &= \langle N_S \rangle \cdot \zeta(N_S), \end{aligned} \quad (\text{G.16})$$

where

$$\zeta(N_S) := 1 - \frac{\langle N_S \rangle}{N_{bx}}. \quad (\text{G.17})$$

The covariances can be obtained from 2-dimensional histograms. Finally, the derivatives of f evaluate to

$$\frac{\partial f}{\partial N_X} = \frac{-1}{\zeta(N_X)} \quad \text{and} \quad \frac{\partial f}{\partial N_{E,W}} = \frac{1}{\zeta(N_{E,W})}. \quad (\text{G.18})$$

Inserting the variances, covariances, and derivatives yields the propagated uncertainty:

$$\begin{aligned} \sigma_{\Omega \cdot N_{rsc}}^2 = & \frac{\langle N_X \rangle}{\zeta(N_X)} + \frac{\langle N_E \rangle}{\zeta(N_E)} + \frac{\langle N_W \rangle}{\zeta(N_W)} - \\ & - \frac{2\sigma_{N_X N_E}}{\zeta(N_X)\zeta(N_E)} - \frac{2\sigma_{N_X N_W}}{\zeta(N_X)\zeta(N_W)} + \frac{2\sigma_{N_E N_W}}{\zeta(N_E)\zeta(N_W)}. \end{aligned} \quad (\text{G.19})$$

In practice, however, it is better to use the Pearson correlation coefficients, which are covariances normalized by the product of the variances: $\rho_{S_1 S_2} := \sigma_{S_1 S_2} / \sigma_{S_1} \sigma_{S_2}$. Typically, these correlation coefficients are close to unity for the present analyses.

Inserting the expression of the variances, the propagated uncertainty can be rewritten

using the Pearson correlation coefficients as

$$\begin{aligned} \sigma_{\Omega \cdot N_{rsc}}^2 = & \frac{\langle N_X \rangle}{\zeta(N_X)} + \frac{\langle N_E \rangle}{\zeta(N_E)} + \frac{\langle N_W \rangle}{\zeta(N_W)} - 2\rho_{N_X N_E} \sqrt{\frac{\langle N_X \rangle \langle N_E \rangle}{\zeta(N_X) \zeta(N_E)}} \\ & - 2\rho_{N_X N_W} \sqrt{\frac{\langle N_X \rangle \langle N_W \rangle}{\zeta(N_X) \zeta(N_W)}} + 2\rho_{N_E N_W} \sqrt{\frac{\langle N_E \rangle \langle N_W \rangle}{\zeta(N_E) \zeta(N_W)}}. \end{aligned} \quad (\text{G.20})$$

Equations [G.13](#) and [G.20](#) represent the quantity used for computing the relative luminosity and its statistical uncertainty. The statistical uncertainty in equation [G.20](#) is further propagated into the nine relative luminosity equations.

Appendix H

Bunch Fitting and Scaler Asymmetries

This appendix explains the bunch fitting algorithm, used to determine the intrinsic scaler asymmetry, S_{LL} , which was used as another method to determine the relative luminosity systematic in section 5.1.3. Refer to chapter 4 of [95] (see also [33]) for the method used to compute ε_3 , the double-spin asymmetry via the bunch fitting algorithm; this appendix is a summary of the method and how it applies to any general spin asymmetry.

H.1 General Bunch Fitting Algorithm

Let r^i be a quantity defined for bunch crossing $i \in B$, where B is the set of bunch crossing numbers under consideration. The quantity r^i could be scaler counts, a ratio of scaler counts, yields, *etc.* The objective of bunch fitting is to fit r^i to the following equation, which is motivated by the general relation of spin asymmetries and cross sections, as outlined in appendix D:

$$r^i = c_a (1 + H_a^i \varepsilon_a), \text{ where } H_a^i = \begin{cases} h_Y^i, & \text{if } a = 1 \\ h_B^i, & \text{if } a = 2 \\ h_B^i h_Y^i, & \text{if } a = 3 \end{cases} \quad (\text{H.1})$$

The fit parameters are c_a and ε_a , for each asymmetry number $a \in \{1, \dots, 9\}$ (see appendix B). The yellow (east-facing) and blue (west-facing) single-spin asymmetries are ε_1 and ε_2 ; the double-spin asymmetry is ε_3 . The parameter c_a is approximately the average value of r^i for the case where $\varepsilon_a \sum_{i \in B} H_a^i \ll |B|$.

The bunch fitting algorithm determines the pair of parameters (c_a, ε_a) , which minimizes

the χ_a^2 of the fit for asymmetry number a , given by

$$\chi_a^2 = \sum_{i \in B} \left[\frac{c_a (1 + H_a^i \varepsilon_a) - r^i}{\sigma_{r^i}} \right]^2, \quad (\text{H.2})$$

where $\sigma_{r^i}^2$ is the variance of r^i . Using $(H_a^i)^2 = 1, \forall a$ and i , the summands expand such that

$$\chi_a^2 = c_a^2 (1 + \varepsilon_a^2) \Sigma(1) - 2c_a \Sigma(r^i) + 2c_a^2 \varepsilon_a \Sigma(H_a^i) - 2c_a \varepsilon_a \Sigma(H_a^i r^i) + \Sigma(r^{i^2}), \quad (\text{H.3})$$

where for a bunch crossing-dependent quantity x^i , the function $\Sigma(x^i)$ is defined as

$$\Sigma(x^i) := \sum_{i \in B} \frac{x^i}{\sigma_{r^i}^2}. \quad (\text{H.4})$$

The pair (c_a, ε_a) which minimizes equation H.3 is the solution to the system

$$\begin{cases} 0 = \frac{\partial \chi_a^2}{\partial \varepsilon_a} = 2c_a^2 \varepsilon_a \Sigma(1) + 2c_a^2 \Sigma(H_a^i) - 2c_a \Sigma(H_a^i r^i) \\ 0 = \frac{\partial \chi_a^2}{\partial c_a} = 2c_a (1 + \varepsilon_a^2) \Sigma(1) - 2\Sigma(r^i) + 4c_a \varepsilon_a \Sigma(H_a^i) - 2\varepsilon_a \Sigma(H_a^i r^i) \end{cases}. \quad (\text{H.5})$$

The solution, which can be expressed solely in terms of the summations $\Sigma(x^i)$ is:

$$\varepsilon_a = \frac{\Sigma(H_a^i) \Sigma(r^i) - \Sigma(1) \Sigma(H_a^i r^i)}{\Sigma(H_a^i) \Sigma(H_a^i r^i) - \Sigma(1) \Sigma(r^i)}, \quad (\text{H.6})$$

$$c_a = \frac{\Sigma(H_a^i) \Sigma(H_a^i r^i) - \Sigma(1) \Sigma(r^i)}{\Sigma(H_a^i)^2 - \Sigma(1)^2}. \quad (\text{H.7})$$

The asymmetry ε_a is thus easy to extract for a given quantity r^i .

H.2 Uncertainty Propagation

Propagation of uncertainty of each r^i gives the uncertainties on the fit parameters:

$$\sigma_{\varepsilon_a}^2 = \sum_{k \in B} \left(\frac{\partial \varepsilon_a}{\partial r^k} \right)^2 \sigma_{r^k}^2, \quad (\text{H.8})$$

$$\sigma_{c_a}^2 = \sum_{k \in B} \left(\frac{\partial c_a}{\partial r^k} \right)^2 \sigma_{r^k}^2. \quad (\text{H.9})$$

The derivative of the function $\Sigma(x^i)$ is nonzero if x^i is dependent on r^i , e.g., for $x^i = f(r^i)$,

$$\frac{\partial}{\partial r^k} \Sigma \circ f(r^i) = \sum_{i \in B} \frac{1}{\sigma_{r^i}^2} \frac{\partial}{\partial r^k} f(r^i) = \frac{1}{\sigma_{r^k}^2} \frac{\partial}{\partial r^k} f(r^k). \quad (\text{H.10})$$

Derivatives of the χ_a^2 -minimizing fit parameters are then

$$\frac{\partial \varepsilon_a}{\partial r^k} = \frac{1}{\sigma_{r^k}^2} \frac{[\Sigma(H_a^i)^2 - \Sigma(1)^2] [\Sigma(H_a^i r^i) - H_a^k \Sigma(r^i)]}{[\Sigma(H_a^i) \Sigma(H_a^i r^i) - \Sigma(1) \Sigma(r^i)]^2}, \quad (\text{H.11})$$

$$\frac{\partial c_a}{\partial r^k} = \frac{1}{\sigma_{r^k}^2} \frac{H_a^k \Sigma(H_a^i) - \Sigma(1)}{\Sigma(H_a^i)^2 - \Sigma(1)^2}. \quad (\text{H.12})$$

The propagated uncertainties are therefore

$$\sigma_{\varepsilon_a}^2 = \sum_{k \in B} \left[\frac{1}{\sigma_{r^k}^2} \frac{[\Sigma(H_a^i)^2 - \Sigma(1)^2] [\Sigma(H_a^i r^i) - H_a^k \Sigma(r^i)]}{[\Sigma(H_a^i) \Sigma(H_a^i r^i) - \Sigma(1) \Sigma(r^i)]^2} \right]^2, \quad (\text{H.13})$$

$$\sigma_{c_a}^2 = \sum_{k \in B} \left[\frac{1}{\sigma_{r^k}^2} \frac{H_a^k \Sigma(H_a^i) - \Sigma(1)}{\Sigma(H_a^i)^2 - \Sigma(1)^2} \right]^2. \quad (\text{H.14})$$

H.3 Scaler Asymmetries

The above procedure can be used to extract raw asymmetries ε_a from a scaler system S , given a minimum-bias relative luminosity measured by detector MB by choosing

$$r^i = \frac{N_S^i}{N_{MB}^i},$$

where N_D^i is the number of scaler counts for bunch crossing i , measured by scaler D . The fractional error on r^i is given by propagation of uncertainty, assuming N_S^i and N_{MB}^i are uncorrelated:

$$\frac{\sigma_{r^i}}{r^i} = \sqrt{\frac{1}{N_S^i} + \frac{1}{N_{MB}^i}}. \quad (\text{H.15})$$

Let $N_D^{+(-)}$ be the total number of scaler counts seen by D , summed over bunch crossings with like (unlike) proton helicities. Then, for example, the raw double-spin asymmetry extracted with the above definition of r^i is

$$\varepsilon_3 = \frac{N_S^+ / N_{MB}^+ - N_S^- / N_{MB}^-}{N_S^+ / N_{MB}^+ + N_S^- / N_{MB}^-} = \frac{N_S^+ - R_3^{MB} N_S^-}{N_S^+ + R_3^{MB} N_S^-}, \quad (\text{H.16})$$

where the minimum bias relative luminosity is $R_3^{MB} := N_{MB}^+ / N_{MB}^-$. This asymmetry is then

seen as a raw double-spin asymmetry in scaler detector S , with respect to a minimum bias scaler detector MB . Including the beam polarizations allows the definition of the scaler spin asymmetries (with respect to MB) as

$$\begin{cases} S_L^Y := \varepsilon_1/P_Y \\ S_L^B := \varepsilon_2/P_B \\ S_{LL} := \varepsilon_3/P_B P_Y \end{cases} . \quad (\text{H.17})$$

This is the expression of S_{LL} used for the relative luminosity systematic uncertainties, where ε_3 was obtained from applying the bunch fit algorithm to $r^i = N_{\text{VPD}}^i/N_{\text{ZDC}}^i$.

Appendix I

Polarization Uncertainties

This appendix is a summary of polarization uncertainty propagation from the analysis note written by the CNI Polarimetry Group at RHIC [103], but with additional details specific to the Run 12 and 13 double-spin analysis.

We begin with a discussion of polarization for a single beam, along with its systematic uncertainty, followed by a section which outlines how the polarization product and product uncertainty is calculated. This is followed by a section concerning the combination of uncertainties for Runs 12 and 13. Finally, the fully averaged polarizations and uncertainties are presented.

I.1 Single Beam Polarization

Let $r \in \{1, \dots, N_r\} \subset \mathbb{N}$ denote a single run number and $f \in \{1, \dots, N_f\} \subset \mathbb{N}$ denote a single fill number, where N_r and N_f are the total numbers of runs and fills, respectively. Let F_f be the set of runs with fill number f , and let $f(r)$ be the fill number of the fill which contains run r .

The CNI Polarimetry Group provides polarimetry parameters for each fill F_f as a pair of parameters $\{P_f^0, P_f^1\}$ along with their uncertainties $\{\sigma_{P_f^0}, \sigma_{P_f^1}\}$. Letting t_r be the time of run r since the beginning of its fill $F_{f(r)}$, the time-dependent polarization for one beam for run r is

$$P_r = P_{f(r)}^0 + P_{f(r)}^1 \cdot t_r. \quad (\text{I.1})$$

The parameter P_f^0 represents the polarization at the beginning of F_f , while P_f^1 represents the rate of polarization change.

For each fill F_f , we may compute a luminosity-weighted average, given the luminosity of

run r is denoted by L_r :

$$\langle P \rangle_f^{\text{LW}} = \frac{1}{L_f} \sum_{r \in F_f} L_r P_r = P_f^0 + \frac{P_f^1}{L_f} \sum_{r \in F_f} L_r t_r, \quad \text{where } L_f := \sum_{r \in F_f} L_r. \quad (\text{I.2})$$

The uncertainties on the polarimetry parameters, $\{\sigma_{P_f^0}, \sigma_{P_f^1}\}$, propagate to an uncertainty on $\langle P \rangle_f^{\text{LW}}$, along with a relative fill-to-fill systematic uncertainty on the pC polarization, $\sigma_{\text{sys}(P)}/P$, as

$$\sigma_{\langle P \rangle_f^{\text{LW}}} = \sigma_{P_f^0} \oplus \frac{\sigma_{P_f^1}}{L_f} \sum_{r \in F_f} L_r t_r \oplus \langle P \rangle_f^{\text{LW}} \cdot \frac{\sigma_{\text{sys}(P)}}{P}. \quad (\text{I.3})$$

Values of $\sigma_{\text{sys}(P)}/P$ are obtained from table 4 in [103]:

- Run 12: 0% for blue beam, 3.1% for yellow beam
- Run 13: 2.8% for blue beam, 1.4% for yellow beam

We may then combine the fill-by-fill luminosity-weighted average polarizations into an overall polarization, denoted by \mathbb{P} , by luminosity-averaging $\langle P \rangle_f^{\text{LW}}$ over each fill:

$$\mathbb{P} = \frac{1}{\mathbb{L}} \sum_{f=1}^{N_f} L_f \langle P \rangle_f^{\text{LW}}, \quad \text{where } \mathbb{L} := \sum_{f=1}^{N_f} L_f. \quad (\text{I.4})$$

The fill-by-fill uncertainties $\sigma_{\langle P \rangle_f^{\text{LW}}}$ from equation I.3 propagate as the quadrature summation

$$\sigma_{\mathbb{P}} = \frac{1}{\mathbb{L}} \bigoplus_{f=1}^{N_f} L_f \sigma_{\langle P \rangle_f^{\text{LW}}}. \quad (\text{I.5})$$

There are two additional systematic uncertainties to consider: uncertainty from overall polarization scale and uncertainty from the profile correction. The overall scale uncertainties $\sigma_{\text{scale}(P)}/P$, which originate from H-jet and pC scale uncertainties and are summarized in table 5 of [103], are:

- Run 12: 3.4% for P_B , 3.4% for P_Y , and 6.6% for $P_B P_Y$
- Run 13: 3.2% for P_B , 3.3% for P_Y , and 6.4% for $P_B P_Y$

The uncertainty due to profile correction, $\sigma_{\text{profile}(P)}/P$ is

- For single beam: $2.2\%/\sqrt{N_f}$
- For both beams together: $3.1\%/\sqrt{N_f}$

At this point, one must be careful not to double-count uncertainties. The uncertainty $\sigma_{\mathbb{P}}$ in equation I.5 actually already contributes to $\sigma_{\text{scale}}(P)/P$. If N_T is the total number of fills used to obtain the polarimetry A_N and, in turn, $\sigma_{\text{scale}}(P)/P$, then we can approximately correct $\sigma_{\mathbb{P}}$ by using a factor:

$$\sigma_{\mathbb{P}} \rightarrow \sigma_{\mathbb{P},\text{corr}} = \sigma_{\mathbb{P}} \cdot \text{Re} \sqrt{1 - \frac{N_f}{N_T}}. \quad (\text{I.6})$$

For the case where more fills were analyzed N_f than were used to obtain polarimetry A_N , then $N_f > N_T$ implies $\sigma_{\sigma_{\mathbb{P},\text{corr}}} = 0$ and the scale systematic is completely double-counted. On the other hand, if $N_f < N_T$, then $\sigma_{\sigma_{\mathbb{P},\text{corr}}}$ accounts for the extra statistical uncertainty from having analyzed fewer than N_T fills. The values of N_T are (from table 6 in [103]):

- Run 12: 49 for blue, 49 for yellow
- Run 13: 138 for blue, 139 for yellow

As for the numbers of fills analyzed, $N_f = 45$ for Run 12 and $N_f = 40$ for Run 13.

All of the above uncertainties are combined together to form a total uncertainty on the \mathbb{P} for a single beam as

$$\sigma_{\mathbb{P}}^{\text{Tot}} = \sigma_{\mathbb{P},\text{corr}} \oplus \mathbb{P} \cdot \frac{\sigma_{\text{scale}}(P)}{P} \oplus \mathbb{P} \cdot \frac{\sigma_{\text{profile}}(P)}{P}, \quad (\text{I.7})$$

which can be written as a relative uncertainty on \mathbb{P} as

$$\frac{\sigma_{\mathbb{P}}^{\text{Tot}}}{\mathbb{P}} = \frac{\sigma_{\mathbb{P},\text{corr}}}{\mathbb{P}} \oplus \frac{\sigma_{\text{scale}}(P)}{P} \oplus \frac{\sigma_{\text{profile}}(P)}{P}. \quad (\text{I.8})$$

I.2 Beam Polarization Product

Equation I.7 represents the uncertainty of the overall polarization of one beam, but the $A_{LL}^{\pi_0}$ analysis uses the product of polarizations from each beam. Let us now consider the polarizations of two beams, denoted P and Q . The product of polarizations for one run r is

$$P_r Q_r = (P_{f(r)}^0 + P_{f(r)}^1 \cdot t_r) (Q_{f(r)}^0 + Q_{f(r)}^1 \cdot t_r), \quad (\text{I.9})$$

and the luminosity-weighted average for one fill f expands to

$$\langle PQ \rangle_f^{\text{LW}} = P_f^0 Q_f^0 + \frac{1}{L_f} \left[(P_f^0 Q_f^1 + P_f^1 Q_f^0) \sum_{r \in F_f} L_r t_r + P_f^1 Q_f^1 \sum_{r \in F_f} L_r t_r^2 \right]. \quad (\text{I.10})$$

The statistical uncertainty, including fill-to-fill systematic uncertainties, is

$$\begin{aligned} \sigma_{\langle PQ \rangle_f^{\text{LW}}} &= \frac{\sigma_{P_f^0}}{L_f} \left(Q_f^0 L_f + Q_f^1 \sum_{r \in F_f} L_r t_r \right) \oplus \frac{\sigma_{P_f^1}}{L_f} \left(Q_f^0 \sum_{r \in F_f} L_r t_r + Q_f^1 \sum_{r \in F_f} L_r t_r^2 \right) \oplus \\ &\oplus \frac{\sigma_{Q_f^0}}{L_f} \left(P_f^0 L_f + P_f^1 \sum_{r \in F_f} L_r t_r \right) \oplus \frac{\sigma_{Q_f^1}}{L_f} \left(P_f^0 \sum_{r \in F_f} L_r t_r + P_f^1 \sum_{r \in F_f} L_r t_r^2 \right) \oplus \langle PQ \rangle_f^{\text{LW}} \cdot \frac{\sigma_{\text{sys}}(PQ)}{PQ}, \end{aligned} \quad (\text{I.11})$$

where $\sigma_{\text{sys}}(PQ)/PQ = \sigma_{\text{sys}}(P)/P \oplus \sigma_{\text{sys}}(Q)/Q = 3.1\%$ for both Runs 12 and 13. The overall luminosity-weighted average polarization product is then

$$\mathbb{PQ} = \frac{1}{\mathbb{L}} \sum_{f=1}^{N_f} L_f \langle PQ \rangle_f^{\text{LW}}, \quad (\text{I.12})$$

and the statistical uncertainty is

$$\sigma_{\mathbb{PQ}} = \frac{1}{\mathbb{L}} \bigoplus_{f=1}^{N_f} L_f \sigma_{\langle PQ \rangle_f^{\text{LW}}}. \quad (\text{I.13})$$

The double-counting correction is

$$\sigma_{\mathbb{PQ}} \rightarrow \sigma_{\mathbb{PQ}, \text{corr}} = \sigma_{\mathbb{PQ}} \cdot \text{Re} \sqrt{1 - \frac{N_f}{\text{Min}(N_T^P, N_T^Q)}}, \quad (\text{I.14})$$

where the lesser of N_T^P and N_T^Q is used, since that would be the number of fills one would need in order to calculate a polarimetry double-spin asymmetry. Finally,

$$\sigma_{\mathbb{PQ}}^{\text{Tot}} = \sigma_{\mathbb{PQ}, \text{corr}} \oplus \mathbb{PQ} \cdot \frac{\sigma_{\text{scale}}(PQ)}{PQ} \oplus \mathbb{PQ} \cdot \frac{\sigma_{\text{profile}}(PQ)}{PQ}, \quad (\text{I.15})$$

where the scale and profile systematic uncertainties are

- $\sigma_{\text{scale}}(PQ)/PQ = 6.6\%$ for Run 12, 6.4% for Run 13
- $\sigma_{\text{profile}}(PQ)/PQ = 3.1\%/\sqrt{N_f}$ for both Runs together

I.3 Combining Uncertainties over Two RHIC Runs

If the analyzed data include polarizations from two RHIC Run periods, there will be two sets of polarimetry uncertainties to propagate, in order to determine an overall polarization uncertainty. This section demonstrates how to combine the two sets of uncertainties from Runs 12 and 13; altogether, four uncertainties need to be considered:

1. The fill-to-fill systematic uncertainty, $\sigma_{\text{sys}}(PQ)/PQ$, is trivial to combine since it enters each term of the quadrature sum in equation I.11.
2. The profile correction uncertainty, $\sigma_{\text{profile}}(PQ)/PQ$ is also straightforward, since it is the same for both Runs 12 and 13.
3. For the scale uncertainty, $\sigma_{\text{scale}}(PQ)/PQ$, [103] suggests to use the larger uncertainty between the two RHIC Runs.
4. For the double-counting correction, adding together the number of fills involved gives the correction factor

$$\sigma_{\text{PQ}} \rightarrow \sigma_{\text{PQ,corr}} = \sigma_{\text{PQ}} \cdot \text{Re} \cdot \sqrt{1 - \frac{N_{f,12} + N_{f,13}}{\text{Min}(N_{T,12}^P, N_{T,13}^Q) + \text{Min}(N_{T,12}^Q, N_{T,13}^P)}}, \quad (\text{I.16})$$

where the numbers of fills are subscripted by the RHIC Run numbers.

I.4 Results

We now list the numerical results of the polarization, following the notation used in this appendix. Run 12 is shown first, followed by Run 13, then the combination of Runs 12 and 13. The printed number of digits is not necessarily the actual number of significant figures, since 4 digits were printed past the decimal point for all numbers.

RUN 12

$$L_{int} = 57.4036 \text{ pb}^{-1}$$

$$\mathbb{P}_B = 0.5434 \quad \sigma_{\mathbb{P}_B} = 0.0187$$

$$\mathbb{P}_Y = 0.5641 \quad \sigma_{\mathbb{P}_Y} = 0.0194$$

$$\mathbb{P}_B \mathbb{P}_Y = 0.3069 \quad \sigma_{\mathbb{P}_B \mathbb{P}_Y} = 0.0204$$

$$\sigma_{\mathbb{P}_B, (\text{fill-to-fill scale})} = Re \left[\sqrt{1 - 45/49} \right] \cdot [0.0066] = 0.0019$$

$$\sigma_{\mathbb{P}_Y, (\text{fill-to-fill scale})} = Re \left[\sqrt{1 - 45/49} \right] \cdot [0.0078] = 0.0022$$

$$\sigma_{\mathbb{P}_B \mathbb{P}_Y, (\text{fill-to-fill scale})} = Re \left[\sqrt{1 - 45/49} \right] \cdot [0.0058] = 0.0017$$

$$\mathbb{P}_B \cdot \sigma_{\text{scale}}(P_B)/P_B = 0.5434 \cdot 0.0340 = 0.0185$$

$$\mathbb{P}_Y \cdot \sigma_{\text{scale}}(P_Y)/P_Y = 0.5641 \cdot 0.0340 = 0.0192$$

$$\mathbb{P}_B \mathbb{P}_Y \cdot \sigma_{\text{scale}}(P_B P_Y)/P_B P_Y = 0.3069 \cdot 0.0660 = 0.0203$$

$$\mathbb{P}_B \cdot \sigma_{\text{profile}}(P_B)/P_B = 0.5434 \cdot 0.0033 = 0.0018$$

$$\mathbb{P}_Y \cdot \sigma_{\text{profile}}(P_Y)/P_Y = 0.5641 \cdot 0.0033 = 0.0018$$

$$\mathbb{P}_B \mathbb{P}_Y \cdot \sigma_{\text{profile}}(P_B P_Y)/P_B P_Y = 0.3069 \cdot 0.0046 = 0.0014$$

RUN 13

$$L_{int} = 6.0140 \text{ pb}^{-1}$$

$$\mathbb{P}_B = 0.5688 \quad \sigma_{\mathbb{P}_B} = 0.0192$$

$$\mathbb{P}_Y = 0.5656 \quad \sigma_{\mathbb{P}_Y} = 0.0194$$

$$\mathbb{P}_B \mathbb{P}_Y = 0.3225 \quad \sigma_{\mathbb{P}_B \mathbb{P}_Y} = 0.0212$$

$$\sigma_{\mathbb{P}_B, (\text{fill-to-fill scale})} = Re \left[\sqrt{1 - 40/138} \right] \cdot [0.0067] = 0.0056$$

$$\sigma_{\mathbb{P}_Y, (\text{fill-to-fill scale})} = Re \left[\sqrt{1 - 40/139} \right] \cdot [0.0057] = 0.0048$$

$$\sigma_{\mathbb{P}_B \mathbb{P}_Y, (\text{fill-to-fill scale})} = Re \left[\sqrt{1 - 40/138} \right] \cdot [0.0054] = 0.0045$$

$$\mathbb{P}_B \cdot \sigma_{\text{scale}}(P_B)/P_B = 0.5688 \cdot 0.0320 = 0.0182$$

$$\mathbb{P}_Y \cdot \sigma_{\text{scale}}(P_Y)/P_Y = 0.5656 \cdot 0.0330 = 0.0187$$

$$\mathbb{P}_B \mathbb{P}_Y \cdot \sigma_{\text{scale}}(P_B P_Y)/P_B P_Y = 0.3225 \cdot 0.0640 = 0.0206$$

$$\mathbb{P}_B \cdot \sigma_{\text{profile}}(P_B)/P_B = 0.5688 \cdot 0.0035 = 0.0020$$

$$\mathbb{P}_Y \cdot \sigma_{\text{profile}}(P_Y)/P_Y = 0.5656 \cdot 0.0035 = 0.0020$$

$$\mathbb{P}_B \mathbb{P}_Y \cdot \sigma_{\text{profile}}(P_B P_Y)/P_B P_Y = 0.3225 \cdot 0.0049 = 0.0016$$

RUNS 12 + 13

$$L_{int} = 63.4177 \text{ pb}^{-1}$$

$$\mathbb{P}_B = 0.5458 \quad \sigma_{\mathbb{P}_B} = 0.0191$$

$$\mathbb{P}_Y = 0.5642 \quad \sigma_{\mathbb{P}_Y} = 0.0199$$

$$\mathbb{P}_B\mathbb{P}_Y = 0.3083 \quad \sigma_{\mathbb{P}_B\mathbb{P}_Y} = 0.0208$$

$$\sigma_{\mathbb{P}_B, (\text{fill-to-fill scale})} = Re \left[\sqrt{1 - 85/187} \right] \cdot [0.0060] = 0.0044$$

$$\sigma_{\mathbb{P}_Y, (\text{fill-to-fill scale})} = Re \left[\sqrt{1 - 85/188} \right] \cdot [0.0071] = 0.0052$$

$$\sigma_{\mathbb{P}_B\mathbb{P}_Y, (\text{fill-to-fill scale})} = Re \left[\sqrt{1 - 85/187} \right] \cdot [0.0053] = 0.0039$$

$$\mathbb{P}_B \cdot \sigma_{\text{scale}}(P_B)/P_B = 0.5458 \cdot 0.0340 = 0.0186$$

$$\mathbb{P}_Y \cdot \sigma_{\text{scale}}(P_Y)/P_Y = 0.5642 \cdot 0.0340 = 0.0192$$

$$\mathbb{P}_B\mathbb{P}_Y \cdot \sigma_{\text{scale}}(P_BP_Y)/P_BP_Y = 0.3083 \cdot 0.0660 = 0.0204$$

$$\mathbb{P}_B \cdot \sigma_{\text{profile}}(P_B)/P_B = 0.5458 \cdot 0.0024 = 0.0013$$

$$\mathbb{P}_Y \cdot \sigma_{\text{profile}}(P_Y)/P_Y = 0.5642 \cdot 0.0024 = 0.0013$$

$$\mathbb{P}_B\mathbb{P}_Y \cdot \sigma_{\text{profile}}(P_BP_Y)/P_BP_Y = 0.3083 \cdot 0.0034 = 0.0010$$

Appendix J

Including Photon Uncertainties in p_T Uncertainty

The p_T uncertainty was approximated in equation 5.21, rewritten here:

$$\frac{\sigma_{p_T}}{p_T} \approx \frac{\sigma_E}{E} \oplus \frac{\sigma_h}{h} \oplus \frac{\sigma_{R_z}}{R_z}. \quad (\text{J.1})$$

A more accurate determination of the p_T uncertainty can be made by making use of invariant mass and taking into account uncertainties on photon separation and energy imbalance; however, it will be shown that the additional terms which correct equation J.1 are suppressed. Given a π^0 with the 4-momentum given in equation 5.19, its invariant mass is

$$M^2 = E^2 - p_T^2 \csc^2 \theta. \quad (\text{J.2})$$

Defining Z as the photon energy imbalance and α as the decay opening angle, the two-photon system invariant mass is

$$M^2 = E^2 (1 - Z^2) \sin^2 \frac{\alpha}{2}. \quad (\text{J.3})$$

Let R be the distance between the nominal vertex and the point on the FMS plane at which the π^0 would have struck had it not decayed; the plane should be the one which was used for photon position reconstruction. Let D be the transverse distance between the detected photon hits. Then

$$\tan \frac{\alpha}{2} = \frac{D}{2R} = \frac{D \cos \theta}{2R_z} =: T(D, \theta). \quad (\text{J.4})$$

Now take $\alpha(D, \theta)$ from equation J.4, insert it into equation J.3 and equate the result to equation J.2:

$$E^2 (1 - Z^2) \frac{T^2}{1 + T^2} = E^2 - p_T^2 \csc^2 \theta. \quad (\text{J.5})$$

Solving for p_T gives

$$p_T(E, Z, \theta, D) = E \sin \theta \cdot \sqrt{\frac{1 + T^2 Z^2}{1 + T^2}}. \quad (\text{J.6})$$

The uncertainty propagates as

$$\sigma_{p_T} = \frac{\partial p_T}{\partial E} \sigma_E \oplus \frac{\partial p_T}{\partial Z} \sigma_Z \oplus \frac{\partial p_T}{\partial \theta} \sigma_\theta \oplus \frac{\partial p_T}{\partial D} \sigma_D. \quad (\text{J.7})$$

By defining X as

$$X := D \cdot \frac{\partial p_T}{\partial D} = E \sin \theta \cdot \frac{(Z^2 - 1) T^2}{(1 + T^2)^{3/2} \sqrt{1 + Z^2 T^2}}, \quad (\text{J.8})$$

the derivatives in equation J.7 are

$$\frac{\partial p_T}{\partial E} = \frac{p_T}{E}, \quad (\text{J.9})$$

$$\frac{\partial p_T}{\partial Z} = \frac{(1 + T^2) Z X}{Z^2 - 1}, \quad (\text{J.10})$$

$$\frac{\partial p_T}{\partial \theta} = p_T \cot \theta - X \tan \theta, \quad (\text{J.11})$$

$$\frac{\partial p_T}{\partial D} = \frac{X}{D}. \quad (\text{J.12})$$

Because $\tan \theta = h/R_z$,

$$\sigma_\theta^2 = \sin^2 \theta \cos^2 \theta \left[\left(\frac{\sigma_h}{h} \right)^2 + \left(\frac{\sigma_{R_z}}{R_z} \right)^2 \right]. \quad (\text{J.13})$$

It is also easy to show that, given $Z = (E_1 - E_2)/E$ and $\sigma_{E_1}/E_1 = \sigma_{E_2}/E_2 = \sigma_E/E$,

$$\sigma_Z = \frac{1 - Z^2}{\sqrt{2}} \cdot \frac{\sigma_E}{E}. \quad (\text{J.14})$$

It turns out that X is quite small when compared to other contributions to σ_{p_T} . If we set $X = 0$, the σ_Z and σ_D terms drop out. The σ_θ term is then the same as that in equation J.1, up to a factor of $\cos^2 \theta$, which is within 2% of unity for relevant values of θ . Since the dominant E term is the same as that in equation J.1, the determinations of σ_{p_T} in equations J.1 and J.7 are approximately the same.

Appendix K

Maximum Likelihood Method for A_{LL} Measurement

This appendix derives the maximum likely value of A_{LL} , given a set of runs; it follows [116], appendix D. We first review the maximum likelihood method (MLM), followed by its application to A_{LL} .

K.1 Maximum Likelihood Method

Let $f(x_i, \alpha)$ be the probability of measuring x_i in the i th measurement of a sequence of repeated measurements, where α represents the actual value of the measurement, *i.e.*, what the measurement is nominally. Such a probability is often a Gaussian distribution:

$$f(x_i, \alpha) = \frac{1}{\sigma\sqrt{2\pi}} \exp\left[-\frac{(x_i - \alpha)^2}{2\sigma^2}\right]. \quad (\text{K.1})$$

Define the likelihood function L as the product of the probability distributions for N measurements:

$$L = \prod_{i=1}^N f(x_i, \alpha). \quad (\text{K.2})$$

The maximum likely value, denoted $\bar{\alpha}$, is the α such that L is maximized: $\bar{\alpha}$ is the solution to

$$0 = \left. \frac{\partial L}{\partial \alpha} \right|_{\alpha=\bar{\alpha}}. \quad (\text{K.3})$$

Because L is a product, it is simpler to evaluate the maximum value of its logarithm:

$$0 = \left. \frac{\partial \ln L}{\partial \alpha} \right|_{\alpha=\bar{\alpha}} = \sum_{i=1}^N \left. \frac{\partial \ln f(x_i, \alpha)}{\partial \alpha} \right|_{\alpha=\bar{\alpha}}. \quad (\text{K.4})$$

With $f(x_i, \alpha)$ as a Gaussian distribution, the likelihood function is

$$L = \left(\frac{1}{\sigma\sqrt{2\pi}} \right)^N \exp \left[-\frac{1}{2\sigma^2} \sum_{i=1}^N (x_i - \alpha)^2 \right]. \quad (\text{K.5})$$

Differentiating the logarithm of L with respect to α yields

$$\begin{aligned} \left. \frac{\partial \ln L}{\partial \alpha} \right|_{\alpha=\bar{\alpha}} &= \left. \frac{\partial}{\partial \alpha} \left[N \ln \left(\frac{1}{\sigma\sqrt{2\pi}} \right) - \frac{1}{2\sigma^2} \sum_{i=1}^N (x_i - \alpha)^2 \right] \right|_{\alpha=\bar{\alpha}} = \\ &= \frac{1}{\sigma^2} \sum_{i=1}^N (x_i - \bar{\alpha}). \end{aligned} \quad (\text{K.6})$$

Setting this to zero returns the solution

$$\bar{\alpha} = \frac{1}{N} \sum_{i=1}^N x_i. \quad (\text{K.7})$$

Now consider the same Gaussian probability distribution, but allow for the width σ to vary from measurement-to-measurement, denoted as σ_i . The modified distribution is

$$f(x_i, \alpha) = \frac{1}{\sigma_i\sqrt{2\pi}} \exp \left[-\frac{(x_i - \alpha)^2}{2\sigma_i^2} \right]. \quad (\text{K.8})$$

Differentiating $\ln L$ gives

$$\begin{aligned} \left. \frac{\partial \ln L}{\partial \alpha} \right|_{\alpha=\bar{\alpha}} &= \left. \frac{\partial}{\partial \alpha} \ln \left\{ \prod_{i=1}^N \left(\frac{1}{\sigma_i\sqrt{2\pi}} \right) \cdot \exp \left[-\sum_{i=1}^N \frac{(x_i - \alpha)^2}{2\sigma_i^2} \right] \right\} \right|_{\alpha=\bar{\alpha}} = \\ &= \left. -\frac{\partial}{\partial \alpha} \sum_{i=1}^N \frac{(x_i - \alpha)^2}{2\sigma_i^2} \right|_{\alpha=\bar{\alpha}} = \\ &= \sum_{i=1}^N \frac{x_i - \bar{\alpha}}{\sigma_i^2}. \end{aligned} \quad (\text{K.9})$$

Setting this equal to zero yields $\bar{\alpha}$ as a weighted average:

$$\bar{\alpha} = \frac{\sum_{i=1}^N x_i/\sigma_i^2}{\sum_{i=1}^N 1/\sigma_i^2}. \quad (\text{K.10})$$

K.2 Maximum Likely A_{LL}

The above MLM can be used to extract a maximum likely value of the asymmetry A_{LL} , denoted \bar{A}_{LL} . Let i represent a single DAQ run. Let

$$\begin{aligned} S_i &:= N_i^{++} + N_i^{--}, \\ D_i &:= N_i^{+-} + N_i^{-+}, \\ P_i &:= P_i^B P_i^Y, \end{aligned} \quad (\text{K.11})$$

where $N^{\text{sign}(h_B)\text{sign}(h_Y)}$ is the number of π^0 s with the initial proton spin states as h_B and h_Y . Let R_i be the relative luminosity R_3 for run i . For a single run, the measurement of A_{LL_i} is written

$$A_{LL_i} = \frac{1}{P_i} \cdot \frac{S_i - R_i D_i}{S_i + R_i D_i}. \quad (\text{K.12})$$

The probability for measuring A_{LL_i} in the i th DAQ run, given a nominal value denoted by \hat{A}_{LL} , is modelled as a Gaussian with run-dependent uncertainty σ_i :

$$f(A_{LL_i}, \hat{A}_{LL}) \propto \exp \left[-\frac{(A_{LL_i} - \hat{A}_{LL})^2}{2\sigma_i^2} \right]. \quad (\text{K.13})$$

Using the MLM technique above, the maximum likely value is

$$\bar{A}_{LL} = \frac{\sum_{i=1}^N A_{LL_i}/\sigma_i^2}{\sum_{i=1}^N 1/\sigma_i^2}. \quad (\text{K.14})$$

The task is to now compute $\sigma_i =: \sigma_{A_{LL_i}}$, which is the uncertainty of A_{LL_i} . From now on, we suppress the i subscripts for brevity. We also assume that statistical uncertainties of R_i and P_i are negligibly small when compared to the statistical uncertainties of the yield (and the statistical uncertainty on P_i is already accounted for in the calculation of the overall

polarization uncertainty in appendix I). The uncertainty in A_{LLi} is

$$\begin{aligned}\sigma_{A_{LL}}^2 &= \left(\frac{\partial A_{LL}}{\partial S}\right)^2 \sigma_S^2 + \left(\frac{\partial A_{LL}}{\partial D}\right)^2 \sigma_D^2 = \\ &= \frac{(1 - A_{LL}P)^2 \sigma_S^2 + (1 + A_{LL}P)^2 R^2 \sigma_D^2}{P^2 (S + RD)^2}.\end{aligned}\tag{K.15}$$

Assume that the raw asymmetry $A_{LL}P \ll 1$ and can be neglected in the calculation of $\sigma_{A_{LL}}$. Also let $\sigma_S = \sqrt{S}$ and $\sigma_D = \sqrt{D}$, because the yield distributions are assumed to be Poissonian. The uncertainty becomes

$$\sigma_{A_{LL}}^2 = \frac{S + R^2 D}{P^2 (S + RD)^2}.\tag{K.16}$$

If the relative luminosity is close to unity, then the assumption $R^2 \sim R$ can be made and the numerator cancels a factor in the denominator, returning

$$\sigma_{A_{LL}}^2 \approx \frac{1}{P^2 (S + RD)}.\tag{K.17}$$

Substituting equation K.17 into equation K.14 gives the MLM value of A_{LL} used in this analysis:

$$\bar{A}_{LL} = \frac{\sum_{i=1}^N P_i (S_i - R_i D_i)}{\sum_{i=1}^N P_i^2 (S_i + R_i D_i)}.\tag{K.18}$$

K.3 Statistical Uncertainty

It remains to propagate statistical uncertainty of S and D to \bar{A}_{LL} :

$$\sigma_{\bar{A}_{LL}}^2 = \sum_{i=1}^N \left[\left(\frac{\partial \bar{A}_{LL}}{\partial S_i}\right)^2 \sigma_{S_i}^2 + \left(\frac{\partial \bar{A}_{LL}}{\partial D_i}\right)^2 \sigma_{D_i}^2 \right].\tag{K.19}$$

The derivatives with respect to S_i and D_i are

$$\frac{\partial \bar{A}_{LL}}{\partial S_i} = \frac{P_i - P_i^2 \bar{A}_{LL}}{\sum_{k=1}^N P_k^2 (S_k + R_k D_k)},\tag{K.20}$$

$$\frac{\partial \bar{A}_{LL}}{\partial D_i} = \frac{-R_i P_i - R_i P_i^2 \bar{A}_{LL}}{\sum_{k=1}^N P_k^2 (S_k + R_k D_k)}.\tag{K.21}$$

Assuming that $P_i^2 \bar{A}_{LL}$ is negligible, inserting these derivatives into equation K.19 gives

$$\sigma_{\bar{A}_{LL}} = \frac{\sqrt{\sum_{i=1}^N P_i^2 (S_i + R_i^2 D_i)}}{\sum_{i=1}^N P_i^2 (S_i + R_i D_i)}. \quad (\text{K.22})$$

Making the approximation $P_i = \bar{P}$, the average polarization, as well as $R_i = 1$, the uncertainty becomes simply

$$\sigma_{\bar{A}_{LL}} \approx \frac{1}{\bar{P}\sqrt{N}}, \quad (\text{K.23})$$

where $N = \sum_{i=1}^N (S_i + D_i)$. It turns out that equation K.23 is extremely close to the value determined from equation K.22; ultimately equation K.22 is used for the statistical uncertainty on $A_{LL}^{\pi^0}$.

Appendix L

Curing Radiation Damage in the FMS by Photobleaching

The problem of radiation damage in the FMS Pb-glass cells was discussed in section [2.3.4](#). This appendix discusses in more detail the photobleaching techniques that were used to reverse the effects of radiation damage, effectively “curing” the FMS.

L.1 Solar Photobleaching

After the end of Run 13, the FMS was unstacked during the summer of 2013 and all cells were exposed to 48 hours of sunlight. During the exposure time, transverse transmittance spectra were measured at three longitudinal depths along a cell. Figure [L.1](#) shows the spectrum of light used for the transmittance measurement; the spike at 656 nm is due to deuterium emission from the light source. Figure [L.2](#) shows the transmittance spectra for a clear (not damaged) large cell, clear small cell, and damaged large and small cells; the colors indicate three longitudinal measurements: one near the front face (green), one in the center (red), and one near the back (blue). The vertical axis is a transmittance *relative* to the average transmittance for wavelengths greater than 900 nm (note that since this is just a relative transmittance, it can be greater than 1). For the large cell, the front measurement shows the most damage, whereas for a small cell, the middle measurement shows the most; for both cells, the back measurement shows the least amount of damage.

Figure [L.3](#) shows the ratio of transmittance of the damaged cell to that of the clear cell, given no sunlight exposure, 15 hours of exposure, and 40 hours of exposure, respectively for each row of plots in the figure. The clear cell was exposed in tandem with the damaged cell exposure. After 40 hours of exposure, the cells were 90–95% cured.

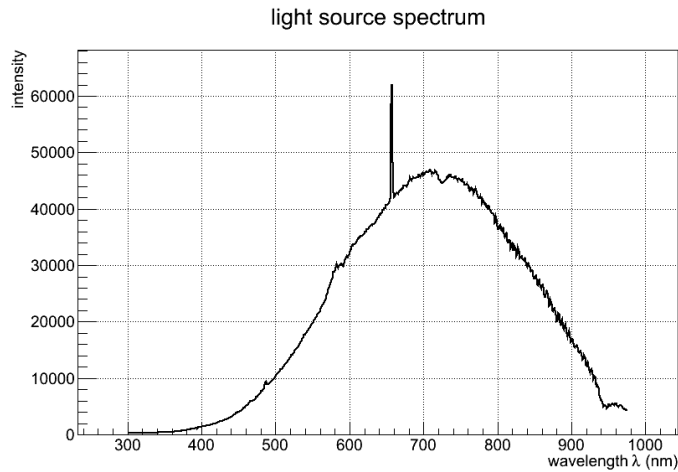


Figure L.1: Light source spectrum used for Pb-glass transmission spectra.

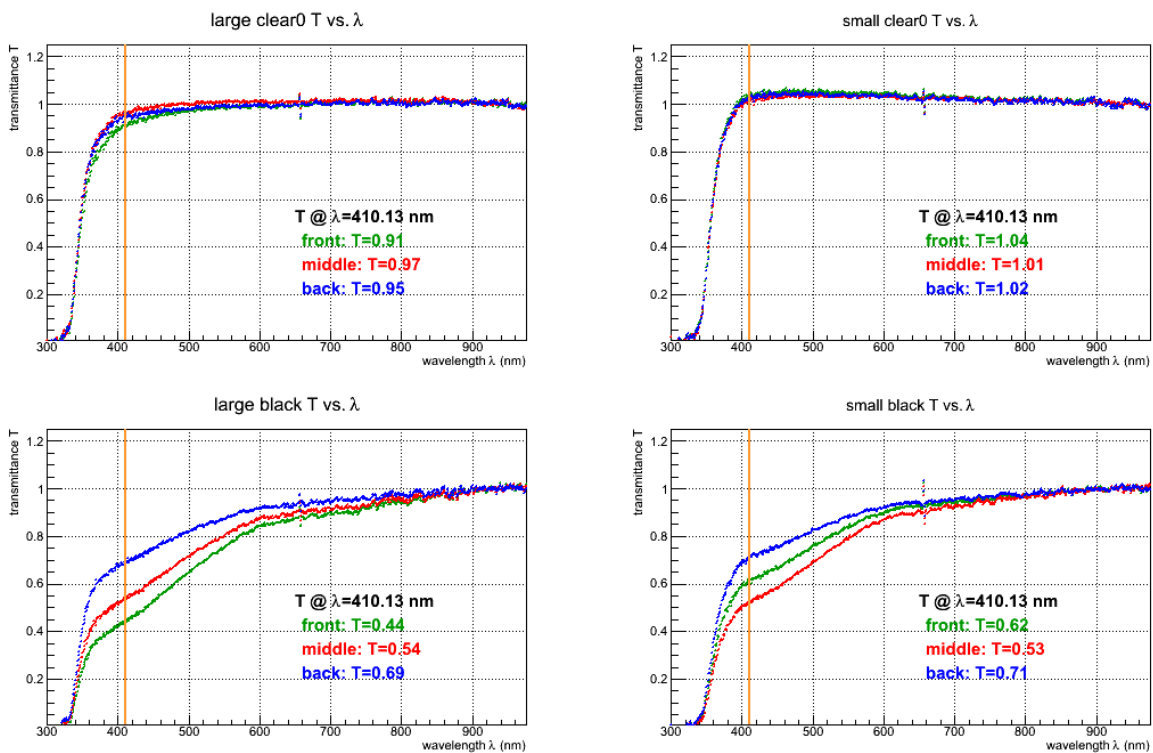
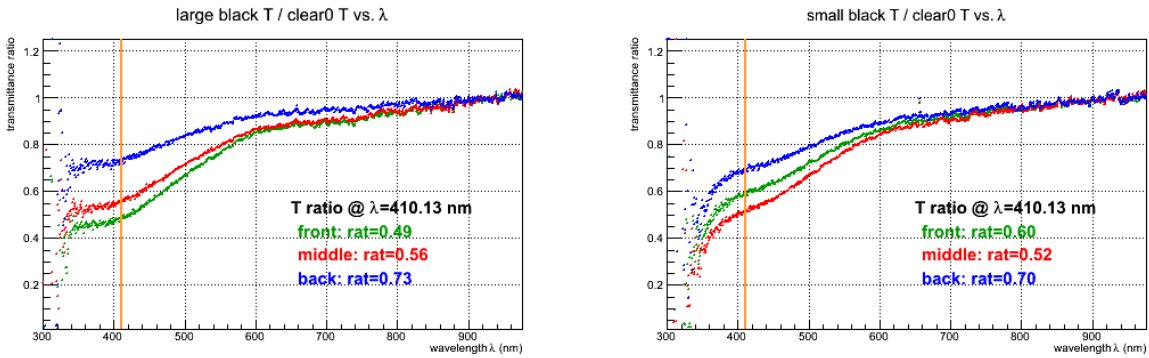
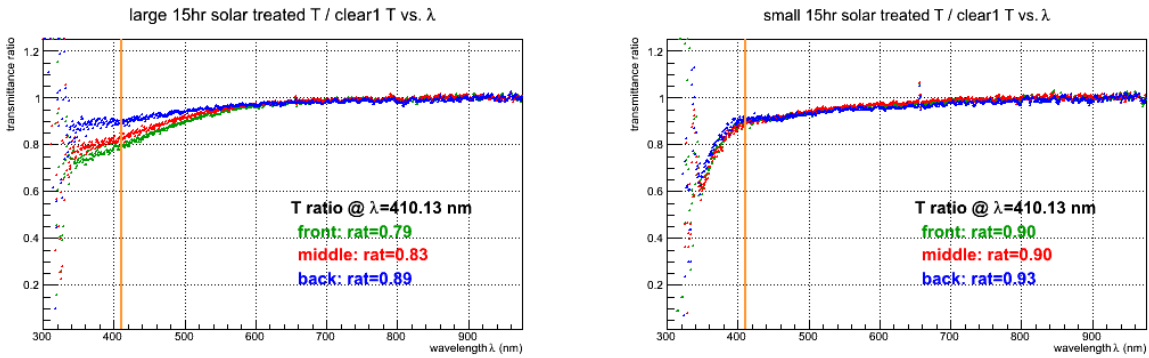


Figure L.2: Transmittance spectra for a large clear (not damaged) cell (top-left), small clear cell (top-right), damaged large cell (bottom-left) and damaged small cell (bottom-right). The colors indicate three longitudinal depths at which the transverse transmittance was measured: near the front (green), near the middle (red), and near the back, where the PMT would be (blue). The relative transmittance at 410 nm is written on each plot.

No Sunlight Exposure



After 15 Hours Exposure



After 40 Hours Exposure

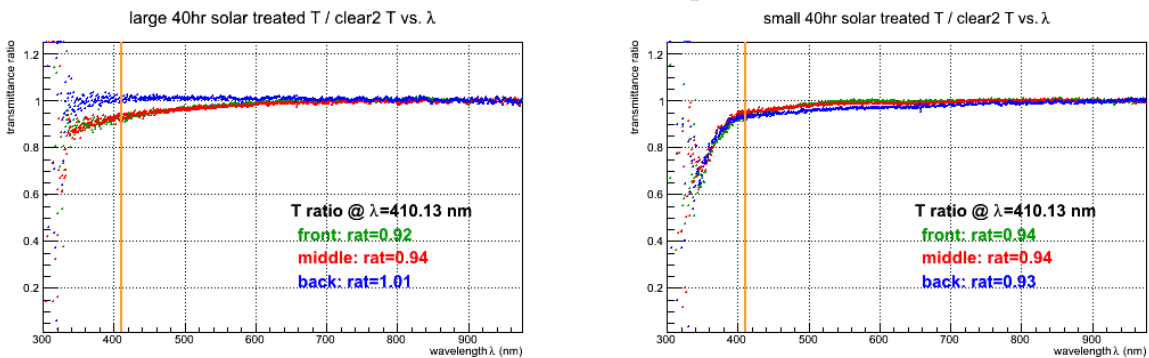


Figure L.3: Ratios of transmittance spectra for a large cell (left) and small cell (right) for 0 hours exposure (top), 15 hours (middle), and 40 hours (bottom). Transmittance ratios at 410 nm are written on each plot.

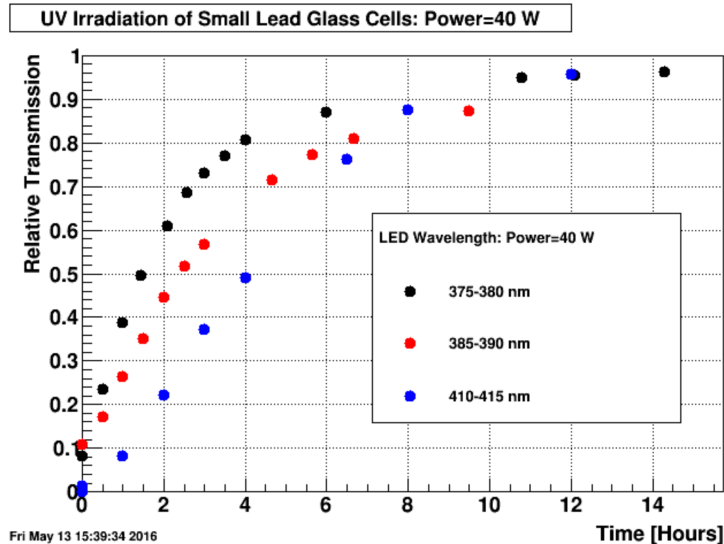


Figure L.4: Relative transmission of a small cell as a function of UV-LED exposure time (hours) for three different wavelengths: 410–415 nm (blue, slowest), 385–390 nm (red, middle), and 375–380 nm (black, fastest).

L.2 Photobleaching with UV-LEDs

After Run 16, the FMS Pb-glass was radiation damaged enough to once again necessitate curing. Since unstacking the FMS again and exposing all cells to sunlight is a laborious task, an alternative idea was employed. After testing multiple UV sources such as tanning bed lights and bug lights, we settled on UV-LEDs and constructed a thin UV-LED array to sit in front of the FMS glass. This array was designed to be turned on between RHIC fills for a few hours per day during Run 17, in order to combat the radiation damage and attempt to keep the glass relatively clear.

A variety of UV-region wavelengths were tested. Figure L.4 shows the relative transmission in a small cell as a function of time (in hours) for 3 different wavelengths of light; the fastest curing was from the lowest wavelength: 375–380 nm. Thus an array of this wavelength of UV-LEDs was constructed. Due to a mistake in construction, however, a fraction ($\sim 1/3$) of the UV-LEDs were not the intended wavelength; they most likely are closer to 400 nm. As a consequence of this mistake, although we were not able to power the array to its *full* intended power, the overall emission spectrum of the array was broader, which may have actually helped clear a broader range of F-centers.

Due to design and installation restrictions, the UV-LED array needed to be built in modules; it also need to be as flat as possible so it could fit in the region in front of the FMS. This region housed the LED flasher array (see section 3.5.1), which also had to be

redesigned. The UV-LED array was positioned approximately 3 inches in front of the FMS glass, with the UV-LEDs facing the glass directly. The LED flasher system, which previously sent LED signals into every single FMS cell via fiber optics, was removed. The flasher LEDs themselves were extracted from the fiber optics system, polished, and then re-connected and mounted on the front face of the FMS, so that they faced *away* from the FMS and toward the UV-LED array. Since the UV-LEDs were mounted on aluminum plates, the aluminum provided enough reflectance of the flasher LEDs such that the flasher system could still be used in the same manner: for time-dependent gain tracking.

Since the UV-LEDs ran rather hot, a method of keeping them cool was needed. The UV-LEDs were mounted on aluminum plates, embedded with copper pipes which carried chilled water; these plates not only served as heat-sinks for the array, but also allowed the array itself to be segmented into small enough pieces such that installation was streamlined. Ultimately during operation, the temperature of the FMS rose only a couple of degrees and returned back to normal about 15 minutes after the UV-LED array was powered down.

Figure L.5 shows the effect of radiation damage as a function of pseudorapidity; the vertical axis is the ratio of flasher LED amplitudes between the end and the beginning of a 47 pb^{-1} period of $\sqrt{s} = 200 \text{ GeV}$ pp collisions. The damage is seen to be more severe at higher pseudorapidities, therefore the density of the UV-LEDs in the array was made to increase as a function of pseudorapidity. Figure L.6 shows a diagram of one quadrant of the UV-LED array, where the beam pipe passes through the bottom left corner. The distribution of UV-LEDs is shown, along with the 7 aluminum plates that make up the array quadrant; the aluminum plates cover the majority of the large and small cells within the quadrant.

Each UV-LED needed 10 W of power, supplied by a voltage drop of 10 V per LED and 1 A of current. Only 1 W of UV radiation power was emitted per LED; the rest was dissipated as heat. Given that there are approximately 768 UV-LEDs, multiple power supplies were used. The power was first distributed to the power supplies via a 3-phase Power Distribution Unit (PDU); one PDU was used for the north half and another for the south half. Each PDU was connected to a 208 V input and contained 3 banks (one for each phase) with 4 power supplies attached to each. On each power supply, there were 2 circuits containing 4 parallel strings of UV-LEDs, each with 4 UV-LEDs in series along with a fuse. Figure L.8 shows a diagram of this power distribution setup.

Both PDUs were connected to the local intranet as well as directly linked to the control room via a fiber optic connection. Since both the PMT HV and UV-LED array were remotely controllable, a graphical user interface was designed in order to simplify operations, as shown in figure L.9. The graphical interface also served as a software interlock between the UV-LED array and the PMT HV system, since having both on at the same time could possibly damage

the PMTs: exposing the sensitive PMTs to the high flux of UV radiation could overpower them. Because of this danger, the system demanded verification that the UV-LEDs were off before permitting the HV to be turned on, and vice versa. Furthermore, for every time any button was clicked on the control interface, a text message was sent to those responsible for FMS operations, the so-called *experts*; if the UV-LEDs were ever detected to be on at the same time, both the UV-LEDs and HV systems were shut down, and the operator in charge would be presented with a message to call the experts immediately. During the entirety of Run 17, this critical state of the UV-LEDs and HV systems being simultaneously on never occurred.

Figure L.7 shows the ratio of flasher LED amplitudes for a 43 hour exposure of the FMS to the UV-LED array; this ratio is plotted as a function of pseudorapidity. Overall, the UV-LED array successfully cleared the Pb-glass and it was used daily for a few hours per day during Run 17 to maintain glass transparency and a relatively constant trigger rate throughout the entire Run. This array was effectively the solution to the problem of radiation damage in the FMS.

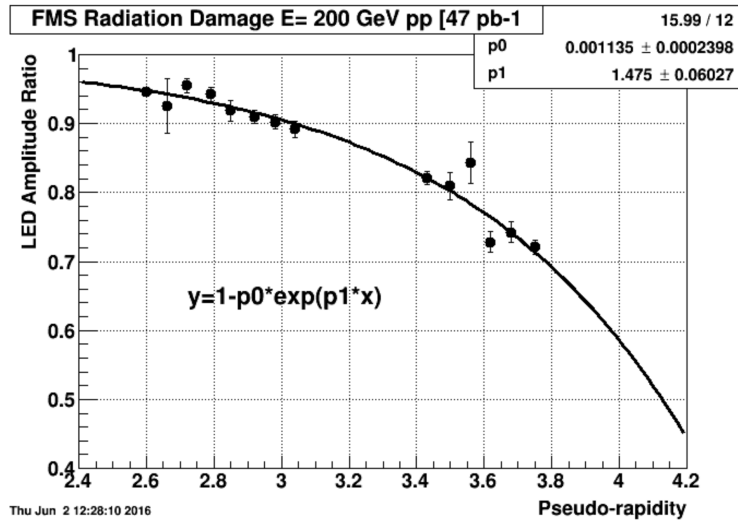


Figure L.5: Ratio of LED flasher amplitudes between end and beginning of a period of radiation damage accumulation, as a function of pseudorapidity.

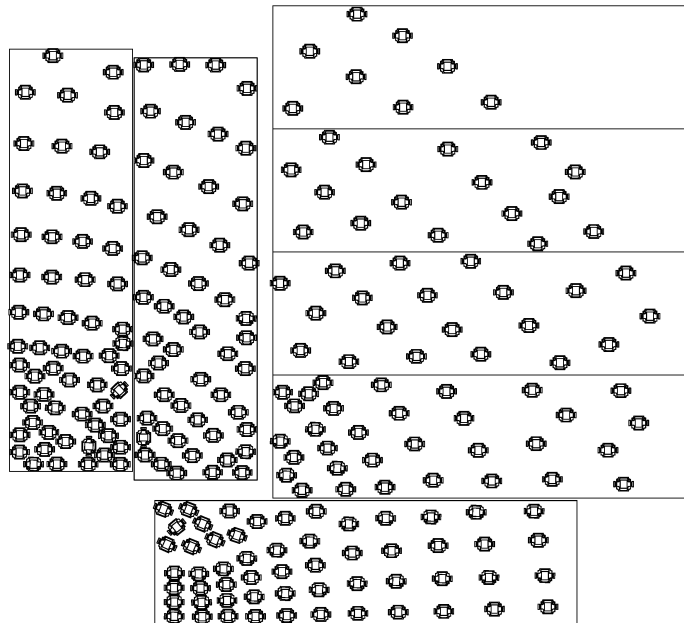


Figure L.6: One quadrant of the UV-LED array, showing the distribution of LEDs and their associated aluminum plates. The UV-LEDs were wired in groups of four (wiring not drawn).

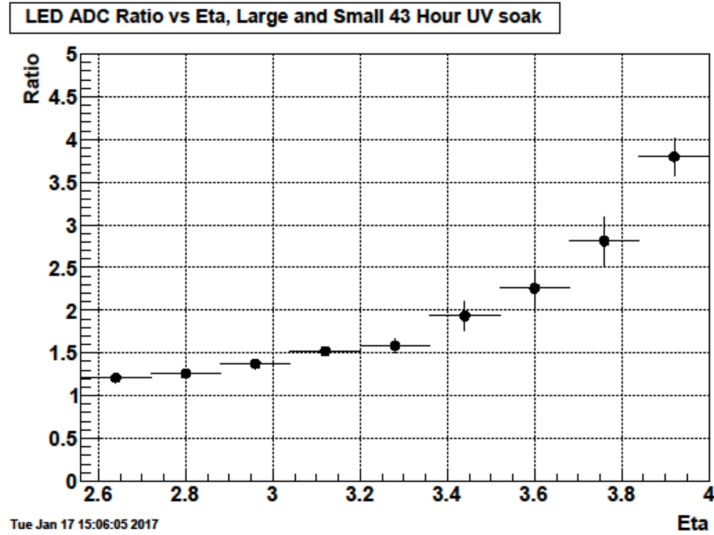


Figure L.7: LED amplitude after 43 hour exposure to UV-LED array, divided by LED amplitude before exposure, vs. pseudorapidity. Radiation-hard cells (which are a few cells that are “hardened” against the effect of radiation damage) were omitted from this diagram, as well as cells with misbehaving PMTs.

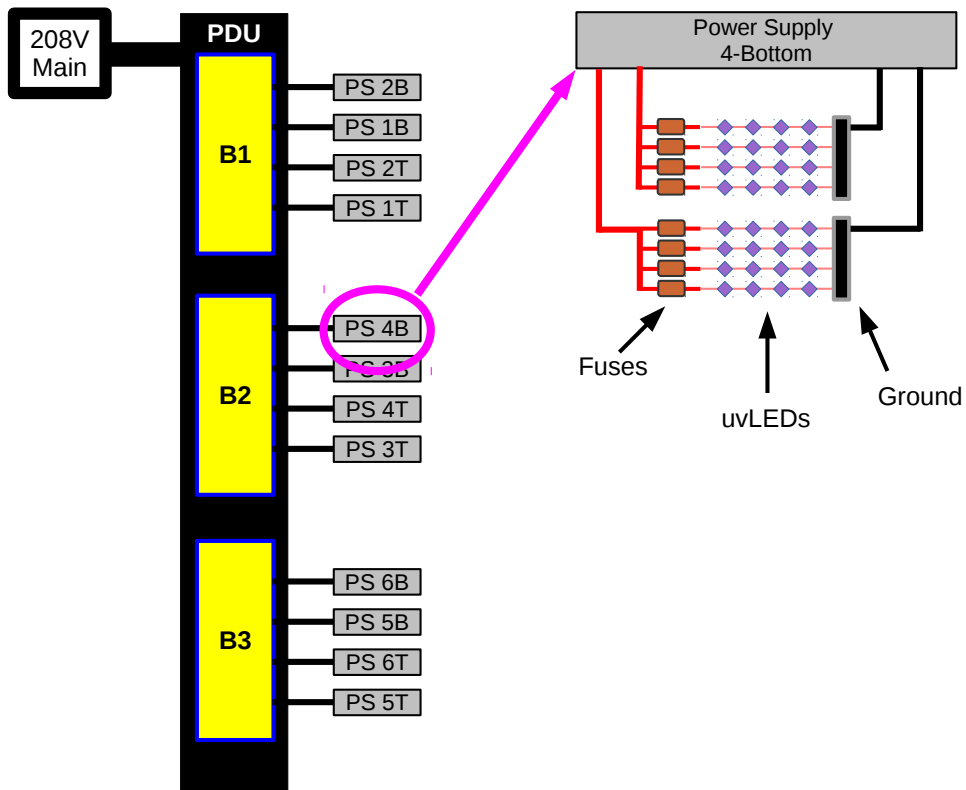


Figure L.8: Diagram of power distribution to the UV-LED array.

FMS Control GUI:

The screenshot displays the FMS Control GUI with several callout boxes pointing to specific elements:

- HV (High Voltage) Controls:** Points to the 'Large Cells HV' and 'Small Cells HV' sections, which include 'Turn Off' buttons and 'Update HV Status' buttons.
- HV Status:** Points to the 'Large Cell HV Status' and 'Small Cell HV Status' sections, which show 'ON' indicators for various cell IDs (e.g., 7005, 7006, 7007, 7008).
- Status Message Box:** Points to the 'UV Status lights updated' message in the 'Interlock Status' section.
- UVLED (Ultraviolet LED) Controls:** Points to the 'SHIFT CREW UVLED CONTROLS' section, which includes 'North uvLEDs' and 'South uvLEDs' with 'locked' indicators and 'Update UV Status' buttons.
- Log Messages:** Points to the bottom section of the interface, which displays a log of system events and status updates.
- HV / UV Interlock Status:** Points to the 'Interlock Status' section, which shows 'HV controls UNLOCKED'.
- Expert Controls:** Points to the 'Show Expert Controls' button in the top right corner.
- UVled Status and Current Loads:** Points to the 'South uvLEDs PDU Status' and 'North uvLEDs PDU Status' sections, which show current loads for Bank 1, Bank 2, and Bank 3.
- Panic Off button (quickly turns off HV and UV):** Points to the 'PANIC' button in the bottom right corner, which includes a warning message: 'Pressing "PANIC" will turn off FMS HV and UVleds, contact an expert if you click this button!'.

Figure L.9: Screenshot of the FMS HV and UV-LED graphical control interface, as well as software interlock.

Bibliography

- [1] LEADER, E. and C. LORC (2014) “The angular momentum controversy: what’s it all about and does it matter?” *Physics Reports*, **541**(3), pp. 163–248.
- [2] ELLIS, J. and R. JAFFE (1974) “Sum rule for deep-inelastic electroproduction from polarized protons,” *Phys. Rev. D*, **9**, pp. 1444–1446.
- [3] ASHMAN, J. *et al.* (1988) “A measurement of the spin asymmetry and determination of the structure function $g(1)$ in deep inelastic muon-proton scattering,” *Phys. Lett.*, **B206**, p. 364.
- [4] ASHMAN, J. *et al.* (1989) “An investigation of the spin structure of the proton in deep inelastic scattering of polarized muons on polarized protons,” *Nucl. Phys.*, **B328**, p. 1.
- [5] DE FLORIAN, D., R. SASSOT, M. STRATMANN, and W. VOGELSANG (2009) “Extraction of spin-dependent parton densities and their uncertainties,” *Phys. Rev.*, **D80**, p. 034030.
- [6] DE FLORIAN, D., R. SASSOT, M. STRATMANN, and W. VOGELSANG (2008) “Global analysis of helicity parton densities and their uncertainties,” *Phys. Rev. Lett.*, **101**, p. 072001.
- [7] BLÜMLEIN, J. and H. BÖTTCHER (2010) “QCD analysis of polarized deep inelastic scattering data,” *Nucl. Phys. B*, **841**(1), pp. 205–230.
- [8] LEADER, E., A. V. SIDOROV, and D. B. STAMENOV (2010) “Determination of polarized parton densities from a QCD analysis of inclusive and semi-inclusive deep inelastic scattering data,” *Phys. Rev. D*, **82**, p. 114018.
- [9] BALL, R. D. *et al.* [NNPDF COLLABORATION] (2013) “Unbiased determination of polarized parton distributions and their uncertainties,” *Nuclear Physics B*, **874**(1), pp. 36–84.

- [10] LEADER, E. and M. ANSELMINO (1988) “A crisis in the parton model: where, oh where is the proton’s spin?” *Zeitschrift für Physik C Particles and Fields*, **41**(2), pp. 239–246.
- [11] JAFFE, R. and A. MANOHAR (1990) “The g_1 problem: deep inelastic electron scattering and the spin of the proton,” *Nuclear Physics B*, **337**(3), pp. 509–546.
- [12] SEHGAL, L. M. (1974) “Angular momentum composition of the proton in the quark-parton model,” *Phys. Rev. D*, **10**, pp. 1663–1665.
- [13] NOCERA, E. *et al.* [NNPDF COLLABORATION] (2014) “A first unbiased global determination of polarized PDFs and their uncertainties,” *Nuclear Physics B*, **887**, pp. 276–308.
- [14] DE FLORIAN, D., R. SASSOT, M. STRATMANN, and W. VOGELSANG (2014) “Evidence for polarization of gluons in the proton,” *Phys. Rev. Lett.*, **113**, p. 012001.
- [15] ADAM, J. *et al.* [STAR COLLABORATION] (2018) “Longitudinal double-spin asymmetries for π^0 s in the forward direction for 510 GeV polarized pp collisions,” *Phys. Rev. D*, **98**, p. 032013.
- [16] THOMSON, M. (2013) “Modern particle physics,” Cambridge University Press.
- [17] GRIFFITHS, D. (2008) “Introduction to elementary particles,” Wiley.
- [18] HALZEN, F. and A. MARTIN (1984) “Quarks and leptons: an introductory course in modern particle physics,” Wiley.
- [19] GERLACH, W. and O. STERN (1922) “Der experimentelle Nachweis der Richtungsquantelung im Magnetfeld,” *Zeitschrift für Physik*, **9**(1), pp. 349–352.
- [20] FRIEDRICH, B. and D. HERSCHBACH (2003) “Stern and Gerlach: how a bad cigar helped reorient atomic physics,” *Physics Today*, **56**(12), pp. 53–59.
- [21] PATRIGNANI, C. *et al.* (2016) “Review of particle physics,” *Chin. Phys.*, **C40**(10), p. 100001.
- [22] RUTHERFORD, E. (1911) “The scattering of α and β particles by matter and the structure of the atom,” *The London, Edinburgh, and Dublin Philosophical Magazine and Journal of Science*, **21**(125), pp. 669–688.

- [23] GEIGER, H. and E. MARSDEN (1909) “On a diffuse reflection of the α -particles,” *Proceedings of the Royal Society of London A: Mathematical, Physical and Engineering Sciences*, **82**(557), pp. 495–500.
- [24] BLOOM, E. D. *et al.* (1969) “High-energy inelastic $e - p$ scattering at 6° and 10° ,” *Phys. Rev. Lett.*, **23**, pp. 930–934.
- [25] BREIDENBACH, M. *et al.* (1969) “Observed behavior of highly inelastic electron-proton scattering,” *Phys. Rev. Lett.*, **23**, pp. 935–939.
- [26] SREDNICKI, M. (2007) “Quantum field theory,” Cambridge University Press.
- [27] SCHWARTZ, M. (2014) “Quantum field theory and the standard model,” Cambridge University Press.
- [28] CASHER, A., H. NEUBERGER, and S. NUSSINOV (1979) “Chromoelectric-flux-tube model of particle production,” *Phys. Rev. D*, **20**, pp. 179–188.
- [29] CAHILL, K. (1978) “Example of color screening,” *Phys. Rev. Lett.*, **41**, pp. 599–601.
- [30] GREENSITE, J. (2003) “The confinement problem in lattice gauge theory,” *Prog. Part. Nucl. Phys.*, **51**, p. 1.
- [31] JAFFE, R. L. (1995) “Where does the proton really get its spin?” *Physics Today*, **48**, pp. 24–30.
- [32] ACCARDI, A. *et al.* (2016) “Electron ion collider: the next QCD frontier,” *Eur. Phys. J.*, **A52**(9), p. 268.
- [33] FUKAO, Y. (2007) “Double helicity asymmetry for π^0 production in polarized $p + p$ collisions at $\sqrt{s} = 200$ GeV : implications for the polarized gluon distribution in the proton,” Ph.D. thesis, Kyoto University.
- [34] DULAT, S. *et al.* (2016) “New parton distribution functions from a global analysis of quantum chromodynamics,” *Phys. Rev.*, **D93**(3), p. 033006.
- [35] AIDALA, C. A., S. D. BASS, D. HASCH, and G. K. MALLOT (2013) “The spin structure of the nucleon,” *Rev. Mod. Phys.*, **85**, pp. 655–691.
- [36] KUHN, S. E., J. P. CHEN, and E. LEADER (2009) “Spin structure of the nucleon - status and recent results,” *Prog. Part. Nucl. Phys.*, **63**, pp. 1–50.

- [37] LORCÉ, C. and K. F. LIU (2016) “Quark and gluon orbital angular momentum: where are we?” *Few Body Syst.*, **57**(6), pp. 379–384.
- [38] JI, X. and Y. ZHAO (2016) “The spin structure of the nucleon,” *International Journal of Modern Physics: Conference Series*, **40**, p. 1660001.
- [39] LEADER, E. (2016) “The photon angular momentum controversy: resolution of a conflict between laser optics and particle physics,” *Physics Letters B*, **756**, pp. 303–308.
- [40] JI, X.-D. (1997) “Gauge-invariant decomposition of nucleon spin,” *Phys. Rev. Lett.*, **78**, pp. 610–613.
- [41] BABCOCK, J., E. MONSAY, and D. W. SIVERS (1979) “Quantum chromodynamic predictions for inclusive spin spin asymmetries at large transverse momentum,” *Phys. Rev.*, **D19**, p. 1483.
- [42] CRAIGIE, N. S., K. HIDAKA, M. JACOB, and F. M. RENARD (1983) “Spin physics at short distances,” *Phys. Rept.*, **99**, pp. 69–236.
- [43] BUNCE, G., N. SAITO, J. SOFFER, and W. VOGELSANG (2000) “Prospects for spin physics at RHIC,” *Ann. Rev. Nucl. Part. Sci.*, **50**, pp. 525–575.
- [44] AIDALA, C. *et al.* (2005) “Research plan for spin physics at RHIC,” RHIC Spin Collaboration Spin Plan.
URL <https://spin.riken.bnl.gov/rsc/report/masterspin.pdf>
- [45] KRETZER, S. (2005) “Fragmentation of partons,” *Acta Phys. Polon.*, **B36**, pp. 179–186.
- [46] KAO, C. W., S. I. NAM, F. J. JIANG, and D. J. YANG (2014) “Fragmentation functions of pions and kaons in the nonlocal chiral quark model,” in *EPJ Web Conf.*, vol. 66, p. 06008.
- [47] COLLINS, J. C., D. E. SOPER, and G. F. STERMAN (1989) “Factorization of hard processes in QCD,” *Adv. Ser. Direct. High Energy Phys.*, **5**, pp. 1–91.
- [48] COLLINS, J. C., D. E. SOPER, and G. STERMAN (1985) “Factorization for short distance hadron-hadron scattering,” *Nuclear Physics B*, **261**, pp. 104–142.
- [49] COLLINS, J. C. and A. METZ (2004) “Universality of soft and collinear factors in hard-scattering factorization,” *Phys. Rev. Lett.*, **93**, p. 252001.

- [50] LEADER, E. (2001) “Spin in particle physics,” Cambridge University Press.
- [51] BASS, S. (2008) “The spin structure of the proton,” World Scientific Publishing Company Pte Limited.
- [52] BOURRELY, C., J. SOFFER, and E. LEADER (1980) “Polarization phenomena in hadronic reactions,” *Phys. Rept.*, **59**, pp. 95–297.
- [53] MANE, S. R., YU. M. SHATUNOV, and K. YOKOYA (2005) “Spin-polarized charged particle beams in high-energy accelerators,” *Rept. Prog. Phys.*, **68**, pp. 1997–2265.
- [54] XU, Q. (2018) “Measurement of longitudinal single-spin asymmetry for W^\pm production in polarized proton+proton collisions at STAR,” *Proceedings of Science*, **DIS2017**, p. 226.
- [55] ADAMCZYK, L. *et al.* [STAR COLLABORATION] (2014) “Measurement of longitudinal spin asymmetries for weak boson production in polarized proton-proton collisions at RHIC,” *Phys. Rev. Lett.*, **113**, p. 072301.
- [56] WANG, Y. (2004) “Measurement of inclusive forward neutral pion production in 200 GeV polarized proton-proton collisions at RHIC,” Ph.D. thesis, The University of Texas at Austin.
- [57] KLEM, R. D. *et al.* (1976) “Measurement of asymmetries of inclusive pion production in proton-proton interactions at 6 and 11.8 GeV/c,” *Phys. Rev. Lett.*, **36**, pp. 929–931.
- [58] HEPPELMANN, S. (2013) “Large p_T forward transverse single spin asymmetries of π^0 mesons at $\sqrt{s} = 200$ and 500 GeV from STAR,” *Proceedings of Science*, **DIS2013**, p. 240.
- [59] SOFFER, J., B. SURROW, and C. BOURRELY (2016) “Transverse double-spin asymmetries for electroweak gauge-boson production in high-energy polarized $p^\uparrow + p^\uparrow$ collisions,” [1611.05214](#).
- [60] WISSINK, S. (2008) “Longitudinal double-spin asymmetries for π^0 production at forward rapidities in pp collisions at $\sqrt{s} = 200$ GeV at STAR,” Presented at *SPIN2008*.
- [61] ADAMCZYK, L. *et al.* [STAR COLLABORATION] (2014) “Neutral pion cross section and spin asymmetries at intermediate pseudorapidity in polarized proton collisions at $\sqrt{s} = 200$ GeV,” *Phys. Rev.*, **D89**(1), p. 012001.

- [62] ADAM, J. *et al.* [STAR COLLABORATION] (2018) “Longitudinal double-spin asymmetries for dijet production at intermediate pseudorapidity in polarized pp collisions at $\sqrt{s} = 200\text{GeV}$,” *Phys. Rev.*, **D98**(3), p. 032011.
- [63] ADARE, A. *et al.* [PHENIX COLLABORATION] (2016) “Inclusive cross section and double-helicity asymmetry for π^0 production at midrapidity in $p+p$ collisions at $\sqrt{s} = 510\text{ GeV}$,” *Phys. Rev.*, **D93**(1), p. 011501.
- [64] ADAMCZYK, L. *et al.* [STAR COLLABORATION] (2015) “Precision measurement of the longitudinal double-spin asymmetry for inclusive jet production in polarized proton collisions at $\sqrt{s} = 200\text{ GeV}$,” *Phys. Rev. Lett.*, **115**(9), p. 092002.
- [65] ADAMCZYK, L. *et al.* [STAR COLLABORATION] (2017) “Measurement of the cross section and longitudinal double-spin asymmetry for di-jet production in polarized pp collisions at $\sqrt{s} = 200\text{ GeV}$,” *Phys. Rev.*, **D95**(7), p. 071103.
- [66] QUINTERO, A. (2018) “Recent STAR measurements to constrain the polarized gluon distribution function of the proton,” *Proceedings of Science*, **DIS2018**, Publication in preparation.
- [67] ALEKSEEV, I. *et al.* (2006) “Configuration manual: polarized proton collider at RHIC,” Brookhaven National Laboratory (BNL) Relativistic Heavy Ion Collider.
- [68] THOMAS, L. H. (1927) “The kinematics of an electron with an axis,” *The London, Edinburgh, and Dublin Philosophical Magazine and Journal of Science*, **3**(13), pp. 1–22.
- [69] BARGMANN, V., L. MICHEL, and V. L. TELEGDI (1959) “Precession of the polarization of particles moving in a homogeneous electromagnetic field,” *Phys. Rev. Lett.*, **2**, pp. 435–436.
- [70] DERBENEV, Y. S. *et al.* (1978) “Radiative polarization: obtaining, control, using,” *Part. Accel.*, **8**, pp. 115–126.
- [71] BLAND, L. C. (2015) “Transverse single spin asymmetries in hadronic interactions: an experimental overview and outlook,” *EPJ Web Conf.*, **85**, p. 01008.
- [72] HARRISON, M. *et al.* (2003) “The Relativistic Heavy Ion Collider project: RHIC and its detectors,” *Nucl. Instr. and Meth. A*, **499**.
- [73] BLAND, L. C. (2004) “STAR results from polarized proton collisions at RHIC,” in *Proceedings, 10th Advanced Research Workshop on High-Energy Spin Physics (SPIN-03): Dubna, Russia, September 16-20, 2003*, pp. 261–270.

- [74] LLOPE, W. J. *et al.* (2014) “The STAR vertex position detector,” *Nucl. Instrum. Meth.*, **A759**, pp. 23–28.
- [75] ADLER, C., A. DENISOV, E. GARCIA, M. J. MURRAY, H. STROBELE, and S. N. WHITE (2001) “The RHIC zero degree calorimeter,” *Nucl. Instrum. Meth.*, **A470**, pp. 488–499.
- [76] BARTOSZEK L. *et al.* (1991) “The E760 lead-glass central calorimeter: design and initial test results,” *Nucl. Instr. and Meth. A*, **301**(1), pp. 47–60.
- [77] BLAND, L. C. *et al.* (2008) “An electromagnetic shower profile in the lead-glass calorimeter in the energy range of 3–23 GeV,” *Instruments and Experimental Techniques*, **51**(3), pp. 342–350.
- [78] ADAMS, J. *et al.* [STAR COLLABORATION] (2006) “Forward neutral pion production in p+p and d+Au collisions at $\sqrt{s_{NN}} = 200$ GeV,” *Phys. Rev. Lett.*, **97**, p. 152302.
- [79] LEO, W. R. (2012) “Techniques for nuclear and particle physics experiments: a how-to approach,” Springer Science & Business Media.
- [80] BIESER, F.S. *et al.* (2003) “The STAR trigger,” *Nucl. Instr. and Meth. A*, **499**(2), pp. 766–777.
- [81] LANDGRAF, J. (2013) “Overview and evolution of the DAQ and trigger systems for the STAR Experiment at RHIC,” Presentation at *Triggering Discoveries in High Energy Physics*.
URL <https://indico.cern.ch/event/246374/contributions/542896/>
- [82] GOLDBERG, M., P. MATTERN, K. LENGWEILER, and P. LEVY (1973) “Radiation induced coloring of Cherenkov counter glasses,” *Nuclear Instruments and Methods*, **108**(1), pp. 119–123.
- [83] DELONG, K. W., V. MIZRAHI, G. I. STEGEMAN, M. A. SAIFI, and M. J. ANDREJCO (1990) “Color-center dynamics in a lead glass fiber,” *J. Opt. Soc. Am. B*, **7**(11), pp. 2210–2216.
- [84] BISHAY, A. (1970) “Radiation induced color centers in multicomponent glasses,” *Journal of Non-Crystalline Solids*, **3**(1), pp. 54–114.
- [85] FRIEBELE, E. J. and M. E. GINGERICH (1981) “Photobleaching effects in optical fiber waveguides,” *Appl. Opt.*, **20**(19), pp. 3448–3452.

- [86] ARAUJO, R. J. (1968) “Kinetics of bleaching of photochromic glass,” *Appl. Opt.*, **7**(5), pp. 781–786.
- [87] SHAHINYAN, A. *et al.* (2007) “An electromagnetic calorimeter for the JLab real Compton scattering experiment,” [0704.1830](#).
- [88] CRAWFORD, H. J., F. S. BIESER, and T. STEZELBERGER (2004) “The STAR scaler board, a 10 MHz 24-bit VME memory module,” *STAR Trigger Group*.
URL https://www.star.bnl.gov/public/trg/TSL/Manual/scaler_paper.pdf
- [89] NAKAGAWA, I. *et al.* (2008) “RHIC polarimetry,” *The European Physical Journal Special Topics*, **162**(1), pp. 259–265.
- [90] LEDNEV, A. (1995) “Electron shower transverse profile measurement,” *Nucl. Instr. and Meth. A*, **366**(2), pp. 292–297.
- [91] PAN, Y. (2015) “Measurement of transverse single spin asymmetries for π^0 and jets at large x_F in $\sqrt{s} = 500$ GeV polarized proton collisions at STAR,” Ph.D. thesis, University of California, Los Angeles.
- [92] EUN, L. (2012) “Transverse single spin asymmetries and cross-sections for forward π^0 and η mesons at large x_F in $\sqrt{s} = 200$ GeV $p^\uparrow + p$ collisions at STAR,” Ph.D. thesis, The Pennsylvania State University.
- [93] HAYS-WEHLE, J., J. SEELE, H. SPINKA, and B. SURROW (2012) “Relative Luminosity Analysis for run9 pp 200 GeV running,” STAR Analysis Note.
- [94] CRONIN-HENNESSY, D., A. BERETVAS, and P. DERWENT (2000) “Luminosity monitoring and measurement at CDF,” *Nucl. Instr. and Meth. A*, **443**(1), pp. 37–50.
- [95] MANION, A. (2014) “Double longitudinal helicity asymmetries in pion production from proton collisions, studies of relative luminosity determination, and the impact on determination of the gluon spin in the proton,” Ph.D. thesis, Stony Brook University.
- [96] “ListDeconvolve,” Wolfram Language and System Documentation Center.
URL <http://reference.wolfram.com/language/ref/ListDeconvolve.html>
- [97] “ImageDeconvolve,” Wolfram Language and System Documentation Center.
URL <http://reference.wolfram.com/language/ref/ImageDeconvolve.html>

- [98] CRAWFORD, H. *et al.* (2003) “Proposed addition of a shower max detector to the STAR zero degree calorimeters,” STAR Note SN0448.
URL <https://drupal.star.bnl.gov/STAR/starnotes/public/sn0448>
- [99] WANG, G. and THE STAR COLLABORATION (2010) “Search for local parity violation with STAR ZDC-SMD,” *Journal of Physics: Conference Series*, **230**(1), p. 012020.
- [100] TRENTALANGE, S., O. TSAI, G. IGO, H. HUANG, Y. X. PAN, J. DUNKELBERGER, W. Q. XU, A. SOHA, S. HEPPELMANN, and C. GAGLIARDI (2011) “T-1018 UCLA Spacordion tungsten powder calorimeter,” Fermilab Technical Scope of Work.
- [101] WIGMANS, R. (2000) “Calorimetry: energy measurement in particle physics,” International series of monographs on physics, Clarendon Press.
- [102] JONES, R.T. *et al.* (2006) “A bootstrap method for gain calibration and resolution determination of a lead-glass calorimeter,” *Nucl. Instr. and Meth. A*, **566**(2), pp. 366–374.
- [103] THE RHIC CNI POLARIMETRY GROUP (2016) “RHIC polarization for runs 9–15,” RHIC Polarimetry Analysis Note.
URL https://wiki.bnl.gov/rhicspin/upload/e/e4/Pol_resultsMay2016.pdf
- [104] “RooFit users manual,” ROOT Documentation.
URL <https://root.cern.ch/guides/roofit-manual>
- [105] DILKS, C. J. (2016) “Double helicity asymmetries of forward neutral pions from $\sqrt{s} = 510$ GeV pp collisions at STAR,” in *International Journal of Modern Physics: Conference Series*, vol. 40, World Scientific, p. 1660024.
- [106] JÄGER, B., A. SCHÄFER, M. STRATMANN, and W. VOGELSANG (2003) “Next-to-leading order QCD corrections to high- p_T pion production in longitudinally polarized pp collisions,” *Phys. Rev. D*, **67**, p. 054005.
- [107] JÄGER, B., M. STRATMANN, and W. VOGELSANG (2004) “Single-inclusive jet production in polarized pp collisions at $\mathcal{O}(\alpha_s^3)$,” *Phys. Rev. D*, **70**, p. 034010.
- [108] BALL, R. D. *et al.* [NNPDF COLLABORATION] (2011) “Reweighting NNPDFs: the W lepton asymmetry,” *Nuclear Physics B*, **849**(1), pp. 112–143.
- [109] PUMPLIN, J. *et al.* (2002) “New generation of parton distributions with uncertainties from global QCD analysis,” *JHEP*, **07**, p. 012.

- [110] DE FLORIAN, D., R. SASSOT, and M. STRATMANN (2007) “Global analysis of fragmentation functions for pions and kaons and their uncertainties,” *Physical Review D*, **75**(11), p. 114010.
- [111] ASCHENAUER, E. C., R. SASSOT, and M. STRATMANN (2015) “Unveiling the proton spin decomposition at a future electron-ion collider,” *Phys. Rev.*, **D92**(9), p. 094030, [1509.06489](#).
- [112] CHANG, Z. (2016) “Gluon polarization in longitudinally polarized pp collisions at STAR,” *Int. J. Mod. Phys. Conf. Ser.*, **40**, p. 1660021, [1512.05400](#).
- [113] ASCHENAUER, E. C., S. FAZIO, J. H. LEE, H. MANTYSAARI, B. S. PAGE, B. SCHENKE, T. ULLRICH, R. VENUGOPALAN, and P. ZURITA (2017) “The electron-ion collider: assessing the energy dependence of key measurements,” [1708.01527](#).
- [114] SURROW, B. (2014) “Future prospects of di-jet production constraining $\Delta g(x)$ at low x at STAR at RHIC,” *Proceedings of Science*, **DIS2014**, p. 241.
- [115] STAR COLLABORATION (2017) “The STAR forward calorimeter system and forward tracking system proposal,” STAR Note SN0648.
URL <https://drupal.star.bnl.gov/STAR/starnotes/public/sn0648>
- [116] PAGE, B. (2013) “Di-jet cross section and double spin asymmetry at mid-rapidity from polarized p+p collisions at $\sqrt{s} = 200$ GeV at RHIC,” Ph.D. thesis, Indiana University.

— Vita —
CHRISTOPHER J. DILKS

Education

- **Ph.D. Physics:** Pennsylvania State University, Fall 2011 to Fall 2018
- **B.S. Physics:** Pennsylvania State University, Fall 2007 to Spring 2011

Research and Teaching Experience

- **STAR Collaboration:** Ph.D. Student and Undergraduate Research, January 2011 to present
- **Teaching Assistant:** Senior Optics Lab, Fall Semester 2011 and Fall Semester 2013
- **Penn State LIGO Group:** Undergraduate Research, Summer 2010

Publications

1. **Longitudinal Double-Spin Asymmetries for π^0 s in the Forward Direction for 510 GeV Polarized pp Collisions**, *Phys. Rev. D*, **98**, p. 032013 (2018)
2. **Measurement of Transverse Single Spin Asymmetries in π^0 Production from $p^\uparrow + p$ and $p^\uparrow + A$ Collisions at STAR**, *Proceedings of Science*, DIS2016, p. 212 (2016)
3. **Double Helicity Asymmetries of Forward Neutral Pions from $\sqrt{s} = 510$ GeV pp Collisions at STAR**, *International Journal of Modern Physics: Conference Series*, vol. 40, World Scientific, p. 1660024 (2016)

Presentations

1. **Searching for Diffractive Contributions to the Forward π^0 Transverse Single-Spin Asymmetry in $\sqrt{s} = 200$ GeV Polarized pp Collisions**, *DNP 2018*, Waikoloa Village, HI (October 2018)
2. **Overview of Gluon Helicity Measurements at STAR**, Invited Talk, *SPIN 2018*, Ferrara, Italy (September 2018)
3. **Measurement of Transverse Single Spin Asymmetries in π^0 Production from $p^\uparrow + p$ and $p^\uparrow + A$ Collisions at STAR**, *DIS 2016*, Hamburg, Germany (April 2016)
4. **Transverse Single Spin Asymmetries in Forward π^0 Production from $p^\uparrow + p$ and $p^\uparrow + A$ Collisions at STAR**, Invited Talk, *RIKEN BNL Research Center Workshop*, Brookhaven National Laboratory (February 2016)
5. **Dependence of Forward π^0 Transverse Single Spin Asymmetries on Roman Pot Triggers from $\sqrt{s} = 200$ GeV pp Collisions at STAR**, *DNP 2015*, Santa Fe, NM (October 2015)
6. **Double Helicity Asymmetries of Forward Neutral Pions from $\sqrt{s} = 510$ GeV pp Collisions at STAR**, *SPIN 2014*, Beijing, China (October 2014)